Haji, Mohsin (2012) *Optical code division multiple access systems in AlGaInAs/InP*. PhD thesis.

http://theses.gla.ac.uk/3515/

Optical code division multiple access systems in AlGaInAs/InP

Mohsin Haji

May 2012

Submitted in fulfilment of the requirements for the degree of
Doctor of Philosophy (Ph.D.) to the School of Engineering
University of Glasgow

Abstract

The rise of photonic integration makes optical code division multiple access (OCDMA) worth revisiting due to its promising role in future all-optical networks. OCDMA has the potential to exploit the surplus bandwidth of optical fibres and to carry over to the optical domain the benefits seen CDMA radio communication systems, such as the effective sharing of the spectrum for multiple network subscribers, and resistance to jamming and eavesdropping. One of the major requirements for the deployment of OCDMA in networks is integration.

This thesis presents a research study of integrated OCDMA systems using the *AlGaInAs/InP* semiconductor material system. This material is considered due to its useful intrinsic properties such as thermal stability, strong electron confinement, and low threshold, making it suitable for fabricating optoelectronic devices. Two bespoke OCDMA systems are considered for integration: coherent temporal phase coding (TPC), and incoherent wavelength-hopping time-spreading (WHTS) OCDMA systems. TPC systems are excellent for high speed communications due to their static en/decoding enabling features. In this research, a 2×2 asymmetric Mach Zehnder interferometer (AMZI) is used to generate a 2-bit phase code, allowing multiplexing for up to four users. A semiconductor mode-locked ring laser is also embedded in the circuit, and using a synchronous mode-locking method, adequate signal en/decoding is achieved. WHTS systems on the other hand fully exploit the spectral and temporal space available in networks by assigning each user with a unique wavelength-time hop sequence for en/decoding data signals. Here, a mode-locked laser array is used with intracavity distributed Bragg reflectors (DBRs) for spectrally tuning each laser, and a 4:1 multimode interference coupler is used to combine the laser signals into a single channel for amplification, modulation and transmission. The integrated system is fully characterised and synchronisation experiments are performed to show the potential for its use in high speed multi-user networks.

Mode-locked lasers play an important role in many OCDMA implementations due to their wide spectrum and discrete temporal properties, which can be easily exploited during data en/decoding. Various mode-locked laser devices have been studied during this research with additional embedded components such as intracavity DBRs and phase controllers for precise tuning of the wavelength and pulse repetition frequency. However, the noisy nature of passively operating mode-locked lasers make them prone to high jitter, which can result in high bit error rates. Synchronisation schemes are thereby explored in order to temporally stabilise the pulse oscillations to make them suitable for use in long haul transmission systems. This includes synchronous and hybrid mode-locking, as well as a passive technique using an optical fibre loop to provide phase feedback, which is shown to promote ultralow RF linewidths in mode-locked lasers.

Publications

Full papers in refereed journals:

1. **M. Haji**, L. Hou, A. E. Kelly, J. Akbar, J. H. Marsh, J. M. Arnold, and C. N. Ironside, “High frequency optoelectronic oscillators based on the optical feedback of semiconductor mode-locked laser diodes,” Optics Express, Vol. 20, No. 3, pp. 3268-3274, 2012.

2. L. Hou, **M. Haji**, J. Akbar, A. C. Bryce, and J. H. Marsh, “160-GHz 1.55μm colliding pulse mode-locked AlGaInAs/InP laser with high power and low divergence angle,” IEEE Photon. Technol. Lett., Vol. 24, No. 12, pp 1057-1059, 2012.

3. A. C. Bryce, L. Hou, **M. Haji**, J. Akbar, and J. H. Marsh, “Low cost light source for optical communication systems,” SPIE Newsroom: Optoelectronics and Communications, 2012.

4. L. Hou, **M. Haji**, J. H. Marsh, and A. C. Bryce, “490-fs pulse generation from a passive C-band AlGaInAs/InP mode-locked laser,” Optics Letters, Vol. 37, No. 5, pp. 773-775, 2012.

5. J. Akbar, L. Hou, **M. Haji**, J. H. Marsh, A. C. Bryce, and A. E. Kelly, “High power (130 mW) 40 GHz 1.55 μm mode locked DBR lasers with integrated optical amplifier,” Optics Letters, Vol. 37, No. 3, pp. 137-143, 2012.

6. L. Hou, **M. Haji**, J. Akbar, J. H. Marsh, and A. C. Bryce, “AlGaInAs/InP monolithically integrated DFB laser array,” IEEE Journal of Quantum Electronics, Vol. 48, No. 2, pp. 137-143, 2012.

7. L. Hou, **M. Haji**, J. H. Marsh, and A. C. Bryce, “10 GHz AlGaInAs/InP 1.55 μm passively mode-locked laser with low divergence angle and timing jitter,” Optics Express, Vol. 19, No. 26, pp. B75-B80, 2011.

8. L. Hou, **M. Haji**, J. Akbar, J. H. Marsh, A. C. Bryce, “CWDM source based on AlGaInAs/InP monolithically integrated DFB laser array,” Optics Letters, Vol. 36, No.21, pp. 4188-4190, 2011.

9. L. Hou, **M. Haji**, B. Qiu, J. Akbar, A. C. Bryce, J. H. Marsh, “10 GHz AlGaInAs/InP 1.55 μm passively mode-locked laser with low divergence angle and timing jitter,” IEEE Photonics Technology Letters, Vol. 23, pp 1079-1081, 2011.

10. L. Hou, **M. Haji**, B.C. Qiu, A. C. Bryce, “Mode-locked laser array monolithically integrated with MMI combiner, SOA and EA modulator,” IEEE Photonics Technology Letters, Vol. 23, pp. 1064-1-67, 2011.

11. L. Hou, **M. Haji**, C. Li, B. C. Qiu, and A. C. Bryce, “80-GHz AlGaInAs/InP 1.55 μm colliding-pulse mode-locked laser with low divergence angle and timing jitter,” Laser Physics Letters, Vol. 8, No. 7, pp. 535–540, 2011.

12. R. P. Green, **M. Haji**, L. Hou, G. Mezosi, R. Dylewicz and A. E. Kelly, “Fast saturable absorption and 10 GHz wavelength conversion in Al-quaternary multiple quantum wells”, Optics Express, Vol.19, pp.9737-9743,2011.

13. L. Hou, **M. Haji**, B. C. Qiu, A. C. Bryce, “Low divergence angle and low jitter 40 GHz AlGaInAs/InP 1.55 μm mode-locked lasers”, Optics Letters, Vol. 36, pp.966-968, 2011.

14. L. Hou, **M. Haji**, R. Dylewicz, B. C Qiu, A. C. Bryce, “10 GHz mode-mocked extended cavity laser integrated with surface-etched DBR fabricated by Quantum Well Intermixing,” IEEE Photonics Technology Letters, Vol. 23, pp. 82-84, 2011.

15. L. Hou, **M. Haji**, R. Dylewicz, B. C. Qiu, and A. C. Bryce, "Monolithic 45-GHz Mode locked surface-etched_DBR laser using quantum well intermixing technology," IEEE Photonics. Technology Letters, Vol. 22, pp. 1039-1041, 2010.

16. L. Hou, **M. Haji**, R. Dylewicz, P. Stolarz, B. C Qiu, E. A. Avrutin, A. C. Bryce, "160 GHz harmonic mode-locked AlGaInAs 1.55 µm strained quantum well compound cavity laser," Optics Letters, Vol.35, pp. 3991-3993, 2010.

17. L. Hou, R. Dylewicz, **M. Haji**, P. Stolarz, B. Qiu, A. C. Bryce, "Monolithic 40 GHz passively mode-locked AlGaInAs/InP 1.55 µm MQW laser with surface-etched distributed Bragg reflector," IEEE Photonics Technology Letters, Vol. 22, pp. 1503-1505, 2010.

18. L. Hou, P. Stolarz, R. Dylewicz, **M. Haji**, J. Javaloyes, B. C. Qiu, A. C. Bryce, "160 GHz passively mode-locked AlGaInAs 1.55 µm strained quantum well compound cavity laser," IEEE Photonics Technology Letters, Vol. 22, pp. 727-729, 2010.

Conference papers:

1. **M. Haji**, L. Hou, A. E. Kelly, J. Akbar, J. H. Marsh, J. M. Arnold, and C. N. Ironside, "Ultralow 192 Hz RF linewidth optoelectronic oscillator based on the optical feedback of mode-locked laser diodes," CLEO/EQEC, San Jose, California USA 2012, oral presentation.

2. L. Hou, **M. Haji**, J. Akbar, J. H. Marsh and A. C. Bryce, "490-fs pulse generation from a passively mode locked laser with an integrated passive waveguide using quantum well intermixing," CLEO/EQEC, San Jose, California USA 2012, oral presentation.

3. J. Akbar, L. Hou, **M. Haji**, R. Dylewicz, M. J. Strain, J. H. Marsh, A. C. Bryce, and A. E. Kelly, "High average power (200 mW) 40 GHz mode-locked DBR lasers with integrated tapered optical amplifiers," CLEO/EQEC, San Jose, California USA 2012, oral presentation.

4. J. Akbar, L. Hou, **M. Haji**, M. Strain, P. Stolarz, J. H. Marsh, A.C. Bryce and A. E. Kelly, "High peak power (550 mW) 40 GHz mode-locked DBR lasers with integrated optical amplifier", IEEE Annual Photonics Meeting 2011, paper ThK4, oral presentation.

5. L. Hou, **M. Haji**, A. C. Bryce, J. H. Marsh, "160 GHz 1.55 µm colliding-pulse mode-locked AlGaInAs/InP laser with reduced optical overlap," IEEE Annual Photonics Meeting 2011, paper ThK2, oral presentation.

6. L. Hou, **M. Haji**, J. Akbar, A. C. Bryce, J. H. Marsh, "Colliding-pulse mode-locked AlGaInAs laser operating at 20 GHz with narrow RF linewidth," IEEE Annual Photonics Meeting 2011, paper ThK6, oral presentation.

7. C. N. Ironside, **M. Haji**, L. Hou, J. Akbar, A. E. Kelly, K. Seunarine, B. Romeira, and J. M. L. Figueiredo. "Review of optoelectronic oscillators based on mode locked lasers and resonant tunneling diode optoelectronics (invited)", Applications of Optics and Photonic (AOP), Braga, 2011, invited oral presentation

8. L. Hou, **M. Haji**, J. H. Marsh, A. C. Bryce, "10-GHz AlGaInAs/InP 1.55 µm mode-locked laser with low divergence angle and timing jitter," ECOC 2011, Geneva, Switzerland, oral presentation.

9. L. Hou, E. A. Avrutin, R. Dylewicz, **M. Haji**, B. C. Qiu and A. C. Bryce, "AlInGaAs mode-locked lasers for ultrashort pulse harmonic ML (invited)," ICTON 2011, Stockholm, Sweden, invited oral presentation.

10. **M. Haji**, A. E. Kelly, L Hou, A. C. Bryce, J. M. Arnold, C. N. Irondside, “A low jitter passively mode locked laser diode at 40 GHz using regenerative feedback via an optical fiber loop,” CLEO/Europe-EQEC Conference 2011, Munich, Germany, CB12.5, oral presentation.

11. R. P. Green, **M. Haji**, L. Hou, G. Mezosi, R. Dylewicz, and A. E. Kelly, “Fast absorption recovery and wavelength conversion in 1.55 µm AlInGaAs MQW lasers,” CLEO/Europe-EQEC Conference 2011, Munich, Germany, poster presentation.

12. L. Hou, **M. Haji**, C. Li, J. Akbar, J. H. Marsh, A. C. Bryce “80-GHz AlGaInAs/InP 1.55 µm colliding-pulse mode-locked laser with low divergence angle and timing jitter,” CLEO/Europe-EQEC Conference 2011, Munich, Germany, CB12.2, oral presentation.

13. L. Hou, J. Akbar, **M. Haji**, P. Stolarz, R. Dylewicz, A. Kelly, M. Sorel, J. Marsh, A. C Bryce; B.C. Qiu, “40 GHz AlGaInAs/InP 1.55 µm passively mode-locked laser with low divergence angle and timing jitter,” CLEO 2011, Baltimore, Maryland, USA, CTuA6, oral presentation.

14. **M. Haji**, L. Hou, A. E. Kelly, J. Akbar, J. M. Arnold, C. N. Ironside, “An all-optical regeneratively mode-locked laser diode with a 40 GHz repetition rate,” 9th Millimeter-wave User Group meeting, UK, Session II, Glasgow 2011, oral presentation.

15. L. Hou, **M. Haji**, R. Dylewicz, Bocang Qiu, A. C. Bryce, “Mode-locked laser array monolithically integrated with SOA and EA Modulator,” OFC 2011, Los Angeles, California, USA, OThG4, oral presentation.

16. L. Hou, **M. Haji**, R. Dylewicz, P. Stolarz , and A. C. Bryce, “160 GHZ passively mode-locked AlGaInAs 1.55um compound cavity laser with single deeply etched intra-cavity reflector (invited),” 14th Laser optics 2011, St. Petersburg, Russia, invited oral presentation.

17. A. C. Bryce, L. Hou, **M. Haji**, R. Dylewicz, P. Stolarz, “High frequency mode-locking of diode lasers (invited),” Optoelectronic and Microelectronic Materials and Devices (COMMAD), 2010 Conference on, The Australian National University Canberra, Australia, invited oral presentation.

18. **M. Haji**, L. Hou, A. E. Kelly, R. Green, G. Mezosi, J. Javaloyes, A. C. Bryce, J. M. Arnold, “Sub-picosecond pulse generation using fast saturable absorption in AlGaInAs/InP Quantum Wells,” 23rd Annual Photonics Society Meeting 2010, Denver, CO, USA, Tuy4, oral presentation.

19. L. Hou, **M. Haji**, R. Dylewicz, J. M. Arnold, A. C. Bryce, “Monolithic 45-GHz mode locked surface-etched DBR laser using quantum well intermixing technology,” 15th ECIO 2010, Cambridge, London, UK, ThD4 oral presentation.

20. L. Hou, **M. Haji**, R. Dylewicz, P. Stolarz, A. E. Kelly, J. M. Arnold, J. H. Marsh, R. M. De La Rue, M. Sorel, A. C. Bryce, B. Qiu, “Monolithic 40 GHz passively mode locked AlGaInAs/InP 1.55 µm MQW laser with surface-etched bragg gratings,” CLEO 2010, San Jose, California , USA, CMII3 oral presentation.

Glossary of symbols and abbreviations

Abbreviations

AC	Alternating current
ADS	Advanced design systems (Agilent software)
AM	Amplitude modulation
AMZI	Asymmetric Mach-Zehnder interferometer
ASE	Amplified spontaneous emission
atten.	Optical attenuator
AWG	Arrayed waveguide gratings
BER	Bit error rate
BOSSNET	Boston South network
BPSK	Binary phase shift keying
CCL	Composite cavity loop
CCM	Compound cavity mode-locking
CDR	Clock and data recovery
CHP	Carrier hopping prime
circ.	Optical circulator
CPM	Colliding pulse mode-locking
CWDM	Course wavelength division multiplexing
DBR	Distributed Bragg reflector
DCA	Digital communications signal analyser (high speed oscilloscope)
DPSK	Differential phase shift keying
DS	Dispersion shifted
EAM	Electroabsorption modulator
EDFA	Erbium doped fibre amplifier
EOM	Electrooptic modulation
ER	Extinction ratio
FBG	Fibre Bragg grating
FDR	Frequency detuning range
FFH	Fast frequency hopping
FFP	Far-field pattern
FH	Frequency Hop
FP	Fabry-Pérot
FR	Free running
FRL	Farfield reduction layer
FSR	Free spectral range
FTTH	Fibre to the home
FWHM	Full-width half-maximum
GND	Ground
GRINSCH	Graded refractive index separate confinement heterostructure
HML	Hybrid mode-locking
HSQ	Hydrogen Silsequixane
ICR	Intracavity reflector
IML	Incomplete mode-locking

ITU	International telecommunication union
LAN	Local area network
LED	Light emitting diode
LI	Light vs. Current
MAI	Multi-access interference
MAN	Metropolitan area network
MCPM	Multiple colliding pulse mode-locking
ML	Mode-locking
MLLD	Mode-locked laser diode
MMI	Multimode interference
MQW	Multiple quantum-wells
MZI	Mach-Zehnder interferometer
MZM	Mach-Zehnder modulator
NOLM	Nonlinear optical loop mirror
OCDMA	Optical code division multiple access
OEO	Optoelectronic oscillator
OFDM	Orthogonal frequency division multiplexing
OFL	Optical feedback loop
OLT	Optical line terminal
ONU	Optical network unit
OOK	On-off keying
OSA	Optical spectrum analyser
PCB	Printed circuit board
PECVD	Plasma enhanced chemical vapour depositing
PML	Pure mode-locking
PMMA	Polymethyl methacrylate
PON	Passive optical network
POS	Psuedo-orthogonal sequence
Q	Quality
QAM	Quadrature amplitude modulation
QCSE	Quantum confined Stark effect
QoS	Quality of service
QPSK	Quadrature phase shift keying
QW	Quantum-well
QWI	Quantum-well intermixing
QWT	Quarter wave transformer
RBW	Resolution bandwidth
RF	Radio frequency
RMS	Root mean square
RZ	Return to zero
SA	Saturable absorber
SAC	Spectral amplitude coding
SHG	Second harmonic generation
SMF	Single mode fibre
SML	Synchronous mode-locking
SOA	Semiconductor optical amplifier
SPC	Spectral phase coding
SPECTS	Spectrally phase encoded time-spreading
SPM	Self-phase modulation

SRL	Semiconductor ring laser
SSB	Single side-band
TBP	Time-bandwidth product
TDM	Time division multiplexing
TE	Transverse electric
TM	Transverse magnetic
TOAD	Terahertz optical asymmetric demultiplexer
TPC	Temporal phase coding
VBW	Video bandwidth
WDM	Wavelength division multiplexing
WHTS	Wavelength-hopping time-spreading
XAM	Cross-absorption modulation
XOR	Exclusive OR logic

Mathematical symbols

A	Area
α	Intrinsic loss
A_{nr}	Monomolecular recombination coefficient
B	Radiative recombination coefficient
B	Complex wave amplitude
c	Speed of light
C	Auger recombination coefficient
C	Capacitance
Cr	Spectrum peak:valley ratio
dG/dN	Differential gain
ΔV_{rf}	RF linewidth
E_b	Barrier energy
E_r	Substrate relative permitivity
E_{sat}	Saturation energy
eV	Electron volt
f	Frequency
f_c	Collective frequency
f_{inj}	Injection frequency
f_{MLLD}	Fundamental frequency of a MLLD
F_r	Pulse repetition frequency
f_{rep}	Mode-locking repetition rate
f_{RF}	RF frequency
g	Material gain
Γ	Confinement factor
$GF(p)$	Galois field sequence
G_{net}	Net gain
h	Plank's constant
I_{gain}	Current applied to the gain section
k	Absorption coefficient

κ	Coupling coefficient
k_bT	Boltzmann's constant
λ	Wavelength
L	Length
L	Inductance
L_{eff}	Effective length
l_{tot}	Total losses
m	Integer multiple, or subharmonic order
m^*	effective mass
N	Carrier density
N_a	Number of lasers in array
N_c	Number of pulses in a code word
n_c	Effective index of cladding region
n_{eff}	Effective index
n_g	Group index
Ω	Ohms
ω	Angular frequency
Φ	Phase change
π	Phase shift
P_{inj}	Injection signal intensity
q	Electron charge
R	Reflectivity
R	Resistance
σ	Cross sectional mode area
τ	Carrier lifetime
t_{gw}	Gate width
T_{oc}	Output coupler transmission
T_{rt}	Cavity round trip time
v	Phase velocity
V_a	Volume of active region
V_{bi}	Diode voltage potential
V_{SA}	Voltage applied to the SA section
W_{eff}	Effective width
W_n	Walsh-Hadamard sequence matrix
y	Waveguide offset
z	Direction of propagation
Z_0	Characteristic impedance
Z_L	Load impedance
Z_S	Source impedance
Z_T	Impedance transformation

Contents

Chapter 1 Optical CDMA in AlGaInAs/InP: Introduction

Chapter 2 III-V semiconductor device technologies using AlGaInAs/InP multiple quantum-wells

Chapter 3 OCDMA subsystem technologies

Chapter 4 Semiconductor mode-locked lasers

Chapter 5 Pulse stabilisation and jitter reduction in MLLDs

Chapter 6 Coherent OCDMA using an asymmetric Mach Zehnder interferometer

Chapter 7 Incoherent OCDMA system using WHTS en/decoder

Chapter 8 Conclusions

Chapter 1

Optical CDMA in *AlGaInAs/InP*: Introduction

This thesis presents a practical research study of optical code division multiple access (OCDMA) systems integrated in the *AlGaInAs/InP* semiconductor material system. The aim of the research was to design and develop specified OCDMA systems on a single chip and to subsequently characterise systems and subsystem components. In this chapter, a brief introduction to OCDMA is given along with a literature review evaluating the progression and current trends in the field. The research aims are then shown followed by an overview of the remainder of the thesis contents.

1.1 OCDMA

OCDMA is a multiplexing technique that allows multiple users to securely and efficiently share a single fibre optic channel by assigning each user a unique code sequence that is multiplied to the data signal during transmission, and descrambled by applying the same code sequence at the receiver circuit. Doing so provides efficient use of the bandwidth available in the channel, and prevents eavesdropping by unintended network recipients. Since the first practical demonstration in the mid 80s [1], there has been a great effort in trying to realise the integration of OCDMA circuits on a single semiconductor chip to see benefits in easing system fabrication, system manageability, and costs that are ultimately passed down to the end-users. As well as telecom networks, there are a number of other applications where OCDMA systems can be applied such as spectroscopy, optical computing, neural networking, radar, and system interconnects for backbone infrastructures [2, 3]. Here however, the importance of OCDMA in optical networks is highlighted as being the primary application.

At present, the prevalent discord between the service requirements of transport networks and access networks will undoubtedly become a serious issue as a result of the ever-increasing bandwidth demands. The expected rise in the popularity of high definition services, and the proposed 6 GB/s super HD class digital movies on a peer-to-peer basis will require bandwidths exceeding 100s of Gb/s per user [4]. Moreover, real time bidirectional applications such as cloud computing, virtual reality, and medical telediagnosis and surgery are expected to become widespread [5, 6]. These, as well as other customised services will require a wide variety of service options in both bit rate and quality of service (QoS), and without an abundant uplink bandwidth either on-demand or an always-on basis, these application can not be well-supported. Therefore, the current criterion of low bit rate uplinks and high bit rate downlink in future networks will be a problem, and upgrading FTTH services towards a gigabit-symmetric category will be necessary to meet users’ needs [7, 8].

1.1.1 Current multiple access systems

TDM passive optical networks (PONs) and Ethernet PONs are currently being deployed into high speed networking systems [9, 10]. Existing TDM PONs provide data rates ranging from 155 Mb/s to 1 Gb/s, shared among 8 – 32 users [11], although this is likely to increase dramatically with recently reported data speeds up to 10.2 THz [12]. However, the time sharing nature of the TDM uplink transmission limits the bandwidth of the individual users due to the time-slot based multi access protocol [11]. Provisioning different bit rates to each user is also a challenge. WDMA systems on the other hand are a natural approach to enhance the uplink capacity [13]. In WDM, large bit rates can be aggregated during transmission since several wavelengths transport several data streams in parallel. Therefore, a smooth migration from TDM PONs to WDMA is expected due to the common specifications and mass productions of integrated circuits which can reduce the cost of the optical network unit (ONU). Coarse WDM (CWDM) with a channel spacing of 20 nm in the spectral range from 1270 to 1610 nm has been linked with the PON architecture according to ITU G.694-2 [14]. This provides a total of 18 usable wavelength channels, which may not be sufficient for multiple access systems with a larger number of users. Dense WDM may offer more bandwidth to more users, with a shorter wavelength spacing between the channels (typically 3.2 nm), however, the wavelength of each light source must be monitored in order to avoid crosstalk between channels. Moreover, the requirement of tunable devices with temperature control will inevitably increase the costs of the system. There are also issues in data backbone networks, such as electronic node bottlenecks, and wasteful subdivision of traffic. For these reasons, a better physical layer model is required to increase the network speed and the number of users.

So far, despite the considerable amount of research, OCDMA has long remained outside the mainstream of optical communications research. This is mainly due to the immaturity of optical devices that are proprietary to OCDMA such as optical en/decoders and optical thresholding devices. Also, the prominent WDM technology adequately provides the demands for current high speed data transmissions and network functionalities. As with Wireless CDMA systems, advanced systems such as OCDMA are often criticised due to their complexity. Over the past decade however, significant progress has been shown in device technologies for optical en/decoding [2, 15], as well as optical thresholding [15-17]. And due to the anticipated issues with current multiplexing schemes, OCDMA is now recognised for its high networking flexibility and providing additional network dimensions (other than wavelength and time), as well as having very good compatibility with the more established TDM and WDM schemes. A schematic of OCDMA over PON scenario is shown in Fig. 1.1.

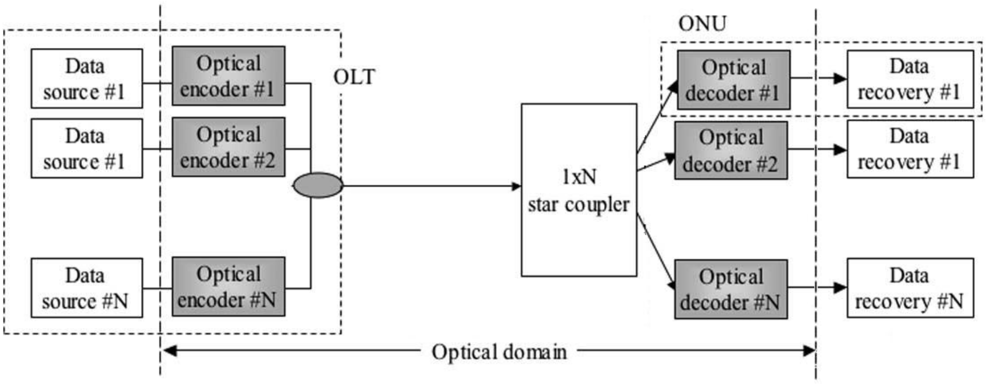

Figure 1.1 OCDMA-PON diagram. (ONU: optical network unit, OLT: optical line terminal) [2].

1.1.2 History of OCDMA

Spread spectrum techniques have been around since the Second World War where it was considered for securing radio wave communications for wirelessly controlling missiles [18]. It works by distributing the generated bandwidth of a communicated signal (e.g. electrical, electromagnetic, or acoustic) over a wider bandwidth to provide robust security when transmitting information. There are two ways in which this is achieved, frequency hopping and direct sequence spreading [3]. These two techniques form the foundations of all CDMA systems.

CDMA systems these days are widely used in mobile communications, particularly in third generation wireless communication systems (3G) [19]. CDMA enables multiplexing by assigning unique codes to users to realise multiple access in networks and support multiple simultaneous transmissions over the same time space and frequency. This concept was first introduced into fibre optic communication systems in the 1970s [20], and soon after realised experimentally in the mid 80s by Prucnal, et al. [1], where encoding and decoding operations were all performed in the optical domain. The advantage of OCDMA over other access methods is that it enables multiple users to fully share temporal and bandwidth allocations in a network. This is particularly useful in bursty networks with large capacities and high number of users. As with TDMA and WDMA systems, OCDMA can enable high speed transmissions with variable data rates and QoS at the physical layer without the use of higher level protocols. It is a simple, cost effective method using mostly passive optical components so that signal multiplexing, routing and switching can be achieved efficiently. On the whole, it enables asynchronous random access, simple management, flexible networking, good compatibility with WDM/TDM, and provides confidentiality of data during transmission [3], making it a current hot topic of research.

In 1986, Prucnal, et al. proposed the first optical encoder/decoder pair for incoherent OCDMA applications, specifically fibre-optic LANs [1]. This work showed that pseudo orthogonal codes could be implemented as tapped optical fibre delay lines. Similarly, all optical processing for encoding and decoding could be carried out using tapped delay lines, which verified that an optical network could be realised by allowing multiple users to share a single transmission line without any electronic intervention. During this time, Weiner et al. embarked on an equally important development, now known as coherent OCDMA [21]. They found that coherent, narrow pulse, ultra wide bandwidth spectra could be produced and manipulated in the spectral domain using phase codes, or in the phase domain, for use in fast reconfigurable OCDMA based networks. Crucially, this work meant that the reputable developments in RF communications could also be applied to optical communications, such as the use of bipolar and spectral encoding schemes.

These two efforts lead to a growing body of work and investigations in OCDMA, spawning new developments, particularly in unipolar codes such as optical orthogonal codes/pseudo orthogonal sequences (OOC/POS) [3, 11, 22-26]. These codes however were criticised due to their one-dimensionality, which were quite poor in terms of spectral efficiency, resulting in low speed data transmission rates. Furthermore, 1D codes have associated low cardinality, as well as problems with multiple access interference (MAI). This led to a huge interest in two-dimensional (2D) codes during the early 90s [3, 11, 26]. Based on fast frequency hopping (FFH), 2D codes create more leeway in allocating resources in time and optical frequency, and were regarded as being more permissive with multiple pulses per row and or column, which was shown to enormously increase the capacity of the system as well as improving code performance [3].

One of the most important works on 2D systems in the 90s was that of Tancevksi and Andonovic in 1994 [27], whom introduced the concept of Wavelength Hopping/Time Spreading OCDMA systems. This work was significant in that it featured an OCDMA scheme that could greatly improve system integrity with truly asynchronous performance. It proved that 2D systems could naturally increase system capacity allowing more users to transmit data signals simultaneously by using an encoding scheme based on prime hop sequences for spreading the signal. This allowed greater spectral efficiency as well as better use of code constructions that provided an autocorrelation function of zero sidelobes, and cross-correlations of at most one. Thus, code orthogonality was harnessed much more effectively compared with 1D prime sequences.

Since then, 2D codes have been rigorously put to test. In [28], a 1.25 Gb/s FFH-OCDMA system was demonstrated supporting up to 16 users over 80 km, using data encoded via fibre Bragg grating arrays. This experimental setup is shown in Fig. 1.2. In 2006, OCDMA over a star network topology was demonstrated at Princeton University, using off the shelf devices to implement 115 Gchip/s 2D WHTS OCDMA, at 5 GB/s per user with less than 10^{-13} bit error rate [29]. Other examples of 2D OCDMA systems can be found in [3, 11, 26].

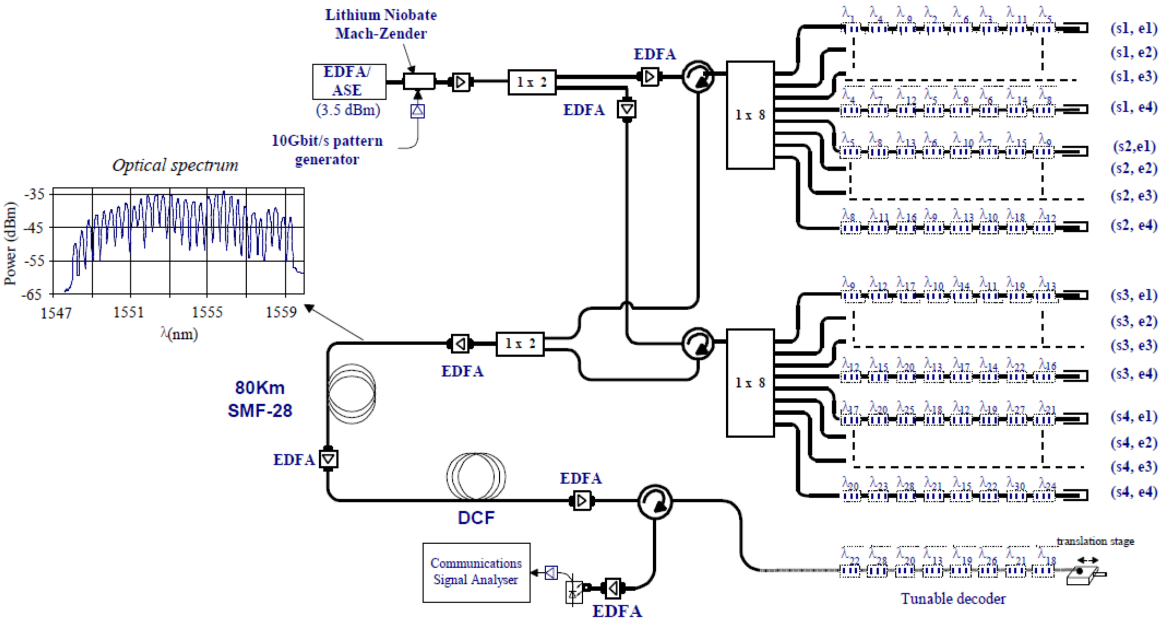

Figure 1.2 Wavelength-time OCDMA system setup operating at 1.25 Gb/s supporting 16 users through 80 km of fibre [28].

As for coherent OCDMA systems, since the efforts of Weiner et al, a number of developments in bipolar codes were proposed. Coherent OCDMA uses binary codes such as *m*-sequences, Gold codes, and Walsh-Hadamard codes [3], which are based on those used in RF CDMA systems. In terms of hardware, many en/decoders have been realised and many reports and field trials have emerged. In 2006, Wang, et al. [30] reported a 111 km transmission of 3-WDM × 10-OCDMA × 10.71 Gb/s/user, using multiport optical en/decoders in the OLT and transverse filter type decoders in the ONU, in the DPSK data format. This truly asynchronous OCDMA system was demonstrated with 10 users per wavelength achieving bit error rates less than 10^{-9} without the use of forward error correction or optical thresholding devices. The experimental setup is shown in Fig. 1.3.

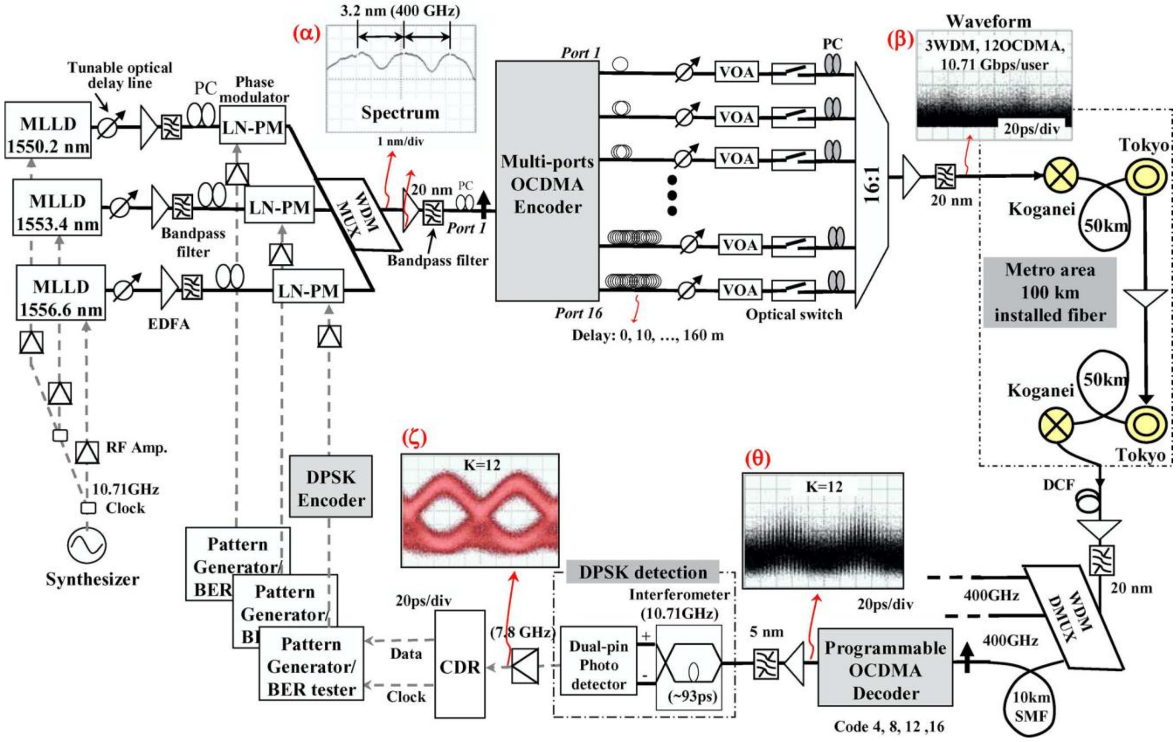

Figure 1.3 Experimental setup for WDM/OCDMA network architecture [30].

1.2 OCDMA challenges and requirements

For OCDMA to become widely adopted as a replacement for existing optical network physical layer technologies, its processes must become fully integrated, with scalable, flexible and highly secure functionalities. With excellent coding algorithms in abundance [3, 11, 31], the main challenges are considered to be purely technical. Previous examples of OCDMA implementations and field trials show data rates as high as 10 GB/s per user, with up to 30 simultaneous users [30]. But for wide-spread approval and deployment across commercial networks, OCDMA systems must be required to support at least 100 subscribers with a bit error rate less than 10^{-9}, and 1,000s of nodes across several kilometres of single mode fibre [32]. Embedded OTDM/WDM functionalities are also crucial for interoperability with existing transparent optical systems.

In addition to technical concerns, another crucial issue for achieving practical implementations of OCDMA is cost, a viable solution to which is to employ novel integrated passive as well as active devices using low cost component integration. This would reduce the overall system parts to test as well as simplifying the nature of manufacturing, while maintaining the high performance standards to meet the rigid system requirements. The greatest benefit of integration however is the smaller form factors, which translate to reductions in power consumption, space and ultimately, costs. However, the integration of the various system devices required in modern OCDMA systems presents difficult challenges, requiring a range of high performance and low cost optical components to reside on a single chip. Furthermore, practical on-chip integration schemes must also provide active and passive functionalities on the same single substrate, and this presents a formidable challenge that is well known to researchers worldwide.

1.2.1 System integration

For manufacturers, the long term goal is to integrate a large number of devices performing elementary functions in as fewer processes as possible, ideally in a single material system. This equates to what is known as monolithic integration. A number of materials have been investigated as a base platform for integration; the two most common platforms are silicon (*Si*) and Indium Phosphide (*InP*). The latter has a very strong potential for integrated optical devices by allowing a combination of different active optical elements, such as lasers, optical amplifiers, modulators and photodetectors, with passive waveguides which distribute the signal around the chip.

InP monolithic integration can potentially enable all of the possible functions required by future ONUs. Together with ternary (e.g. *InGaAs*) and quaternary (e.g. *InGaAsP*, or *AlGaInAs*) derivatives, the *InP* material can provide devices that can operate across the extended low loss range of single mode optical fibres (1.3 - 1.6 μm). The refractive indices of *InP* (and its derivatives) are relatively high compared to other optical materials, which translates into smaller chip sizes as bends can be made much sharper with bend radii ranging from 50 – 500 μm, and thus yielding smaller devices with die sizes typically less than 5 mm [33]. The energy bandgap is also closer to that of light energy and as a consequence, electro-optic effects are stronger than in other materials, which translate to benefits in either shorter interaction regions or lower drive voltages. However, integrated circuits in *InP* often suffer from poor yield, and the integration of several active components on a single substrate can easily lead to a degrading performance of at least one of the devices.

In comparison, *Si*-based integration is often more reliable due to its maturity, given its more established role in electronic device fabrication. The material is also significantly cheaper due to its abundant availability. *Si* is mostly optically transparent for the wavelengths in question, making it useful for interconnection between active components. Active devices can also be realised by introducing additional materials such as silicon dioxide, standard electronic dopants, and silicon germanium alloys to enhance the electro-optic interactions [3][34]. However, realising efficient light sources in *Si* is extremely challenging, which is why systems in this material often contain tapered waveguides to effectively couple light into with external optical sources [35, 36].

At the moment, given the rate of research in photonic integration, *InP* is in pole position, but *Si* and its bandgap engineered versions, will potentially provide a range of cost effective solutions in future [3]. For now however, *InP*-based systems seem to dominate and are likely to meet the requirements set by future high speed network standards. The last few years has seen an increasing number of *InP*-based integration of OCDMA systems on chip. The main advances are highlighted in the next section.

1.2.2 Integrated OCDMA systems

In 2005, Takiguchi presented an integrated arrayed waveguide grating (AWG) based en/decoder for WHTS OCDMA [36]. A wavelength multi/demultiplexer was fabricated using silica based planar lightwave circuit technology. Data rates of up to 10 Gb/s were achieved. The device mainly consisted of passive waveguides and thermo-optic based phase shifting elements along the 16 delay line paths (Fig. 1.4). Bit error rates less than 10^{-10} were achieved up to 30 km of transmission. Similar designs can also be found in [3, 11]; however, due to the passive nature of silica and silicon photonics, an external laser source was required to generate light in all of these examples. It is apparent that further work is required to fully integrate all optical components onto a *Si*-based chip before any real applications can emerge.

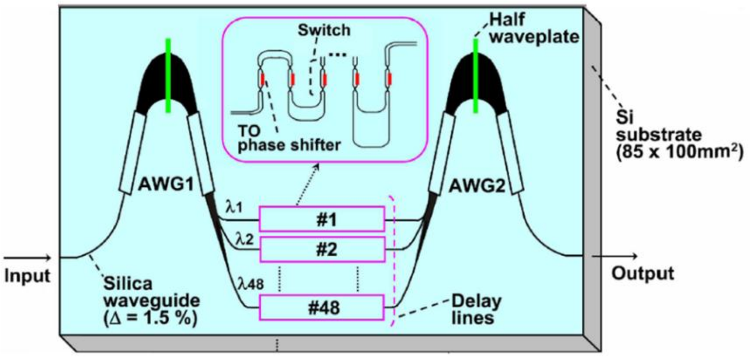

Figure 1.4 Chip design for integrated wavelength hopping time spreading OCDMA in *Si* [36].

Latterly, a demonstration of *InP*-based OCDMA with active components was given in [33]. Here, the authors proposed the growth multiple active and passive *InGaAsP/InP* devices on a silicon substrate to provide an optical source (mode-locked laser), encoder (AWG with phase shifters), semiconductor optical amplifier (SOA), and high speed electroabsorption modulator (EAM) operating up to 40 Gb/s, all on a single substrate. Hybrid vapour phase epitaxy was used in each device for simultaneous passivation and planarization of the passive waveguide sections. The transmitter design consisted of an integrated 10 GHz mode-locked laser and a spectral phase encoder using AWGs, and the receiver design consisted of a AWG decoder integrated with an MZI based threshold detector and photodetector. A schematic of the fully integrated chip design layout is shown in Fig. 1.5.

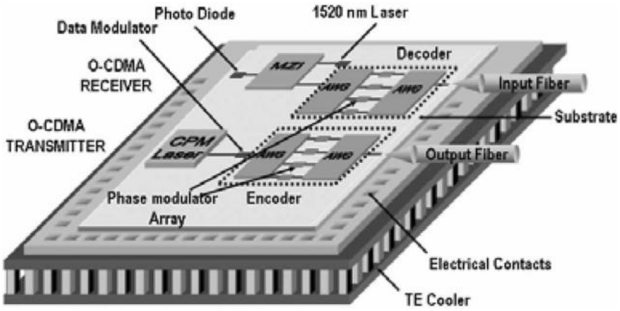

Figure 1.5 Schematic of a fully integrated OCDMA en/decoder in *InP* on *Si* substrate [33].

In this work, however, each device was in turn fabricated and characterised individually, and fibre based experimental demonstration were carried out, but critically not as a whole integrated system. This paper aimed to show the potential of device technology in *InP*. A field trial of the AWG based en/decoder was performed in 2007 over the 80.8 km link within the Boston-South network (BOSSNET) [37], and bit error rates less than 10^{-9} were achieved for two users operating at 2.5 Gb/s per user without any forward error correction. Other examples of AWG en/decoders in *InP* can be found in [3, 11, 26].

In 2007, Huiszoon, et al. proposed an integrated Mach-Zehnder based spectral amplitude coded (SAC) en/decoder system, also using the *InGaAsP/InP* substrate [38]. The device consisted of passive waveguides, multimode interference (MMI) couplers, and electro-optical phase shifters. There was no integrated optical source, and high power emissions from LEDs were instead coupled into the substrate. Spot size converters were used at the edges of the chip to maximise coupling efficiency. Insertion losses of ~10 dB were reported. The chip layout is shown in Fig. 1.6. This system was designed for use in OCDMA-PON networks and the chip was characterised as upstream and downstream links, and successful en/decoding was achieved, albeit with relatively low extinction ratios (< 35 %).

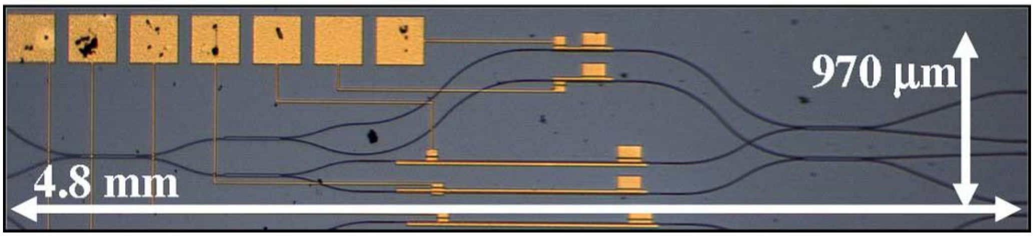

Figure 1.6 Microscope picture of Mach-Zehnder based tree en/decoder for SAC OCDMA, integrated in *InGaAsP/InP* [38].

In 2010, X. P. Zhou, et al. fabricated a monolithically integrated SPECTS-OCDMA transmitter in *InGaAsP/InP* which included seven 10 GHz colliding pulse mode-locked lasers integrated with a 16 channel AWG pair (100 GHz channel spacing) for phase encoding each spectral component provided by the CPM pulse train [39]. Passivation was achieved using selected area regrowth. The chip layout is shown in Fig. 1.7. In this report, the device was considered to be excessively lossy, although no value of insertion loss was quoted. This was likely to be due to the extensive waveguide bends on the chip. Only two of the 16 channels were measured and the results appear to be extremely noisy, indicating more work was required to optimise the integrated system.

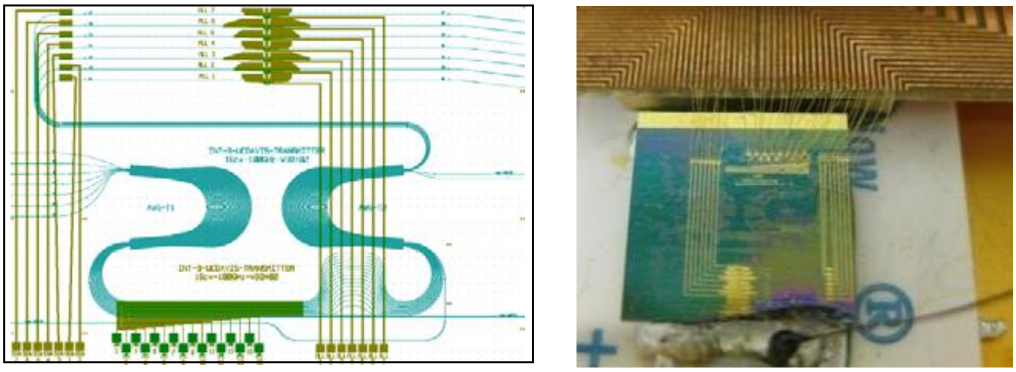

Figure 1.7 Chip design for fully integrated 16 channel SPECTS-OCDMA transmitter with a CPM laser in *InGaAsP/InP* [39].

1.3 Research aims and objectives

To date, there have been no reports on fully integrated OCDMA systems (source combined) with satisfactory en/decoding performance. This has formed the motivation of this research. Since previous implementations of integrated OCDMA systems have been chiefly performed on the familiar *InGaAsP/InP* material, often achieving low quality results, it is worthwhile to explore other materials. In this research, the *AlGaInAs/InP* is considered as a potential candidate due to its superior thermal and gain characteristics making it suitable for fabricating lasers on, as well as its ample availability and low cost. However, because of the relative immaturity of the *Al*-quaternary material some additional material characterisation is also required.

Of all the OCDMA techniques available, the WHTS method is considered most attractive since it provides enhanced security, higher scalability, and greater service flexibility over other system topologies [3]. The scheme uses fast wavelength-hopping codes, in which wavelength hops take place at every pulse of a code sequence. Security is thus enhanced as the entire code sequence is not transmitted by the same wavelength, making eavesdropping and hostile attacks difficult to carry out. For these reasons, a WHTS system was considered as the criterion of this research. Additionally, since Mach-Zehnders have been recently successfully integrated at Glasgow University [40], this was seen as a good opportunity to utilise and optimise these devices for use as coherent optical coders/decoders.

The main aims of this research are as follows:

- To investigate the unknown material characteristics and properties of *AlGaInAs/InP* for aiding the design and monolithic integration of multiple components on a single chip.
- To characterise suitable mode-locked laser diodes for use in high speed, discrete wavelength optical systems.
- To address the issue of pulse stability in semiconductor mode-locked lasers in *AlGaInAs/InP* for minimising bit error rates during long haul transmissions.
- To characterise a fully integrated semiconductor mode-locked laser and Mach-Zehnder interferometer for coherent OCDMA encoding/decoding functions.
- To design and characterise all-optical incoherent CDMA system on a single chip using a mode-locked laser array for use as WHTS OCDMA en/decoder.

1.4 Contents summary

Chapter 2 introduces the *Al*-quaternary substrate which is the platform under consideration for integrating devices. A comparison of the laser parameters is given for the five- and three-quantum-well material system, and waveguide passivation using quantum-well intermixing is discussed.

Chapter 3 describes various integration issues and explains each stage of the OCDMA processes, including the laser source (i.e. mode-locked laser), en/decoder designs, phase controlling via high frequency microstrips, phase shifters, semiconductor optical amplifiers (SOA), and electro absorption modulators (EAM).

Chapter 4 shows characterisation results from various mode-locked laser topologies, such as DBR lasers, harmonic lasers, and colliding pulse, all of which are potential candidates for use in high speed OCDMA systems.

Chapter 5 addresses the issues relating to the stability of passively mode-locked lasers and various stabilising experimental results are shown using hybrid and synchronous mode-locking. A passive stabilisation method based on regenerative mode-locking techniques is also presented for potential use as an all optical system clock.

Chapter 6 shows characterisation results for temporal phase coded (TPC) OCDMA using integrated MZIs. Signal en/decoding is achieved using 2-bit binary phase codes using a back-to-back encoder-decoder pair.

Chapter 7 shows characterisation results for WHTS OCDMA using mode-locked DBR laser array. Wavelength spreading and synchronisation experiments are performed, indicating the system's potential for use in incoherent OCDMA applications.

And finally chapter 8 concludes this thesis with some suggestions for future work.

1.4.1 Acknowledgements and collaborations

This work was partly a collaborative effort with the optoelectronics research team at the University of Glasgow, and the following table recognises all joint contributions to the work presented in this thesis:

Chapter	Activity	Contributor(s)
2	*AlGaInAs/InP* three-quantum-well wafer epitaxial structure design	Prof. John Marsh Dr Lianping Hou
2	FP laser fabrication	Dr Lianping Hou
2	Farfield and nearfield modelling/simulations and measurements	Dr Jehan Akbar Dr Lianping Hou
2	Quantum-well intermixing characterisation and optimisation	Dr Steven McMaster
3	Semiconductor absorber sample fabrication	Dr Lianping Hou Dr Gabor Mesozi Dr Rafal Dylewicz
4	Mode-locked laser devices fabrication and modelling	Dr Lianping Hou
4	Analysis and review of data	Dr Mohsin Haji Dr Lianping Hou
6	Coherent OCDMA integrated system design	Prof John Arnold Dr Marc Sorel Dr Hin Wong Dr Steven McMaster
6	Mach Zehnder and integrated ring laser design and fabrication	Dr Steven McMaster
6	MMI modelling and characterisation	Dr Steven McMaster
6	System characterisation: en/decoding experiments	Dr Mohsin Haji Dr Steven McMaster
6	Linear intensity autocorrelation measurements	Dr Piotr Stolarz
7	Incoherent OCDMA integrated system design	Dr Mohsin Haji Dr Lianping Hou Prof John Arnold Dr Anthony Kelly Dr Marc Sorel Prof Ivan Glesk
7	Mode-locked laser array with integrated MMI combiner, SOA and EAM chip design and fabrication	Dr Lianping Hou

1.5 References

[1] P. R. Prucnal, M. A. Santoro, and T. R. Fan, “Spread spectrum fiberoptic local area network using optical processing,” J. Lightw. Technol., Vol. LT-4, No. 5, pp 547–554, 1986.

[2] X. Wang, K. Matsushima, A. Nishiki, N. Wada, F. Kubota, and K.-I. Kitayama, “Experimental demonstration of 511-chip 640 Gchip/s superstructured FBG for high performance optical code processing,” ECOC, Stockholm, Sweden, Paper Tu1.3.7, 2004.

[3] P. R. Prucnal, et al., “Optical code division multiple access – Fundamentals and applications,” CRC Taylor and Francis, 2006.

[4] T. Fujii, K. Shirakawa, M. Nomura, and T. Yamaguchi, “Cinema-class digital content distribution via optical networks (Invited),” Proc. OpNeTec, Pisa, Italy, p. 11-18, 2004.

[5] T. Tomita, and S. Kuribayashi, “Congestion control method with fair resource allocation for cloud computing environments,” IEEE Pacific Rim Conference on Comms. Computers Signal Processing., pp 1-6, 2011.

[6] K. Kitayama, X. Wang, and N. Wada, “OCDMA over WDM PON – Solution path to gigabit symmetric FTTH,” J. Lightwave Technol., Vol. 24, No. 4, pp 1654-1662, 2006.

[7] K. Kitayama, X. Wang, and H. Sotobayashi, “State of the art and applications of optical code division multiple access (Invited),” ECOC, Stockholm, Sweden, Paper Tu4.6.1, 2004.

[8] K. Kitayama, X. Wang, and H. Sotobayashi, “Multi-gigabit symmetric FTTH—OCDMA over WDM PON,” Proc. ONDM, Milano, Italy, pp. 273–281, 2005.

[9] P. Green, “Paving the last mile with glass,” IEEE Spectrum, Vol. 39, No. 12, pp 13-14, 2002.

[10] H. Shinohara, “FTTH development in Japan and its enabling technologies,” presented at the Broadband Europe 2005, Bordeaux, France, Paper Mo2., 2005.

[11] H. Yin and D. J. Richardson, “Optical code division multiple access communication networks – theory and applications,” Tsinghua University press, Springer, 2008.

[12] T. Richter, E. Palushani, C. Schmidt-Langhorst, M. Nolle, R. Ludwig, J. K. Fischer, and C. Schubert, Single wavelength channel 10.2 Tb/s TDM-data capacity using 16-QAM and coherent detection,” OFC, paper PDPA9, 2011.

[13] A. Banerjee, Y. Park, F. Clarke, H. Song, S. Yang, G. Kramer, K. Kim, and B. Mukherjee, “Wavelength-division-multiplexed passive optical network (WDM-PON) technologies for broadband access: a review (invited),” J. Opt. Networking, Vol. 4, No. 11, pp 737-758, 2005.

[14] ITU Draft Recommendation G.694-2: Spectral grids for WDM applications: CWDM wavelength grid. 2004.

[15] J. H. Lee, P. C. Teh, P. Petropoulos, M. Ibsen, and D. J. Richardson, “A grating-based OCDMA coding-decoding system incorporating a nonlinear optical loop mirror for improved code recognition and noise reduction,” J. Lightw. Technol., Vol. 20, No. 1, pp 36–46, 2002.

[16] Z. Jiang, D. S. Seo, S.-D. Yang, D. E. Leaird, R. V. Roussev, C. Langrock, M. M. Fejer, and A. M. Weiner, “Four-user, 2.5-Gb/s, spectrally coded OCDMA system demonstration using low-power nonlinear processing,” J. Lightw. Technol., Vol. 23, No. 1, pp 143–158, 2005.

[17] R. P. Scott, W. Cong, K. Li, V. J. Hernandez, B. H. Kolner, J. P. Heritage, and S. J. B. Yoo, “Demonstration of an error-free 4 × 10 Gb/s multiuser SPECTS O-CDMA network testbed,” IEEE Photon. Technol. Lett., Vol. 16, No. 9, pp 2186–2188, 2004.

[18] R. Malik, “Spread spectrum – Secret military technology to 3G,” IEEE History of Telecommunications Contest, 2001.

[19] S. Dennett, “3GPP2 3G deployments and the future of IP core networks,” ITU seminar on IMT-2000, 2002.

[20] C. Delisle and P. Cielo, “Application de la modulation spectrale a la transmission de I’information (in French),” Can. J. Phys., Vol. 53, pp 1047–1053, 1975.

[21] A. M. Weiner, J. P. Heritage, and J. A. Salehi, “Encoding and decoding of femtosecond pulses,” Optics Lett., Vol. 13, No. 4, pp 300-302, 1988.

[22] J. A. Salehi, “Code division multiple access techniques in optical fiber networks – part I: Fundamental principles,” IEEE Trans. Comms, Vol. 37, No. 8, pp 824-833, 1989.

[23] J. A. Salehi, “Code division multiple access techniques in optical fiber networks – part II: Systems performance analysis,” IEEE Trans. Comms, Vol. 37, No. 8, pp 834-842, 1989.

[24] J. A. Salehi, F. R. K. Chung, and V. K. Wei, “Optical orthogonal codes: design, analysis and applications,” IEEE Trans. Information Theory, Vol. 35, No. 3, pp 595-605, 1989.

[25] H. Chung and P. Kumar, “Optical orthogonal codes – new bounds and optimal construction,” IEEE Trans. Information Theory, Vol. 36, No. 4, pp 866-873, 1990.

[26] J. A. Salehi, “Emerging OCDMA communication systems and data networks (invited),” J. Optical Networking, Vol. 6, No. 9, pp 1138-1178, 2007.

[27] L. Tancevski, and I. Andonovic, “Wavelength hopping/time spreading code division multiple access systems,” Electron. Lett., Vol. 30, No. 9, pp 721-723, 1994.

[28] H. B. Jafaar, S. LaRochelle, P. Y. Cortes, and H. Fathallah, “1.25 Gbit/s transmission of optical FFH-OCDMA signals over 80 km with 16 users,” OFC, paper TuV3-1, 2001.

[29] C. Bres, I. Glesk, and P. R. Prucnal, “Demonstration of eight-user 115-Gchip/s incoherent OCDMA system using supercontinuum generation of optical time gating,” IEEE Photon. Techno. Lett., Vol. 18, No. 7, pp 889-891, 2006.

[30] X. Wang, N. Wada, T. Miyazaki, G. Cincotti, and K. Kitayama, “Field trial of 3-WDM x 10-OCDMA x 10.71Gbps, truly asynchronous, WDM/DPSK-OCDMA using hybrid E/D without FEC and optic threshold,” OFC, paper PDP44, 2006.

[31] G. C. Yang, and W. C. Kwong, “Prime codes with application to CDMA optical and wireless networks,” Norwood: Artech House, 2002.

[32] I. Glesk, V. Baby, C. Bres, P. R. Prucnal, and W. C. Kwong, “Is optical CDMA viable technique for broadband networks?,” Proc. of SPIE, Vol. 6180, 2006.

[33] R. G. Broeke, J. Cao, C. Ji, S. W. Seo, Y, Du, N. K. Fontaine, J. Baek, J. Yan, F. M. Soares, F. Olsson, S. Lourdudoss, A. H. Pham, M. Shearn, A. Scherer, and S. J. B. Yoo, “Optical CDMA in InP,” IEEE J. Sel. Top. Quant. Electron., Vol. 13, No. 5, pp 1497-1507, 2007.

[34] D. Liang, and J. E. Bowers, “Recent progress in lasers on silicon,” Nat. Photon., Vol. 4, pp 511, 2010.

[35] D. J. Lockwood, and L. Pavesi, “Silicon Photonics: Monolithic silicon microphotonics,” Top. Appl. Phys., Vol. 94, pp 89-120, 2004.

[36] K. Takiguchi and M. Itoh, “Integrated-optic encoder/decoder for time spreading/wavelength hopping optical CDMA,” IEEE J. Sel. Top. Quant. Electron., Vol. 11, No. 2, pp 300-306, 2005.

[37] R. P. Scott, V. J. Hernandez, N. K. Fontaine, F. M. Soares, R. G. Broeke, K. Perry, G. Nowak, C. Yang, W. Cong, K. Okamoto, B. H. Kolner, J. P. heritage, and S. J. B. Yoo, “80.8 km BOSSNET SPECTS O-CDMA field trial using subpicosecond pulses and a fully integrated compact AWG based encoder/decoder,” IEEE Sel. Top. Quant. Electron., Vol. 13, No. 5, pp 1455-1462, 2007.

[38] B. Huiszoon, L. M. Augustin, E. A. J. M. Bente, H. de Waardt, G. D. Khoe, M. K. Smit, and A. M. J. Koonen, “Integrated Mach-Zehnder based spectral amplitude OCDMA on a passive optical network,” IEEE J. Sel. Top. Quant. Electron., Vol. 13, No. 5, 2007.

[39] X. P. Zhou, F. M. Soares, K. Fontaine, J. H. Baek, S. Cheung, M. Shearn, A. Scherer, F. Olsson, S. Lourdudoss, K. Y. Liu, W. T. Tsang, and S. J. B. Yoo, “16 channel x 100 GHz monolithically integrated O-CDMA transmitter with SPECTS encoder and seven 10 GHz mode locked lasers,” OFC, paper JWA32, 2010.

[40] S. McMaster, "Monolithically integrated mode-locked ring lasers and Mach-Zehnder interferometers in AlGaInAs," Ph.D. thesis, University of Glasgow, 2010.

Chapter 2

III-V semiconductor device technologies using *AlGaInAs/InP* multiple quantum-wells

III-V semiconductors are excellent platforms for fabricating low-cost and compact devices. For optoelectronic devices, quantum-well structures can be used to generate and confine light within the material to allow a variety of electro-optic processes to be carried out. Recently, the *Al*-quaternary based material structure has gained a high level of interest owing to its useful intrinsic properties and relatively low cost, which is why many of the devices fabricated during the course of this project were done so using this material. This chapter provides an overview of the *Al*-quaternary material system, and offers an insight into its attributes as a semiconductor platform for integrated systems.

First, the theory of semiconductor quantum-wells is explained followed by an overview of the fabrication stages of a semiconductor Fabry-Pérot laser. Next, the *AlGaInAs/InP* based multiple quantum-well epitaxial structure is described and its gain and loss properties will be discussed. During the course of this research, substantial improvements have been made to the design of the *AlGaInAs/InP* quantum-well structure by reducing the number of quantum-wells for increasing the gain saturation energy of the lasers, which subsequently increases the output power. Therefore, a comparison of a three- and five-quantum-well Fabry-Pérot laser is then given, with experimental and modelling results. Finally, a process known as quantum-well intermixing – an alternative technique used for reducing waveguide losses will be explained, while stressing its importance for photonic circuit integration in III-V based lightwave circuits.

2.1 Quantum-wells

A quantum-well (QW) structure can be described as a thin layer of active semiconductor material (typically less than 50 nm) with a narrow bandgap, sandwiched between two wider bandgap semiconductors, forming a type of heterostructure. These materials are usually lattice matched, which minimises the interface defects due to the crystal dimensions of the neighbouring semiconductor layers. For example, *GaAs* can be used as the active layer, and *AlGaAs* can be used as the surrounding layers [1]. There are instances however where lattice mismatching can be used to provide distinctive semiconductor structures, such as the quantum dot structure, where “dots” of active material, such *InAs*, are grown over a *GaAs* substrate. These types of material systems are usually more expensive to grow, but can provide unique and outstanding properties for semiconductor lasers, including a large bandwidth, excellent thermal characteristics, and high material gain [2, 3].

Because of the potential energy differences of the QW materials, conduction electrons are confined in the active layer, with the two surrounding higher energy materials forming a barrier for these electrons. Quantised energy levels are then formed in the active layer due to the density of states, which are step-like (i.e. constant for each energy level) in QWs. This means a large concentration of electrons can easily form at the interfaces of the wells and increase rapidly as the current is increased, resulting in an improvement of the differential gain characteristics, and therefore population inversion is achieved at much lower energies than in bulk materials. This leads to lower threshold currents and improved thermal characteristics. Moreover, the range of emitted photon energies that are generated by a QW are restricted to the interface of the quantised energy levels (mostly near the smallest bandgap), leading to narrower linewidths in the optical spectrum, and therefore, less noise [4].

Finite energy levels in a well however, will cause the gain to saturate when the electron and hole states are fully inverted [5]. This can be resolved by using multiple quantum-wells (MQWs), where several alternating ultrathin layers of wide and narrow bandgap materials are stacked upon one another. This increases the optical confinement in the material and also provides a larger differential gain, which subsequently reduces the threshold current since more QWs can deliver the same gain with fewer carriers [6]. The next section describes how a laser is fabricated in III-V material systems containing MQWs.

2.2 The Fabry-Pérot Resonator

A Fabry-Pérot (FP) laser is the simplest type of laser to fabricate in semiconductor. Two facet mirrors are formed by cleaving at both sides of a laser cavity, which is typically a ridge-like structure, and these mirrors are used to increase the stimulated emission in the laser. Sometimes, a facet is metallised to increase the reflectivity and thus increase the rate of stimulated emission, which in turn can reduce the threshold current and increase the lasing intensity. Anti-reflection coatings can also be applied to a facet to reduce the reflectivity, which in turn reduces the mirror losses. This is particularly useful for devices such as distributed Bragg reflectors (DBRs) and semiconductor optical amplifiers (SOAs), and can also be used with FP lasers if one facet is highly reflective to increase the output emissions at the opposite facet [7]. This section will highlight and summarise the steps used to fabricate a simple FP ridge laser, thus providing a basis on how active devices are made in a MQW epitaxial wafer. Passivation of the MQW material will be discussed later in this chapter in section 2.4.

Figure 2.1 shows step by step diagrams of the fabrication processes used to make a FP laser. To begin, a piece of wafer is cleaned using various chemicals to remove any contamination particles from the surface (Acetone, Methanol, and Isophthalic acid). An electron beam (e-beam) lithography tool is then used to write a predefined pattern on the wafer. Initially, markers are written onto the sample to aid the alignment of the impending processes. A layer of polymethyl methacrylate (PMMA), a type of acrylic glass, is used as a resist during the e-beam process, which allows for the selective removal of areas that are to be exposed for writing. A metallic layer (*NiCr:Au*) is then deposited onto the wafer, since it is highly reflective and visible under the microscope. The metal will only form on the regions that were exposed by the e-beam, whereas all other regions protected by the PMMA layer remain intact. The PMMA is then removed using a hot bath of acetone. Next, the ridge waveguides are defined. This is performed by etching the *P*-cap layer on either sides of the waveguide, such that a “ridge” shape is formed. This is again achieved by applying a layer of PMMA resist, and then using e-beam to protect only the ridge waveguide pattern. The exposed areas are then etched away using a method known as dry-etching.

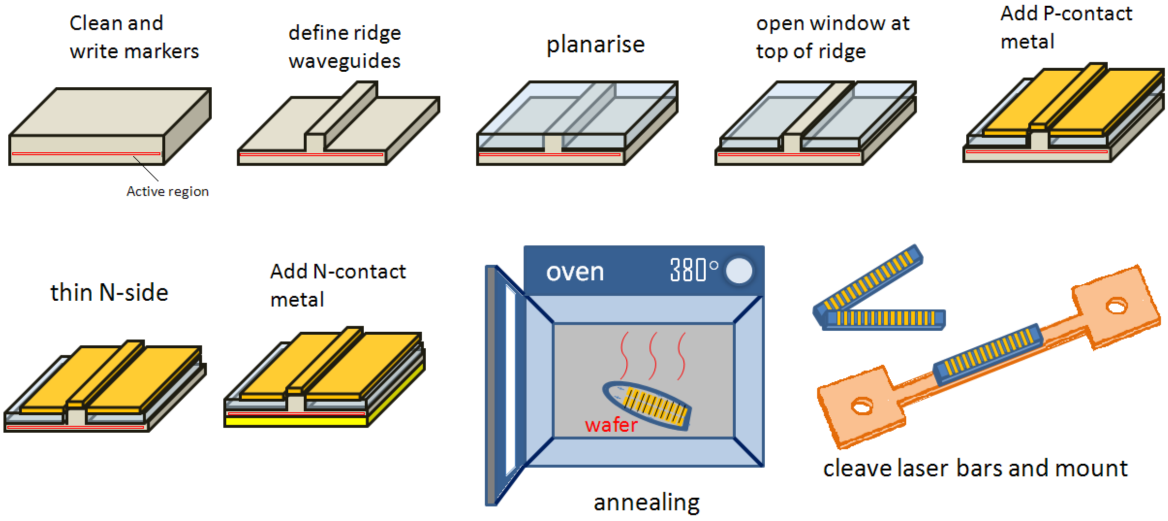

Figure 2.1 Fabrication stages of a semiconductor FP laser.

Once the ridges on the wafer have been defined, the next stage is to form electrical contacts on the structures, so that a current can flow through the ridge. It is important to ensure that only the top of the ridge is electrically connected so that the current is confined to the ridge waveguide and current leakage around the ridge is prevented. This can be achieved by planarising the ridge using a resin of SiO_2 and Hydrogen Silsequioxane (*HSQ*), followed by the removal of the top of the ridge waveguide via e-beam. A contact metal can now be placed over the ridge window and SiO_2/*HSQ* resin. A metal mixing and sputtering tool can be used to deposit the metal contact, but first, the resist and e-beam process must be used to select the area of the contact. Once the metal is formed over the wafer, the sample is placed in a hot bath of acetone for metal lift-off in regions that are protected by PMMA. Following this, the *N*-side of the material is thinned, before the attachment of an *N*-contact metal to complete the electrode pair of the structure. Annealing is performed to remove any oxidised compounds from the wafer, and finally, the lasers are scribed and cleaved into multiple bars. These then sit on conductive T-cut sub-mounts, which can be positioned onto temperature controlled stages for subsequent probing and testing. An optical fibre is usually aligned at the active region of a laser to couple the output emissions for measurement on various instruments, such as an optical spectrum analyser.

2.3 The *Al*-quaternary Structure

In comparison to other MQW structures, and in particular the *P*-quaternary (*InGaAsP/InP*) as it is another commonly used material system at 1.5 μm, *Al*-quaternary devices are more tolerant to thermal instabilities due to a larger conduction band offset (72%), and smaller valence band discontinuities, as depicted in Fig. 2.2. This subsequently leads to improved electron confinement and therefore lower carrier leakage and as a result, lasers in the *Al*-quaternary material system provide a lower threshold current density and a higher differential gain over those made using *P*-quaternary [8, 9, 10].

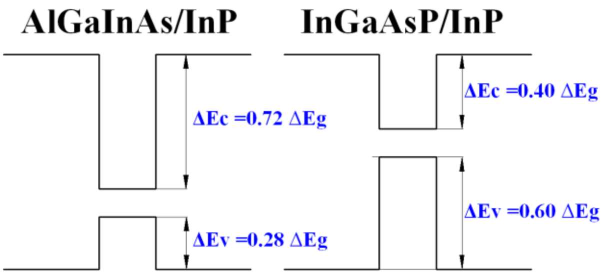

Figure 2.2 Band discontinuities of a well in *AlGaInAs* and *InGaAsP* materials.

2.3.1 Five-QWs

The *AlGaInAs/InP* epitaxial structure is a commercially available, compressively strained multiple quantum-wells (MQW) design, a schematic of which is shown in Fig. 2.3. The material contains five *AlGaInAs* based QWs sandwiched between two graded refractive index separate confinement heterostructure (GRINSCH) layers to better confine the light within the active region, and two wider band gap layers on either side to prevent electrons and holes from escaping the QW region. Two *InP* cladding layers are located on either side (upper and lower), and finally a contact layer is added to the *p*-side to complete the structure. The *Al*-quaternary structure has gained much interest lately and has been used as a platform for many optoelectronic devices, particularly mode-locked lasers [11, 12].

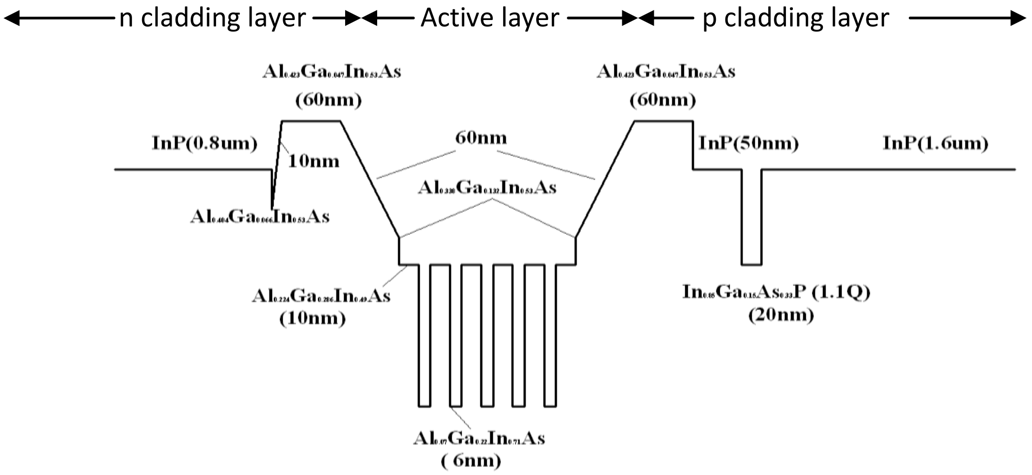

Figure 2.3 Band diagram of *AlGaInAs/InP* semiconductor substrate with five-QWs.

The band-gap energy of the wells is equivalent to a ~1.55 μm wavelength; which falls into the fibre optics communication band C, and also lies in the erbium window for amplification [13]. The polarity of light emitted from this structure is naturally TE mode due to stronger coupling between the heavy-hole and electron transitions as a result of compressively straining the material [14]. Conversely, applying a tensile strain to the QWs will induce greater TM mode coupling by facilitating greater light-hole and electron interactions. In addition, mirror reflectivity and device geometry may also promote TE mode operation of a device due to the lower threshold current required to stimulate TE modes [15].

As the *Al*-quaternary material contains five-QWs, it provides a much larger differential gain than in bulk materials. However, while a larger differential gain leads to a steeper increase in the output power, it also leads to a lower saturation energy (E_{sat}) which may limit the maximum output power. From the equation: $E_{sat} = hvA/(\Gamma dg/dN)$ (where hv is the photon energy, A is the mode area, dg/dN is the differential gain, and Γ is the optical confinement factor), three solutions are apparent: decreasing the confinement factor, increasing the spot size, and decreasing the differential gain; all of which will increase the value of E_{sat}. It has been shown that these conditions can be satisfied by reducing the number of quantum-wells in the active layer [16], which will also reduce spontaneous emissions in the cavity [6], a beneficial feature for pulsed lasers in particular due to reduced phase noise and timing jitter of the emitted pulses (see chapter 4).

Furthermore, a semiconductor laser will often require its output emissions to be coupled into an optical fibre for subsequent transmission. Large mode areas in inadequately designed material systems may result in greater coupling losses. For this reason, a vast amount of research has been carried out recently in order to achieve spot size converters, which enlarge the near-field in order to couple more efficiently to a single mode fibre (SMF); however, many of these techniques require etching and regrowth over the active region. This poses a problem in the *AlGaInAs/InP* structure since the *Al*-containing surfaces will experience rapid oxidisation if exposed for a given length of time, which can contaminate the material and increase the rate of absorption [17]. This may also be resolved by adapting the epitaxial structure to contain fewer quantum-wells in order to increase the spot size, and hence, reduce the far-field pattern.

2.3.2 Three-QWs

A new structure was thereby designed using three-QWs instead of five (epitaxial structure shown in Fig. 2.4). The epitaxial layer parameters were kept the same as the five-QW material, though, an additional layer was added into the *n*-cladding region. This is known as a far-field reduction layer (FRL), and is used to expand and reposition the near-field towards the *n*-cladding in order to reduce the internal loss of the cavity that is primarily driven by higher transverse mode lasing in the *p*-cladding region [18]. This is better understood by interpreting the following loss equation: $\alpha_{in} = \Gamma_{QW} \cdot k_{QW} + \Gamma_p \cdot k_p + \Gamma_n \cdot k_n$, where Γ is the optical confinement of the QW, *p*-cladding, and *n*-cladding, respectively, and k is the absorption coefficient for the same parameters [19]. Using values quoted in various publications, it can be assumed that k_{QW} = 35 cm^{-1} for compressively strained QWs at threshold [20], k_n = 1 cm^{-1} in *n-InP*, and k_p = 22 cm^{-1} in *p-InP* [21]. It is then apparent that the *p*-cladding absorption is the main contributor to the internal cavity losses, which is mainly due to the absorption by holes being greater than that by electrons. The FRL width and spacer layer thicknesses were thereby optimised by using a beam propagation simulator [22], such that the fundamental mode was widened and pulled towards the lower cladding layer, reducing the overlap with the *p*-cladding layer resulting in reduced free carrier absorption and higher order transverse mode suppression. The FRL was placed 750 nm below the active region, and consisted of a 160 nm *InGaAsP* layer with a bandgap corresponding to a wavelength of 1.1 μm.

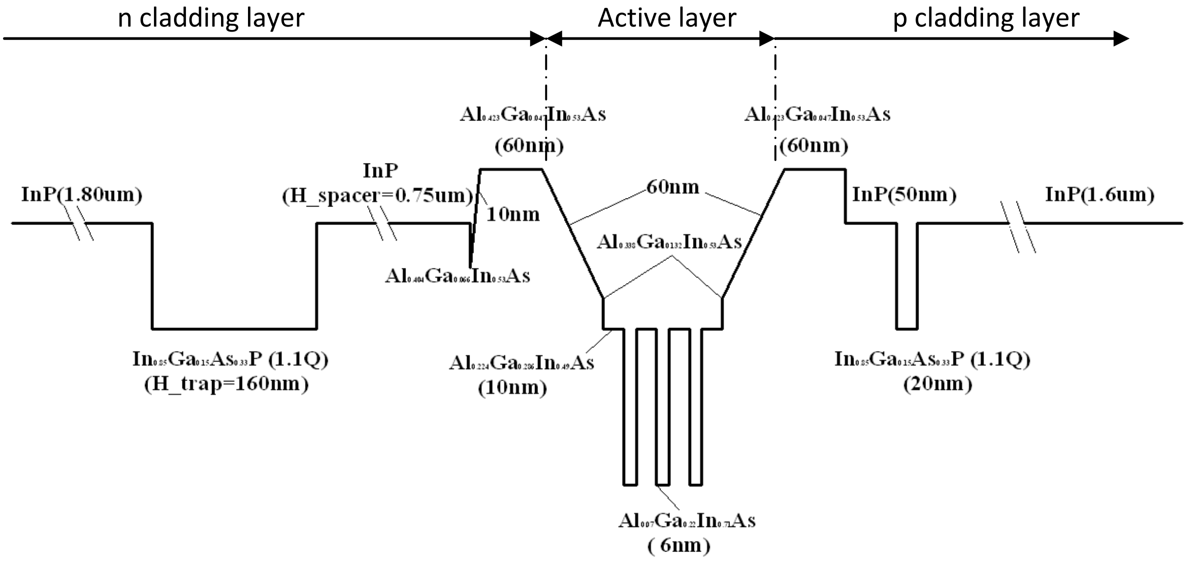

Figure 2.4 Band diagram of *AlGaInAs/InP* semiconductor substrate with three-QWs and FRL.

2.3.3 FP laser comparisons

To compare the performance of the newly designed material, a simple FP laser was designed and fabricated using the same methods on both the five-QW, and three-QW epitaxial structures [16]. These were both cleaved at the same cavity length of 1070 µm, with both facets left uncoated. The devices were then mounted on a temperature controlled copper heat sink, set at 20°C, and tested under continuous wave (CW) conditions. A broad area photodetector was positioned close to the facet and the intensity of the emissions was measured using an optical power meter. Figure 2.5 shows the light vs. current (*LI*) results obtained from this measurement. The threshold current in both cases were almost identical, with a slightly dearer threshold current required for the three-QW laser, which was likely to be due to the lower differential gain. The slope efficiency however was greatly improved for the three-QW laser at ~0.21 W/A, and was ~0.14 W/A for the five-QW laser. This improvement can be attributed to the lower internal cavity losses, which was predominantly promoted by the FRL.

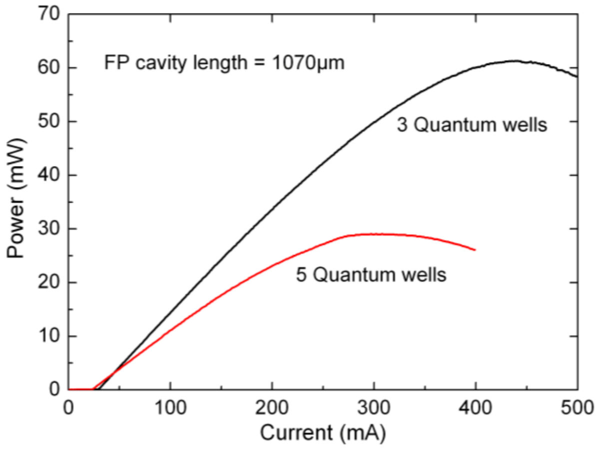

Figure 2.5 Comparison of the *LI* curves of three-QW and 5-QW materials

To calculate the coupling efficiency to a SMF, the *LI* curves were also acquired using a cleaved (flat-faced) SMF, which was aligned to the active region at the facet. The coupling efficiency to the cleaved SMF was ~20% using the three-QW laser; double that of the five-QW laser without the FRL. To explain this, the near and far field patterns (FFP) of each laser were examined. The simulated near field patterns of both structures are shown in Fig. 2.6(b), with reference to the ridge waveguide. The dependence of the near field, and thus the far field to the ridge height is shown in Fig. 2.6(a), together with the simulated coupling efficiency to a SMF. Due to the trade-off between these two parameters, ridge height values of 1.65 µm and 1.85 µm were fabricated. The simulated near field pattern of these, along with the five-QW laser pattern is shown in Fig. 2.6(b). It is distinctly shown that the near fields of the three-QW lasers (1.65 µm - blue trace, 1.85 µm – red dashed trace) were somewhat larger than the five-QW laser (green trace), and elongated towards the *n*-cladding due to the FRL.

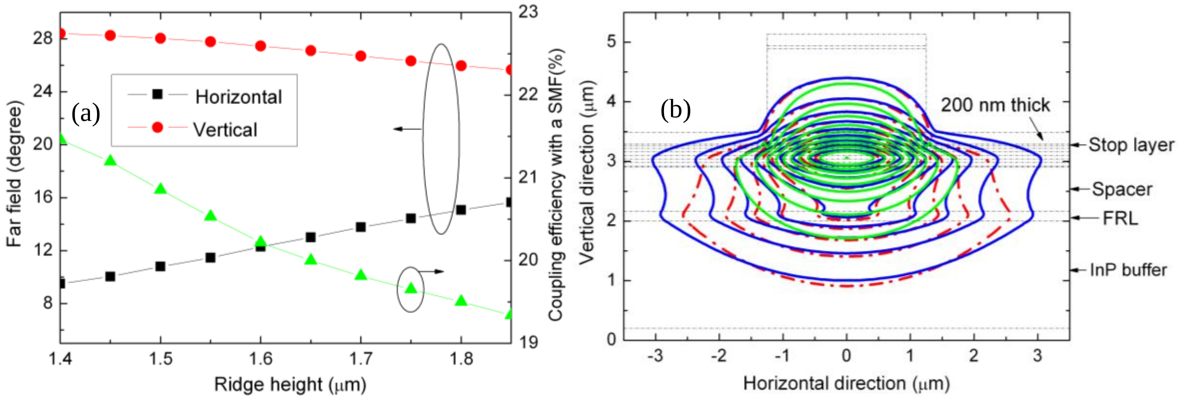

Figure 2.6 (a) Calculated far field and coupling efficiency to a flat cleaved SMF as a function of ridge height, and (b) the simulated near field pattern of the five-QW substrate (green line), 1.65 μm ridge three-QW substrate (red dash-dot line), and 1.85 μm ridge three-QW substrate (blue line), plotted with reference to the substrate layers. (Results obtained using Beamprop™ mode-solver tool.)

It is understood that a near field leads to a reduction in the optical far field through Fourier transformation, and to confirm this, the FFP was measured using a far-field analyser by J. Akbar [16]. The plots depicted in Fig. 2.7 show the measured FFPs for the five-QW, 1.65 μm ridge three-QW, and 1.85 μm ridge three-QW, respectively. For the five-QW laser, the FFP was 34.7° x 35.1°, with a 1 dB alignment tolerance of ±1.7 μm (in both horizontal and vertical directions) and 8.3 μm in the optical axis. For the three-QW laser with a 1.65 μm ridge, the divergence angles were reduced to 12.7° x 26.3°. The butt-coupling efficiency to a cleaved SMF was about 20 %, double that achieved using a five-QW laser, and a 1 dB increase in coupling loss corresponding to alignment tolerances of ±2.2 μm (horizontal), and ±1.9 μm (vertical) and 13.7 μm in the optical axis. For the 1.85 μm ridge laser, the asymmetry of the FFP was greatly improved to 23.7° x 25.1°, albeit with a lower coupling efficiency; whereas the broader FFP of the five-QW laser would result in greater losses when coupling to a SMF.

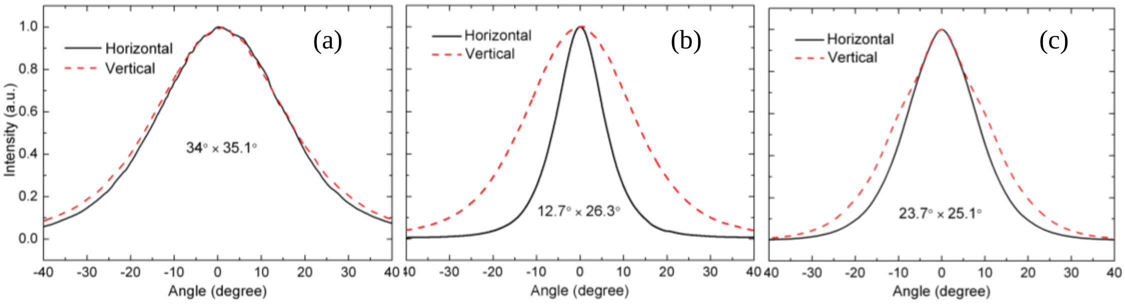

Figure 2.7 Experimental results of the FFP at FWHM for (a) five-QW laser, (b) 1. 65 μm ridge three-QW laser, and (c) 1. 85 μm ridge three-QW laser.

The net modal gains for the five-QW and three-QW (ridge height = 1.85μm) devices were calculated using the Hakki-Paoli method [23], in which the ratio of the maximum and minimum of the amplified spontaneous emission (ASE) spectrum are used in the following relations:

$$G_{net} = \Gamma g - a = \frac{1}{L}\ln\left(\frac{\sqrt{C_r-1}}{R\sqrt{C_r+1}}\right) + \frac{1}{2L}\ln\left(\frac{1}{R_1+R_2}\right) \qquad (2.1)$$

where Γg is the product of the optical confinement factor and material gain for one well, respectively, a is the intrinsic loss, C_r is the maximum and minimum ratio of the ASE spectrum, L is the cavity length, and R_1 and R_2 are the reflectivities of the mirrored facets. Using this equation, and the ASE spectra with FP modulation shown in Fig. 2.8(a) and (b), for the five and three-QW lasers respectively, the internal loss for the three-QW epitaxial structure was estimated at ~8/cm^{-1} (Fig. 2.8(d)), with a differential modal gain of 2.7×10^{-17} cm^2, whereas the five-QW design was ~15/cm^{-1} (Fig. 2.8(c)) and 4.9×10^{-17} cm^2, agreeing well with the modelled results for this material.

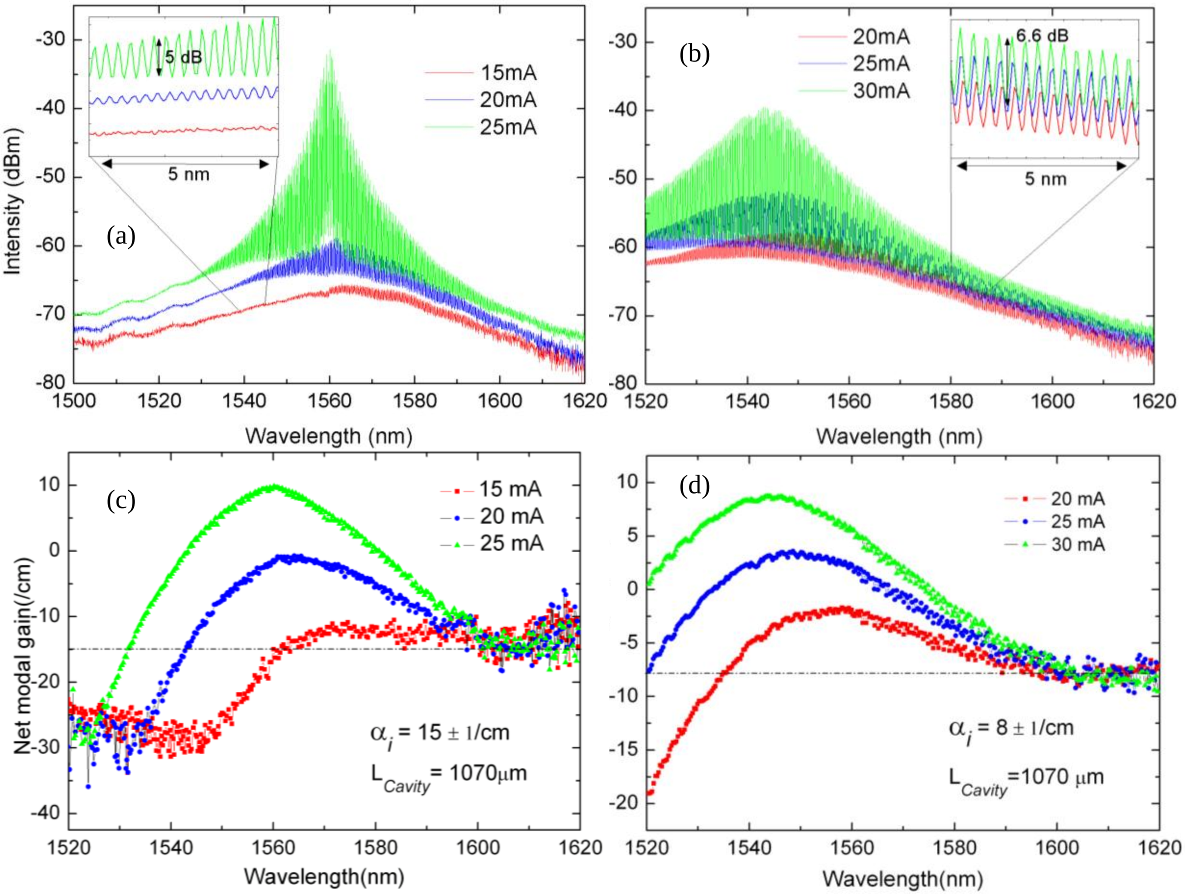

Figure 2.8 (a) ASE spectra with FP modulation for five-QW laser, and (b) three-QW laser. (c) Hakki-Paoli gain and loss measurements for (c) five-QW structure, and (d) three-QW structure using ASE data.

2.4 Waveguide passivation using quantum-well intermixing

Due to the restricted active regions in semiconductor devices, localised passivation is required to reduce waveguide losses due to the direct interband absorption in regions that do not require electrical biasing. This is increasingly important for monolithically integrating optical components on a single chip, which is the universal ambition for researchers working on semiconductor optics. Monolithic integration eases alignment issues and coupling losses, and reduces system size and costs considerably. In general, waveguide passivation is achieved by widening the band gap of the passive regions, which is usually carried out by selective etch-and-regrowth of those regions [24]. Quantum-well intermixing (QWI) is an alternative and relatively simpler technique that widens the band gap by permeating the well material with its neighbouring barrier compounds, such that the step-like band structure is adapted to a more progressive energy level transition between the materials (Fig. 2.9). This means that photons propagating in this region with energy less than the bandgap will not be readily absorbed by interband transitions, thereby preserving the intensity of the optical signal.

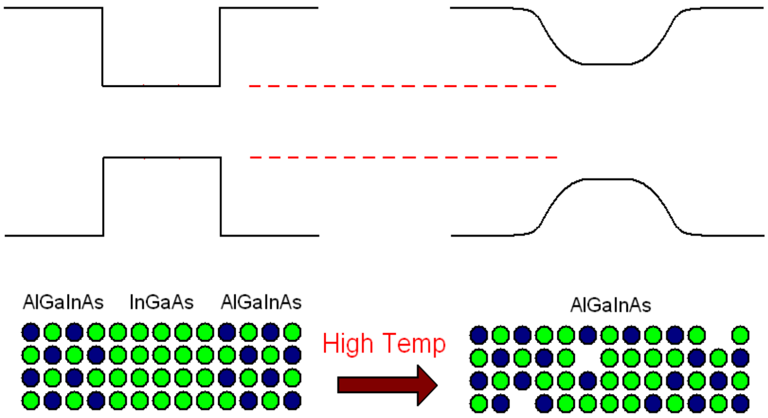

Figure 2.9 Schematic representation of the diffusion caused by sputtering induced vacancy disordering QWI.

QWI is performed by sputtering silica onto the sample under consideration with a composition that generates point defects in the semiconductor when annealed [25]. This is achieved as the group III elements leaving the semiconductor lattice are diffused into the silica, promoting group III vacancies that diffuse into the semiconductor and through the QWs to cause the intermixing. Figure 2.10 shows the bandgap shift as a function of annealing temperature for an annealing time of 60 s, performed by S. McMaster [26]. It is shown that a bandgap wavelength shift takes place for annealing temperatures above 600°C and the shift increases with increasing annealing temperature. Shifts of more than 100 nm can be achieved with a temperature of 665°C. Also shown on the graph is the effect of annealing samples capped with plasma enhanced chemical vapour deposited (PECVD) silica, where no discernible bandgap shift was observed in the range of temperatures investigated. Therefore selective intermixing can be achieved by capping areas with the sputtered silica to intermix the passive sections and capping the active sections with PECVD silica to suppress the QWI and prevent desorption of the group V elements.

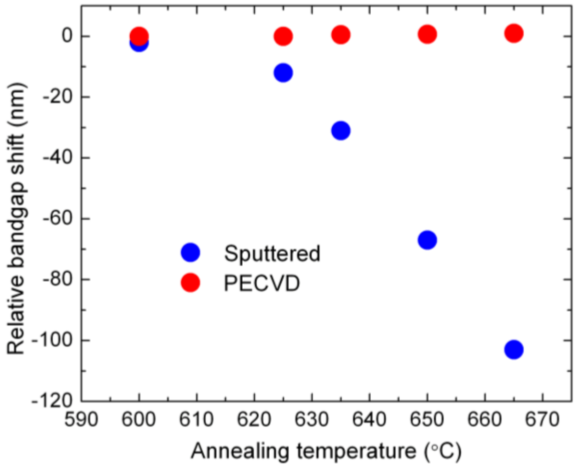

Figure 2.10 Bandgap wavelength shift as a function of annealing temperature for PECVD and sputtered silica covered samples after 60 seconds of rapid thermal annealing [27].

Similar to the steps shown in section 2.2, PMMA is spun onto the sample and the areas not to be intermixed are patterned by e-beam writing. The silica layer is sputtered onto the sample with the PMMA protecting the surface of the active regions during the sputtering process. Chemical lift-off is then performed removing the sputtered silica from the active sections of the device. The sample is then capped with 200 nm of PECVD silica and annealed at 660°C for 60 s resulting in a bandgap shift of 100 nm in the passive sections only, whereby the active section will not exhibit any shift.

The waveguide losses in the intermixed material were measured using the Fabry-Pérot fringe method, also performed by S. McMaster [27]. The total passive waveguide propagation loss α can be defined as [1, 26]:

$$\alpha = -\frac{1}{L}\ln\left(\frac{\sqrt{C_r}-1}{R\sqrt{C_r}+1}\right) \tag{2.2}$$

where L is the length of the cavity, C_r is the maximum and minimum ratio of the FP fringes in the optical spectrum, and R is the mean facet reflectivity. Using this equation, the losses were found to be 4.5 ± 0.5 cm^{-1} for the TE mode in the wavelength range of 1500 to 1580 nm. Figure 2.11 shows the waveguide losses in the intermixed material, with its wavelength shifted by 100 nm. The losses are shown to be reduced at the desired wavelengths (1500 – 1580 nm).

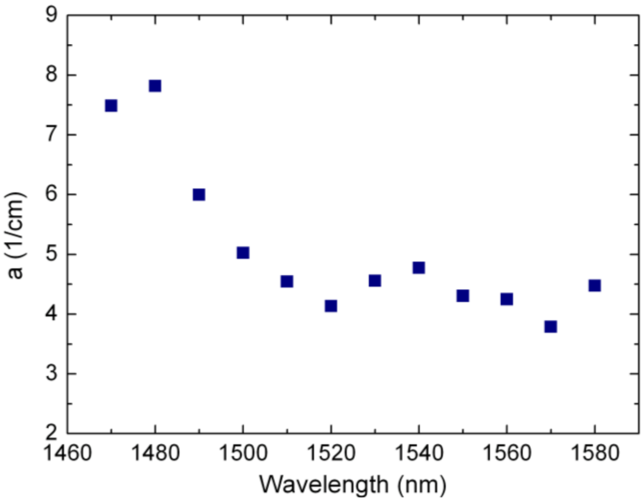

Figure 2.11 Losses in single mode waveguide fabricated from epilayer material bandgap blue shifted by 100 nm [27].

2.5 Chapter Summary

This chapter presented the *AlGaInAs/InP* material system as a platform for system integration. A brief guide to fabricating a simple FP ridge laser was given. The five-QW *Al*-quaternary substrate was introduced and its beneficial functions detailed, such as the superior thermal characteristics due to the larger conduction band offset, and smaller valence band discontinuities compared with the *P*-containing QWs. An improved layer structure was presented, based on the *Al*-quaternary material containing three-QWs along with an FRL, which was used to enlarge the fundamental transverse mode area while suppressing higher order modes. Using fewer QWs meant that the confinement factor was reduced, along with the differential gain, which in turn provided an increased saturation energy. A detailed comparison of the *LI* characteristics, along with the near and far fields of the five- and three-QW structures were shown, highlighting the improvements of the newly designed wafer structure. And finally, QWI was explained with some experimental results revealing the capacity to shift the bandgap energy to the equivalent wavelength of up to 100 nm by annealing at temperatures over 600°C. QWI is particularly useful for integrating multiple devices on a single chip by locally passivating the otherwise active material, such as waveguides and distributed Bragg reflectors (DBRs), and thus has obvious benefits in integrated circuits. This technique was used to develop many of the devices that are discussed in the proceeding chapters. The next chapter will discuss OCDMA subsystems and system processes using these integrated techniques.

2.6 References

[1] S. M. Sze, “Modern Semiconductor Device Physics,” New York: John Wiley and Sons, 1998.

[2] Z. G. Lu, J. R. Liu, S. Raymod, P. J. Poole, P. J. Barrios, and D. Poitras, “312-fs pulse generation from a passive C-band InAs/InP quantum dot mode-locked laser,” Opt. Express, Vol. 16, No. 14, pp 10835-10840, 2008

[3] E. U. Rafailov, M. A. Cataluna, and W. Sibbett, “Mode locked quantum dot lasers,” Nature Photon., Vo. 1 pp 395-401, 2007.

[4] S. O. Kasap, “Optoelectronics and Photonics - Principles and Practices,” New Jersey: Prentice-Hall Inc., 2001.

[5] W. T. Silvfast, “Laser fundamentals”, 2nd Ed., Cambridge, Cambridge University Press, 2004.

[6] K. Yvind, D. Larsson, L. J. Christiansen, C. Angelo, L. K. Oxenlowe, J. Mork, D. Birkedal, J. M. Hvan, and J. Hanberg, “Low-jitter and high-power 40-GHz all-active mode-locked lasers,” IEEE Photon. Technno. Lett., Vol. 16, No. 4, pp 975-977, 2004.

[7] D. E. Morton, L. Stevenson, and M. Garcia, “Design and Development of Optical Coatings on Laser Bar. Facets,” Proc. SPIE, Vol. 5280, pp 413, 2004.

[8] M. T. C. Silva, J. P. Sih, T. M. Chou, J. K. Kirk, G. A. Evans, and J. K. Butler, “1.3 μm strained MQW AlGaInAs and InGaAsP ridge-waveguide laser a comparative study,” MTT-S IMOC’99 Proc., Vol. 1, pp 10-12, 1999.

[9] T. Higashi, S. J. Sweeney, A. F. Phillips, A. R. Adams, E. P. O’Reilly, T. Uchida, and T. Fujii, “Experimental analysis of temperature dependence in 1.3-μm AlGaInAs-InP strained MQW lasers,” IEEE J. Sel. Top. Quant. Electron., Vol. 5, No. 3, pp 413-419, 1999.

[10] P. McIlroy, A. Kurobe, and Y. Uematsu, “Analysis and application of theoretical gain curves to the design of multi-quantum-well lasers," IEEE J. Quant. Electron., Vol. 21, No. 12, pp 1958-1963, 1985.

[11] L. Hou, M. Haji, R. Dylewicz, P. Stolarz, B. C Qiu, E. A. Avrutin, A. Catrina Bryce, “160 GHz harmonic mode-locked AlGaInAs 1.55 μm strained quantum well compound cavity laser,” Opt. Lett., Vol. 35, pp 3991-3993, 2010.

[12] L. Hou, M. Haji, R. Dylewicz, B. C Qiu, A. C. Bryce, “10 GHz mode-mocked extended cavity laser integrated with surface-etched DBR fabricated by Quantum Well Intermixing,” IEEE Photon. Technol. Lett., Vol. 23, pp 82-84, 2011.

[13] R. J. Mears, L. Reekie, M. Jauncey, and D. N. Payne, “Low-noise erbium-doped fiber amplifier operating at 1.54 μm”, Electron. Lett. 26, pp 1026, 1987

[14] J. Singh, “Optoelectronics: An introduction to materials and devices,” McGraw-Hill, Inc., 1996.

[15] F. K. Reinhart, I. Hayashi, and M. B. Panish, “Mode reflectivity and waveguide properties of double-heterostructure injection lasers," J. App. Phys., Vol. 42, No. 11, pp 4466-4479, 1971.

[16] L. Hou, M. Haji, J. Akbar, B.C. Qiu, and A. C. Bryce, "Low divergence angle and low jitter 40 GHz AlGaInAs/InP 1.55 μm mode-locked lasers," Opt. Lett., Vol. 36, pp 966-968, 2011.

[17] D. Klotzkin, J. S. Huang, H. Lu, T. Nguyen, T. Pinnington, R. Rajasekaran, H. Tan, and C. Tsai, "An overgrowth-free design for InGaAlAs spot-size-converted ridge waveguide lasers" IEEE Photon. Technol. Lett. 19, pp 975-977, 2007.

[18] B. Qiu, S. D. McDougall, X. Liu, G. Bacchin, and J. H. Marsh, "Design and fabrication of low beam divergence and high kink-free power lasers," IEEE J. Quantum Electron. Vol. 41, No. 9, pp 1124-1131, 2005.

[19] D. Garbuzov, L. Xu, S. R. Forrest, R. Menna, R. Martinelli, and J. C. Connolly, "1.5 μm wavelength, SCH-MQW InGaAsP/InP broadened-waveguide laser diodes with low internal loss and high output power," Electron. Lett., Vol. 32, No. 18, pp 1717-1719, 1996.

[20] J. Joindot, and J. L. Beylat., "Intervalence band absorption coefficient measurements in bulk layer, strained and unstrained multiquantum well 1.55 μm semiconductor lasers," Electron. Lett., Vol. 29, pp. 604-606, 1993.

[21] A. A. Ballman, A. M. Glass, R. E. Nahory, and H. Brown, "Double-doped low etch pit density InP with reduced optical absorption," J. Cryst. Growth, Vol. 62, pp 198-202, 1982.

[22] L. Hou, M. Haji, J. Akbar, J. H. Marsh, and A. C. Bryce, "AlGaInAs/InP monolithically integrated DFB laser (invited)," IEEE J. Quant. Electron., V. PP, No. 99, pp 1-1, 2011.

[23] J. Minch, S. H. Park, T. Keating, and S. L. Chuang, "Theory and experiment of $In_{1-x}Ga_xAs_yP_{1-y}$ and $In_{1-x-y}Ga_xAl_yAs$ long wavelength strained quantum-well lasers," IEEE J. Quant. Electron., Vol. 35, No. 5, pp 771-782, 1999.

[24] J. Binsma, M. Geemert, F. Heinrichsdor, T. van Dongen, R. Broeke,E. Bente, and M. Smit, "MOVPE waveguide regrowth in InGaAsP/InP with extremely low butt-joint loss," IECICE Trans. Electron., E80-C, pp. 675-681, 1997.

[25] S. D. McDougall, O. P. Kowalski, C. J. Hamilton, F. Camacho, B. Qiu, M. Ke, R. M. De La Rue, A. C. Bryce, and J. H. Marsh, "Monolithic integration via a universal damage enhanced quantum-well intermixing technique," IEEE J. Sel. Top. Quant. Electron., Vol. 4, pp 636–646, 1998.

[26] R. G. Walker, "Simple and accurate loss measurement technique for semiconductor optical waveguides," Electron. Lett., Vol. 21, No. 13, pp 581-583, 1985.

[27] S. McMaster, "Monolithically integrated mode-locked Ring lasers and Mach-Zehnder interferometers in AlGaInAs," PhD thesis, University of Glasgow, 2010.

Chapter 3

OCDMA subsystem technologies

The various stages of an OCDMA system's processes are described in this chapter, with a particular focus on integratable technologies. OCDMA methods can be grouped into two categories based on the way in which the codes are applied. Coherent OCDMA relies on the phase of the optical signal being modulated with bipolar codes. Alternatively, incoherent OCDMA methods use amplitude modulation. A number of OCDMA architectures utilise wideband optical sources, such as mode-locked lasers. Mode-locked lasers are beneficial due to their ability to generate high frequency ultrashort optical pulse trains that are suitable for temporal en/decoding as well as modulating. Therefore, a detailed review of mode-locking is given, including the crucial semiconductor saturable absorber dynamics which are essential for achieving passive mode-locking with ultrashort pulses. This is followed by optical data modulation techniques, including those based on phase and absorption modulation.

There is an abundance of optical encoding and decoding techniques, and therefore a summary of the main categorical methods is given, followed by a description of the requirements of the two OCDMA systems considered in this research: temporal phased coded (coherent) OCDMA and wavelength-hopping time-spread (incoherent) OCDMA systems. This is followed by an explanation of the various specialised optical coding algorithms, both bipolar (for phase codes) and unipolar (for incoherent codes) depending on the type of OCDMA implementation used. Finally, post-processing techniques for reducing noise from multiple access interference are discussed.

3.1 Semiconductor mode-locked lasers

There are several ways of generating pulses in semiconductor lasers: *Q*-switching is a phenomenon which describes the effect of self-pulsation, where the cavity losses, or "*Q*-factor" is periodically varied over many round trip resonances due to a build-up of gain, releasing high intensity pulses at proportionally lower frequencies [1]. Gain switching is another method in which the carrier density is modulated in an oscillatory fashion, taking the laser above and below threshold at periodic intervals and thereby producing optical pulses [2]. While these techniques are quite flexible in operation, they tend to produce relatively wide pulses in the order of around 10 ps, with large timing jitter and chirp [3, 4]. Mode-locked laser diodes (MLLD) on the other hand can provide sub-picosecond pulses at repetition rates exceeding 100s of GHz, making them suitable for high speed systems [5]. Moreover, with conventional temperature controlling and pulse synchronisation techniques (discussed in chapter 5), MLLDs can achieve the high stability that is required for operating in long haul communications systems [6, 7].

3.1.1 Mode-locking in semiconductor lasers

Mode-locking works by establishing a fixed phase relationship between the optical modes of a laser cavity. The optical modes can be described as the frequencies of light that are able to oscillate within the laser cavity structure over a finite gain bandwidth. Figure 3.1 illustrates the evolution of the optical field of a semiconductor MLLD, with each mode separated in wavelength by a distance determined by:

$$\Delta\lambda_m = \frac{\lambda_0^2}{2n_g L} \tag{3.1}$$

where λ_0 is the centre wavelength, n_g is the group index of the resonator, and L is the laser cavity length. The spectrum is defined by the bandwidth of the laser medium, and spectral filtering is performed by the laser cavity. Optical pulses are then determined through Fourier transformation of the optical spectrum. The temporal width of each pulse, Δt, is proportional to $1/(N \cdot f)$, where $f = c/2n_gL$, and N is the number of cavity modes [8].

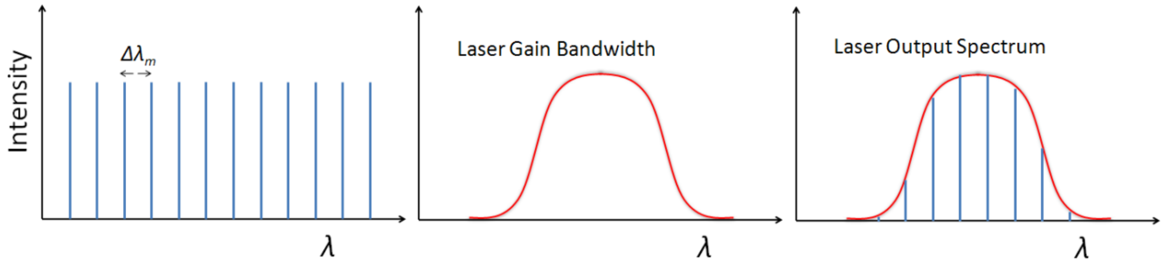

Figure 3.1 The evolution of the optical field of a semiconductor MLLD.

Mode-locking can be achieved using active or passive techniques. Active mode-locking uses an external reference clock to pump the laser and modulating the amplitude such that the phases of the optical modes align to a single frequency determined by an injected clock signal. Conversely, passive mode-locking is achieved by incorporating an intercavity saturable absorber (SA) into the resonant cavity, providing a nonlinear loss modulation at each round trip by low intensity filtering. Passive mode-locking techniques are able to provide much shorter pulse widths than the active counterpart due to the low amplitude filtering of the leading and trailing edges of the pulse, whereas the pulse peak is preserved due to absorber saturation [3]. Moreover, due to the fast modulation via the SA, no electronic modulator is required for mode-locking to occur; however, this in turn leads to issues with timing jitter and synchronisation. To solve this, hybrid solutions can be employed in which active and passive techniques are combined to reduce the modal noise by direct modulation of the SA segment (see chapter 5 for more on noise reduction techniques).

Mode-locking via saturable absorption is generally categorised by two regimes, fast and slow, which differ depending on the period of the window of amplification around the pulse: Fast saturable absorption uses an absorber recovery time that is quicker than the pulse width [9], whereas the slow absorption regime uses a longer recovery duration due to a longer carrier lifetime in the absorber [10]. The latter is more predominant in monolithically integrated mode-locked lasers. Generally, as the gain builds up in the cavity, it saturates after a given period and remains constant, with the modes operating at random phases. The implementation of cavity losses via an SA provides modal phase selection due to selective amplification of high intensity signals, while lower intensity signals are duly absorbed, and after several round trips the phases collectively align due to modal competition for gain. These result in the formation of an optical pulse of a duration that is inversely proportional to the number of modes aligned [11]. Moreover, the pulse width will tend to reduce with decreasing SA lengths and decreasing carrier sweep out times, i.e. absorption lifetime [3, 12].

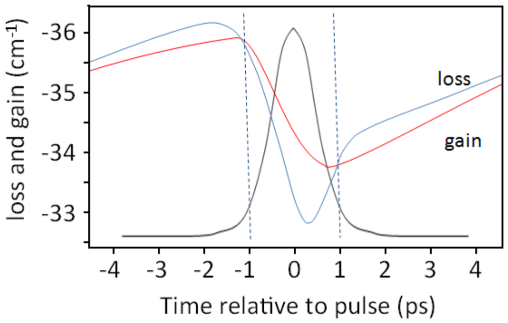

Figure 3.2 Gain and absorber dynamics in the time domain.

For a better understanding of the pulse narrowing mechanism via the SA in passive mode-locked lasers, it is worthwhile considering the time-dependent nonlinearities in the gain and absorption per round trip. In Fig. 3.2, the net gain in the gain section and the net loss in the absorber section are plotted relative to a single pulse traversing within the laser cavity. As the optical pulse enters the SA, the leading edge experiences a loss until the absorber becomes saturated, at which point the net gain and losses are equal. As the gain is increased during absorption saturation, the pulse is amplified until the SA recovers just after the trailing edge of the pulse. Thus, for pulses to form within a laser resonator, the losses must saturate faster than the gain [13], such that $E_a^{sat} < E_g^{sat}$, where:

$$E_{g,a}^{sat} = \frac{h\omega\, \sigma_{g,a}}{d(g,a)/dN(g,a)} \tag{3.2}$$

in which $h\omega$ is the photon energy, σ is the cross sectional area of the laser mode, and $d(g,a)/dN(g,a)$ is the differential gain or absorption coefficient [14]. The condition can then be rewritten as:

$$\frac{h\omega\ \sigma_a}{da/dN_a} < \frac{h\omega\ \sigma_g}{dg/dN_g} \tag{3.3}$$

Absorption saturation is more readily achieved in reverse biased MQW based structures due to the screening of excitons by free carriers (which is qualitatively distinct from filling the conduction and valence band states in the wells). Also, given the large ratio of the respective sections, a larger differential gain is provided in the absorber section (due to a lower carrier density) compared to that of the gain section, and therefore the saturation condition shown in (3.3) is duly met [15].

Another requirement for mode-locking is that the recovery time τ of the absorber must be shorter than that of the gain such that the condition $\tau_a < \tau_g$ holds true. Values of τ_g can be approximated by calculating the carrier lifetime in the material using the following equation [16]:

$$\tau_g = \frac{1}{A_{\text{nr}} + 2B(N)N + 3CN^2} \tag{3.4}$$

where A_{nr}, $B(N)$, and C are the monomolecular, radiative, and Auger recombination coefficients respectively, and N is the carrier density. Thus, using the parameters: $A_{\text{nr}} = 7 \times 10^7 \text{s}^{-1}$, $B = 1.5 \times 10^{-10} \text{cm}^{-1}$, and $C = 1.4 \times 10^{-28}\ \text{cm}^6\text{s}^{-1}$, and $N = 1 \times 10^{18} \text{cm}^{-3}$ [17], we can estimate the gain lifetime in the *AlGaInAs/InP* substrate to be around 1.27 ns cm^{-1} for a moderate carrier density value. This value is of course relative to the injection current, *I*, and the volume of the active region V_a, which both affect the carrier density value as shown by [18]:

$$\frac{I}{qV_a} = (A_{\text{nr}}N + 2B(N)N^2 + CN^3) \tag{3.5}$$

Thus, for a larger active region, the carrier density is reduced. But as the applied current is increased, the carrier density also increases, leading to a shorter τ_g. Typically, values of τ_g are in the order of several hundreds of ps [19, 20].

As for τ_a, a shorter value provides narrower pulses due to a reduction in the gain window period, as illustrated in Fig. 3.2 [21]. Therefore, to encourage a shorter τ_a, fabrication processes such as proton bombardment [22] ion implantation [23] or non-stoichiometric growth [24] techniques are often used to create lattice defects so that faster recombination rates can be achieved. However, since the *AlGaInAs/InP* MQW system is natively an active structure (i.e. it will absorb light without any bias or passivation techniques such as quantum-well intermixing (QWI)), devices are able to be monolithically integrated without the use of such material defecting or epitaxial regrowth steps. This makes mode-locked lasers relatively easier to fabricate; however, in order to make a comparison of absorption recovery time to other passive materials, such as the prevalent *InGaAsP/InP* MQW system, an experimental study was required to attain the values of τ_a in the *Al*-quaternary material. The next section describes in detail the effects of applying a reverse bias voltage across a QW based structure before explaining the measurements and characterisation of absorption in the five-QW *AlGaInAs/InP* material system.

3.1.2 Saturable absorption in *AlGaInAs/InP*

Saturable absorption is related to the interband transitions between the valence and conduction bands. The energy of absorbed photons is transferred to the electrons in the valence band, which are then bought up to the conduction band due to carrier excitation. At low optical intensities, the degree of carrier excitation is small, and so the absorber remains unsaturated. At high optical intensities however, the accumulation of electrons in the conduction band causes a depletion of the absorbing transition. This effect is known as Pauli blocking [25], and results in a reduced absorption of photons. After saturation, the absorber quickly recovers due to interband thermal relaxation and recombination, the rate of which is a crucial parameter for designing SA sections and EAMs. Other key parameters are the wavelength range, and the saturation fluence [26].

In QW structures, it is the quantum confined stark effect (QCSE) that is predominantly triggered by an applied electric field, i.e. a reverse bias voltage. The application of a reverse bias voltage across the wells causes the electron states to shift to lower energies and the hole states to shift to higher energies, such that the conduction and valence bands are tilted, as shown in Fig. 3.3. This effect subsequently provides a shifting of the absorption band edge to longer wavelengths. Moreover, the applied reverse bias voltage will shift the electrons and holes to opposite sides of the well, which reduces the recombination efficiency of the system. The separation of the electrons and holes are confined by the potential barriers surrounding the well, which means that excitons can exist.

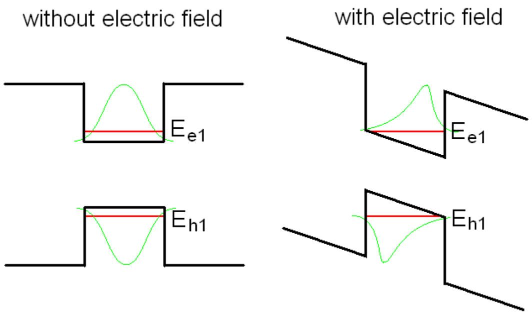

Figure 3.3 Quantum-well band diagram without and with and applied electric field. E_{e1} and E_{h1} represent the 1st electron and hole levels, respectively. The curved lines represent the envelope wave functions for electrons and holes.

Excitons can be described as the Coulomb attraction between an electron and hole pair, which in QWs are compressed perpendicularly to the QW layers thus providing a stronger binding energy than in bulk materials. The excitons provide a response of the QCSE as explained in the Kramers-Kronig relations, which describe the change in the refractive index relative to the change in the absorption [27], and subsequently provides a photo-generated electron recombination in the QWs depending on the bias voltage and temperature. This occurs over a discrete bandwidth, corresponding to the band gap energy of the QW under a reverse bias less the binding energy of the exciton (which is in the order of a few meV [28]), forming a set of discrete peaks within the 'forbidden' energy levels of the semiconductor, close to the conduction band edge. Higher applied voltages cause the exciton absorption spectra to broaden due to a greater tilt of the band gap, which also causes an expansion of the absorption spectral width as a result of the exciton peaks merging with the conduction energy band [29].

The exciton absorption peak must therefore lie close to the gain peak in order to modulate the modal interactions to achieve mode-locking [30]. For example, if the exciton peak, and thus the SA band-edge is red-shifted, the absorption will always be low and barely saturable. Conversely if the SA band-edge is largely blue shifted, the absorption will be too high and remain bleached. Optimally, the gain peak should only scarcely coincide with the SA band edge, in order for strong modulation of the absorption losses to be expected. Typical values for the band gap shift in the *Al*-quaternary material are in the order of 1 THzV^{-1} [21].

As well as exciton absorption, there are two known escape mechanisms in which a carrier may leak away from the wells during the application of a reverse bias: Tunnelling is the process of escape via transportation out of the lower bound electronic state, and thermionic emission is a thermally assisted leap over the barrier. Thermally assisted tunnelling may also occur by tunnelling out of the upper weakly bound state. Thermionic emission usually occurs above room temperature, whereas tunnelling escape occurs at relatively lower temperatures (< 70 K) [31].

It can then be assumed that as the reverse bias increases, the rate of thermionic emission of carriers dominates over any tunnelling process [32]. Based on this assumption, it is possible to calculate the rate of absorption recovery as a function of reverse bias (V), using the expression [33]:

$$\tau_a = \sqrt{\frac{2\pi m^* L_w^2}{k_B T} \cdot \exp\left(\frac{E_b - \dfrac{L_w e(V + V_{bi})}{2d}}{k_B T}\right)} \tag{3.6}$$

where e is the carrier charge and m^* is the effective mass, $k_B T$ is Boltzmann constant with temperature, L_w is the width of the QW, E_b is the height of the barrier, V_{bi} is the diode voltage potential, and d the width of the depletion region. Using this equation, an approximation for the expected recovery times in the *AlGaInAs* substrate can be attained, using the parameters T = 295K, a conduction band offset of 280 meV, $m^* = 0.0035m_e$, and a depletion region width of 185 nm. These values are plotted in Fig. 3.4.

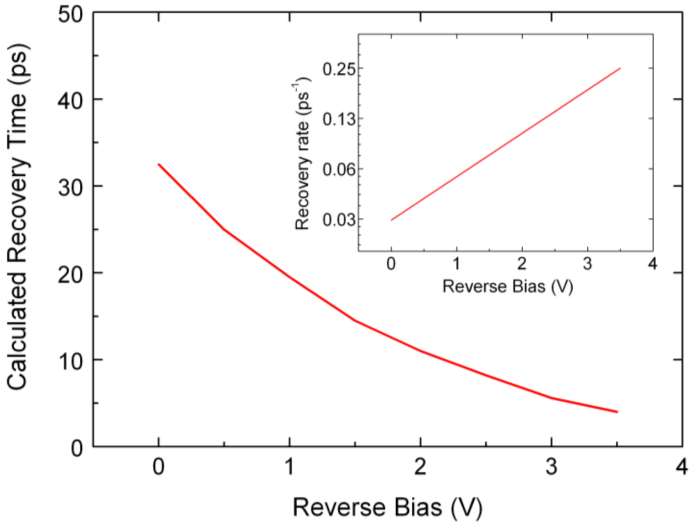

Figure 3.4 Absorption recovery times calculated for the *Al*-quaternary material using eq. 3.6. Inset: recovery rate as a function of bias.

To acquire the recovery time of the material, and to ascertain the wavelength range and saturation fluence, a series of experiments were performed. A 50 μm long deeply etched cavity was used with a 10° angled front facet, and a deeply etched mirror serving as a back facet. This allowed for light to be injected into the cavity with reduced front facet reflections, and relatively higher back facet reflections, so that the material properties in the active region could be probed. First, the wavelength range of the absorption spectrum was measured. The experimental setup is shown in Fig. 3.5(a). A tunable CW laser covering the C-band was used to inject light into the test sample using a lensed fibre. The reflections were then sent back along the fibre and passed through an optical circulator to isolate the reflected signal for subsequent detection and observation using an optical spectrum analyser (OSA). The injected signal wavelength was varied at 0.5 nm steps from 1500 – 1580 nm at -10 dBm, and the intensity of the reflected signal was measured at each step using the OSA. This measurement was repeated while the reverse bias (0-4 V) was incremented and applied to the test sample cavity.

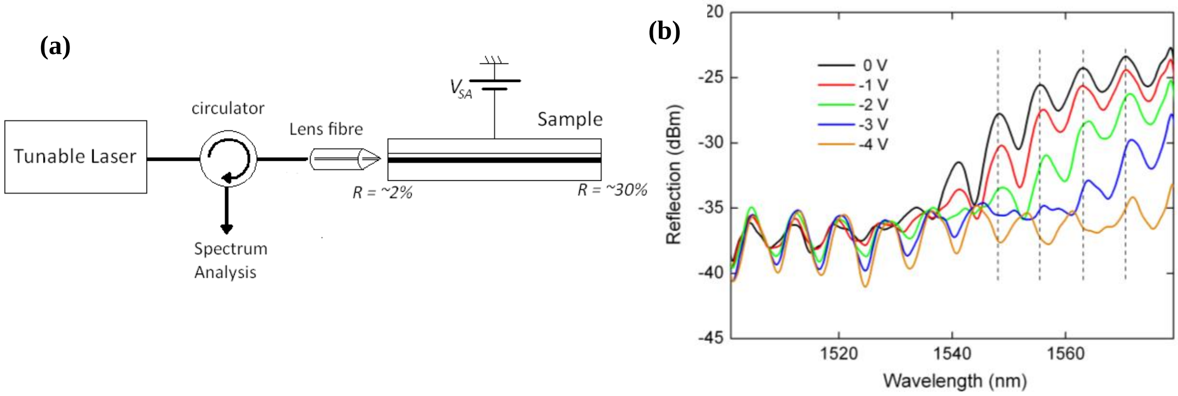

Figure 3.5 (a) Schematic of the experimental setup used to measure absorption in the wavelength domain. (b) Experimental results showing the intensity of the reflected signal, per wavelength, while applying a reverse bias voltage to the sample.

Figure 3.5(b) shows the reflection spectra of the sample measured under applied biases from 0 to -4V, at 1V intervals. The absorbing region is clearly shown as well as the band-edge red shift as the bias was increased. The apparent residual Fabry-Pérot resonances were present due to the finite reflectivity within the cavity, giving rise to cavity modal structures. These resonances are also shown to experience a red shift as the voltage is increased due to QCSE, which is emphasised at and around 1550 nm due to the greater energy transitions in the QWs. Similarly, the band edge experienced QCSE as the voltage was increased. Alternatively, applying gain to the sample would shift the band edge towards slightly higher energies due to the plasma effect (see section 3.2.2).

For measuring the recovery time, the experimental setup was adapted to include a pump signal (Fig. 3.6). A 10 GHz pulse stream was coupled with the continuous wave (CW) signal (probe), operating at a slightly different wavelength such that only the probe signal reflections remained after subsequent band pass filtering at the output. This technique is known as cross absorption modulation (XAM), and is often used for wavelength conversion [34]. A high speed sampling oscilloscope (85 GHz nominal bandwidth) was then used to observe the effects in the time domain.

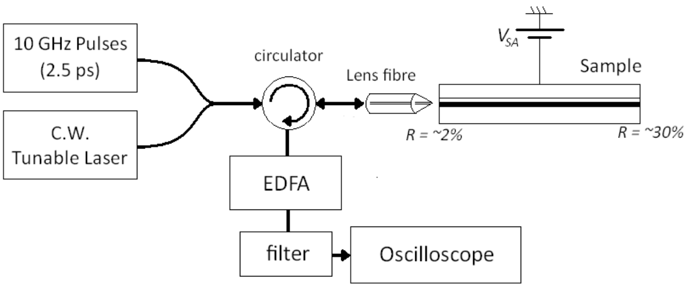

Figure 3.6 Schematic of the experimental setup used to measure the recovery time.

The wavelength converted pulses are shown in Fig. 3.7(a), under different reverse biases, together with the incident pulses. Due to the stark shift of the modes as the reverse bias was increased, the CW signal wavelength was chosen to lie close to a Fabry-Pérot peak, which would provide the highest extinction ratio for the wavelength converted pulses at a given bias. The reduction in τ_a as the bias was increased is evident.

Figure 3.7(b) shows the recovery times of these traces fitted to a single exponential decay function of the temporal decay with respect to the applied reverse bias voltages greater than 0.5 V (where the recovery between successive pulses was sufficient). The recovery time of the input pulses is also shown as a reference (3 ps). Due to the bandwidth limitations of the oscilloscope, the full width half maximum (FWHM) of the input pulses was measured as 7.5 ps, whereas an autocorrelation measurement showed pulse durations of 2.5 ps. At a bias of 4 V, the measured output FWHM from the oscilloscope was 9.8 ps, but the actual width is much shorter than this value, and so the recovery time may also be shorter. The values plotted from the calculated recovery time values are also plotted in Fig. 3.7(b), and agree well with the experimental data, particularly at higher values of reverse bias.

.

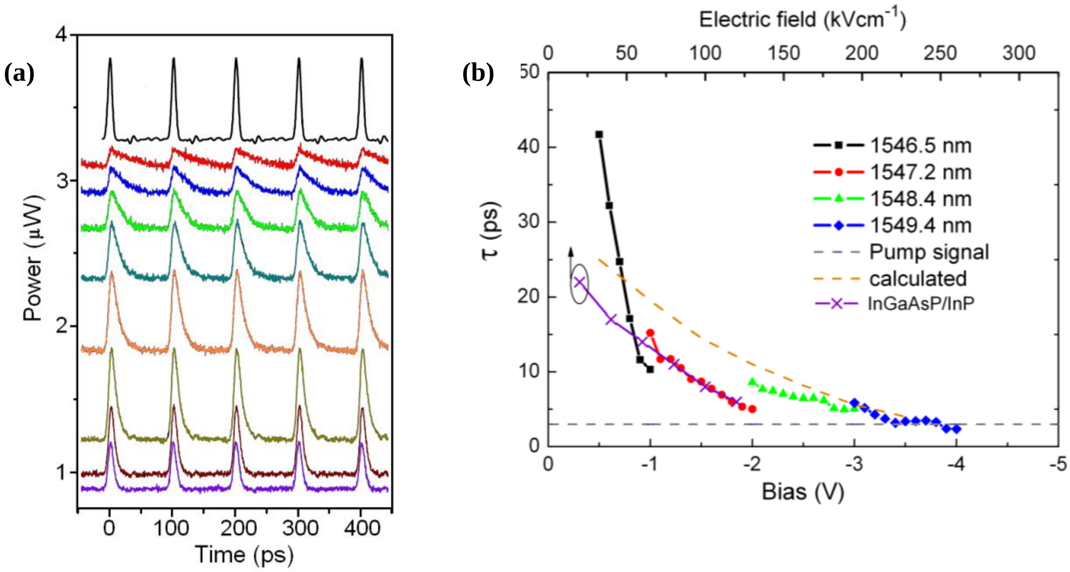

Figure 3.7 (a) Measured pump probe traces as viewed on a high speed oscilloscope. The top trace indicated the injected pump signal, while the other traces show the output signal as the voltage was increased from 0 – 4V by steps of 0.5 V (top to bottom). (b) Recovery time of wavelength converted pulses as a function of bias.

Also, to show a comparison, values of τ_a reported in [35] from pump probe measurements in an electroabsorption modulator (EAM) based on *InGaAsP/InP* quantum-wells have also been plotted in Fig. 3.7(b). It is apparent that the values of τ_a in both materials are similar in terms of applied electric field, particularly from 50 to 120 kVcm^{-1}. Values above 120 were not measured in [35], so a further comparison cannot be made for higher electric field values. These results do however explain the recent short pulse durations in the order of 700 fs obtained in both materials considered here, which can be explained by their fast recovery time dynamics [36, 37].

3.2 Optical data modulation/demodulation

At the transmission stage of an OCDMA system, digital data conversion must be transformed from the electrical domain to the optical domain. This can occur either before, during or after encoding, depending on the particular type of encoding used. Electrical digital signals generally use the on-off keying (OOK) format, where a binary “1” is encoded as the presence of an electrical signal, and a “0” is represented by the absence of such signal, although several variations of this exist [8]. There are two common implements used to apply OOK modulation in the optical domain. The Mach-Zehnder based modulator (MZM) is often used in fibre based systems (due to its input polarisation dependence). This involves splitting a signal into two channels, and applying a π phase shift to one channel for every binary “0” before recombining them, causing the signal to destructively interfere with itself. This method is also known as electro-optic modulation (EOM). For integrated semiconductor systems however, electro-absorption based modulators (EAM) are often favoured due to their compactness, high speed, polarisation insensitivity, lower insertion loss, lower voltage requirements, and better extinction ratios [38-41].

3.2.1 Amplitude modulation

As with saturable absorbers, QW based EAMs use the QCSE effect, in which the band gap energy is varied with an applied electric field, causing changes in the absorption spectrum (i.e. absorption band edge) [38, 41]. It is this feature of QWs that is exploited in EAMs to rapidly absorb light propagating through a waveguide.

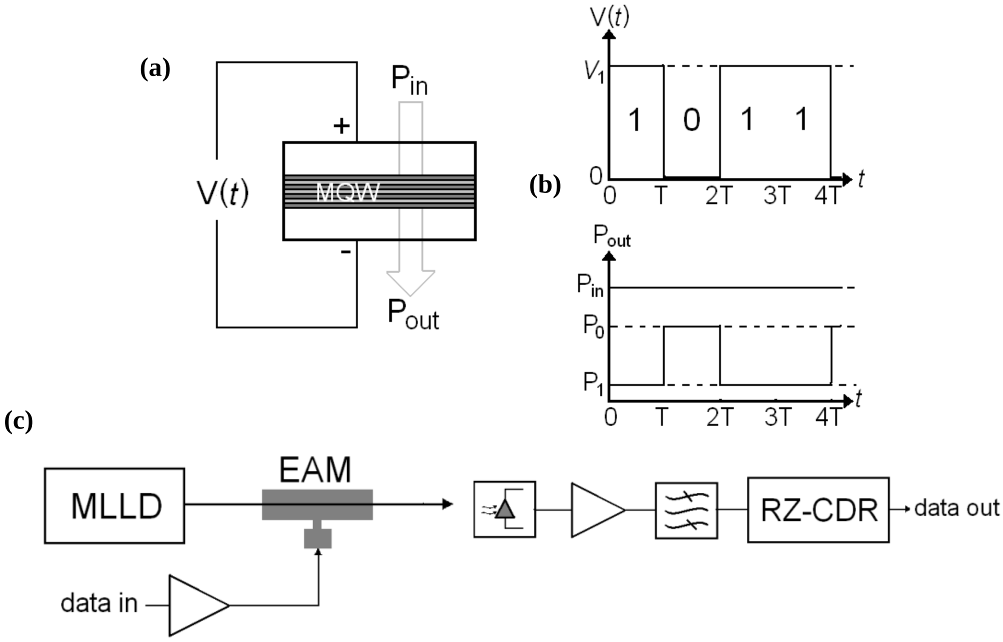

Figure 3.8 (a) Schematic of electrical circuit of waveguide under reverse bias, (b) data conversion from the electrical domain to the optical domain via an EAM, and (c) schematic of the setup used for data modulation and subsequent detection circuit.

Figure 3.8(a) shows the modulation technique applied using an EAM. The pulse stream from a MLLD is sent through the waveguide of the EAM, while the data encoded electrical signal is applied along with a reverse bias voltage, causing rapid variations of the electric field within the band structure, thus absorption of the light occurs at periods defined by the frequency and bit pattern of the electrical data (Fig. 3.8(b)). For return-to-zero (RZ) OOK modulation the data frequency is equal to the round trip frequency of the laser. At the receiver, carrier translation is performed by a high speed photodetector, which converts the optically modulated data into its original electric form for subsequent transimpedence amplification and noise filtering (Fig. 3.9(c)) [8]. Following this, a clock and data recovery circuit (CDR), which extracts a clock for timing synchronisation purposes, will include a decision circuit to decide when the signal is a “1” or a “0”. Fortunately, since the incoming data signal is pulsed, clock signals are relatively easier to recover.

3.2.2 Phase modulation

Rather than modulating the amplitude via an electric field, forward biasing the material can provide phase modulation, which is particularly useful for differential-phase-shift-keying (DPSK) based data modulation. The application of a current to an active waveguide causes the absorption band edge to shift due to a change in the refractive index of the material. More specifically, the electro-optic effects of an active waveguide under forward bias are associated with the following three carrier effects: Band filling, band-gap shrinkage, and free carrier absorption [42].

The absorption of a photon can only occur if there is a vacancy in the conduction band state and an occupied valence band state. Band filling occurs when the carriers occupying the available states of a nominal band gap energy causes an increase in the optical energy required to excite a carrier. This causes a decrease in the absorption of photon energies slightly above the band gap energy, and therefore a decrease in the change of the refractive index, which is largest for photon energies near the band gap and smallest for energies far above and below the band gap.

Alternatively, band gap shrinkage refers to a reduction of the conduction band energy and an increase of the valence band energy due to electron screening effects. This occurs when there is a large concentration of electrons in the bottom state of the conduction band, promoting Coulomb forces to repel the electrons from one another due to an overlap of the electron wave functions (Fig. 3.3). The shrinkage of the band gap energy will influence absorption, and unlike band filling, a positive change in the refractive index will occur leading to a phase shift of a propagating signal. This is different to the excitonic behaviour previously described, which occurs when applying a reverse bias, and in addition to colliding particles (and/or phonons) in the crystal is mutually known as the many-body effects [28].

A photon may also be absorbed by a free carrier, moving to a higher energy state within a band. This type of interband absorption, known as the plasma effect, results in a negative change in refractive index, and is directly proportional to the carrier concentrations and the square of the wavelength. Because of this wavelength dependence, the plasma effect is increased as the photon energy decreases below the band gap, as opposed to the band filling effect, in which the refractive index change is largest near the band gap wavelength and approach zero for energies well below the band gap. For an efficient electro-optic device, i.e. phase shifting, it is important to induce maximum changes in refractive index in order to promote large phase changes.

Considering all of these effects, it is important that the laser source operates as close to the band gap wavelength of the material as possible for a maximum phase shift effect.

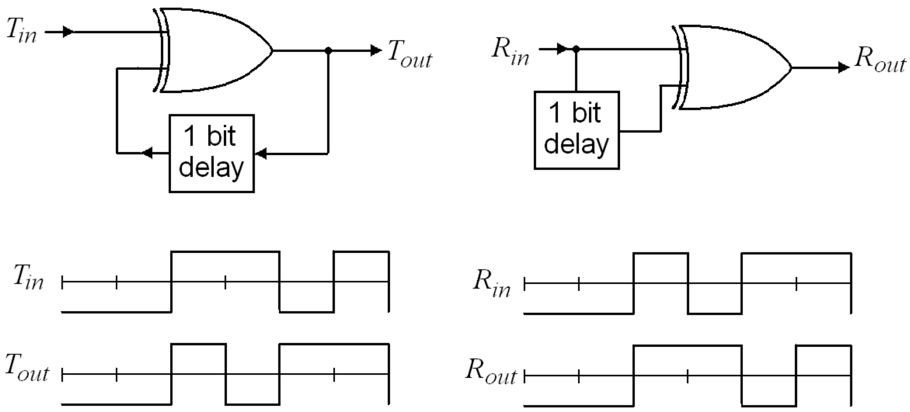

Figure 3.9 Logic block diagrams and example timing diagrams for differential encoding and decoding [8].

Achieving DPSK modulation of a data signal requires an additional electrical precoding sequence to introduce a differential series. Figure 3.9 shows an example of the logic steps required by the electrical precoder. Here, a 1 bit delay is implemented and is passed through an XOR logic gate along with the original sequence so that the output is a 0 if the delayed input bit is the same as the current input bit, or a 1 if it is different. Reversing this process can be achieved by delaying the received signal by 1 bit and feeding this into an XOR logic gate together with received signal, such that the output is 0 if the current bit is the same as the previous, or a 1 if it is different (Fig. 3.10). An optical interferometer, such as an asymmetric Mach Zehnder interferometer (explained in more detail in chapter 6) can be used to provide the delay of the optical signal, thus forming a differential demodulator in this case. Balanced detection techniques can also be implemented at the output to achieve an intrinsic 3 dB receiver sensitivity advantage over the conventional RZ-OOK methods. This is due to the separation of the two DPSK symbols, which is relatively larger in optical power by a factor of 2 or 3 dB [43].

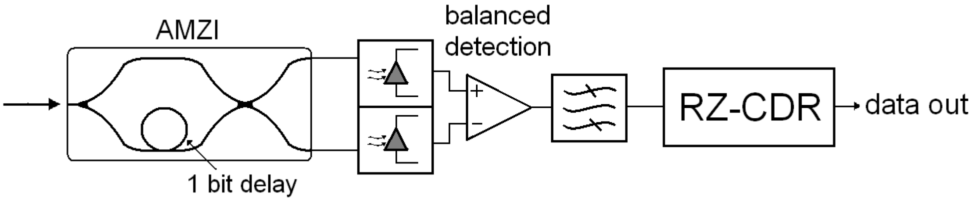

Figure 3.10 Receiver circuit design for a balanced detection based DPSK demodulator [8].

DPSK is often favoured over OOK based modulation due to its spectral efficiency [44], and higher data rates achievable due to its flexibility over binary constellations. Applications include the wireless LAN standards (IEEE 802.11b/g™), which use variations of DPSK modulation such as binary- (BPSK) and quadrature- (QPSK) based methods, depending on the data rate required [45, 46]. Bluetooth™ technology also uses variations of this scheme [47], as well as low rate wireless personal area networks (IEEE 802.15) [48]. Other modulation schemes include quadrature amplitude modulation (QAM), and amplitude shift keying, for use in digital communications systems [44].

3.3 Optical encoding/decoding methods

Coherent and incoherent OCDMA are distinct in the way in which the codes are applied. Coherent OCDMA techniques generally use phase modulation, whereas incoherent OCDMA utilizes amplitude modulation [8]. In this section, Coherent OCDMA encoding and decoding methods shall be described first, followed by incoherent methods. Since there are a number of variations in the encoding processes in both schemes, only those which are relevant to this research shall be discussed.

3.3.1 Coherent OCDMA

Coherent OCDMA methods can be divided into the two following categories; spectral (SPC-OCDMA) and temporal phase coded OCDMA (TPC-OCDMA). In SPC-OCDMA systems, each spectral component of a multiwavelength source (such as a broadband mode-locked laser) is phase coded with a unique set of *N*-element spectral phase codes, where each user is assigned a unique code sequence. In general, encoding involves separating the modulated spectrum into discrete ‘spectral bins’ and a distinct phase shift is then applied to each bin. Examples of this can be found in [49, 50, 51].

In TPC-OCDMA systems, encoding is applied rather in the temporal domain. A mode-locked laser may be employed as the optical source; however it is not the multiwavelength spectral characteristics of the laser that is exploited. Instead, the short pulses generated at the source are replicated into N pulse copies (where N is the number of temporal positions in a bit period), and each copy is delayed such that they lie on an equally spaced time grid. Each pulse copy undergoes a phase change depending on the user's assigned phase code sequence. As with most coherent OCDMA systems, the pulses are generally modulated with data prior to encoding and each data bit corresponds to a temporal chip interval (i.e. the spacing between each set of pulses). Therefore, a larger temporal chip interval with shorter delays is required as the number of users is increased. Moreover, employing ultrashort pulses may ease the crosstalk between each temporal component and will thus improve the efficiency of the system [8].

Phase coding can be applied using binary codes (1s and 0s, or the equivalent π or 0 phase change), or more advanced codes consisting of multilevel phase codes. Section 3.4.1 describes coherent coding in more detail. Decoding subsequently requires an inversion of the phase changes and delays that were performed at the transmitter. Each temporal chip is then summed up coherently, providing a single pulse output which may then be detected and processed via a photodiode and subsequent digital electronics based post-processing. An example of a TPC-OCDMA encoder/decoder pair is shown in Fig. 3.11.

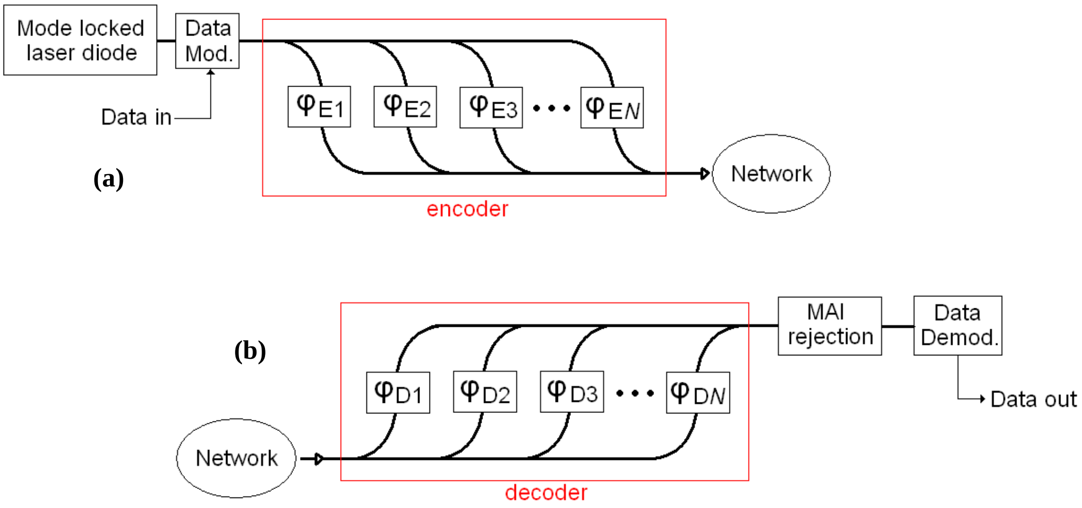

Figure 3.11 Block diagram of TCP-OCDMA system architecture, including (a) encoder circuit, and (b) decoder circuit designs. φ_{EX}: Encoder phase sequence, φ_{DX}: Decoder phase sequence.

In this example, a mode-locked laser producing optical pulses at a fixed repetition rate is modulated with data prior to encoding. The pulse is then sent through a multitude of delays using waveguide path splitting via integrated multimode interference (MMI) coupling. The path length difference between the longest and shortest delay corresponds to the temporal chip period, in which a binary signal is stored. Each pulse copy will then undergo a discrete phase change using integrated phase shifting sections along the waveguide path, before being recombined into a single channel. The signal is then ready for synchronous transmission over the network, which may be occupied by signals from other users using different phase codes.

At the receiver, the signals from the routed network are collected and passed through a direct encoder phase imitation, in which the temporal and phase changes are reversed. If the phase shifters are the same as those used during encoding, a traversing pulse shall correctly realign and form a single strong autocorrelation peak by constructive and coherent interference. In the case of phase mismatch, the signal will destructively interfere due to uncorrelated code words, remaining noise-like, and therefore no information is retrieved. Multi access interference (MAI) rejection techniques can be employed following the decoder to eliminate noise from unmatched codes in the TPC-OCDMA system. MAI filtering techniques are discussed later in this chapter (section 2.5). Data can be recovered using photodetection and subsequent electronics based post processing.

Experimental demonstrations of the coherent TPC-OCDMA technique using Mach-Zehder interferometer based delay lines with integrated phase shifters is described in chapter 6.

3.3.2 Incoherent OCMDA

Incoherent OCDMA encoders, in general, use amplitude modulation and rely on the summation of powers to determine the presence of a binary “1”. Due to its incoherent nature, long and sparse unipolar codes are often employed to distinguish each user’s data pattern within the multiple access network. Coding techniques are more fully explained later in section 3.5. The most common techniques for encoding/decoding in incoherent OCDMA systems include: spectral-amplitude coding [52], spatial coding [53], temporal spreading [54], and wavelength hopping time spreading (WHTS) [55, 56, 57].

Spectral-amplitude coding systems are typically implemented via spectral decomposition of a broadband laser followed by amplitude modulation of each spectral component, before recombining them. Spatially coded systems take several forms, such as encoding/decoding by spatial masking, parallel transmission via multicore fibres, and encoding using tapped delay lines in multiple fibres. Temporal spreading approaches were one of the first OCDMA schemes to be researched [54], and generally operate by dividing each bit period into smaller time intervals called chips. An optical code is then formed by placing optical pulses at different temporal positions within each chip per user. Finally, the WHTS system is a two dimensional coding scheme in which spreading occurs in both the time and wavelength domains simultaneously, and each user is given a unique spreading pattern. In comparison to other schemes, the WHTS technique provides more flexibility in code designing as well as better code performance, zero autocorrelation side lobes, low cross-correlation, and higher cardinality for a given code length, thus leading to an increased system capacity [8].

Design considerations for WHTS system implementations may require laser sources that rapidly hop from one wavelength to another, although using a single laser source to perform this will limit the bit rate performance of system, with signal degradation and speed impediments due to the lasers transitory wavelength hopping mechanism. Therefore, most implementations of WHTS-OCDMA use either a multiwavelength source with spectral slicing, or an array of lasers, with each laser operating at a fixed wavelength [8]. It is ideal for data modulation to be carried out before the encoding stage to avoid degradation of the code words due to the rising and falling edges of the data modulation window period; although, in the case of multi-laser array based systems, it is more energy efficient to perform modulation after the encoding stage.

WHTS encoding requires a number of wavelength and chips positions (N_T) within the bit period, providing a 2D pattern comprising a wavelength hopping pattern, and a time-spreading pattern. Implementations of wavelength hopping can be performed using a variety of technologies, such as arrayed waveguide gratings (AWG) [56], and fibre Bragg gratings (FBG) [57]. Temporal spreading is achieved using tunable time delay elements such as serial delay line switching [58], gated delay lines [59], and compression based gated delay lines [60]. However, for integrated systems, temporal delays must be embedded into the lightwave circuit. The most straightforward geometry is to implement 1:P power splitters/combiners, where P is the number of “1”s in the code. Fixed waveguide path length can be used as delays corresponding to the temporal position of the chip within the code. Each user then requires a splitter/combiner pair, which introduces limitations such as waveguide path losses due to bending and splitting losses, long path length requirements, and the lack of tunability [8]. Optical path switching constructions such as the Mach-Zehnder interferometer (MZI) design can be employed to switch a signal between different delay paths, however, this significantly increases the system design complexity, since each path requires a MZI controller to govern the delay. On the other hand, when using MLLDs, it is important to control the jitter of the pulse train emitted from the laser via synchronisation to a high frequency electrical oscillator clock. There are various techniques for this as described at length in chapter 5. Since MLLDs are optimal for high speed integrated circuits, the application of an RF drive to the laser is inevitable, and therefore, implementing electrical delays to the MLLD rather than optical would avert increasing waveguide losses and save chip space, thus reducing costs.

A schematic of a WHTS OCDMA system based on multiple wavelength generating laser array is shown in Fig. 3.12(a). In this configuration, there are N mode-locked lasers generating optical pulses, which undergo a fixed delay via integrated optical delay lines determined by the optical code sequence employed. These pulses are then modulated with data using methods described in section 3.2, before being sent into a network. The temporal and wavelength characteristics of this signal shall provide sufficient data integrity within the network, where other signals may interfere. This is provided via careful non-orthogonal code selections with low cross-correlations.

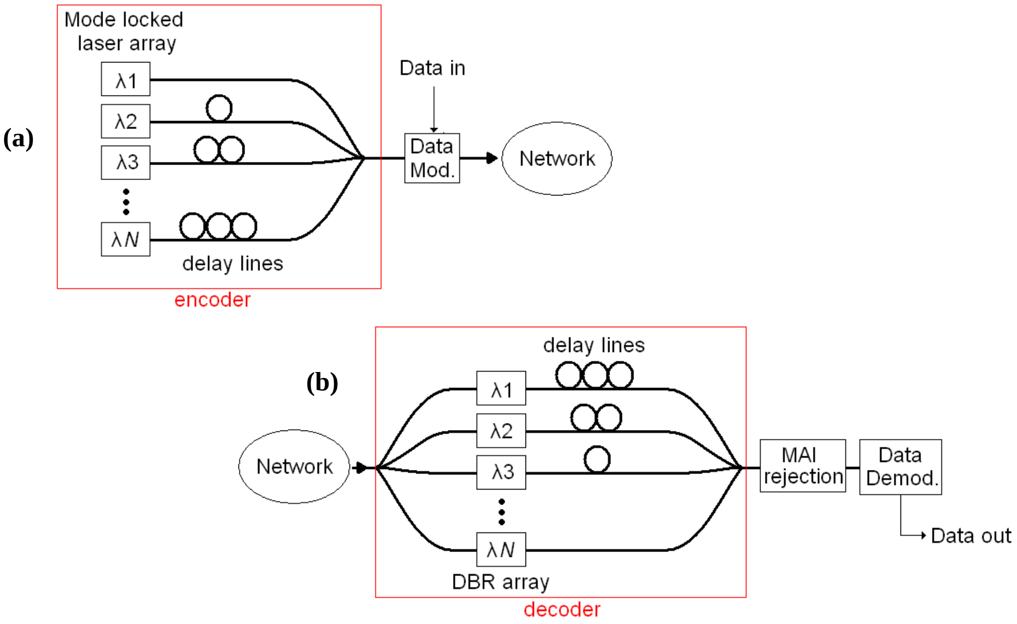

Figure 3.12 Block diagram of WHTS-OCDMA system architecture, including (a) MLLD and DBR array for the encoder circuit, and (b) DBR and delay line array for decoder circuit.

At the receiving end of the network, a decoder, shown in Fig 3.12(b), is used to reverse the encoding procedures. In this case, the signal must be spectrally divided using a similar array of integrated DBRs along the propagation path, and thereby splitting the multiple wavelengths produced at the encoder, forming multiple pulses operating at different wavelengths. Each pulse will then undergo a fixed delay, undoing the coding sequence which was performed at the encoding stage, before being recombined into a single channel. If the WHTS sequence is appositely matched at the decoder, the pulses should temporally align to form a single strong autocorrelation peak, otherwise the signal will become further spread in time, causing additional noise. MAI rejection techniques may follow the decoding procedure in order to filter out noise from unmatched signals, before demodulating the data using optical to electrical conversion via a photodetector.

The foundations of this research is based around the development of such a system, and further details regarding the design, integration and experimental results for the WHTS OCDMA system is presented in chapter 7.

3.4 OCDMA codes

Codes are fundamental to any OCDMA system. The coding sequences applied to a multiple access system allow each user to distinguish their signal over other transmissions occupying the same optical pass-band and temporal space. Since the early 1980s a vast number of coding schemes have been developed, partly owed to the expansion of wireless CDMA networks [8]. In OCDMA, various dedicated codes have been proposed. These codes can be classified into six main categories: (1) pulse amplitude coding [54], (2) pulse phase coding [61], (3) spectral amplitude coding [52], (4) spectral phase coding [62], (5) spatial coding [63], and (6) wavelength-hopping time-spreading (WHTS) coding [55, 56, 57]. These groups are separated by the type of optical source used (wideband, or narrowband), the detection schemes employed and the encoding techniques applied in the system (i.e. coherent, or incoherent). Moreover, the choice of code influences many network issues, such as the number of users that can be simultaneously active (i.e. the number of available codes), the expected performance of the system (i.e. multi-access interference levels), and whether a centralised server is required. Since there are abundant variations of coding schemes, this section will only cover those applicable to the integrated OCDMA systems proposed in this research, i.e. the coherent TPC-OCDMA system, and the incoherent WHTS-OCDMA system.

3.4.1 Coherent coding via TPC-OCDMA

In coherent OCDMA systems, the phase of the optical signal field is modulated using bipolar code sequences. Temporal phase codes can be categorised as either orthogonal or non-orthogonal codes. Orthogonal codes are designed to have close-to-zero cross-correlation functions which greatly reduces MAI; however, they must be operated in a synchronous fashion to preserve orthogonality. Conversely, non-orthogonal codes do not require synchronisation between transmitters, at the cost of a larger cross-correlation between users' codes, and thus, an increased MAI. Both of these are well utilised in wireless CDMA systems [64], where orthogonal codes are generally used for downstream links (i.e. server to client) since all users are co-located at a mobile tower, and non-orthogonal codes are used for the upstream connections. Wireless CDMA based on IS-95 and wideband CDMA (3G) both use the binary Walsh-Hadamard coding scheme, which is a primary example of an orthogonal code. Pseudorandom sequences, such as maximal length sequences and Gold sequences may also be used [64].

Walsh codes are based on the well-known Hadamard matrices to map out sequences of 1's and -1's, corresponding to the relative phase change (0 and π) [8]. This forms mutually orthogonal code words which, if synchronised in time, have zero cross-correlation functions. Walsh codes can be defined as a set of N sequences of length $N = 2^n$, which is described by $W_N^{(j)}$, where n is a positive integer, and $j \in [0, N-1]$ represents the jth row of the bipolar sequence extracted from the code set of W_N, generated by the recursive procedure:

$$W_1 = [+1],\ W_2 = \begin{bmatrix} +1 & +1 \\ +1 & -1 \end{bmatrix},\ W_4 = \begin{bmatrix} +1 & +1 & +1 & +1 \\ +1 & -1 & +1 & -1 \\ +1 & +1 & -1 & -1 \\ +1 & -1 & -1 & +1 \end{bmatrix}, \dots, \tag{3.7}$$

$$W_{2^{n+1}} = \begin{bmatrix} W_{2^n} & W_{2^n} \\ W_{2^n} & \bar{W}_{2^n} \end{bmatrix}$$

where $\bar{W}_{2^n}$ is the compliment of W_{2^n}. For example, the code set W_2 has two sequences: [+1, +1], and [+1, -1], which are each assigned to a network user. During encoding, each pulse is transformed via the bespoke phase shift and transmitted through the network, in which the integrity of the pulse stream is preserved by the distinctive phase shift sequence. Coding is only established between matched encoders and decoders.

An interesting observation of the Walsh-Hadamard coding system is that multiplying two different codes results in a different code in the set [65, 66]. This enables passive routing to occur between sender and receiver using a cascaded interchange. A code translator may be used as an intermediate stage between each node to dynamically address the recipients of the transmitted signals. This is shown schematically in Fig. 3.13(a) [8]. Another benefit of code translation is the ability for users to share codes without compromising each user's data, which in turn can increase the number of users. Cascaded interchanging using Walsh codes is performed by passing an encoded signal through another encoding operator (the translator) that has a dynamically interchangeable phase change that is programmed as a set code, which when multiplied together will re-establish a different code in the set, as shown in the table in Fig. 3.13(b). For example, if data encrypted with code 4 is passed through a translator T_r set to code 6, the phase changes occurred will be equivalent to that of code 7.

(a)

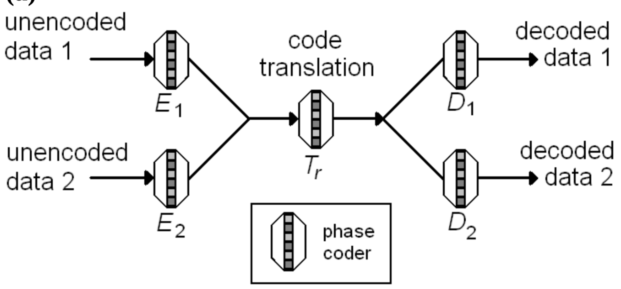

(b)

Incoming code

Translator	1	2	3	4	5	6	7	8
1	1	2	3	4	5	6	7	8
2	2	1	4	3	6	5	8	7
3	3	4	1	2	7	8	5	6
4	4	3	2	1	8	7	6	5
5	5	6	7	8	1	2	3	4
6	6	5	8	7	2	1	4	3
7	7	8	5	6	3	4	1	2
8	8	7	6	5	4	3	2	1

Figure 3.13 (a) Code translation using an addition phase coder to multiply the input signal with, and (b) code translation table for Hadamard 8 codes.

This means that a user accommodating a fixed code set can establish communications with another user by means of code translation. Given this ability, a variety of network topologies can be implemented [8]. For instance, the star network can be composed comprising end users with fixed codes and adjustable hubs can be used to reroute the data around the network by adjusting their entrance and exit ports to establish a connection between users (Fig. 3.14). A central hub can also be employed to scramble codes via translation via a larger set of Walsh Hadamard codes to increase security of the transmitted signals by increasing the complexity of the coded signal, which can otherwise be tapped by an eavesdropper using a variable phase coder.

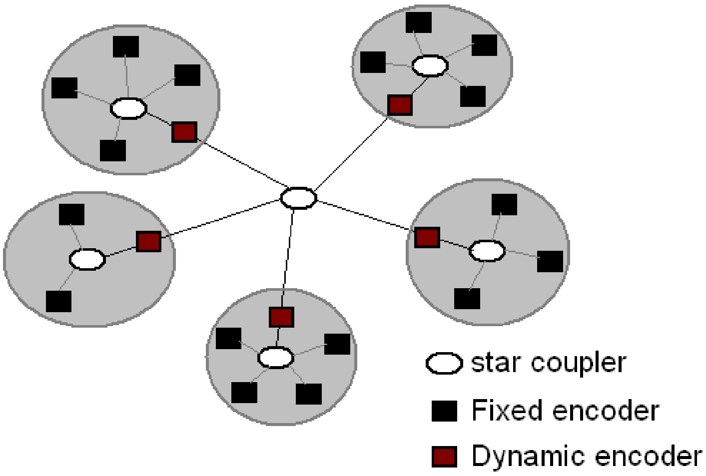

Figure 3.14 Secure LAN networks with Hadamard coders interconnected with dynamic code translation for sharing codes within a MAN while maintaining data integrity.

3.4.2 Incoherent coding via WHTS-OCDMA

Incoherent OCDMA encoders use unipolar code sequences to modulate the amplitude of a pulsed signal. In general, there are four types of incoherent OCDMA systems: spectral amplitude coding (SAC), spatial coding, temporal spreading, and WHTS. As with coherent codes, there are a large number of coding regimes associated with each type of system, such as optical orthogonal codes, gold codes, and prime codes [67]. The latter is particularly useful since it can easily be transformed into two-dimensional codes (2D) [68]. WHTS systems require 2D pulse assignments to spread the codes in both the wavelength and time domains simultaneously to provide better code design flexibility, low cross-correlation functions and higher code cardinality with shorter code lengths, compared to temporal spreading systems [55].

WHTS codes are generally represented as 2D matrices, with wavelength along one axis and time along the other. Pulses are positioned in the matrix at positions depending on the assigned code. The benefit of this is that all users can share the available wavelength and time space, providing a fair division of the bandwidth, as opposed to time division multiplexed- (TDM) or wavelength division multiplexed- (WDM) systems. Many wavelength-time codes have been constructed [8, 55, 63, 67, 68], however, the carrier-hopping prime (CHP) coding scheme, as first proposed in [55], is advantageous since only one pulse per row of available wavelengths is used, providing zero autocorrelation side lobes and a cross-correlation function of at most 1 if codes are met asynchronously.

In wireless communications, CHP coding is usually referred to as frequency hop (FH) coding [69]. Many of the FH codes studied are based on Reed-Solomon coding [67], in which cardinality is better achieved using relaxed cross-correlation rules. This subsequently increases the MAI, although a solution for this is to increase the number of available wavelengths. However, the available bandwidth generated by semiconductor based MLLDs may be a limiting factor. Therefore it is imperative to study alternative families of CHP codes, in which the cardinality is a function of the code length, rather than a preselected cross-correlation value.

The original prime code uses a linear congruency technique, in which a number of code sequences are generated using the Galois field theorem: $GF(p)$, where p is a prime number. The minimum Hamming distance of each code, in other words the bit period, is then equal to $p - 1$, and subsequently, each entry of the matrix is multiplied under modulo-p to generate $p - 1$ prime code sequences. An example of the prime code $GF(5)$ (i.e. multiplications of {0, 1, 2, 3, 4,}) is shown in Fig. 3.15.

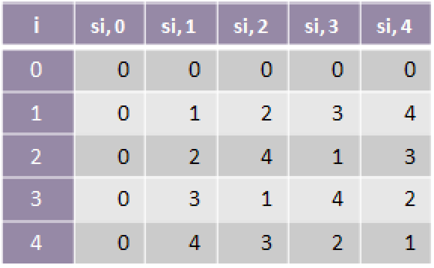

i	si, 0	si, 1	si, 2	si, 3	si, 4
0	0	0	0	0	0
1	0	1	2	3	4
2	0	2	4	1	3
3	0	3	1	4	2
4	0	4	3	2	1

Figure 3.15 Prime code sequence table for $GF(5)$

The number of coincidences of a code element of any prime code is at most one, and therefore the maximum cross-correlation is one. To construct binary sequences from the prime codes, each one of the prime sequences is mapped into a binary sequence $C_i = (c_{i,0}, c_{i,1}, c_{i,2}, \dots, c_{i,k}, \dots, s_i, p_{2-1})$ is constructed by the element $s_{i,j} = i \times j \pmod{p}$, where $s_{i,j}$, i, and j are all in $GF(p)$. For example, the binary sequences over $GF(5)$ are: (10000, 10000, 10000, 10000, 10000), (10000, 01000, 00100, 00010, 00001), (10000, 00100, 00001, 01000, 00010), (10000, 00010, 01000, 00001, 00100), and (10000, 00001, 00010, 00100, 01000).

Generating 2D prime hopping codes is simply a matter of transmitting each one in the binary pattern at a different wavelength [55]. This will generate p time spread patterns of length p^2 and $p-1$ wavelength hopping patterns (as one of the codes shares the same temporal space across all wavelengths). Since there are now two dimensions of the prime sequence, each designation of a prime hop code can be distinguished by a spreading pattern S_t, and a hopping pattern H_λ, where $S_t = H_\lambda = \{0, 1, 2, \dots, p\text{-}1\}$, which means the total number of unique codes is $p(p-1)$. For example, the prime hop sequences for $p = 3$ are: ($\lambda_1 00\ \lambda_2 00\ \lambda_3 00$), ($\lambda_1 00\ \lambda_3 00\ \lambda_2 00$), ($\lambda_1 00\ \lambda_2 00\ 00\lambda_3$), ($\lambda_1 00\ \lambda_3 00$

00λ_2), ($\lambda_1$00 0$\lambda_2$0 0$\lambda_3$0), ($\lambda_1$00 0$\lambda_2$0 0$\lambda_3$0). It is then apparent that the number of codes is greatly increased as well as the code efficiency, compared with the original 1D prime code. An asynchronous implementation of the prime hop code, therefore provides a maximum cross-correlation of 1, and an autocorrelation function with zero side lobes.

There have been an abundance of adaptations made to the prime code since the publication of [55], with improvements leading to increased number of users, cross-correlations, and most notably, the facilitation of quality of service (QoS) using multi length codes [8, 67].

3.5 MAI rejection techniques

Further processing is necessary to reduce autocorrelation side lobes and multi user interference after decoding. A typical photoreceiver will detect unwanted signals from other network users that are identical to the desired signal, resulting in bit errors at the detector. Therefore, further noise reduction techniques are necessary in order to minimise bit error rates at the receiver. It is preferable to perform MAI rejection techniques after signal decoding due to the large bandwidth requirements of an OCDMA system, and several optical methods may be used based on optical time gating and optical thresholding.

An all-optical gate can be constructed by using an optical clock pulse to trigger a window period in which a propagating signal is transparent. A good example of this is shown in the XAM experiment explained in section 3.1.2, in which an absorbing material sample was pumped periodically by a clock pulse to intermittently reduce the absorption for a period determined by the recovery time, i.e. the amount of voltage applied. Thus a "gate" was provided to filter out the signals that reside out with the window period. Other examples of optical gating devices are the nonlinear optical loop mirror (NOLM) [70], and terahertz optical asymmetric demultiplexer (TOAD) [71].

The basic principle behind the NOLM gating is to accomplish a phase change through a distributed medium, often an optical fibre due to the requirement of long propagation lengths for a nonlinearity to occur. A schematic of a NOLM is illustrated in Fig. 3.16(a), which shows an input signal split into two counter-propagating pulse replicas via a 3 dB coupler. Without the presence of an optical clock pulse, the signals will propagate through the loop and recombine at the splitter, interfering destructively at the output port, and constructively at the input port, thereby reflecting the signal back (hence the term "loop mirror"). Conversely, when a clock pulse operating at a slightly different wavelength and situated at an asymmetric distance from the coupler is triggered, the interferometric balance of the coupler is disturbed due to a nonlinear phase shift, in which case the interference condition is altered such that the input signal can travel through to the output port. An optical band pass filter can provide suppression of the optical clock signal, so that only the data pulses remain. The width of the time gate is determined by the relative overlap of the clock signal and counter propagating data pulses [8].

A NOLM based interferometer may also be used for all-optical thresholding, using a similar construction as the gating interferometer, with the exception of the clock pulse input port. The 3 dB coupler is instead replaced by an asymmetric coupling ratio, such as a 70:30 splitter, which provides large differences in the relative nonlinear phase shift of the two counter propagating data pulses [72]. This results in the large intensity signals, such as the input pulses, which interfere constructively and traverse through to the output port, whereas weaker noise signals are reflected due to the smaller relative phase shifts. NOLM based gating along with optical thresholding techniques has been successfully demonstrated along with the implementation of a phase coded OCDMA system [70].

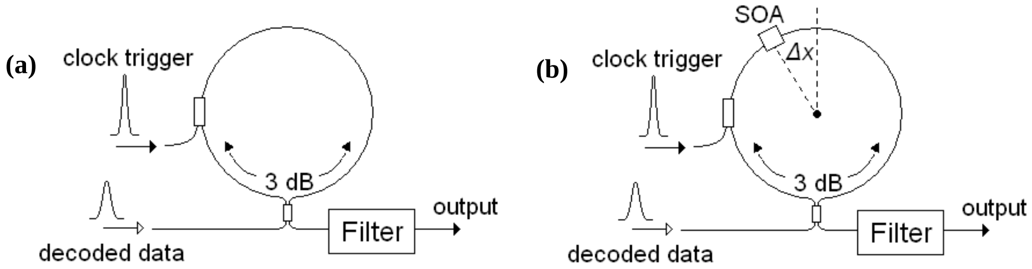

Figure 3.16 Schematic diagram of (a) NOLM time gate and threshold limiter, and (b) TOAD time gate

The TOAD technique uses the same interferometric architecture as that of the NOLM (Fig. 3.16(b)), although the nonlinear phase change is instead performed via the use of a semiconductor optical amplifier (SOA). This means that shorter loop lengths can be used, and therefore it has the potential for device integration. The SOA is offset from the centre of the loop by a distance corresponding to $\Delta x = 2\,\Delta t_{gw}\,c\,n_g$, where Δt_{gw} is the nominal gate width, c is the speed of light, and n_g is the group index of the material [71]. Similar to the NOLM concept, in the absence of a control pulse, the signal is reflected back towards the input. Alternatively, a clock pulse with a large enough amplitude (at least 10 dB larger than the data pulse intensity) travelling in a clockwise direction will saturate the SOA and thereby alter its refractive index to provide a relative phase shift to a data pulse. Since the SOA is offset, the clockwise data pulse has the opportunity to propagate through the SOA before the clock pulse saturates the SOA index. The counter propagating pulse arrives immediately after the SOA has recovered in approximately the same relative state and therefore does not experience a relative phase shift. The signals then recombine at the splitter, in which the interference condition permits the output of a data pulse, and thus a gating period is achieved.

3.6 Chapter summary

This chapter presented a description of the various stages of the OCDMA system processes. Optical pulse sources, particularly the mode-locked laser diode, were described at length, including the saturable absorption dynamics of the *AlGaInAs/InP* MQW material system, which was shown to achieve < 5 ps recovery times at biases greater than 3V. Modulation methods were discussed, including EAM based devices, and optical phase shifting sections for use in DPSK based systems. This was followed by an explanation of the various types of encoding and decoding techniques available for both coherent and incoherent based OCDMA. For coherent systems, the TPC based system is considered, along with techniques for implementation on integrated circuits using AMZI for both encoding and decoding. Incoherent systems were then explained, with a particular focus on WHTS based encoding and decoding using a mode-locked DBR laser array. Further to this, optical coding schemes were explained, focussing on the Walsh-Hadamard code for coherent OCDMA, and the PHC code for 2D incoherent OCDMA. And finally, methods for MAI rejection at the receiver were discussed, with a brief discussion on XAM, NOLM and TOAD based devices.

The remainder of this thesis will mainly present experimental results on a variety of components mentioned in this chapter. The next chapter delves into the mechanisms of mode-locked laser diodes for use as optical sources in the bespoke OCDMA systems. Chapter 6 further describes the implementation of coherent TPC-OCDMA system and experiments performed using integrated dual AMZIs for encoding and decoding operations. And finally, Chapter 7 provides a discussion on the employment of the WHTS OCDMA system developed for this research, with the final design and experimental results shown.

3.6 References

[1] J. J. Degnan, “Optimization of passively Q-switched lasers,” IEEE J. Quant. Electron., Vol. 31, No. 11, pp 1890-1901, 1995.

[2] K. Y. Lau, “Gain switching in semiconductor injection lasers,” Appl. Phys. Lett. Vol. 52, No. 4, pp 257-259, 1988.

[3] K. A. Willaims, M. G. Thomson, and I. H. White, “Long wavelength monolithic mode locked lasers,” New J. Phys., Vol. 6, No. 1, pp 179, 2004.

[4] K. A. Willaims, I. H. White, D. Burns, and W. Sibbett, “Jitter reduction through feedback for picosecond pulsed InGaAsP lasers,” IEEE J. Quant. Electron., Vol. 32, No. 11, pp 1988-1994, 1996.

[5] L. Hou, et. al, “160 GHz harmonic mode locked AlGaInAs 1.55μm strained quantum well compound cavity laser,” Optics Lett., Vol. 35, No. 23, pp 3991- 3993, 2010.

[6] A. Sano, et. al, “Field experiments on 480 Gbit/s repeaterless transmission over 198 km dispersion managed submarine cable using a monolithic mode locked laser diode,” Electron. Lett., Vol. 32, No. 13, pp 1218-1219, 1996.

[7] J. L. Augé, M. Cavallari, M. Jones, P. Kean, D. Watley, and A. Hadjifotiou, “Single channel 160 GB/s OTDM propagation over 480 km of standard fiber using a 40 GHz semiconductor mode locked laser pulse source,” OFC 2002, TuA3, pp 4, 2002.

[8] P. R. Prucnal, et al., “Optical code division multiple access – Fundamentals and applications,” CRC Taylor and Francis, 2006.

[9] H. A. Haus, “Theory of mode locking with a fast saturable absorber," J. App Phys., Vol. 46, No. 7, pp. 3049-3058, 1975.

[10] H. A. Haus, “Theory of mode locking with a slow saturable absorber," J. Quant. Electron., Vol. 11, No. 9, pp. 736-746, 1975.

[11] C. Rulliére, et al., “Femtosecond laser pulses: principles and experiments,” Springer; 2nd Edition, 1998.

[12] D. J. Jones, L. M. Zhang, J. E. Carroll, and D. D. Marcenac, “Dynamics of monolithic passively mode locked semiconductor lasers,” J. Quant. Electron., Vol. 31, No. 6, pp 1051-1058, 1995.

[13] H. A. Haus, “Mode-locking of lasers," Selec. Top. Quant. Electron., Vol. 6, No. 6, pp. 1173-1185, 2000.

[14] P. Vasil’ev, “Ultrafast diode lasers: fundamentals and applications,” Artech House, Boston, 1995.

[15] P. W. A. McIlroy, A. Kurobe, and Y. Uematsu, “Analysis and application of theoretical gain curves to the design of multi quantum well lasers,” IEEE J. Quant. Electron., Vol. QE-21, No. 12, pp 1958-1963, 1985.

[16] A. E. Kelly, “Optimisation of semiconductor optical amplifiers for optical networks,” Ph.D. thesis, University of Strathclyde, 1999.

[17] J. Minch, S. H. Park, T. Keating, and S. L. Chuang, “Theory and experiment of $In_{1-x}Ga_xAs_yP_{1-y}$ and $In_{1-x-y}Ga_xAl_yAs$ long wavelength strained quantum-well lasers,” IEEE J. Quant. Electron., Vol. 35, No. 5, pp 771-782, 1999.

[18] G. P. Agrawal, and N. K. Dutta, “Long-wavelength semiconductor lasers,” Van Nostrand Reinhold, Michigan, 1986.

[19] A. J. Zilkie, J. Meier, P. W. E. Smith, M. Mojahedi, J. S. Aitchison, P. J. Poole, C. N. Allen, P. Barrios, D. Poitras, R. H. Wang, T. J. Rotter, C. Yang, A. Stinz, K. J. Malloy, “Comparison of the gain recovery times in low dimenstional semiconductor amplifiers at 1.55 μm,” 19th Annual meeting of the IEEE Society (LEOS) 2007, pp 276-277, 2007.

[20] G. Eisenstein, J. M. Wiesenfeld, M. Wagener, G. Sucha, D. S. Chemla, S. Weiss, G. Raybon, and U. Koren, “Ultrafast gain dynamics in 1.5 μm multiple quantum well optical amplifiers,” App. Phys. Lett., Vol. 58, No. 2, pp 158-160, 1991.

[21] J. Javaloyes, and S. Balle, “Mode locking in semiconductor Fabry-Perot lasers,” IEEE J. Quant. Electron., Vol. 46, No. 7, pp 1023-1030, 2010.

[22] J. P. Gopinath, et al., “Recovery dynamics in proton-bombarded semiconductor saturable absorber mirrors,” App. Phys. Lett., Vol. 78, No. 22, pp 3409-3411, 2001.

[23] E. L. Delpon, et al., “Ultrafast excitonic saturable absorption in ion implanted InGaAs/InAlAs multiple quantum wells,” Appl. Phys. Lett., Vol 72, pp 759-761, 1998.

[24] R. Takahashi, “Low temperature grown surface reflection all optical switch (LOTUS),” Opt. and Quant. Electron., Vol. 33, pp 999, 2001.

[25] J. M. An, A. Franceschetti, and Alex Zunger, “Pauli blocking versus electrostatic attenuation of optical transition intensities in charged PbSe quantum dots,” Phys. Rev. B, Vol. 76, pp 161310, 2007.

[26] M. Haiml, R. Grange, and U. Keller, “Optical characterization of semiconductor saturable absorbers,” Appl. Phys. B, Vol. 79, 331-339, 2004.

[27] B. O. Seraphin and N. Bottka, “Franz-Keldysh Effect of the Refractive Index in Semiconductors," Phys. Rev. B, Vol. 139, No. 2A, pp A560-A565, 1965.

[28] L. A. Coldren, and S. W. Corzine, “Diode lasers and photonic integrated circuits,” John Wiley and Sons, Inc., New York, 1995.

[29] G. Ghione, “Semiconductor devices for high-speed optoelectronics,” University Press, Cambridge, 2009.

[30] D. Kunimatsu, S. Arahira, Y. Kato, and Y. Ogawa, “Passively mode locked laser diodes with bandgap wavelength detuned saturable absorbers,” IEEE Photon. Technol. Lett., Vol. 11, No. 11, pp 1363-1365, 1999.

[31] D. P. Halliday, D. Moss, S. Charbonneau, G. Aers, F. Chatenoud, and D. Landheer, “Time resolved photoluminescence studies in a reverse biased quantum well laser structure,” Appl. Phys. Lett., Vol 61, No. 21, pp 2497-2499, 1992.

[32] D. B. Malins, A. Gomez-Iglesias, S. J. White, W. Sibbett, A. Miller, and E. U. Rafailov, “Ultrafast electro-absorption dynamics in in InAs quantum dot saturable absorber at 1.3 μm,” Appl. Phys. Lett., Vol. 89, pp 171111, 2006.

[33] H. Schneider, and K. v. Klitzing, “Thermionic emission and Gaussian transport of holes in a GaAs/AlxGa1-xAs multiple quantum well structure,” Phys. Rev. B, Vol. 80, pp 075303, 2009.

[34] K. Nishimura, R. Inohara, M. Usami, and S. Akiba, “All optical wavelength conversion by electroabsorption modulator,” IEEE J. Sel. Top. Quant. Electron., Vol. 11, pp 278-284, 2005.

[35] W. Bingbing, et al., “Investigation of InGaAsP quantum well EAM based pump probe configuration for ultrafast optical signal processing,” IEEE J. Quant. Electron., Vol. 47, No. 8, pp 1113-1122, 2011.

[36] L. Hou, et al., “Subpicosecond pulse generation at quasi-40-GHz using a passively mode locked AlGaInAs/InP 1.55 μm strained quantum well laser,” IEEE Photon. Technol. Lett. Vol. 23, pp 1731-1733, 2009.

[37] K. Merghem, et al., “Short pulse generation using a passively mode locked single InGaAsP/InP quantum well laser,” Optics Express, Vol. 16, No. 14, pp 10675-10683, 2008.

[38] J. Liu, et al, “Waveguide integrated, ultralow energy GeSi electro absorption modulators,” Nature Photon. Lett., Vol. 2, pp 433-437, 2008.

[39] K. Wakita, et al., “High speed InGaAlAs/InAlAs multiple quantum well optical modulators,” J. Lightwave Technol., Vol. 8, No. 7, pp 1027-1032, 1990.

[40] H. S. Cho, and P. R. Prucnal, “Effects of parameter variations on the performance of GaAs/InGaAs multiple quantum well electroabsorption modulators,” IEEE J. Quant. Electron., Vol. 25, No. 7, pp 1682-1690, 1989.

[41] N. Dagli, “Wide bandwidth lasers and modulators for RF photonics,” IEEE Trans. Microwave Theory and Techniques, Vol. 47, No. 7, pp 1151-1171, 1999.

[42] B. Bennett, R. Soref, and J. Del Alamo, “Carrier-induced change in refractive index of InP, GaAs and InGaAsP," IEEE J. Quant. Electron., Vol. 26, No. 1, pp 113-122, 1990.

[43] C. Xu, X. Liu, and X. Wei, “Modulation formats for high spectral efficiency fiber optic communications,” IEEE J. Sel. Top. Quant. Electron., Vol. 10, pp 281-293, 2004.

[44] M. Yoshida, H. Goto, K. Kasai, and M. Nakazawa, “64 and 128 coherent QAM optical transmission over 150 km using frequency stabilized laser and heterodyne PLL detection,” Opt. Express, Vol. 16, No. 2, pp 829-840, 2008.

[45] IEEEStd802.11b-1999(R2003), Supplement to IEEE standard for information technology, Part 11: Wireless LAN medium access control (MAC) and physical layer (PHY) specifications. Available from: http://standards.ieee.org/getieee802/download/802.11b-1999.pdf, (Accessed on 9th Aug 2011).

[46] IEEEStd802.11g-2003, IEEE standard for information technology, Part 11: Wireless LAN medium access control (MAC) and physical layer (PHY) specifications. Available from: http://standards.ieee.org/getieee802/download/802.11g-2003.pdf, (Accessed on 9th Aug 2011).

[47] H. Kobayashi, S. Kousai, Y. Yoshihara, and M. Hamada, “An all digital 8-DPSK polar transmitter with second order approximation scheme and phase rotation constant digital PA for Bluetooth EDR in 65 nm CMOS,” ISSCC, Wireless and mm-wave connectivity, 9.8, 2011.

[48] IEEEStd802.15-2009, IEEE standard for information technology, Part 15.4: Wireless LAN medium access control (MAC) and physical layer (PHY) specifications for low-rate wireless personal area networks (WPANs). Available from: http://standards.ieee.org/getieee802/download/802.15.4c-2009.pdf, (Accessed on 9th Aug 2011).

[49] A. M. Weiner, J. P. Heritage, and J. A. Salehi, “Encoding and decoding of femtosecond pulses,” Opt. Lett., Vol. 13, pp 300-302, 1988.

[50] J. A. Salehi, A. M. Weiner, and J. P. Heritage, “Coherent ultrashort light pulse code division multiple access communication systems,” J. Lightwave Technol., Vol. 8, pp 478-491, 1990.

[51] S. Etemad, et al., “Optical CDMA incorporating phase coding of coherent frequency bins: Concept, simulation, experiment,” Proc. Opt. Fiber Comms. Conf., FG5, 2004.

[52] D. Zaccarin, and M. Kavehrad, “An OCDMA system based on spectral coding of a LED,” IEEE Photon. Technol. Lett., Vol. 4, No. 4, pp 479-482, 1993.

[53] K. I. Kitayama, “Novel spatial spread spectrum based fiber optic CDMA networks for image transmission,” IEEE J. Sel. Areas Comms., Vol. 12, No. 4, pp 762-772.

[54] P. R. Prucnal, M. A. Santoro, and T. R. Fan, “Spread spectrum fiber optic local area network using optical processing,” IEEE J. Lightwave Technol., Vol. 4, No. 5, pp 170-172, 1986.

[55] L. Tancevski, and I. Andonovic, “Wavelength hopping/time spreading code division multiple access systems,” Electron. Lett., Vol. 30, No. 9, pp 721-723, 1994.

[56] S. Yegnanarayanan, A. S. Bushun, and B. Jalali, “Fast wavelength hopping time spreading encoding/decoding for optical CDMA,” IEEE Photon. Technol. Lett., Vol. 12, No. 5, pp 573-575, 2000.

[57] H. B. Jaafar, S. LaRochelle, P. Y. Cortes, and H. Fathallah, “1.25 Gbit/s transmission of optical FFH-OCDMA signals over 80 km with 16 users,” Proc. Opt. Fiber Comms., TuV3-1- TuV3-2, 2001.

[58] P. R. Prucnal, M. F. Krol, and J. L. Stacey, “Demonstration of rapidly tunable optical time division multiple access coder,” IEEE Photon. Technol. Lett., Vol. 3, No. 2, pp 170-172, 1991.

[59] K. L. Deng, I. Glesk, K. I. Kang, and P. R. Prucnal, “Influence of crosstalk on the scalability of large OTDM interconnects using a novel rapidly reconfigurable highly scalable optical time-slot tuner,” IEEE Photon. Technol. Lett., Vol. 10, No. 7, pp 1039-1041, 1998.

[60] V. Baby, B. Wang, L. Xu, I. Glesk, and P. R. Prucnal, “Highly scalable serial parallel optical delay line,” Opt. Comms, Vol. 218, No. 4-6, pp 235-242, 2003.

[61] W. Huang, I. Andonovic, and M. Tur, “Decision direct PLL used for coherent optical pulse CDMA in the presence of multiuser interference laser phase noise and shot noise,” J. Lightwave Technol., Vol. 16, No. 10, pp 1786-1794, 1998.

[62] H. P. Sardesai, C. C. Chang, and A. M. Weiner, “A femtosecond code division multiple access communication system test bed,” J. Lightwave Technol., Vol. 16, No. 11, pp 1953-1964, 1998.

[63] G. C. Yang, and W. C. Kwong, “Two-dimensional spatial signature patterns,” IEEE Trans. Comms., Vol. 44, No. 2, pp 184-191, 1996.

[64] E. H. Dinan, and B. Jabbari, “Spreading codes for direct sequence CDMA and wideband CDMA cellular networks,” IEEE Comms. Mag., Vol. 36, No. 7, pp 48-54, 1998.

[65] D. S. Seo, Z. Jiang, D. E. Leard, and A. M. Weiner, “Pulse shaper in a loop: demonstration of cascadable ultrafast all optical code translation,” Opt. Lett., Vol. 29, pp 1864-1866, 2004.

[66] Z. Jiang, et al., "Reconfigurable all-optical code translation in spectrally phase coded OCDMA," J. Lightwave Technol., Vol. 23, pp 1979-1990, 2005.

[67] G. C. Yang, and W. C. Kwong, "Prime codes with application to CDMA optical and wireless networks," Norwood: Artech House, 2002.

[68] E. L. Titlebaum, "Time-frequency hop signals, Part I: coding based upon the theory of linear congruences," IEEE Trans. Aerospace Electron. Systems, Vol. 17, No. 4, pp 490-494, 1981.

[69] R. Kohno, R. Meidan, and L. B. Milstein, "Spread spectrum access methods for wireless communications," IEEE Comms. Mag., Vol. 33, No. 1, pp 58-67, 1995.

[70] H. Sotobayashi, W. Chujo, and K. Kitayama, "1.6 b/s/Hz 6.4 Tb/s QPSQ-OCDM/WDM (4 OCDM x 40 WDM x 40 Gb/s) transmission experiment using optical hard thresholding," IEEE Photon. Technol. Lett., Vo. 14, pp 555-557, 2002.

[71] J. P. Sokoloff, P. R. Prucnal, I. Glesk, and M. Kane, "A Terahertz optical asymmetric demultiplexer (TOAD)," IEEE. Photon. Technol. Lett., Vol. 5, pp787-790, 1993.

[72] J. H. Lee, P. C. The, P. Petropulow, M. Ibsen, and D. J. Richardson, "Reduction of interchannel interference noise in a two-channel grating based OCDMA system using a nonlinear optical loop mirror," IEEE Photon. Technol. Lett., Vol. 13, pp 529-531, 2001.

Chapter 4

Semiconductor mode-locked lasers

One of the most important components in an OCDMA circuit is the optical source. Mode-locked laser diodes (MLLD) are excellent candidates due to their wide bandwidth and discrete temporal pulse producing capabilities [1]. The previous chapter described how mode-locking is achieved in semiconductor lasers. During this project, several types of MLLDs were fabricated and characterised for use in high speed optoelectronic systems, and the results obtained showed that the *Al*-quaternary material is highly suitable for fabricating lasers on. The results from the lasers that are most relevant to the selected integrated OCDMA systems are presented in this chapter. First, a simple two-section 40 GHz MLLD is presented along with characteristic results from both five- and three- quantum-wells (QW) materials for a comparison of the laser performance. Next, a 10 GHz MLLD with an integrated phase section and distributed Bragg reflectors (DBR) is presented, which is useful for fine tuning both the wavelength and round trip frequency of the laser. Since the mode-locking frequency is ultimately dependent on the cavity length, it is difficult to generate very high frequencies (> 50 GHz) due to device cleaving limitations. Intracavity slot reflectors can be used to provide a sub-cavity with a repetition rate that is much faster than the round trip time of the entire cavity. This technique is called harmonic mode-locking, and a detailed look at the optimisation and characterisation is shown in both colliding pulse and coupled cavity configurations.

4.1 Two-section MLLDs

The simplest type of mode-locked laser in semiconductor consists of two sections – a saturable absorber (SA) and a gain section. Fabricating two-section MLLDs in *AlGaInAs/InP* requires the same steps as those used to make Fabry-Pérot lasers (see chapter 2); however, it is important for the gain and SA sections to be electrically isolated so they can be biased independently. This is usually achieved by an additional etching stage, in which a 10 µm window of PMMA resist is opened using electron beam lithography between the two sections, where a shallow etch is made down to the cap layer (that is the heavily doped *P*-contact layer) separating the contacts of the two sections. The typical resistance across a 10 µm gap is ~ 20 kΩ. A schematic of a two-section device is shown in Fig. 4.1.

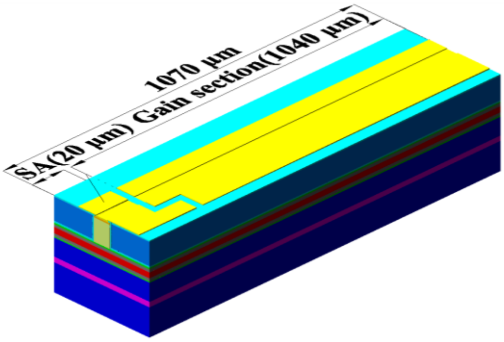

Figure 4.1 Schematic diagram of a two section mode-locked laser diode.

A two-section 40 GHz MLLD was fabricated in both the five- and three- QWs epitaxial structure. Both laser bars were made to exactly the same specifications: The devices consisted of a 20 µm long SA and a 1040 µm gain section, with a 10 µm electrical isolation gap between the sections. The SA:Gain section ratio was optimised by characterising multiple lasers on the same bar (i.e. having the same device length) with a varied SA length, and the minimum pulse width along with the largest mode-locking (ML) operating range were the chosen criteria for optimisation. Table 4.1 summarises the pulse widths obtained for three of the devices, and from this it is clear that an absorber which is approximately 2 % of the total cavity length provides both the narrowest pulse width and largest biasing range of operation.

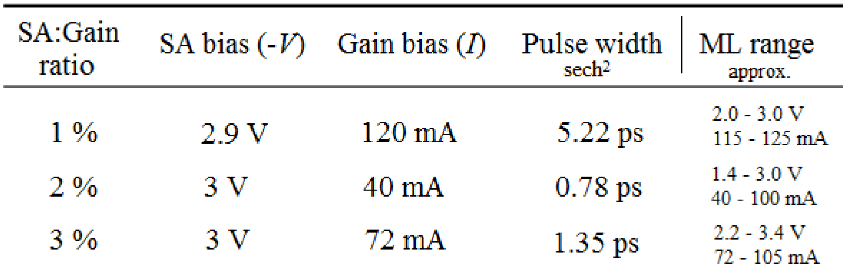

SA:Gain ratio	SA bias (-*V*)	Gain bias (*I*)	Pulse width sech^2	ML range approx.
1 %	2.9 V	120 mA	5.22 ps	2.0 - 3.0 V 115 - 125 mA
2 %	3 V	40 mA	0.78 ps	1.4 - 3.0 V 40 - 100 mA
3 %	3 V	72 mA	1.35 ps	2.2 - 3.4 V 72 - 105 mA

Table 4.1 Summary of the performance of mode-locked laser diodes with different saturable absorber and gain section ratios.

The ridge waveguides were 2.5 µm wide and 1.6 µm high. The fabrication processes are more fully discussed in [2]. The device bars were cleaved and mounted epilayer side up. Both facets on each device were left uncoated to provide a reflectivity of ~30 %. The bars then sat on a temperature controlled heat sink set at 20°C and tested under CW conditions.

4.1.1 MLLD using five-QWs

Section 3.1 described the mode-locking theory of a two section laser, which is achieved when the carrier lifetimes in the absorber and gain sections are well-adjusted such that $\tau_a < \tau_g$, and these lifetimes can be varied with bias. The amount of bias also determines the amount of gain and loss in the laser, which consequently affects the output power. Figure 4.2(a) shows a plot of the output power as a function of bias current (*LI*) characteristics of the five-QW based MLLD. It can be seen that the slope efficiency is decreased with increasing SA reverse voltage, due to the increasing absorption. For this device, the slope efficiency was ~0.14 with 0 V applied to the SA.

To determine whether the lasers were mode-locking, the second harmonic autocorrelation, RF and optical spectra were measured while the laser biases were varied. The region of bias in which the lasers mode-locked were then analysed, and the results associated with the narrowest pulse width measured on the autocorrelator are presented later in this section. The pulse width is particularly important in OCDMA systems among other parameters since the pulses are temporally modulated. In a temporal phase coded (TPC) OCDMA system, each pulse is split into several channels with an incremental delay per channel; thus, a narrower pulse is ideal to prevent each pulse copy from being overlapped during the encoding process, which could lead to increasing noise levels at the detector. Similarly with wavelength-hopping time-spread (WHTS) OCDMA systems, each pulse should be as narrow as possible within a large time slot window to avoid interchannel interference.

The optical spectra width, $\Delta\omega$, and pulse width, τ, are inversely related through Fourier transformation. This is better understood by considering a larger bandwidth providing more spectral components and subsequently more modal interferences, resulting in shorter pulse durations. In general, the pulse duration is defined by the full-width half-maximum (FHWM) of the intensity profile, and the spectral width (or bandwidth) is defined as the FWHM of the spectral profile. As a rule, the bandwidth and pulse width can not vary independently of one another due to their relationship via Fourier transformation. Various types of specially calibrated autocorrelators are used to measure optical pulses in the time domain, and deconvolution pulse fitting is then required to extract the actual pulse width. Because of the difficulty in declaring the exact pulse shape when using second-order autocorrelation measurements (such as the second-generation harmonic (SHG) autocorrelation method, as used in this research), standard pulse waveforms such as the Gaussian and sech^2 are commonly assumed for approximating the pulse width values, The inherent link between the temporal and spectral domain also allows the best pulse fit to be chosen using the spectral profile obtained. The relationship of the spectral and temporal profiles of the three most commonly used envelopes are highlighted in table 4.1, which summarises the pulse characteristics and the associated minimum time-bandwidth product (TBP) [3].

Shape	Intensity profile $I(t)$	Spectral profile $S(\Omega)$	TBP
Gauss	$e^{-2(t/\tau_G)^2}$	$e^{-\left(\frac{\Omega\tau_G}{2}\right)^2}$	0.441
Sech	$\operatorname{sech}^2(t/\tau_s)$	$\operatorname{sech}^2\frac{\pi\Omega\tau_s}{2}$	0.315
Lorentz	$[1+(t/\tau_L)^2]^{-2}$	$e^{-2\|\Omega\|\tau_L}$	0.142

Table 4.1 Relationship between pulse intensity and spectral profiles via Fourier transform and the associated TBP of the three most commonly used deconvolution fittings [3].

From the table, it is evident that the intensity and spectral profiles of a single pulse bare some resemblance, particularly for Gaussian and sech^2 pulse shapes. Lorentzian pulses however, are transformed to a slightly narrower profile in the spectral domain and have a much lower TBP as a result. Nevertheless, these relationships become increasingly blurry when pulses are very narrow

(< 1ps), mainly due to the uncertainty in the pulse shape. In these circumstances, it may be of benefit to use time resolved gating methods, such as the sonogram, to acquire the actual shape of the pulses and then gather real pulse width values [4, 5].

The measured optical spectrum of the laser is shown in Fig. 4.2(b). The bandwidth at full width half maximum (FWHM) was 5.47 nm at a peak wavelength of 1557 nm for the bias of V_{SA} = -3V and the gain current I_{gain} = 40 mA. Increasing the gain would initially increase the centre wavelength due to the plasma effect (see chapter 3 - free-carrier absorption) [6, 7], until the prevailing bandfilling effects became dominant and caused a red-shift thereafter [6]. The mode spacing was ~ 0.35 nm, corresponding to a round trip frequency of ~40 GHz. This was confirmed by observing the RF spectrum, as shown in Fig. 4.2(c). The centre frequency was 40.17 GHz (10 kHz resolution bandwidth (RBW)), which was determined by the cavity length and effective group index, which varies with bias. The RF linewidth was 194 kHz measured at the FWHM of the peak, which is indicative of the level of noise and jitter [8]. This shall be discussed more fully later in this chapter.

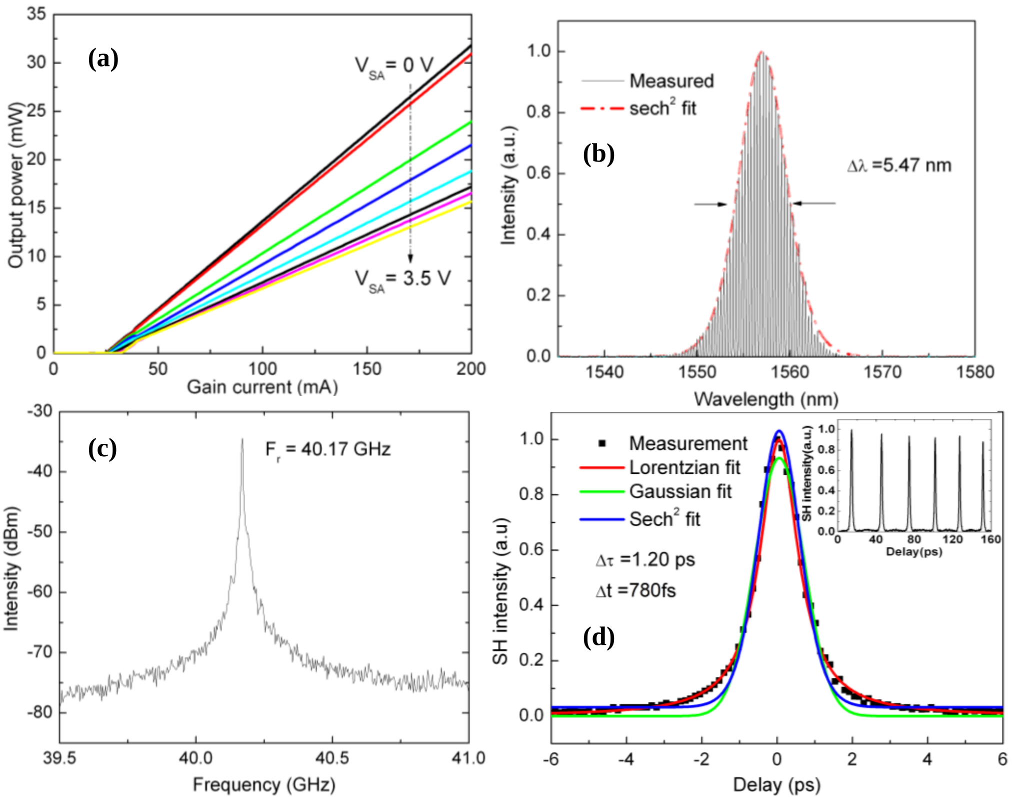

Figure 4.2 Characterisation results of a five-QW MLLD showing (a) *LI* curves, (b) optical spectrum when mode-locking with the shortest pulse width, (c) corresponding RF spectrum, and (d) measured autocorrelation trace with fittings (Inset: larger time span showing pulse spacing and peak uniformity).

The measured autocorrelation trace is shown in Fig. 4.2(d), and shows a lorentzian-like pulse shape, which each pulse separated by ~25 ps. It is very difficult to assume a pulse shape when pulse durations are in the order of femtoseconds; however, deconvolution is usually performed using sech^2 fitting because of the corresponding spectral shape of the laser gain, which is principally defined by the density of states to provide bandwidth limited pulses; and this is likely to be the closest fit here because of the complimentary fitting of the optical spectrum (Fig. 4.2(b)), making the measured pulse deconvolve to 780 fs. The appearance of a lorentzian pulse in the autocorrelation trace may be a result of substructures which exist at the skirts of the pulses due to an imbalance between the gain and losses caused by unoptimised bias conditions, opening a short gain window beside each pulse. These are often referred to as satellite pulses [9]. Other influences on the pulse shape are time varying effects and pulse asymmetries, as described in [10]. These can lead to a wider averaging of the pulse skirt, making it fit better to lorentzian shape. As a compromise for this uncertainty, the three most quoted fittings are shown together in the figure (sech^2, Gaussian, and lorentzian), and nevertheless, all fittings confirm the laser’s ability to produce subpicosecond pulses (Gaussian – 848 fs, lorentzian – 600 fs).

4.1.2 MLLD using three-QWs

In section 2.3, the three-QW counterpart was shown to have better gain characteristics due to its lower differential gain and higher saturation energy. The *LI* curves for the three-QW MLLD are shown in Fig. 4.3(a). Again, the typical trends, i.e. increasing threshold and slope efficiency reduction with increasing reverse bias voltage, can be observed. The slope efficiency was ~0.24 W/A at 0 V_{SA}. The spectrum is shown in Fig. 4.3(b), with a bandwidth at FWHM of 4.89 nm. The mode spacing was ~0.35 nm, corresponding to a ~40 GHz round trip frequency. This was validated by the RF spectrum measurement, where a single peak at 40.7 GHz was observed (Fig. 4.3(c)). The 3 dB linewidth of the RF peak was 25 kHz. The pulse width measured using a SHG autocorrelator was 1 ps, assuming a sech^2 pulse shape. The autocorrelation trace was free of any *Q*-switching instabilities and pedestal modulation (Fig. 4.3(d)).

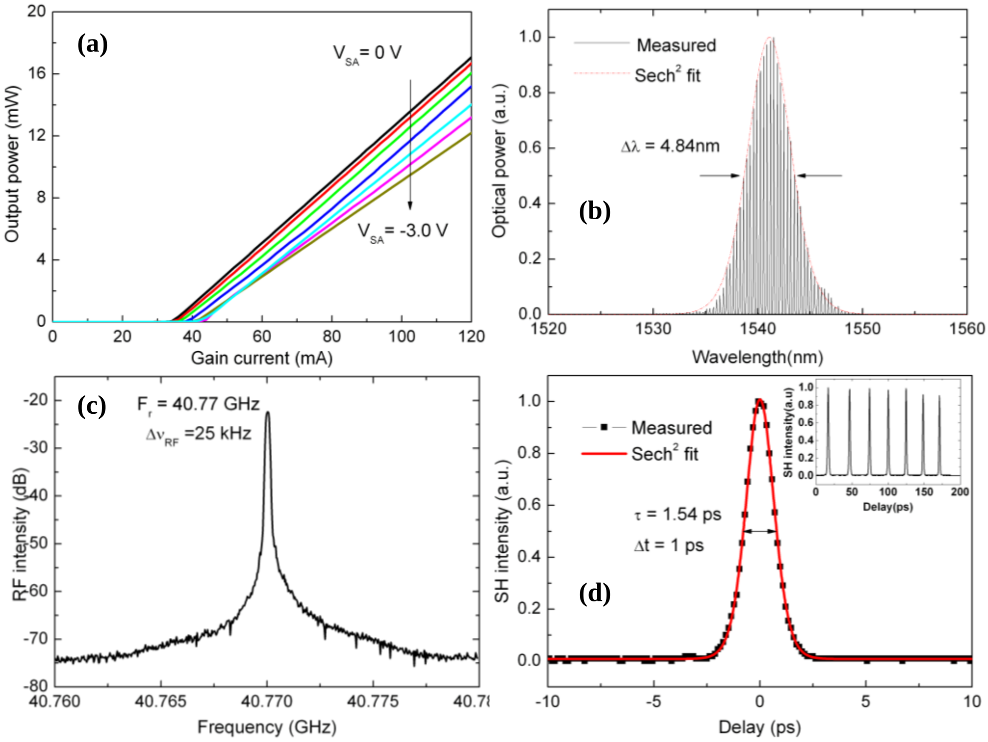

Figure 4.3 Characterisation results of a three-QW MLLD showing (a) *LI* curves, (b) optical spectrum when mode-locking with the shortest pulse width, (c) corresponding RF spectrum, and (d) measured autocorrelation trace with fittings (Inset: larger time span showing pulse spacing and peak uniformity).

4.1.4 Comparisons

It is apparent that the output power per gain current ratio was slightly higher in the three-QW laser (0.21 W/A) than in the five-QW laser (0.14 W/A), due to the lower internal cavity losses. The threshold current for both devices were ~30 mA with 0 V applied to the SA. Similar findings were shown in chapter 2 using Fabry-Pérot lasers and were due to the lower differential gain and higher saturation energy in the three-QW material. Moreover, for the three-QW laser, the optical bandwidth was measured as 4.84 nm with a peak wavelength at 1540 nm, using the bias values: I_{gain} = 54 mA, and V_{SA} = -2.7 V. Similar wavelength shifts were observed with bias changes as with the five-QW laser. The relatively shorter bandwidth was due to the reduced group index value of the three-QW material, which along with the higher gain bias also led to a slightly higher RF frequency than the five-QW laser.

Furthermore, both lasers were passively mode-locked which gave rise to substantial noise occurrences due to the lack of a reference clock. However, the noise can be reduced by a number of methods, which are better understood by considering Henry's linewidth formula [11]:

$$\Delta v_{RF} = \frac{hv\,(1+\alpha^2) l_{tot} T_{OC}}{4\pi\, T_{RT}} \tag{4.1}$$

where hv is the photon energy, α is the linewidth enhancement factor (which takes into account the coupling of the amplitude and phase), l_{tot} is the total cavity losses, T_{OC} is output coupler transmission, and T_{RT} is the round trip time. From this equation it is evident that a narrow linewidth requires low losses, increasing coupling efficiency, low spontaneous emission (which affects α) and a low repetition rate. Δv_{RF} refers to the linewidth in the optical domain, and is directly proportional to the RF frequency (f_{RF}) as described in [12]. The linewidth of the three-QW laser was 25 kHz, which was lower than that for the five-QW laser (194 kHz) due to the lower internal losses and reduced spontaneous emission, mainly resulting from the larger differential gain.

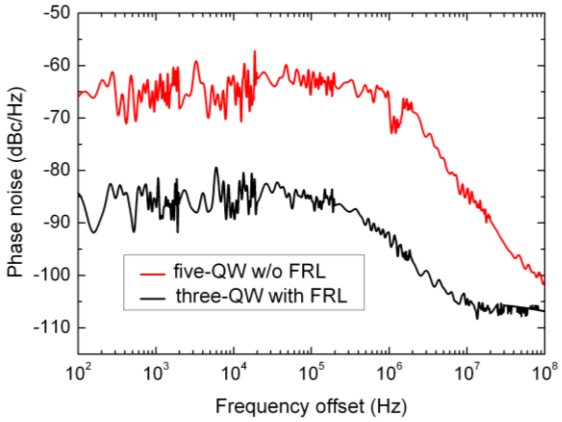

Figure 4.4 Single sideband phase noise comparison of the three- and five-QW MLLDs.

Moreover, the timing jitter is directly proportional to the square root of the RF linewidth [8]. The timing jitter was measured using single sideband analysis of the RF spectrum. It is shown in Fig. 4.4 that the phase noise was significantly lower using a laser made in three-QWs than in five-QWs. The phase noise of the three-QW laser was -93 dBc/Hz at a 1 MHz offset, compared to that of the five-QW, which was -66.5 dBc/Hz. The RMS timing jitter of the three-QW laser, calculated by integrating the SSB phase noise from 10 kHz to 10 MHz was 1.5 ps, whereas that of the five-QW laser was 4.4 ps. This confirms that lowering the number of QWs in a laser can reduce the jitter.

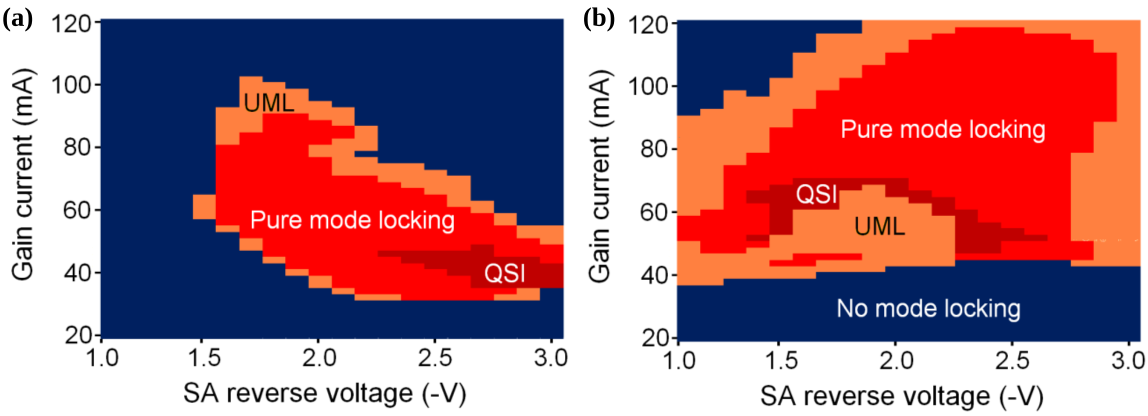

Figure 4.5 Mode-locking regions of (a) five-QW MLLD, and (b) three-QW MLLD. (QSI: *Q*-switching instabilities, UML: unstable mode-locking, i.e. pedestal modulation).

Another interesting finding was the mode-locking range of the three-QW laser was significantly larger than the five-QW laser (Fig. 4.5). This is likely to be due to smaller increments in the wavelength detuning with both gain and reverse bias due to the lower differential gain, which means that the absorption band edge is more often in line, or nearby the gain peak, promoting short pulse generation over a wider bias detuning range [13, 14]. It can also be assumed that a reduction in QWs leads to an increasing electric field for a given reverse bias voltage, which means that mode-locking would occur at lower bias values as shown in Fig. 4.5. A larger mode-locking area is useful for integrating in optical systems as it could potentially reduce packaging tolerances by easing the bias constraints.

4.2 10 GHz MLLD with integrated phase section and DBR using QWI

Distributed Bragg reflectors (DBRs) are essential for controlling the spectral bandwidth and the centre wavelength, while additionally providing tuning possibilities of the pulse repetition rate [15, 16]. These features are indispensable for optical sources in OCDMA systems, particularly in incoherent systems, which require precise wavelength and time control. In comparison with the traditional approach of buried gratings, surface etched DBRs are simpler to fabricate due to the non-requirement of etch and regrowth processes. In [17], a surface etched DBR laser operating at 10 GHz was demonstrated, although the DBR coupling efficiency κ was very low (~ 7/cm, taking the DBR loss into account). The DBR requires a wider bandgap that the active region, to reduce the interband absorption when applying little or no bias. Rather than performing etch and regrowth steps, quantum-well intermixing (QWI) can be used for passivation [18]. Moreover, optimising the DBR design of the surface etched DBRs can minimise the scattering losses [19]. During this project, an low loss grating design was fabricated with integrated third order Bragg gratings, achieving a moderate coupling efficiency (κ ~ 65/cm), as well as low absorption and scattering losses using the QWI approach. The bandgap of the DBR and phase sections were blue shifted relative to the active regions (i.e. gain and SA sections). A schematic of the mode-locked DBR laser is shown in Fig. 4.6.

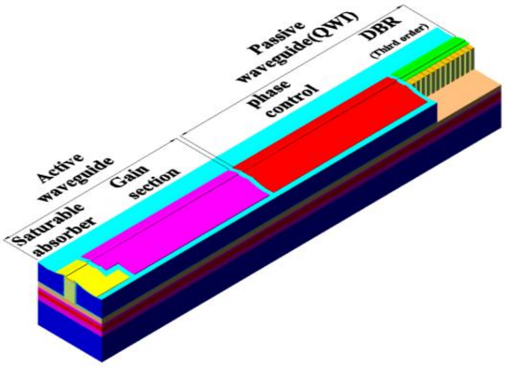

Figure 4.6 Schematic diagram of a MLLD with integrated phase control and DBR sections using QWI technology.

The device had a total length of 4365 μm and consisted of a gain section (1018 μm), SA section (60 μm), phase section (1100 μm) and a DBR (60 μm long). The period of the gratings was 740 nm with a slot with of 180 nm, providing a duty cycle of ~76%, which was chosen as a compromise between scattering loss reductions and fabrication feasibility, while achieving adequate reflectivity [19]. The effective length of the DBR was ~ 55 μm (see Fig. 4.8) providing an effective total cavity length of ~4280 μm, corresponding to a round trip frequency of ~10 GHz. The laser was fabricated in the five-QW *Al*-quaternary material due to its availability and similar to the previously reported lasers, HSQ was used to planarise the 2.5 μm wide, 1.92 μm high ridge waveguide. The DBR gratings were etched down to the dry-etch stop layer, just above the active layers (i.e. 1.92 μm). The QWI step during fabrication provided a bandgap shift of ~100 nm (blueshift) in the passive sections, whereas the gain and SA sections' peak remained at ~1.5 μm. Further details about the fabrication can be found in [20].

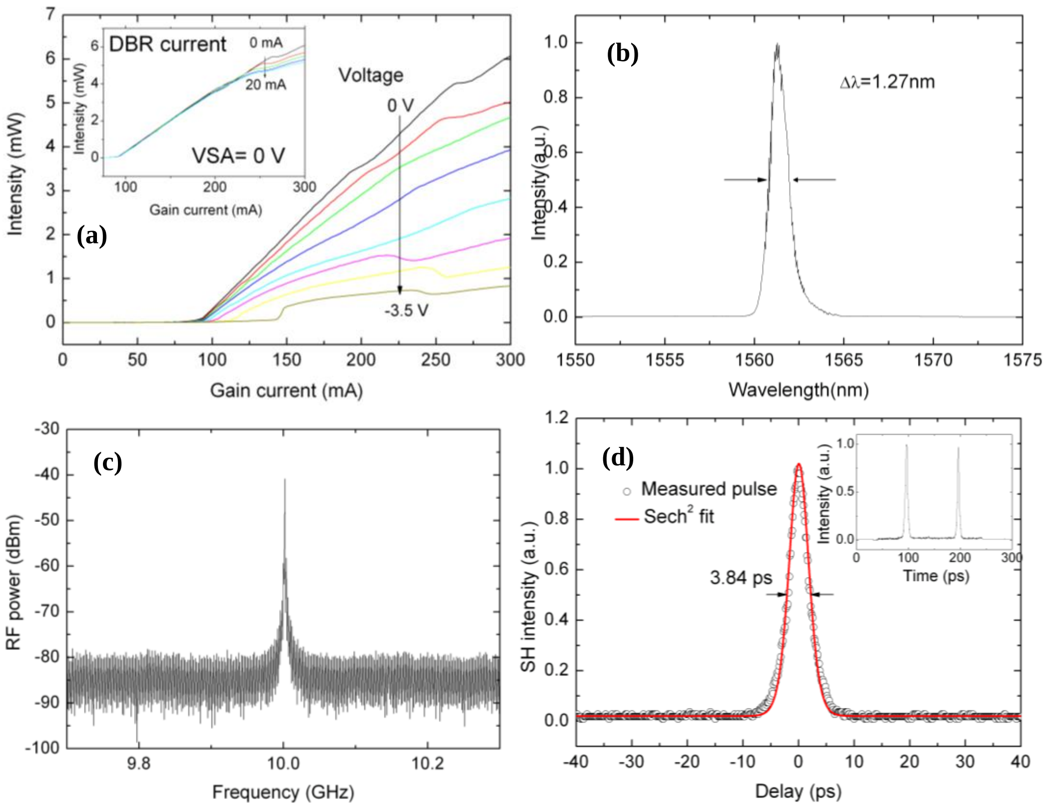

Figure 4.7 Characterisation results of a three-QW MLLD showing (a) *LI* curves with varied reverse voltage on SA section, inset: *LI* curves at 0V, with a varied DBR current, (b) optical spectrum when mode-locking with the shortest pulse width, (c) corresponding RF spectrum, and (d) measured autocorrelation trace with fittings (Inset: larger time span showing pulse spacing and peak uniformity).

Figure 4.7(a) shows the *LI* curve of the laser. The threshold was 74 mA, which is larger than that of the 40 GHz laser described earlier due to the distribution of the electron concentration across the longer cavity length (i.e. larger current density). Kinks were observed on some of the *LI* curves due to the thermal detuning of the gain and reflector sections. Tuning the DBR section from 0 mA – 20 mA had minimal effect on the threshold current or slope efficiency, although at higher gain currents a noticeable increase of power was evident with an increase in the DBR current (inset of Fig. 4.7(a)). This was due to the increasing saturation energy of the entire device as the DBR current was promoting more gain. Figure 4.7(b) shows the spectrum of the laser, which was centred at 1561.3 nm with a 3 dB bandwidth of 1.27 nm. The measured peak reflectivity was 47 %, which is in accordance with the coupling efficiency κ = 65/cm, using $R = \tanh^2(\kappa L)$ [21], where L is the length of the grating section (60 μm) (Fig. 4.8(a)). Using this value of κ, the effective length could subsequently be calculated using: $L_{eff} = \frac{1}{2\kappa}\tanh(\kappa L)$ [22], as plotted in Fig. 4.8(b). The effective propagation loss coefficient could then be obtained using:

$$\alpha_{eff} = \frac{1}{L_{eff}} \int_0^L \alpha(z) e^{-\frac{z}{L_{eff}}} (1 \pm \cos 2\beta z)\, dz \qquad (4.2)$$

where $\alpha(z)$ represents the constant loss of the material along the propagation axis z, and β is the complex wave amplitude of the incident and reflected waves. This equation has been plotted in Fig. 4.8(c), where it is shown that for a κ of 65/cm, using a L_{eff} of 55 μm, the loss coefficient was around 5/cm.

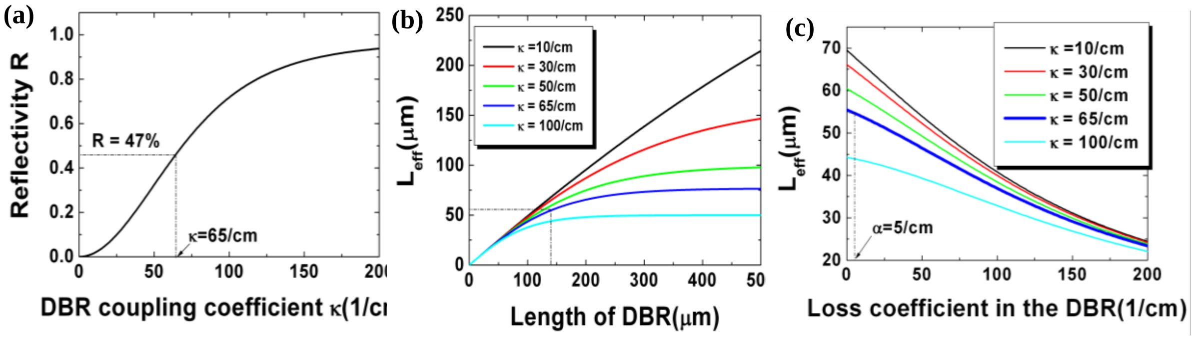

Figure 4.8 Calculated DBR optimisation properties: (a) Coupling coefficient vs. reflectivity, (b) Length of DBR at different κ values indicating the effective length, and (c) Loss coefficient vs. effective length for different values of κ.

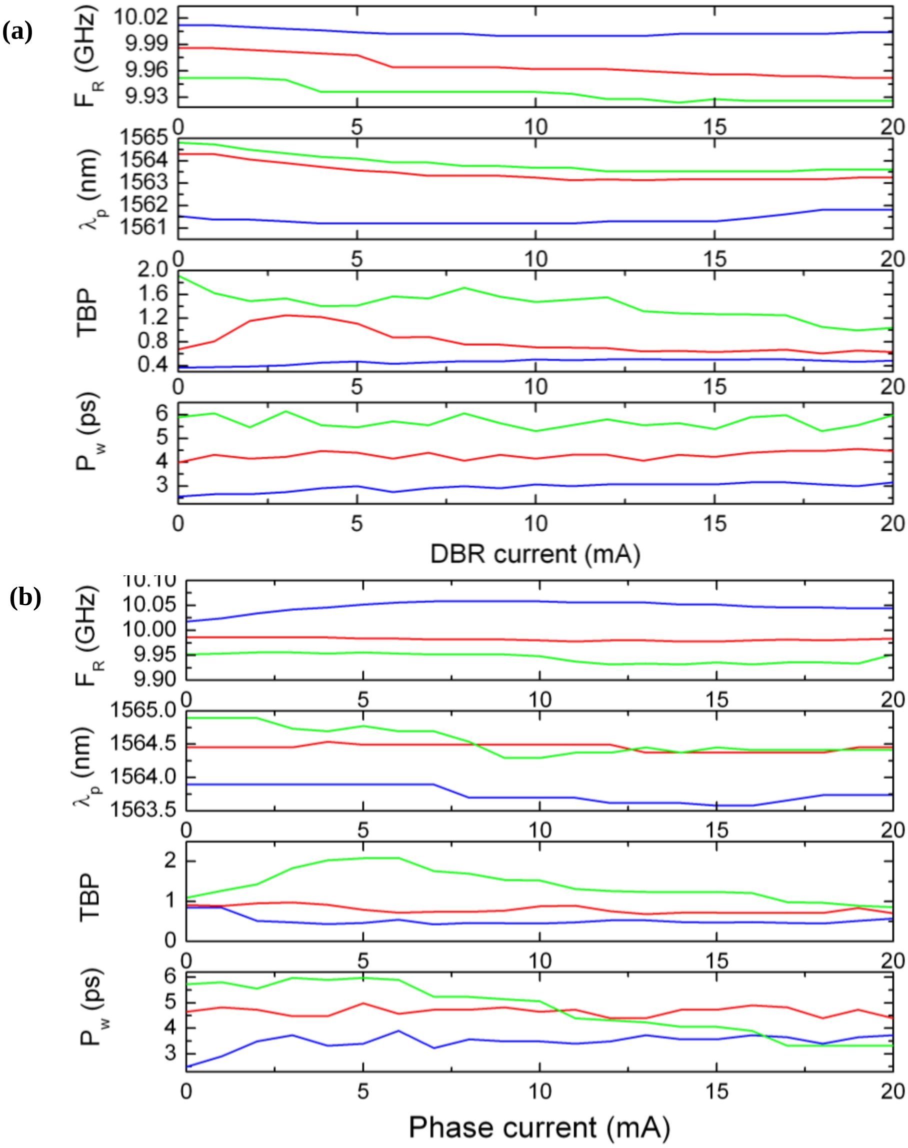

Figure 4.9 Characterisation results of (a) DBR section current tuning and (b) phase section current tuning for gain currents 120 mA (blue trace), 180 mA (red trace), and 240 mA (green trace). (F_R = pulse repetition rate, λ_p = peak wavelength, TBP = time-bandwidth product, P_w = pulse width).

Figure 4.9 summarises the dependence of the peak wavelength (λ_p), pulse repetition frequency (F_R), pulse width and TBP on the DBR and phase sections tuning current, where the total injection current to the gain sections and the absorber reverse bias were fixed at 120, 180, 240 mA and -3.0 V, respectively. For all investigated gain current values, the peak wavelengths initially experienced an almost continuous blue-shift as the DBR current was increased from 0 mA to 15 mA due to the carrier effect of band-filling. At higher DBR currents (greater than 15mA), the thermally induced red-shift began to dominate the carrier induced blueshift, so that the peak wavelength experienced an overall red-shift. λ_p could also be tuned by varying the injection current to the phase section. For all investigated reverse bias voltages applied to the SA section and for a fixed gain current, F_R decreases as the DBR section current is increased. A tuning range of about 28 MHz was obtained when the DBR current was varied from 0 mA to 20 mA with the gain current set to 120 mA. The frequency reduction with an increasing DBR current was consistent with the increase in the effective length caused by the lower absorption loss [16]. On the other hand, for a fixed value of DBR current and SA voltage, the F_R decreased with increasing gain current. These anomalously high frequency shifts are mainly caused by the detuning of the cavity roundtrip frequency by gain/absorber saturation effects [23]. A tuning range of about 60 MHz was obtained when the gain current varied from 120 mA to 240 mA for all DBR currents set at 0 mA. Tuning of the F_R could also be achieved by varying the reverse voltage on the SA section or the injection current to the phase section.

From Fig.4.9, it is shown that for a fixed DBR current, as the gain current was increased, the pulse width was broadened due to chirp induced by SPM [24]. This is more explicitly shown in Fig. 4.10(b). When the gain current was set to 120 mA, as the DBR current was increased, the TBP initially increased and then stabilised at around 0.49, which is very close to the transform-limited value. For gain current values of 180 and 240 mA, the TBP initially decreased and then stabilised at 0.6 and 1.0 respectively, which is somewhat larger than the transform-limited value. This is likely to be due to SPM in the gain section.

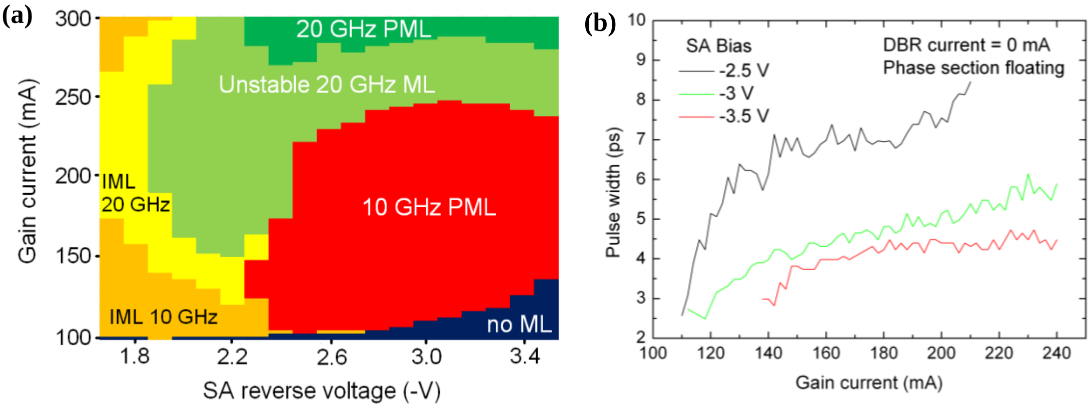

Figure 4.10 (a) Mode-locking region of 10 GHz MLLD, (PML: Pure mode-locking, IML: Incomplete mode-locking, i.e. pedestal modulation), and (b) the pulse width as a function of bias current over three V_{SA} conditions: -3.5 V, -3 V, and -2.5 V, with the DBR operating at 0 mA and the phase section left floating.

Another interesting observation here was the occurrence of 20 GHz operation at a small range of bias conditions, as shown in Fig. 4.10(a). This phenomena has recently been modelled in [9], and can be described as the promotion of harmonic ML effects caused by the increased spontaneous emissions in the cavity, which eventually lock in phase giving rise to two pulses that are counter propagating, and thus the frequency of the output pulses are doubled. This behaviour is characteristic of harmonic mode-locked lasers, as will be discussed later in this chapter. In Fig. 4.10(a), it is shown that stable harmonic mode-locking is obtained at relatively high gain bias conditions.

According to the famous Henry's linewidth formula stated in eq. 4.1, a longer cavity length should decrease the width of each longitudinal mode, leading to reductions in the noise of the laser since the round trip frequency, T_R, is increased [11]. Moreover, longer cavity lasers in turn have a lower threshold current density, leading to lower spontaneous emission noise. This was observed in the phase noise measurement, which is shown in Fig. 4.11. The timing jitter was measured as 3.1 ps, integrated from 10 kHz to 100 MHz, which is slightly lower compared to the 40 GHz laser (4.4 ps).

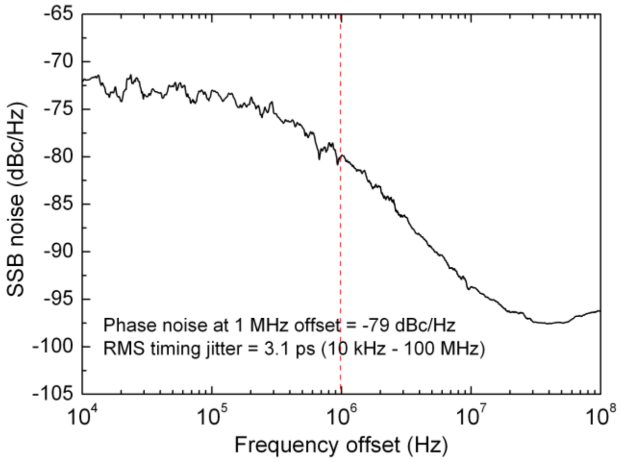

Figure 4.11 Single sideband phase noise of the 10 GHz MLLD with integrated DBR and phase sections.

4.3 Harmonic mode-locking via compound cavity

High data rates in OCDMA systems are essential if it is to supersede current multiple access technologies [25]. High pulse repetition frequency MLLDs are the obvious solution for achieving this criterion. One of the most effective ways of producing high frequency pulses is to introduce harmonic mode-locking techniques. A harmonic MLLD produces an optical pulse train at a harmonic of the fundamental round trip frequency, which is principally defined by the cavity length. This can be achieved in a number of ways, such as harmonic optical injection [26, 27], colliding pulse, and compound cavity MLLDs (CCM). Frequencies of up to 1.5 THz have been realised using CCM effects in DBR lasers [28], although results of this publication show the device operates over a very limited bias range and results are yet to be improved. Using CCMs in standard MLLDs with intracavity reflectors (ICRs) however has shown to produce frequencies up to 2.1 THz at a wavelength of 850 nm (made using the *AlGaAs/GaAs* material) [29]. The theoretical analysis shown in this paper implied that using more ICRs at integer fractions of the cavity length could provide a more stable operation due to the stronger linear modal selection within the cavity, as well as a more accurate harmonic number selection than single ICRs since they can be defined lithographically [30]. However, due to cleaving limitations, a single ICR was defined to allow flexibility of the harmonic number selection at the cleaving stage (i.e. the cleaving accuracy is more tolerable to error). A schematic of the CCM laser is shown in Fig. 4.12.

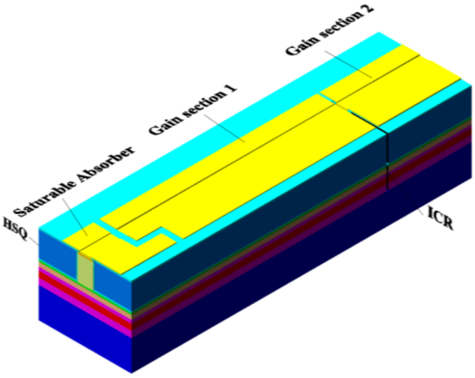

Figure 4.12 Schematic diagram of a compound cavity laser with an ICR used to form an additional harmonic cavity section.

The device was fabricated using the five-QW *Al*-quaternary material. The cavity was 1070 μm long with a 20 μm long SA, and two gain sections; the shorter cavity was approximately a quarter of the total cavity length to provide fourth harmonic oscillations in the cavity. A single slot was deeply etched down between the two gain sections by 3.2 μm for isolating the sections and the slot width was ~364 nm. The ridge waveguide was 2.5 μm wide and 1.92 μm high. Using a single slot provided an intracavity reflectivity of ~38 %, which was optimised to provide the highest modal gain discrimination (i.e. higher order mode selectivity), such that stable harmonic mode-locking could be achieved [31]. And finally, HSQ was used to planarise the ridge waveguide.

The *LI* curves of the CCM are shown in Fig. 4.13(a) for different SA and short cavity gain biases. The threshold current with an unbiased SA section, and with 5 mA applied to the short gain section was 20 mA, which increased with reverse voltage on the SA section, as expected. Increasing the short cavity gain reduced the threshold current due to the reduction in absorption losses resulting from the increased gain within the cavity. Kinks were observed on some of the *LI* curves which are likely to be caused by thermal detuning of the long and short gain sections, and are linked to the mode hopping in the optical spectrum [32]. Figure 4.13(b) shows the progression of the wavelength modes as the gain current of the long gain section is increased. It is evident that in certain regions of gain, with a fixed short gain current and SA voltage (chosen to show the largest harmonic mode-locking range), that the spectrum is indeed organised effectively for 160 GHz

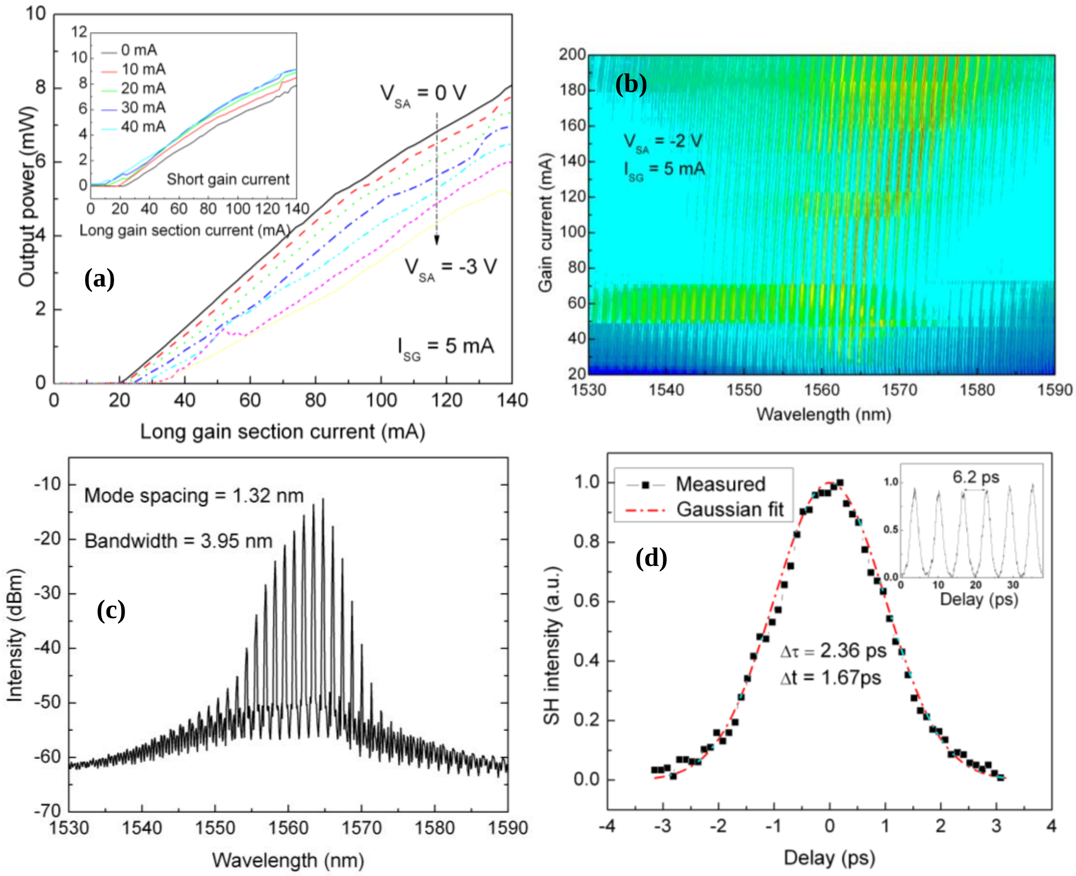

Figure 4.13 Characterisation results of a CCM laser showing (a) *LI* curves with varying LG current and V_{SA} (Inset: with varied SG section current), (b) optical spectrum contour map as bias current is increased (V_{SA} was set to -2V and I_{SG} set to 5 mA), (c) optical spectrum when laser was mode-locked, and (d) corresponding measured autocorrelation trace with fittings (Inset: larger time span showing pulse spacing and peak uniformity).

mode-locking operation (i.e. 1.32 nm mode spacing). Using the most ideal bias conditions to provide the shortest pulse width with pure mode-locking, the optical spectrum and pulse width are shown in Fig. 4.13(c) and (d) respectively. The 3 dB bandwidth of the optical spectra was 3.95 nm (Gaussian) and the corresponding pulse width was measured as 1.67 using a Gaussian pulse fit. The spacing between each pulse of the pulse train was 6.2 ps, which corresponds to a round trip frequency of 161.29 GHz. Due to this high frequency oscillation, a confirmation of the frequency on a RF spectrum analyser was unavailable due to measuring equipment limitations.

4.4 Colliding pulse mode-locking

An alternative method of achieving high repetition pulse frequencies is the colliding pulse method (CPM). In this regime, the SA is situated at the centre of the cavity, with two gain sections on either side enabling the generation of the second harmonic [26]. CPMs offers many advantages over other MLLD topologies as they provide relatively stable and better pulse shapes during mode-locking operation [33]. A monolithic 160 GHz CPM laser was recently reported in [26], with a 540 μm cavity and a 50 μm SA located at the centre of the cavity. Due to the short cavity length, the output power was relatively low at 10 mW. One way of achieving higher output power in CPM laser via higher gain is to extend the cavity length, having multiple SAs along the cavity at equidistant spaces apart, separated by a length corresponding to the desired repetition frequency. This is known as multiple-CPM (MCPM), in which higher order harmonics occur in the cavity corresponding to the number of gain sections. During this research a MCPM was fabricated, a microscope picture of which is shown in Fig. 4.14.

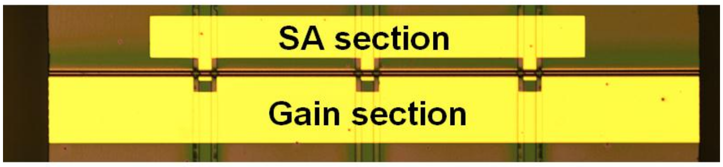

Figure 4.14 Microscope picture of the MCPM laser

The device was fabricated on the three-QW substrate, and has a total cavity length of 1070 μm, with three 20 μm long SAs located at every quarter along the cavity length, providing the fourth harmonic. The three SAs were electrically connected using a single contact, and the remaining four gain sections were also connected. 10 μm slots were used to separate the gain and SA sections using 200 nm deep etched slots in the contact layer. Figure 4.15(a) shows the *LI* curves obtained during device characterisation. The threshold current was 46 mA and the slope efficiency was 18.8 % with an unbiased SA section. Increasing the SA voltage would decrease the threshold and slope efficiency as expected due to the increase in interband absorption and exciton absorption.

Passive mode-locking was achieved over a wide range of bias conditions, from V_{SA} < -1.6 V, and I_{gain} > 190 mA. The spectrum and autocorrelation trace of the output of the CPM are shown in Fig. 4.15(c) and (d), respectively, with -1.6 V applied to the absorbers and 200 mA applied to the gain sections. These bias conditions were chosen to be optimal for short pulse operation of the CPM. The wavelengths were centred at 1569 nm with a 3 dB bandwidth of 4.96 nm (sech^2) (Fig. 4.15(b)). The mode spacing was 1.3 nm, corresponding to the required 160 GHz operation. The pulse width was measured as 0.98 ps using a sech^2 fit, giving a TBP of 0.47. Each pulse was separated in time by 6.2 ps, verifying the fourth harmonic mode-locking at ~161.3 GHz. The average output power was 20.4 mW, which is more than twice that reported in [23]. This is likely to be due to the higher saturation energy of the three-QW material, as discussed in chapter 2.

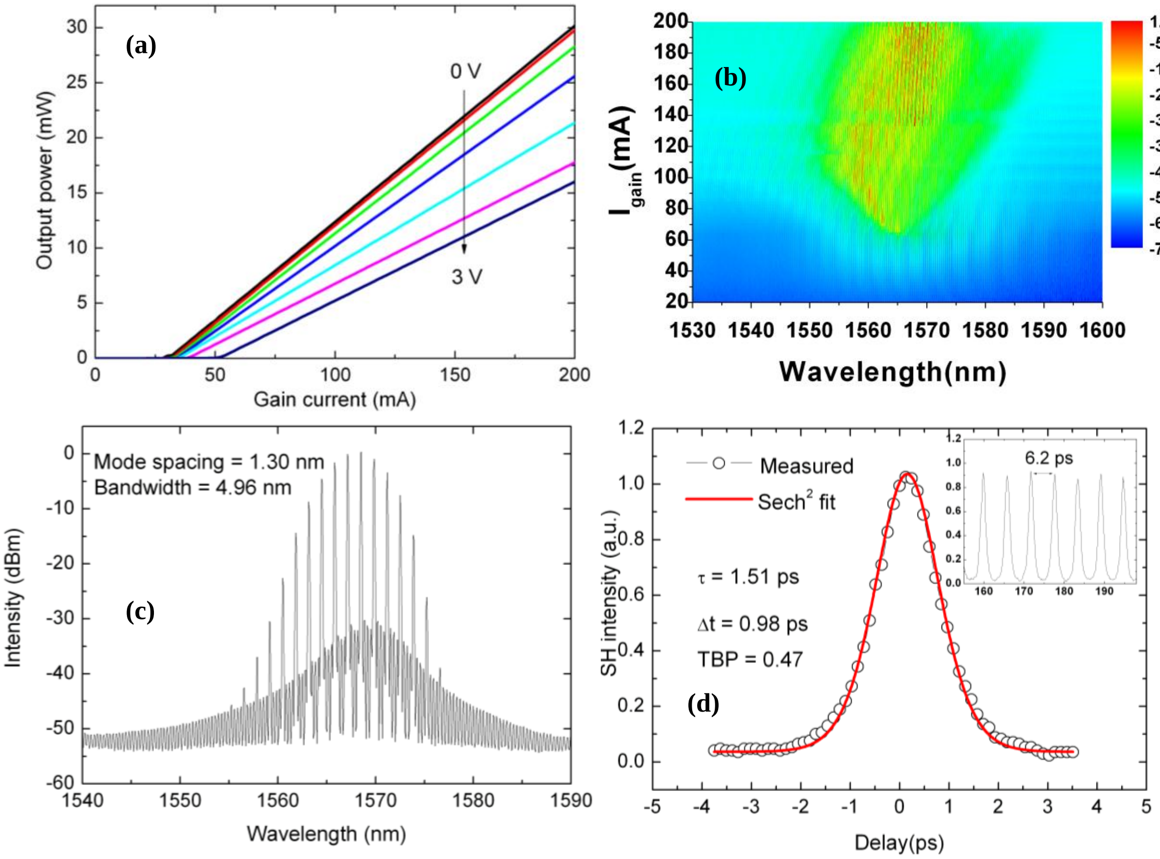

Figure 4.15 Characterisation results of a CPM laser showing (a) *LI* curves, (b) optical spectrum contour map as bias current is increased (V_{SA} was set to -2V and I_{SG} set to 5 mA), (c) optical spectrum when laser was mode-locked, and (d) corresponding measured autocorrelation trace with fittings (Inset: larger time span showing pulse spacing and peak uniformity).

4.5 Chapter Summary

This chapter presented a number of useful MLLD topologies that can be used as optical sources for high speed OCDMA systems. The *AlGaInAs/InP* material system has been demonstrated to be an excellent material choice for monolithically fabricating lasers on, given its ability to generate high frequency subpicosecond pulses without the need for advanced fabrication techniques. QWI can also be used to passivate discrete sections and laser components, such as DBRs and phase sections, to enable fine tuning of the operating wavelength and pulse repetition frequency. Both three- and five-QW two section MLLDs were shown and their performances compared, and the former was shown to enable higher power and lower jitter values, making it highly suitable for integrated systems.

As well as the two-section MLLDs, multi-segment MLLDs were presented for harmonic mode-locking generation, namely, CCM, and CPM lasers. The stability of the CCM approach could potentially be better than that of the CPM approach due to the strong longitudinal mode selection of the compound cavity. Moreover, the literature shows that one can achieve much higher repetition rates using the CCM approach, and frequencies of over 1000s of GHz have been recently demonstrated [34].

Overall, the results shown in this chapter demonstrate the strong ability and desirable features of *Al*-quaternary based MLLDs for serving as optical sources in monolithically integrated optical systems.

4.6 References

[1] P. R. Prucnal, et al., "Optical code division multiple access – Fundamentals and applications," CRC Taylor and Francis, 2006.

[2] L. Hou, P. Stolarz, J. Javaloyes, R. P. Green, C. N. Ironside, M. Sorel, and A. C. Bryce, "Subpicosecond pulse generation at quasi-40 GHz using a passively mode locked AlGaInAs-InP 1.55-μm strained quantum-well laser," IEEE Photon. Technol. Lett., Vol 21, No. 23, pp 1731-1733, 2009.

[3] J. C. Diels and W. Rudolph, "Ultrashort pulse phenomena: Characteristics of fs light pulses," San Diego: Acad. Press, pp 1-12, 1996.

[4] P. Stolarz, "Development of a phase-sensitive pulse measurement technique for semiconductor mode-locked lasers," Ph.D. thesis, University of Glasgow, 2012.

[5] P. M. Stolarz, G. Mezosi, M. J. Strain, A. C. Bryce, and M. Sorel, "Highly-sensitive sonogram for assessment of chirp in semiconductor mode-locked lasers", IEEE J. Quant. Electron., Vol. 48, pp 995 - 1003, 2012.

[6] B. Bennett, R. Soref, and J. Del Alamo, "Carrier-induced change in refractive index of InP, GaAs and InGaAsP,", IEEE J. Quant. Electron., Vol. 26, No. 1, pp 113-122, 1990.

[7] H. Tsang and I. White, "Polarisation dependent optical modulation using the plasma effect in a GaAs-GaAlAs quantum well waveguide," Optics Comms., Vol. 74, No. 6, pp 365-369, 1990.

[8] F. Kefelian, S. O'Donoghue, M. T. Todaro, J. G. McInerney, and G. Huyet, "RF linewidth in monolithic passively mode locked semiconductor laser," IEEE Photon. Technol. Lett., Vol. 20, No. 16, pp 1405-1407, 2008.

[9] U. Bendelow, R. Mindaugas, A. Vladimirov, B. Huttl, and R. Kaiser, "40 GHz mode locked semiconductor lasers: Theory, simulations and experiment," Opt. Quant. Electron., Vol. 38, pp 495-512, 2006.

[10] K. Yvind, "Semiconductor mode locked lasers for communication systems," PhD thesis, Technical University of Denmark, 2003.

[11] C. H. Henry, "Theory of the Linewidth of Semiconductor Laser," IEEE J. Quant. Electron., vol. QE-18, No. 2, pp 259 – 264, 1982.

[12] T. Habruseva, S. O'Donoghue, N. Rebrova, F. Kefelian, S. P. Hegarty, and G. Huyet, "Optical linewidth of a passively mode locked semiconductor laser," Opt. Lett., Vol. 34, No. 21, pp 3307-3309, 2009.

[13] J. Javaloyes, and S. Balle, "Mode locking in semiconductor Fabry-Perot lasers," IEEE J. Quant. Electron., Vol. 46, No. 7, pp 1023-1030, 2010.

[14] D. Kanimatsu, S. Arahira, Y. Kato and Y. Ogawa, “Passively mode locked laser diodes with bandgap wavelength detuned saturable absorbers,” IEEE Photon. Technol. Lett., Vol. 11, No. 11, 1363-1365, 1999.

[15] E. Zielinski, E. Lach, J. Bouyad-Amine, H. Haisch, E. Kuhn, M. Schilling, and J. Weber, “Monolithic multisegment mode-locked DBR laser for wavelength tunable picosecond pulse generation,” IEEE Sel. Top. Quant. Electron., Vol. 3, No. 2, pp 230-232, 1997.

[16] I. Ogura, H. Kurita, T. Sasaki, and H. Yokoyama, “Precise operation frequency control of monolithic mode locked laser diodes for high speed optical communication and all optical signal processing,” Opt. Quant. Electron., Vol. 33, pp 709-725, 2001.

[17] D. Larsson, K. Yvind, and J. M. Hvam, “Long all-active monolithic mode locked lasers with surface-etched Bragg gratings,” IEEE Photon. Technol. Lett., Vol. 19, No. 21, pp 1723-1725, 2007.

[18] L. Hou, M. Haji, R. Dylewicz, B. Qui, and A. C. Bryce, “Monolithic 45 GHz mode locked surface etched DBR laser using quantum well intermixing technology,” IEEE Photon. Technol. Lett., Vol. 22, No. 14, pp 1039-1041, 2010.

[19] L. Hou, R. Dylewicz, M. Haji, P. Stolarz, B. Qui, and A. C. Bryce, “Monolthic 40 GHz passively mode locked AlGaInAs-InP 1.55 μm MQW laser with surface-etched distributed Bragg reflector,” IEEE Photon. Technol. Lett., Vol. 22, No. 20, pp 1503-1505, 2010.

[20] L. Hou, M. Haji, A. E. Kelly, J. M. Arnold, and A. C. Bryce, “Mode locked laser array monolithically integrated with SOA and EA modulator,” OFC 2011, paper OThG4, 2011.

[21] G. P. Agrawal, and N. K. Dutta, “Long-wavelength semiconductor lasers,” Van Nostrand Reinhold, Michigan, 1986.

[22] L. A. Coldren, and S. W. Corzine, “Diode lasers and photonic integrated circuits,” John Wiley and Sons, Inc., New York, 1995.

[23] S. Arahira, and Y. Ogawa, “Repetition frequency tuning of monolithic passively mode locked semiconductor lasers with integrated extended cavities,” IEEE J. Quant. Electron., Vol. 33, No. 2, pp 255-264, 1997.

[24] G. P. Agrawal, and N. A. Olsson, “Self phase modulation and spectral broadening of optical pulses in semiconductor laser amplifiers,” IEEE J. Quant. Electron., Vol. 25, No. 11, pp 2297,-2306, 1989.

[25] I. Glesk, V. Baby, C. Bres, P. R. Prucnal, and W. C. Kwong, “Is optical CDMA viable technique for broadband networks?,” Proc. of SPIE, Vol. 6180, 2006.

[26] S. Arahira, Y. Katoh, D. Kunimatsu, and Y. Ogawa, “Stabilization and timing jitter reduction of 160 GHz colliding-pulse mode-locked laser diode by subharmonic-frequency optical pulse injection,” IEICE Trans. Electron., Vol. E83-C, pp 966-973, 2000.

[27] Y. Wen, D. Novak, H. Liu, and A. Nirmalathas, “Generation of 140GHz optical pulses with suppressed amplitude modulation by subharmonic synchronous modelocking of Fabry-Perot semiconductor laser,” Electron. Lett., Vol. 37, No. 9, pp 581-582, 2001.

[28] S. Arahira, Y. Matsui, and Y. Ogawa, “Mode-locking at very high repetition rates more than terahertz in passively mode-locked distributed-Bragg-reflector laser diodes,” IEEE J. Quant. Electron., Vol. 32, No. 7, pp 1211-1224, 1996.

[29] D. A. Yanson, M. W. Street, S. D. McDougall, I. G. Thayne, J. H. Marsh, and E. A. Avrutin, “Ultrafast harmonic mode-locking of monolithic compound-cavity laser diodes incorporating photonic-bandgap reflectors,” IEEE J. Quant. Electron., Vol. 38, No. 1, pp 1-11, 2002.

[30] L. Hou, P. Stolarz, R. Dylewicz, M. Haji, J. Javaloyes, B. Qui, and A. C. Bryce, “160-GHz passively mode-locked AlGaInAs 1.55-μm strained quantum-well compound cavity laser,” IEEE Photon. Technol. Lett., Vol. 22, No. 10, pp 727-729, 2010.

[31] L. Hou, M. Haji, R. Dylewicz, P. Stolarz, B. Qui, E. A. Avrutin, and A. C. Bryce, “160 GHz harmonic mode locked AlGaInAs 1.55 μm strained quantum well compound cavity laser,” Opt. Lett., Vol. 35, No. 23, pp 3991-3993, 2010.

[32] J. Fricke, H. Wenzel, M. Matalla, A. Klehr, and G. Erbert, “980-nm DBR lasers using higher order gratings defined by i-line lithography,” Semicon. Sci. Technol., Vol 20, pp 1149, 2005.

[33] Y. K. Chen, and M. C. Wun, “Monolithic colliding-pulse mode-locked quantum-well lasers,” IEEE J. Quant. Electron., Vol 28, No. 10, pp 2176-2185, 1992.

[34] D. Yanson, M. W. Street, S. D. McDougall, I. G. Thayne, J. H. Marsh, and E. A. Avrutin, “Terahertz repetition frequencies from harmonic mode locked monolithic compound cavity laser diodes,” App. Phys. Lett., Vol 78, pp 3571-3573, 2001.

Chapter 5

Pulse stabilisation and jitter reduction in MLLDs

The majority of mode-locked lasers that have been tested and characterised in the previous chapter and during the course of this research were primarily passively operating, i.e. the lasers were free running and had no permanently fixed phase oscillations during measurement. Passively mode-locked laser diodes (MLLD) are known to produce shorter pulses than the active counterpart due to pulse narrowing effects via the saturable absorber (SA); however, due the lack of a reference clock, the phase will tend to fluctuate during mode-locking operation as a result of various sources of noise, such as mechanical noise, thermal noise, high intercavity losses, and most critically, spontaneous emission [1, 2]. It is then vital to introduce a stabilising mechanism before these lasers can be used in any practical application including optical communication systems, where unsynchronised system clocks will result in high bit error rates.

In this chapter, various methods for stabilising the MLLDs pulse timing shall be discussed. The two most widely used techniques, namely synchronous mode-locking (SML) and hybrid mode-locking (HML) have been investigated. SML employs an external active mode-locked laser source to provide a fixed periodic carrier excitation to the MLLD at the fundamental or a subharmonic of the round trip frequency. Alternatively, HML requires an RF signal being injected into part of the laser to directly stimulate the generation of pulses at the electrically defined AC frequency. While these methods are somewhat comparable (i.e. they correct the temporal phase of the pulse train via cyclic stimulation of carriers), the applications of each may vary greatly. This shall be discussed further in the final summary section of this chapter. The latter part of this chapter will describe an alternative method of providing pulse stability and reductions in jitter using a fibre based extension of the cavity, similar to the methods used in high speed optoelectronic oscillators (OEOs) for *Q*-factor enhancements.

5.1 Synchronous mode-locking

Also known as optical injection mode-locking, SML is a widely used pulse stabilisation technique in which the temporally defined pulse stream of an actively mode-locked laser source (also referred to as the *master laser*) is injected into a partially reflecting facet of a passively operating MLLD (i.e. *slave laser*) at the fundamental or a sub-harmonic of its cavity round trip frequency. By doing so, the slave laser's oscillations are forced to closely resemble that of the master laser's. Pulse synchronisation via SML has been vastly researched and is considered to be the most versatile method of pulse stabilisation. It is particularly attractive since it avoids limitations imposed by high frequency driving electronics and device parasitics, as opposed to the HML technique. Recent studies have also shown SML to perform better than the HML scheme as it provides greater reductions in phase noise, amplitude modulation, and is able to provide a wider locking range (also known as the frequency detuning range (FDR)) of MLLDs [3].

5.1.1 Principle of operation

Pulse synchronisation is realised when an integer multiple of the pulse repetition rate of the injected pulse stream ($m \cdot f_{inj}$, where m is an integer multiple and f_{inj} is the repetition frequency of the master laser) coincides with that of the slave laser, such that $f_{MLLD} = m \cdot f_{inj}$. Synchronisation is then established because the MLLD is pumped by an external periodic excitation at its resonant frequency, forcing the mode phases of the passive laser to lock to a narrowband, electrically defined frequency. The absorber segment of the MLLD is modulated via the external pump signal, such that bleaching (i.e. saturation) occurs intermittently [4]. This bleaching effect is mainly the result of carrier band filling via photoabsorption of the injected carriers, which forces the absorber to transmit light generated within the gain cavity until these carriers are swept out (further explanations on absorber dynamics are discussed in chapter 3). This induces a greater temporal precision of the pulse period, and hence reductions in phase noise as the MLLD oscillations are aptly synchronised to a permanent and invariable oscillator.

5.1.2 Experiments

A series of experiments were carried out in order to study the stabilisation mechanism under the SML scheme and to gain a fuller understanding of the fundamental parameters over which synchronisation to an external optical signal may occur. One of the greatest benefits of SML is that synchronisation is achievable using subharmonic frequency injection. This means that an actively mode-locked laser operating at a considerably lower pulse repetition frequency (driven by a convenient electronic frequency, i.e. < 50 GHz) may be employed to stabilise MLLDs operating at much higher frequencies (> 50 GHz).

The subharmonic SML method was tried using a 36 GHz MLLD, synchronised to a 9 GHz actively locked master laser (i.e. such that $m = 4$). A schematic of the experimental setup is shown in Fig. 5.1. The injected laser was an actively mode-locked fibre laser (Pritel ultrafast optical clock) with a variable pulse repetition frequency (~6 – 45 GHz, using a clock multiplier) and wavelength tuning from 1535 – 1570 nm. The MLLD under test was a two-section *AlGaInAs/InP* multiple quantum-wells (MQW) laser with a 1040 μm long gain section and a 30 μm long inter-cavity saturable absorber (SA). The experiment was carried out in the reflective geometry, similar to that used in [5] and [6]. A circulator was positioned in order to isolate the synchronised pulse stream emitted from the laser, which was then observed using a 40 GHz RF spectrum analyser via a high frequency matched photodiode (45 GHz). A polarisation controller was placed before the MLLD to maximise the TE polarity of the injected signal to promote better carrier coupling effects in the quantum-wells [7].

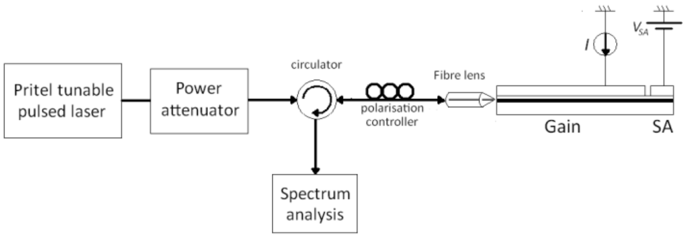

Figure 5.1 Schematic of experimental setup used for SML characterisation

The MLLD was mode-locked at 36.2 GHz when the gain section was forward biased with 250 mA and the SA was reversed biased with -1.6 V (Fig. 5.2(a)). The pulse width was 6.6 ps (assuming a sech^2 pulse shape) and its centre wavelength at 1570 nm. The master laser pulse repetition frequency was 9.05 GHz, with a pulse width of ~ 3 ps and its centre wavelength at 1550 nm. The harmonics generated by the injected signal are clearly shown in Fig. 5.2(b), which adequately extends up to the fundamental frequency of the MLLD. The resulting RF spectrum when the MLLD was synchronised is shown in Fig. 5.2(a) (blue trace). A noticeable reduction in linewidth is evident and is comparable to that of the injected signal (due to frequency pulling towards a single carrier), which is a clear indication of stability enhancement via injection locking. The full width at half maximum (FWHM), also referred to as the 3 dB of the measured RF linewidth was 1.5 MHz for the free running laser, and <100 kHz when synchronised (using a RBW of 100 kHz and VBW of 10 kHz). The power of the injected signal was then attenuated while the 3 dB linewidth was observed, indicating the minimum power required to synchronise the MLLD (inset of Fig. 5.3). The laser was considered to be adequately locked when the 3 dB linewidth of a single peak was less than 100 kHz.

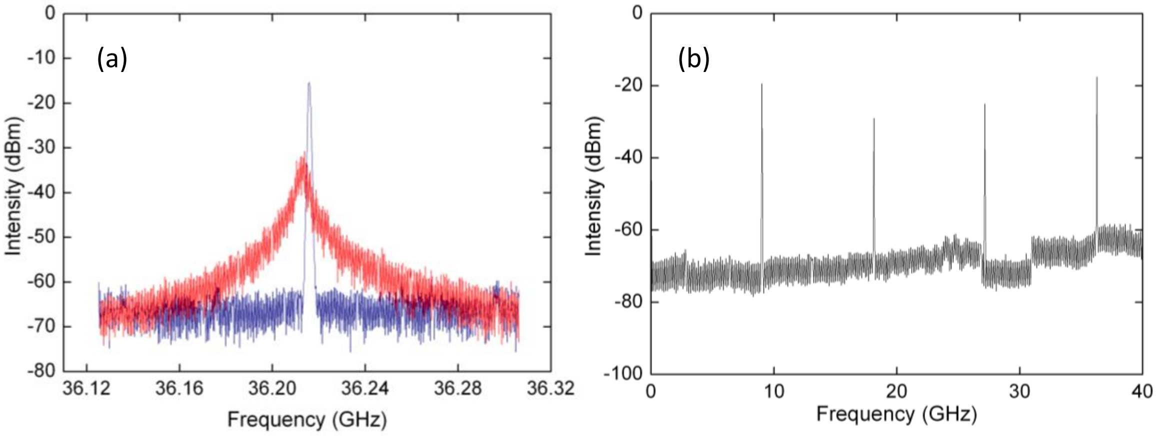

Figure 5.2 (a) RF spectrum of free running (red trace) and optically pumped (blue trace) MLLD, and (b) harmonics generated by 9 GHz injected signal, as viewed on an RF spectrum analyser.

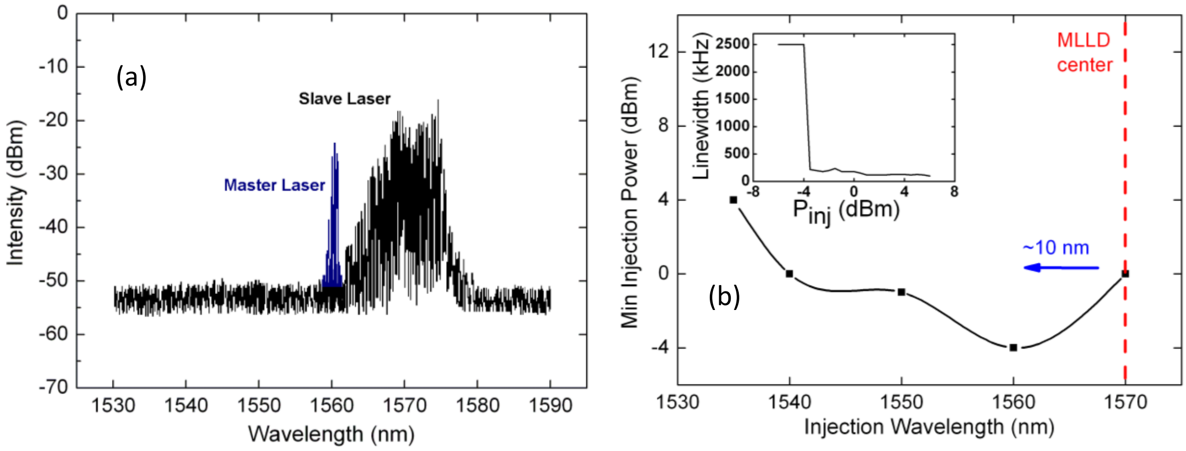

Figure 5.3 (a) Optical spectra of MLLD under optical injection , and (b) minimum injection power required to lock the MLLD at wavelengths across the C-band.

The measurement was repeated while the injection signal wavelength was varied across the C-band (1535 – 1570 nm). The minimum power required to synchronise the MLLD was -4 dBm (average) when the injected laser was operating at 1560 nm, and was therefore considered the optimum wavelength of injection (Fig. 5.3(b)). This was also confirmed by detuning the master lasers pulse repetition frequency down at small steps, while attenuating the injection power. The wavelength was tuned until the injected signal ceased to pull the MLLD frequency. The MLLD's frequency was pulled the furthest when the wavelength was operating at ~1560 nm [8, 9].

The parameters of this pulling effect were further studied to determine the frequency locking range (LR). The LR is the span of injection frequencies that the MLLD can lock to, and a larger span is often desired for many systems applications [3-7, 10, 11]. First, the LR was measured at different subharmonics (m) of f_{inj}. An optical clock multiplier was used to double and quadruple the pulse repetition frequency of the master laser, such that the fourth (9 GHz) and second (18 GHz) subharmonic and the f_{MLLD} were generated. The average power for the harmonic frequencies were matched at 2 dBm. The frequency was detuned around the centre frequency of the MLLD (36.2 GHz) and the 3 dB linewidth for each detuning was noted (Fig. 5.4(a)). A near linear correlation between the LR and subharmonic value is shown in Fig. 5.4(b). The LR appears to be the widest when the master laser was injected at the fundamental frequency of the MLLD. This is because the laser had more temporal components to synchronise with. There is an apparent discrepancy at lower frequency detunings of f_{inj} at different m values, which may have been caused by a slight variation of the operating frequency of the MLLD during measurement due to thermal changes within the laser cavity during measurement. However, the general theory of the LR decreasing as m increased was observed and is in good agreement with the experimental data reported in both [12] and [13]. Also, the asymmetrical LR plots for each m appear to favour higher frequency detunings as a result of an increasing carrier density within the laser gain due to the injected signal, which in turn causes a weaker refractive index in the gain medium, and therefore a change in carrier frequency (i.e. the plasma effect).

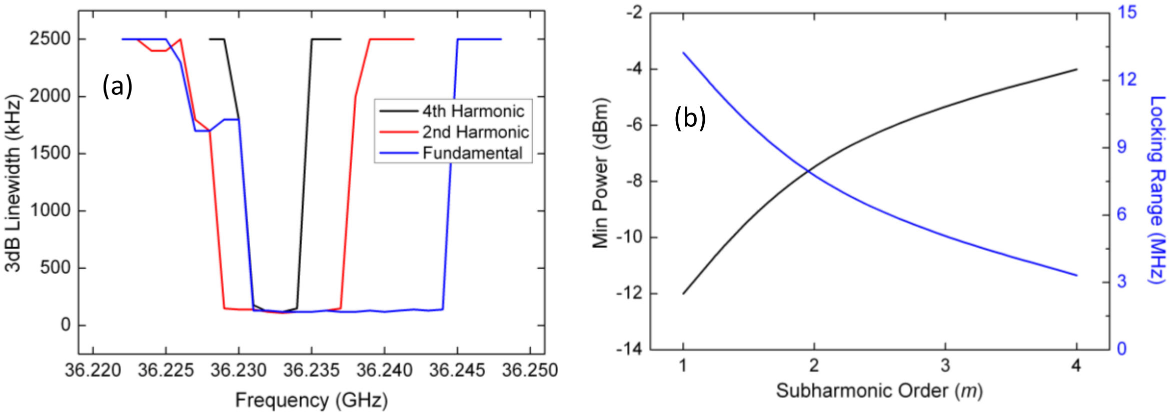

Figure 5.4 (a) Locking range of MLLD under 9 GHz (4th Harmonic), 18 GHz (2nd Harmonic), and 36 GHz (Fundamental) injection frequencies, and (b) the effects of injection power and locking range as a function the subharmonic order.

Figure 5.4(b) also shows the minimum injection power required for each subharmonic injection frequency. A greater injection power is needed as m is increased. This is likely to be a result of the cavity resonant effect, where a subharmonic pulse entering the cavity will multiply within the cavity and resonate for a period determined by the intensity of the pulse (P_{inj}) [14]. If P_{inj} is sufficient, the resonance of the subharmonic pulse will maintain synchronisation until the next pulse enters the cavity. If however, the period between pulses entering the cavity is too long (i.e. higher subharmonic orders), the phase control will become weakened due to a greater decay of the control resonance and therefore phase matching is more susceptible to diminish. The dependence of P_{inj} and the LR will be further examined later in this section.

In more recent studies of SML, it has been preferred to direct the external pump pulses at the SA side of the MLLD cavity since the saturation energy is much lower [4, 7], and therefore providing a greater effect on the LR while reducing the minimum required P_{inj}. Figure 5.5 shows the LR with the pump pulses directed at the SA side. The LR was increased to 80 MHz and the minimum power required to synchronise the laser at the centre frequency was -17 dBm. Compressing the injection pulse train, as suggested in [5] and [15], would further increase the LR to 150 MHz (also plotted in Fig. 5.5), with a minimum P_{inj} of -25 dBm at the centre frequency of the MLLD. The pulses emitted from the master laser source were compressed using a length dispersion compensated fibre to enlarge the optical bandwidth to form 800 fs pulses.

It is also purported in [7] that narrower pulses may provide a larger LR due to a widening of the spectrum, which promotes a greater overlap of optical frequencies, and thus, inducing greater modal interaction. To explain this in the temporal domain, consider a wider pulse with the same energy that averages out its pulse projection over time to therefore provide a weaker peak power and longer period of carrier excitation when injected into the cavity [15]. For this reason, higher order harmonics are also stronger if the pulses are narrower, which makes subharmonic locking is more effective, particularly when using higher order subharmonic frequencies [5].

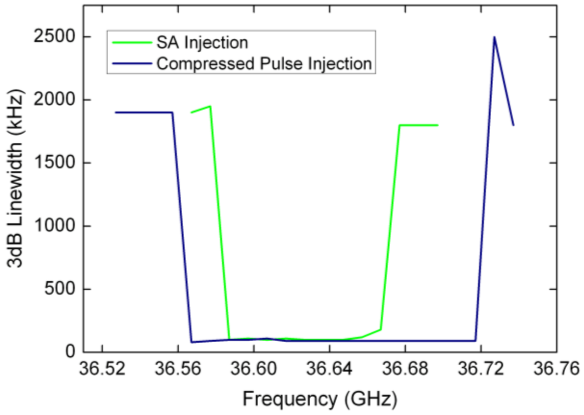

Figure 5.5 Locking range of MLLD under subharmonic optical injection into the SA side of the MLLD (green trace), and while also compressed (blue trace).

Shortly after this experiment, the laser had become unworkable due to some material defects caused by high and constant stimulation of carriers, and therefore overheating. However based on conclusions gained from the previous results, the setup was then adapted for a new device (Fig. 5.6) and further measurements were performed to study the purported amplitude modulation (AM) effects [3, 5, 12, 16]. AM is usually a negative artefact of injecting subharmonic frequencies into the MLLD, and can be described as the disproportionate signal intensities of the injected signal and the higher order harmonics generated within the cavity, causing a change in the pulse intensity at every *m*'th round trip period.

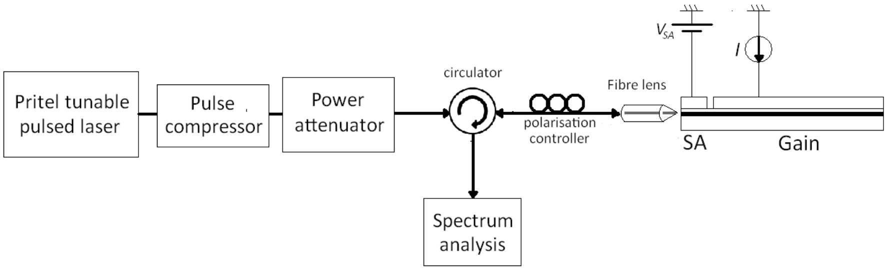

Figure 5.6 Experimental setup of SML using pulse compression, while injecting into the SA side of the MLLD cavity.

To study the effects of AM, a 40 GHz MLLD with a 1040um long gain section and a 20 um SA was used for this experiment. The gain section was biased at 53 mA, and the SA was reverse biased at -2.5 V. The centre wavelength was ~1550 nm (Fig 5.7(a) – black trace), and the RF frequency was 40.5 GHz (Fig 5.8(a) – blue trace). The compressed master laser was operated at 10.125 GHz and the centre wavelength was optimised at 1550 nm using the techniques previously stated. The resulting spectrum of the synchronised signal is shown in Fig 5.7(b).

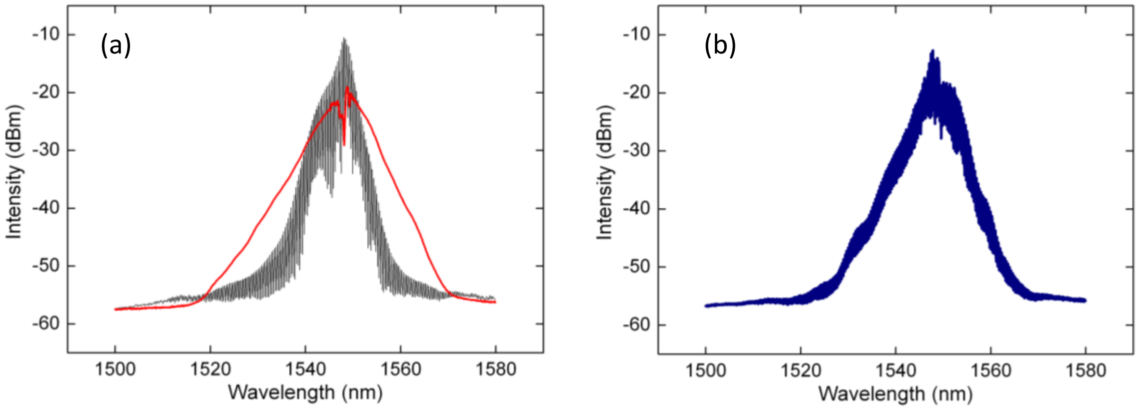

Figure 5.7 (a) Optical spectra of the master laser (Pritel 10 GHz pulsed signal) (red trace) and passive MLLD (black trace), and (b) optical spectra of optically synchronised output.

A comparison of the RF linewidth of the MLLD while free running (blue trace) and synchronised (red trace) is depicted in Fig. 5.8(a). The 3 dB linewidth was reduced from 5.9 MHz to 80.7 kHz at an injection power of 3 dBm. This had remained less than 100 kHz until the injection power fell below -37 dBm, where two peaks were present at the same intensity (one of f_{inj} and the other of f_{MLLD}). This indicated that synchronisation was diminishing due to a weaker injection signal intensity, i.e. P_{inj} was not sufficient to modulate the MLLD. Figure 5.8(b) shows the corresponding harmonics generated by the master laser extending up to f_{MLLD}. The first and third harmonics are shown as well as the synchronised signal at 40.5 GHz.

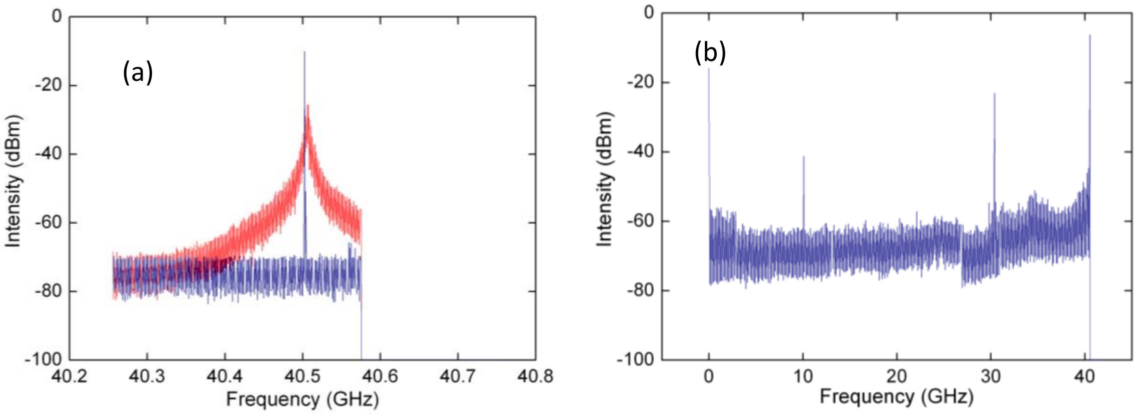

Figure 5.8 (a) RF spectra of the master laser (Pritel 10 GHz pulsed signal) (blue trace) and passive MLLD (red trace), and (b) RF spectra of optically synchronised output showing AM effects.

A second harmonic generation (SHG) autocorrelator was then used to visualise the pulses on a sampling oscilloscope. The traces were scaled such that pulse width and relative peak intensities could be ascertained, which was useful for detecting the presence of AM. Figure 5.9 shows the autocorrelation traces for (i) the free running MLLD (blue trace), (ii) the injected signal at the fourth subharmonic frequency at 13 dBm (red trace), and (iii) the laser under SML using the fourth subharmonic frequency (green trace). These traces have each been independently normalised in the y-axis and are therefore not relatively represented in this direction.

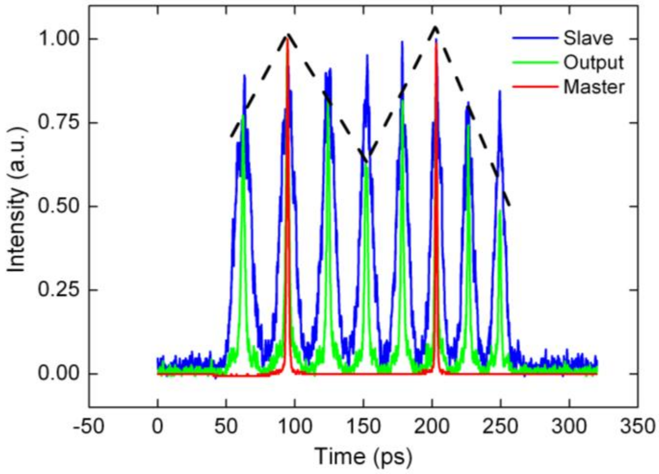

Figure 5.9 Autocorrelation trace of the master laser (red), passive MLLD (blue) and optically synchronised output (green). The black dotted line indicates the peaks of the output trace with AM.

A very distinctive variation in amplitude is depicted in the synchronised output trace; the dashed black line is used to emphasise the peak intensities of the synchronised trace. It is also evident that the peaks are tallest when an injected pulse is encountered. The pulse widths have been reduced from 5 ps (free running) to 1.1 ps (synchronised). The injected pulses were 736 fs after compression. When the injection power was reduced to 3 dBm, the synchronised peaks became consistently planar, i.e. no AM effects were observed (Fig. 5.10(a)).

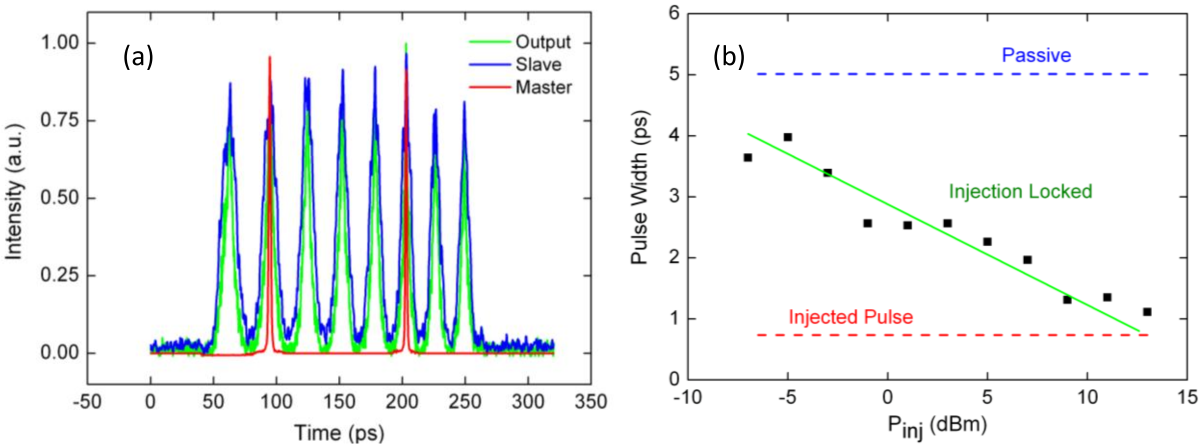

Figure 5.10 (a) Autocorrelation traces with P_{inj} = -5dBm, and (b) pulse widths as a function of P_{inj}.

However, a noticeable widening of the pulse width was evident as the injection power was reduced. This is apparent from the pulse width difference of the output traces in Fig. 5.9 and 5.10(a). Figure 5.10(b) shows the decreasing pulse width trend as the injection power was increased. This is likely to be a result of the weakening cavity resonance effect due to weaker injection intensities, and therefore implies that pulse shaping under the SML technique is, by some means, a stimulated emission related process, contrary to that reported in [7], where it is assumed that the laser itself characterises the pulse features, with the injected signal solely used for providing a clock reference. The arguments against this assumption stem from the following two factors: (i) in [7] the laser was primarily driven by very high subharmonic orders (*40 GHz slave laser locked to a 1 GHz*), and thus the injected signal had a much weaker cavity resonance effect, and (ii) the master laser pulse width in [7] was much larger than that used in this research (*6 ps pulse widths when free running, with 3ps pulse widths from the master laser*), which means pulse narrowing effect was weaker. It is therefore inferred that the pulse width of the injection pulse may contribute to the pulse shaping mechanism within the cavity of the MLLD.

The LR could not be measured using methods previously described in this work due to a limited bandwidth of the RF spectrum analyser (40.57 GHz, shown deliberately in Fig. 5.8(a)). As an alternative, the temporal behaviour was observed via the optical input of a high speed sampling oscilloscope (Agilent Digital Communications Analyser (DCA)). The AC synthesiser used to trigger the master laser was divided to simultaneously trigger the DCA oscilloscope at the same frequency (Fig. 5.11).

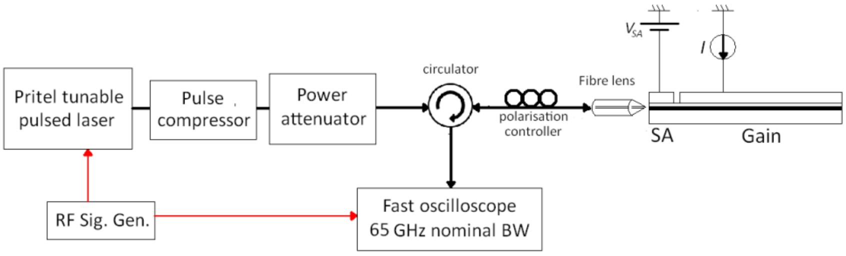

Figure 5.11 Schematic of setup used for SML, with an output viewed directly on an oscilloscope.

The traces observed for a varied P_{inj} are plotted in Fig. 5.12. Due to the limited bandwidth of the oscilloscope, the few picosecond pulse widths were under-sampled and pulse durations appeared longer. However, AM effects were very noticeable, and the results shown here are similar to those observed via the SHG autocorrelator.

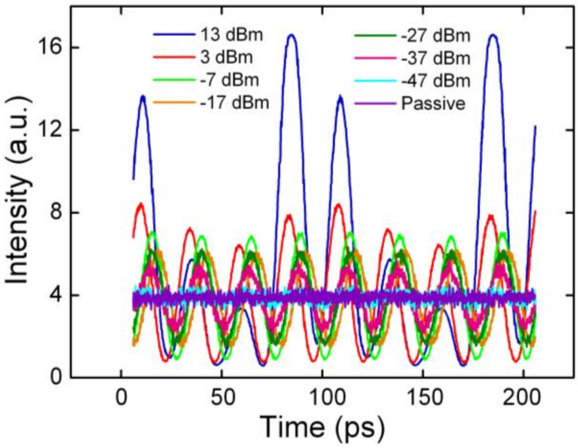

Figure 5.12 Temporal view of pulses as observed on a high speed oscilloscope.

The pulse separation was ~25 ps, which corresponds to a pulse repetition frequency of 40 GHz. A noticeable decline in pulse amplitude was apparent, particularly as P_{inj} was increased. This decline was apparent until P_{inj} was reduced to 3 dBm, where the peaks became much more uniform with little modulation. When P_{inj} fell below -37 dBm, the trace became flat-lined, indicating the MLLD was no longer synchronising to the oscilloscope trigger, and hence the master laser. The LR was then established by varying f_{inj}, and is plotted in Fig. 5.13(a). The minimum and maximum P_{inj} curves are shown to denote the necessary injection power for synchronisation to occur, and prevention of AM, respectively, with a maximum pedestal modulation tolerance of ~30 % (to compensate for the low sampling frequency of the DCA). No pedestal was observed when viewed on SHG autocorrelator with signals lower than ~30% pedestal on DCA, therefore it was assumed that the y-offset shown on the DCA was a result of under sampling.

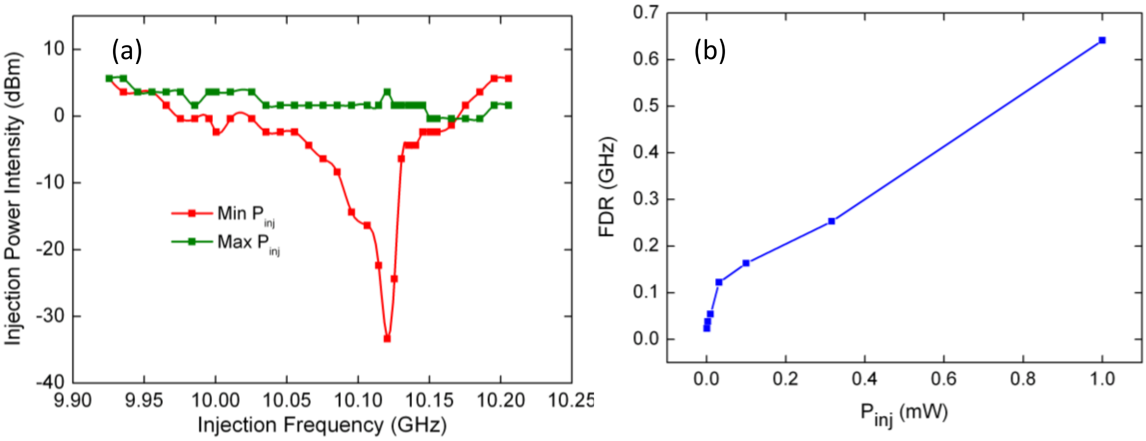

Figure 5.13 (a) Locking range obtained using power parameters (minimum and maximum P_{inj}), and (b) locking range as a function of P_{inj}.

Moreover, a larger P_{inj} will extend the LR [4, 6, 17], and the dependence is linear based on the ratio between the injected and locked repetition rates. This is consistent with the theoretical model derived in [13].

4.1.3 Discussions

It was shown that using the SML technique is highly versatile technique for stabilising the timing jitter of a pulse train emitted from a free running MLLD. The 3 dB linewidth was reduced from 5.9 MHz to less than 100 kHz. Subharmonic frequencies may also be injected; however, higher order subharmonics will cause a reduction in the LR to due fewer temporal components and weaker cavity resonances. A 36 GHz MLLD was injected with 9, 18, and 36 GHz actively locked pulse stream, and the LR was largest when injecting at the fundamental frequency. Injecting into the SA side of a two-section MLLD further increased the LR because of the direct carrier modulation of the SA, which is the primary driving mechanism for SML to occur. It was also found that compression of the pulse width of the injection pulses also enhanced the LR, due to a wider modal overlap of optical frequencies in the spectral domain, thus providing a better coherent interaction between f_{inj} and f_{MLLD}. The pulse width injected can influence the pulse duration of the synchronised pulse (particularly if it is considerably narrower than that of the MLLD), which indicates some contribution to the pulse forming mechanism via the master laser. The injection intensity parameter, P_{inj}, was shown to have a linear dependence on the LR; however, there is an apparent trade-off between P_{inj} and AM particularly when using subharmonic frequency injection.

On the whole, SML is a versatile method of pulse stabilisation. The main advantage is the ability to achieve synchronisation with subharmonic frequencies, which means relatively low frequency electronics can be employed to synchronise high repetition rate MLLDs, which may reduce systems costs considerably. A good example of this can be found in [18], where Arahira et al demonstrated the locking of a 480 GHz laser to a 10 GHz hybrid mode-locked source (described in section 5.2).

On analysis of Arahira's demonstration, a similar experiment was tried using a 140 GHz coupled cavity MLLD to a 10 GHz (corresponding to the 14th subharmonic frequency) actively mode-locked fibre laser as that used in previous experiments. The experimental setup conditions were the same as that shown in Fig. 5, however on this occasion, the RF spectrum analyser was redundant due to frequency restrictions of both the photodiode and spectrum analyser. The pulse period shown on the SHG autocorrelator (Fig. 5.14(a)) and modal spacing of the optical spectrum were then relied on to determine the approximate pulse repetition frequency of the pseudo-140 GHz MLLD, such that the master laser could resonate at a nearby frequency within its LR.

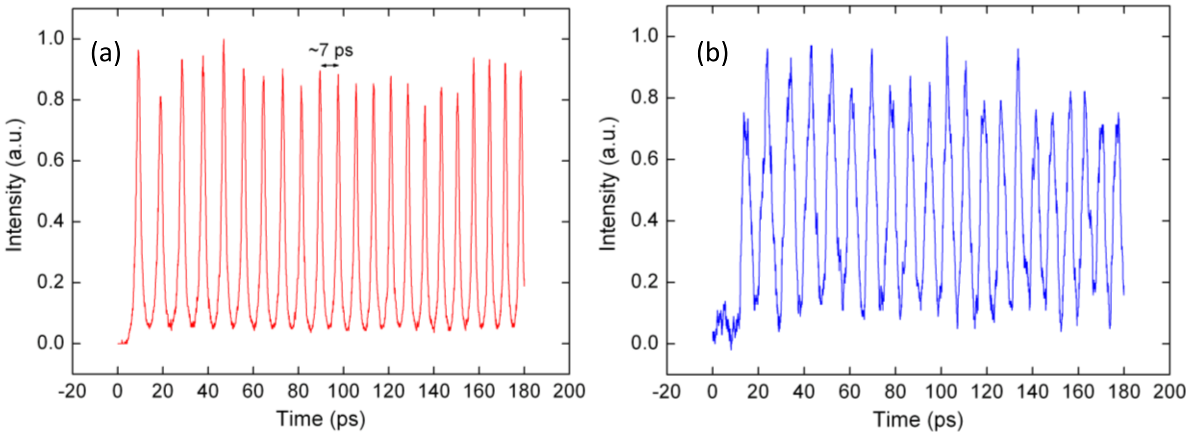

Figure 5.14 (a) Autocorrelation trace of free running MLLD, and (b) MLLD under 14$^{\text{th}}$ subharmonic injection.

The 14th subharmonic of the approximated f_{MLLD} was injected, and resulted in that shown in Fig. 5.14(b). The pulse width became wider as the jitter had increased due to a mismatch in pulse repetition frequencies. Several attempts were made to improve the synchronisation, including detuning of f_{inj} and laser bias parameters, to no avail. The signal was also observed using a high speed sampling oscilloscope, triggered with the same signal as that used to drive the master laser; although the signal remained flat, indicating that no oscillations were occurring at any multiple of f_{inj}. It was then concluded that a more accurate measure of the pulse repetition frequency of the MLLD was required since the subharmonic frequency was of a very high order (m = 14), and thus the LR bandwidth was deemed to be quite narrow. A viable solution in such case is to use frequency mixing, which allows for much higher frequencies to be observed on the RF spectrum analyser by creating beat tones at lower frequencies via cross phase modulation [18].

5.2 Hybrid mode-locking

Rather than carrier modulation by optical pulse injection, the HML technique relies on the application of a high frequency electrical oscillation applied to the SA at the fundamental carrier frequency of the MLLD pulse repetition rate [19-22]. This method does not require an external master laser and is therefore considered a much simpler pulse stabilising approach. HML does however call for careful experimental consideration, particularly at high frequencies where device parasitics may attenuate the RF throughput intensity [21]. It is then important to develop a transmission line circuit to ensure the injection of high frequency RF can be efficiently applied to the device. It has been purported in [19, 22] that HML via subharmonic frequency injection can be applied. This was tried using a 10 GHz RF signal being applied to synchronise a 40 GHz MLLD. Microstrip transmission lines were designed to maximise the throughput intensity of the injected RF signal at 10 GHz. This section will describe the design and performance of the microstrip and its use in subharmonic HML experiments.

5.2.1 Theory of operation

HML is achieved when a reverse bias voltage modulated by an RF electrical signal (f_{RF}) is applied to the SA section at the pulse repetition frequency, or a subharmonic repetition rate such that $V_{SA}(t) = V + A\sin(2\pi f_{RF}t)$, where $f_{RF} = f_{MLLD}/m$. Subharmonic electrical injections signals are able to generate higher order harmonics via the nonlinearities of the laser medium [12]. The oscillation of the absorption of carriers within the SA will then correct the phase timing of the MLLD pulses by articulating the loss modulation within the cavity, thereby synchronising the laser to a stable oscillatory source.

5.2.2 Microstrip transmission lines

Impedance matching become necessary when using high frequency electrical signals above ~100 MHz, as unmatched circuits may result in heavy power attenuations and high back reflections. Transmission lines can be used to minimise these effects. Microstrip transmission lines are particularly attractive since they are compact and relatively easy to design and fabricate. Design parameters are often derived from the translation of a 50 Ω source (Z_S) to a load impedance (Z_L) (e.g. the device under test) which has a real impedance: resistance (R), and the reactive components: capacitance (C), and inductance (L), all of which are resolved by the microstrip transmission line such that most of the signal can propagate through the load and is then suitably grounded.

The SA section of a sample MLLD was reverse biased, and the nonlinear resistance was acquired (Fig. 5.15). Since the SA was most likely to be biased at reverse bias voltages from 2.5 – 3 V (as it is where the laser tends to mode-lock), a resistance of 250 Ω was used as an approximation for the device load R for the transmission line design. Since the reactive components of the device were not measured, only the real impedance was considered as a design parameter (*given the material structure, C was approximated at over 1.3 µF and was therefore deemed negligible as a design parameter*). The microstrip was then modelled and the S-parameters were simulated using Agilent Advanced Design Systems version 2008 modelling tool, with an additional inbuilt S-parameter simulator called Momentum. Two well-known microstrip designs were constructed for matching the impedance of the RF circuit, both using quarter wave tricks, namely: the stub design, and the quarter-wave transformer (QWT) design [23], and each were tested using a network analyser to determine the optimal design to be used for HML.

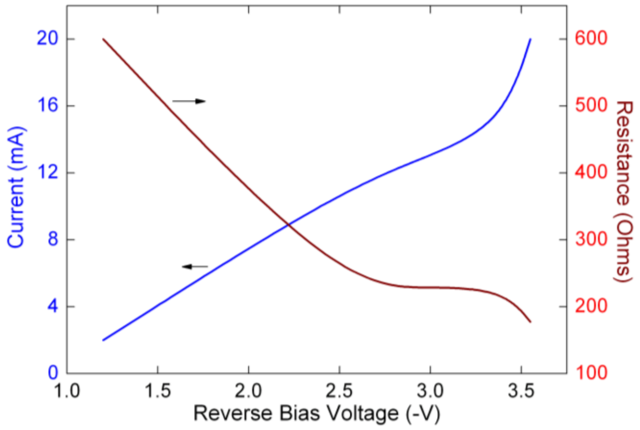

Figure 5.15 Nonlinear SA resistance as a function of bias voltage

The stub design can be described as an open circuit to short circuit transformation (or vice versa) using adjacent microstrip lines, known as stubs, placed at a distance corresponding to a quarter wavelength transmission. Each stub is approximately one quarter wavelength or less in length, and causes a pure reactance at the attachment point at a frequency determined by its width and length. The reactance can be tuned such that the transmission (S_{21}) and reflections (S_{11}) can be optimised at a particular operating frequency. Stub matching is known to be useful when matching a very narrowband circuit, which is why in some cases it is preferred to use multiple stubs to stretch the bandwidth over more frequencies. On the other hand, QWT can be used to transform the impedance of a transmission line to that of the load via a quarter wavelength microstrip using an intermediate strip line which is the geometric mean of the impedances of the load and source, (i.e.$Z_T = \sqrt{Z_L \times Z_S}$). While QWTs are known to provide a wider bandwidth than the stub-based counterpart, there is still a natural bandwidth limitation due to the quarter-wave design being matched only to a single frequency (i.e. the designed quarter wave length will be too short for lower frequencies and too long for higher frequencies). As a solution, QWT can employ multiple intermediate strips at exponential transformations from Z_S to Z_T to increase the bandwidth of transmittance.

The two transmission lines were fabricated using back-to-back designs to test and compare the *S*-parameters, (since analysing the S_{21} parameter requires a two-port model). First, the circuits were designed and fabricated using Rogers® XT/duroid™ 8000 of high frequency, double sided printed circuit boards (PCB). The circuit diagram of the stub matching design is shown in Fig. 5.16. The width (*w*) and length (*l*) of each microstrip line can be seen in the diagram as well as the substrate parameters (*MSub*). Most of the *w* and *l* parameters were calculated using the LineCalc™ tool in ADS, where a quarter wavelength of a particular frequency was converted into stripline dimensions. For example, the first stripline that was calculated was the 50 Ω line, which was positioned on the far left of the design where the substrate could be cleaved so that an SMA adapter could be attached. Since the impedance was known, the *w* could be approximated using [24]:

$$w = \frac{2h}{\pi}\left[\frac{377\pi}{2Z_0\sqrt{\varepsilon_r}} - 1 - \ln\left(2\frac{377\pi}{2Z_0\sqrt{\varepsilon_r}} - 1\right) + \frac{\varepsilon_r - 1}{2\varepsilon_r}\left\{\ln\left(\frac{377\pi}{2Z_0\sqrt{\varepsilon_r}} - 1\right) + 0.39 - \frac{0.61}{\varepsilon_r}\right\}\right] \tag{5.1}$$

where h is the height of the substrate, Z_0 is the characteristic impedance, and ε_r is the relative permittivity of the substrate. And *l* could be approximated using:

$$l = \frac{c}{f\sqrt{\varepsilon_r}} \cdot \frac{1}{4} \tag{5.2}$$

for a quarter wavelength, where *c* is the speed of light, and *f* is the frequency of operation. It can then be inferred from these equations that the length of the microstrip is primarily determined by *f*, whereas the width is a function of Z_0. Using the equations above, the length of a 50 Ω line was estimated at 3.9 mm, and *w* = 1.56 mm, which were very close to the simulated values (*l* = 4.5 mm, *w* = 1.64 mm), optimised using LineCalc™ and the *S*-parameter tuning tool in ADS.

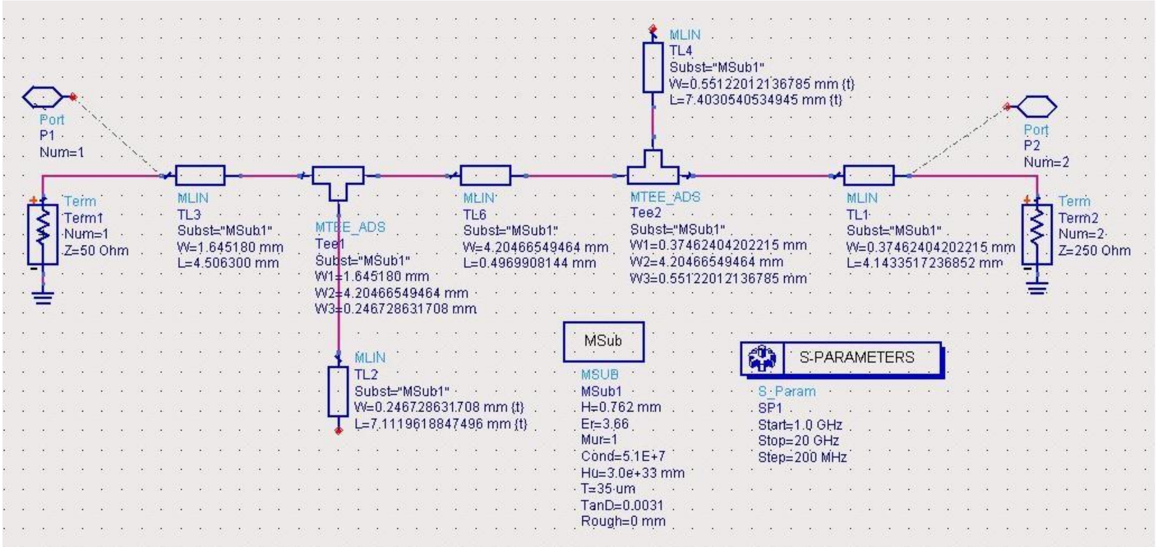

Figure 5.16 Microstrip double stub design layout with stripline and substrate parameters.

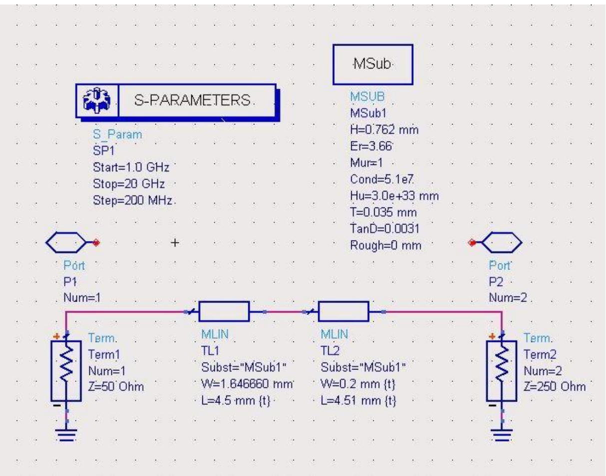

Figure 5.17 QWT design layout using and stripline parameters.

The circuit design for the QWT circuit is show in Fig. 5.17. Two striplines were constructed, a 50 Ω line, and a 111 Ω (-used as an intermediate impedance between the Z_S and Z_L). The S_{11} parameter provided was sufficient in both bandwidth and intensity. A comparison of the simulated and back-to-back experimental *S*-parameter results are plotted in Fig 5.19, preceded by the outlays of the final strip lines in Fig. 5.18.

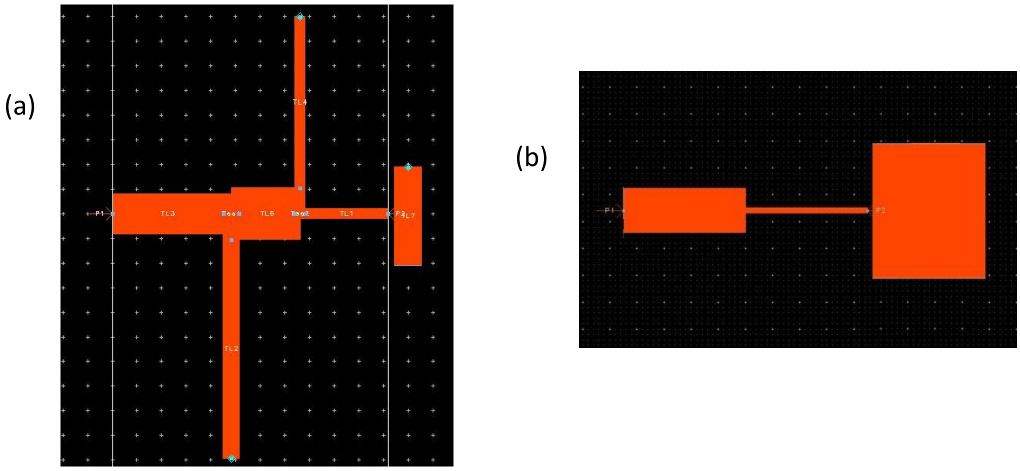

Figure 5.18 (a) Top view of microstrip design, as printed on substrate, (b) QWT design.

The actual results were obtained using a 2-port network analyser. A 5 GHz wide S_{21} transmission is clearly shown in the stub design transition (Fig. 5.19(b)), with a back scattered signal below -20 dB at 10 GHz, and importantly, the experimental results resemble the simulation results (Fig. 5.19(a)). Only a 1 GHz bandwidth was observed using the QWT design, although the back reflections were -25 dB at 10 GHz, providing a much larger transfer of signal intensity than the stub-design counterpart.

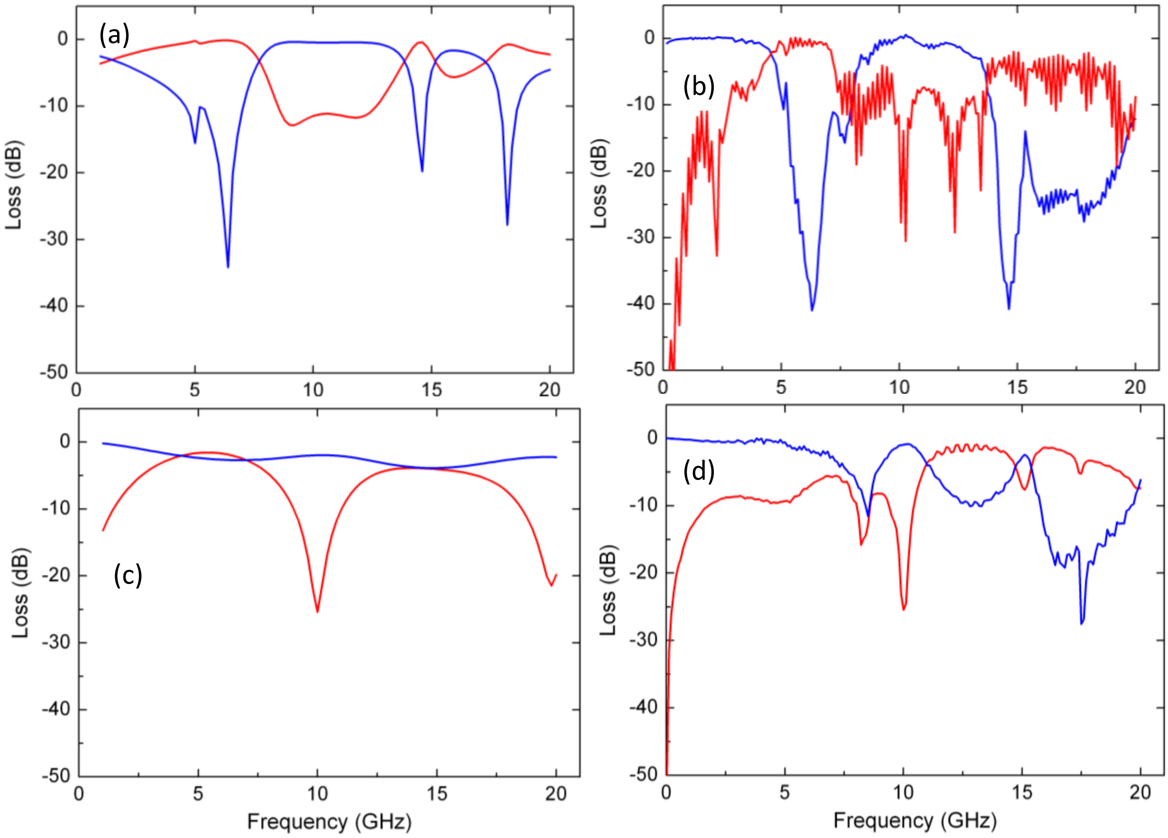

Figure 5.19 (a) Simulated *S*-parameters for stub design, (b) measured *S*-parameters of stub design, (c) simulated *S*-parameters for QWT design, and (d) measured *S*-parameters of QWT design.

After observing the *S*-parameters of both designs, the stub based design was considered for implementation in the HML experiment since the bandwidth was wider. This would allow for greater frequency detuning around the resonance of the MLLD under test. Using a single microstrip, an isolated strip was placed perpendicular to the strip line and was connected to the GND plane via holes through the substrate. A 40 GHz MLLD was then positioned on this section, with the gain side facet facing away from the stripline to provide access for a lensed fibre to accumulate the output light (Fig 5.20). A gold wire bond was then made across the end of the strip line to the SA contact of a device to provide an electrical bridge suitable for RF biasing.

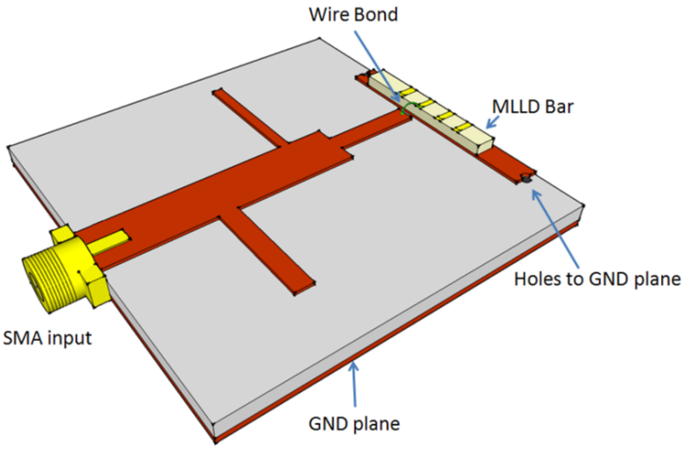

Figure 5.20 Schematic of the microstrip with embedded MLLD for HML applications. A wire bond is made from the end of the strip line to the SA section of the MLLD.

5.2.3 Experiments

The microstrip structure was positioned on a temperature controlled heatsink, which was set to operate at 20°C throughout the experiment. A schematic of the experimental setup is shown in Fig. 5.21. The laser was passively mode-locked at 38.9 GHz, with 2.6 V was applied to the SA and 200 mA to the gain section. A bias-*T* was used to inject a ~10 GHz signal along with the reverse bias to the SA section via the microstrip transmission line. A lensed fibre was used to couple the light from the gain facet of the MLLD, which was then observed on a RF spectrum analyser and SHG autocorrelator.

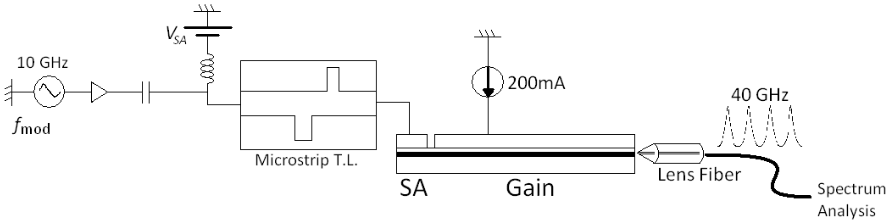

Figure 5.21 Schematic of the HML experiment.

A 9.72 GHz RF signal was injected into the device, corresponding to the fourth subharmonic of the MLLD round trip frequency. A RF amplifier was positioned between the RF source and the microstrip. When the injected power was set to 20 dBm, a peak at 9.72 GHz was observed with a peak power of -70 dBm, which indicates the active modulation of the injected signal (Fig 5.22(a)). However, the RF peak of the MLLD at 39 GHz was reduced to -56 dBm, and no linewidth enhancement was observed, which suggested that mode-locking was being inhibited. This was also confirmed by the autocorrelation measurement (Fig. 5.22(b)). Another peak was presented at 3.9 GHz, which was likely to be the result of *Q*-switching.

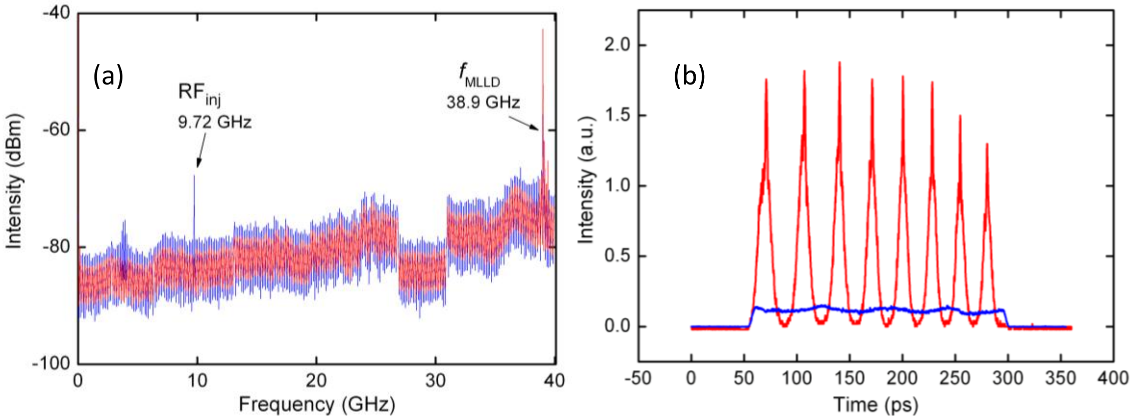

Figure 5.22 (a) RF spectrum of the free running MLLD (red trace) and while under electrical subharmonic injection (blue trace), and (b) the respective autocorrelation traces.

Detuning the RF injection power would increase the passive mode-locking signal until the power fell below 6 dBm, where the RF signal had almost no effect on the mode-locking performance. Attempts were also made to establish synchronisation by directly applying an RF signal to the SA using a high frequency RF probe rather than the microstrip at the second subharmonic signal. However, the unmatched interface between the probe (47 Ω) and device provided further impediments, and the injected signal was attenuated further. It is believed that subharmonic HML is increasingly power demanding, particularly at larger subharmonic orders since the sinusoidal RF wave is required to lock to a signal which overlaps several resonances, causing temporal instabilities. The findings in [20] suggest that a larger RF power (~23 dBm) is required when using subharmonic RF injection. It was also suggested that using higher order subharmonics ($m > 3$) caused stability issues and tended to result in self-pulsation, which is similar to that observed in this work. This is likely to be attributed to the RF driving frequency approaching the relaxation frequency of the laser.

Therefore, for synchronisation to occur, it was necessary to use either a higher RF frequency injection or a slower pulse repetition rate laser. By tuning the bias of the laser, such that the gain was ~ 108mA and -1.1 V was applied to the SA section, a region of pure and passive *Q*-switching was apparent. The RF frequency was stable at 3.8 GHz, and this oscillation was then synchronised to an RF clock, operating at the same frequency. The RF signal power was set at -15 dBm. Figure 5.23(a) shows the RF frequency spectrum when passively *Q*-switched, and Fig. 5.23(b) shows the resonances with the fundamental frequency excited.

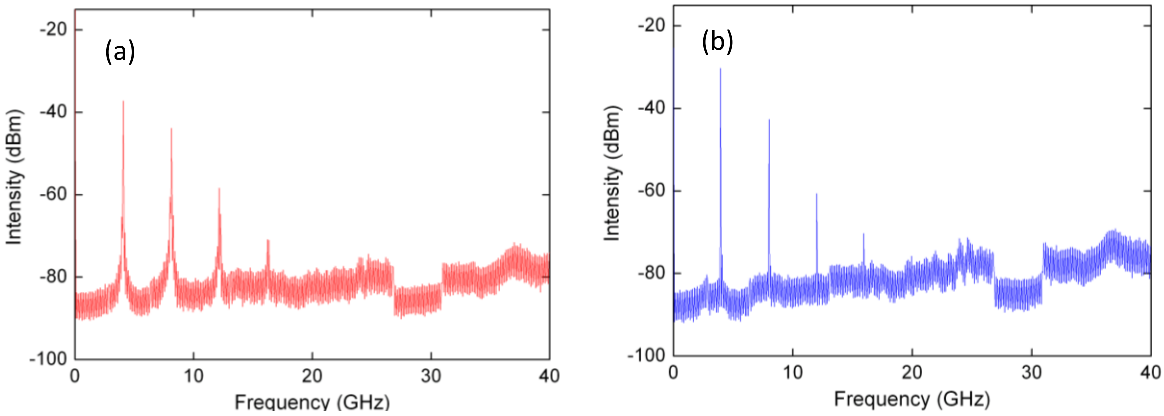

Figure 5.23 (a) RF spectrum of passive MLLD operating in Q-switched mode (red trace), and (b) while under electrical injection at the fundamental carrier frequency (blue trace).

The spectra were both free from any mode-locking peaks. The application of the electrical oscillation at the fundamental *Q*-switched frequency would greatly enhance the linewidth by enforcing a strict oscillation of the pulse frequency. The linewidth was reduced from 6.5 MHz to 1 kHz. Figure 5.24 shows the effect of detuning the electrical signal around the fundamental frequency.

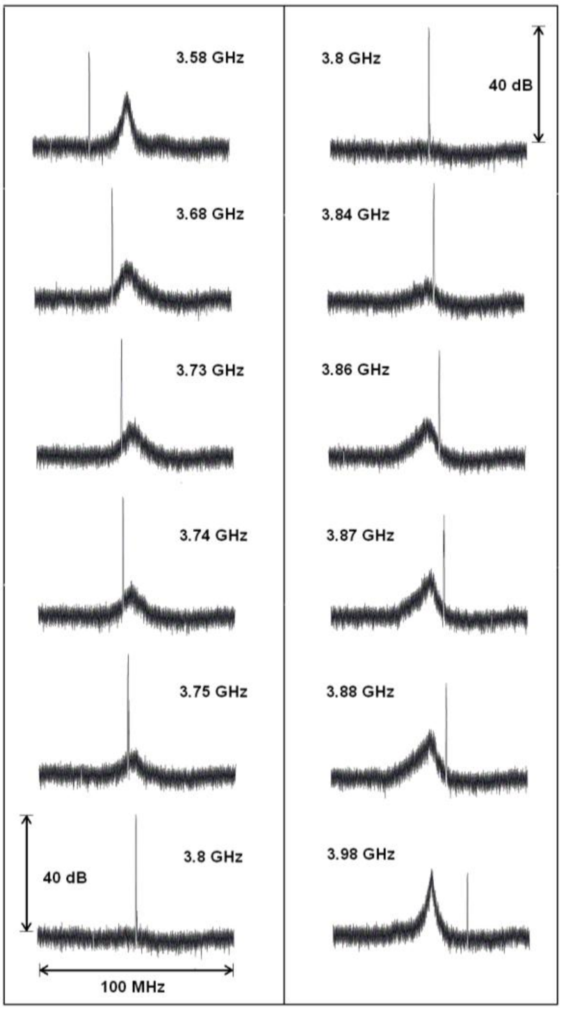

Figure 5.24 Frequency detuning of the *Q*-switched MLLD. The narrow peak indicates the RF signal.

The LR over which the electrical signal would lock with the *Q*-switched laser was 70 MHz at an injection power of -15 dBm. As the injection power was increased, so too was the LR, as shown in Fig. 5.25. Using a maximum injection power of 10 dBm, a locking rage of 819.18 MHz was observed. Since the laser was *Q*-switching, the LR was much wider than that achievable when mode-locked. This is due to wider tunability of the *Q*-switched laser due to index changes by carrier injection [25].

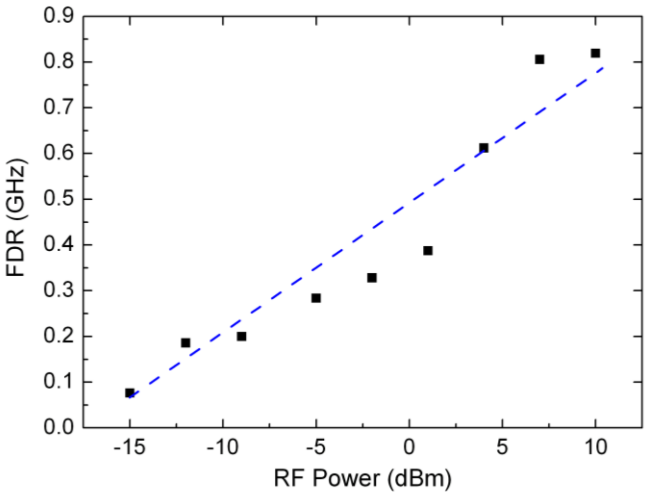

Figure 5.25 Locking range as a function of RF power injected into the MLLD.

5.2.4 Discussions

Microstrip transmission lines were designed using two different impedance matching topologies, stub-matching and QWT, to transform the resistance of a 50 Ω source to that of an SA section of a 40 GHz MLLD. The *S*-parameters were optimised to minimise back scattering (S_{11}) of the injected signal by over 20 dBm at 10 GHz, while maximising the throughput intensity (S_{21}). Of the two designs, double stub-matching was shown to provide the largest bandwidth, and was thus implemented to perform the HML experiments. The MLLD was embedded onto the microstrip substrate and was able to passively mode-lock at 38.9 GHz, however, the application of an RF signal at the fourth subharmonic frequency was shown to impede the mode-locking effects due to weak harmonic generation of the injected electrical signal, which instead gave rise to self-pulsation effects of the laser due to the close proximity of the relaxation oscillation.

It was therefore concluded that either a higher frequency injection signal was required or a slower repetition rate laser, such that the frequency difference between the generated higher order harmonics were minimised. The MLLD was then operated to provide a 3.8 GHz *Q*-switched oscillation, which was stabilised by injection of an RF signal at the fundamental frequency. The *Q*-switched signal linewidth was subsequently enhanced from 6.5 MHz to less than 1 kHz. The LR was 70 MHz when the RF input power was -15 dBm, which was increased to over 800 MHz as the power was increased.

In retrospect, much improved *S*-parameters could have been obtained using better impedance matching techniques, such as the de-embedding method referred to in [26]. In this reference, the authors used a standard 50 Ω microstrip transmission line with the device embedded as the load with a mesh wire bond connecting the signal plane to the p-contact of the device, An RF signal was then applied through the transmission line and the *S*-parameters analysed on a network analyser smith chart to acquire the precise impedance at the frequency of interest, including the parasitic effects presented within the device. This is ideal as it provides a more accurate indication of the device properties as well as other peripheral impedances such as the substrate height differences and wire bond (which were neglected in this experiments transmission line analysis) which can then be used to match and model the transmission line designs accordingly. In this work, only the DC resistance of the device was characterised due to the limited availability of devices for the experiment, and all complex (reactive) components at the RF drive frequency were neglected. This would undoubtedly lead to some losses and reflections of the RF signal at the device interface, particularly as the frequency is increased.

In any case, there was sufficient RF signal travelling through the laser at the driving frequency in the HML experiment, as indicated by the RF spectrum in Fig. 5.22(a), and this is likely to be a result of an adequate microstrip impedance matching design, which is predominantly determined by the transmission line length (corresponding to a quarter-wave of the drive frequency), and a width somewhat corresponding to the impedance, which in this case was reasonably close enough to the real impedance of the laser to provide some modulation. Improving the transmission line design may have increased the throughput of the RF signal, thus maximising the power transfer, but achieving a modulation at the fourth harmonic (40 GHz) is likely to remain a challenge due to the sinusoidal nature of the signal. These issues should be adequately addressed for this application to work successfully.

It is now commonplace to minimise the frequency of the electrical injection for optical applications for the sake of costs and manageability. For this reason, HML is not considered for pulse stabilisation at high repetitions rates. However, HML at lower frequencies can be useful when used as a master laser to serve as an on chip clock, and to even provide optical pulses to perform subharmonic SML [27]. This could provide adequate jitter and phase noise reductions of multiple integrated MLLDs and other electro-optic components, providing reductions in cost and system complexity.

5.3 Noise reduction via optical feedback using a fibre loop

There have been several recent reports of regenerative feedback systems used to stabilise the jitter and linewidth of a MLLD. These are based on using a delayed signal from the laser itself as a phase reference, which can provide significant improvements in both linewidth and jitter. For example, in [28] an electrical feedback loop was employed to provide a self-phase referencing mechanism for a MLLD, in which the intensity profile of a pulse was extracted via the photocurrent from the *P*-contact of the SA section, and was then amplified and refined using high-*Q* RF filters before being fed back into the absorber at a 2π, or an equivalent phase shift. This technique is called regenerative mode-locking, and similar arrangements are shown in [28-35]. In terms of phase noise and jitter performance at 40 GHz, the electrical regenerative mode-locking method was shown to be similar to that of actively mode-locked lasers (via HML) [28]. This technique is however limited to operate within the finite bandwidths imposed by electrical components, and so using this technique at higher frequencies (>100 GHz) may become very expensive and intricate to perform.

In [36], K. Mergham, et al. proposed an all-optical regenerative noise reduction method based on external feedback into a 17 GHz quantum-dash MLLD. The stability of the laser was improved and a RF linewidth of 500 Hz was observed over a wide biasing range, although the use of an external fibre cavity produced additional RF resonances due to superfluous modal interactions, giving rise to large amplitude and phase fluctuations separated in frequency by a distance corresponding to the length of the external fibre cavity. More recently however in [37], C. Lin, et al. used a similar method, in which the linewidth of a 5.1 GHz quantum dot based passive MLLD was characterized under resonant feedback via an optical fibre. An RF linewidth of 350 Hz was achieved, although this required a dielectric coated fibre with high reflectivity in order to induce the feedback and precise external cavity length matching. Such low linewidths and jitter could be used to drive high speed optoelectronic oscillators (OEOs), however, this method can also become increasingly intricate to carry out when using high repetition rate lasers, since alignment tolerances of the external mirror become much more stringent.

Upon studying OEOs, it is understood that storing the energy of a laser could provide better enhancements of the *Q*-factor, and hence the linewidth of the RF signal [38]. This can also be applied to MLLDs using an optical feedback loop (OFL) via optical fibre, such that the phase memory of the pulses is extended, and therefore the noise and jitter can be reduced. To investigate this effect, an experiment was carried out using an OFL, where a length of optical fibre was used to relay the output pulse stream of the laser back into the SA facet of the MLLD to induce a self-intensity beating, and thus, self-phase referencing of the pulses. This allows the memory of the phase to increase, which reduces the noise in the laser. The main advantage of this technique is that it is not limited to the bandwidth restrictions imposed by electrical components and can therefore be scaled to operate at much higher pulse repetition frequencies.

5.3.1 Experiments

Figure 5.26 shows a schematic of the experimental setup used to carry out the OFL delay line method. The laser was a 40 GHz two-section MLLD, fabricated on a five-QW *AlGaInAs/InP* epitaxial structure. The output of the laser was coupled into a lensed fibre, which was fed through a circulator to minimise back reflections from component interfaces. The signal was then fed into a dispersion shifted erbium doped fibre amplifier (EDFA) before being coupled back into the SA end of the MLLD cavity. A polarisation controller was positioned to ensure the injected signal was TE polarised in order to promote better carrier coupling effects in the QWs. A 3 dB fibre splitter was used to form an output arm for subsequent signal and spectral analysis. The total length of the fibre loop was ~ 20 m.

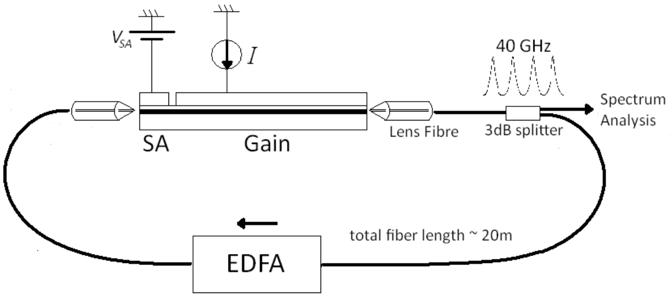

Figure 5.26 Schematic of the experimental setup used to implement the OFL technique.

Given the length of single mode fibre (SMF) used in this experiment, chromatic dispersion would inevitably play a critical role. It was noted that the length of SMF would impose restrictions on the maximum pulse repetition frequency attainable using the OFL delay (i.e. while longer lengths of fibre will improve the *Q* of the signal, thereby reducing the linewidth, the pulse width is subsequently affected as a result of chromatic dispersion); therefore a trade-off is enforced between the amount of linewidth enhancement and pulse repetition frequency. This can be resolved using dispersion shifted/compensating elements along the propagation path length while maintaining the linewidth and jitter reductions of the signal. In this experiment, ~20 m of fibre was used, of which ~11 m was dispersion shifted via the EDFA, resulting in a total dispersion of approximately 194 fs/nm.

The laser was passively mode-locked when the gain section was forward biased with 53 mA and the SA section was reverse biased with 2.3 V. The resulting output as viewed on a RF spectrum analyser via a high speed photodetector (matched up to 45 GHz) is shown in Fig. 5.27 (red dashed trace). The 3 dB linewidth was 1.6 MHz (10 kHz RBW, 1 kHz VBW), with a single-side-band (SSB) phase noise of 67 dBc/Hz at a 1 MHz offset. The corresponding RMS timing jitter was 8 ps (integrated from 10 kHz – 100 MHz). For a direct comparison, the linewidth at the output of the OFL is also shown in Fig. 5.27 (blue trace), with the MLLD operating under the same conditions. The EDFA was adjusted to supply enough gain to compensate for the losses in the delay system. A noticeable reduction of the linewidth was observed at the centre frequency, which was reduced to less than 20 kHz, with a phase noise of 96 dBc/Hz at a 1 MHz offset, and an RMS jitter of 650 fs. The pulse width, measured using a second harmonic generation (SHG) autocorrelator, was 1.2 ps (assuming a sech^2 pulse shape) while free running, and 2.1 ps at the output of the OFL. This broadening was due to chromatic dispersion in the optical fibre used in the experiment, other than that of the EDFA. The average output power of the signal from the fibre loop was 4 mW.

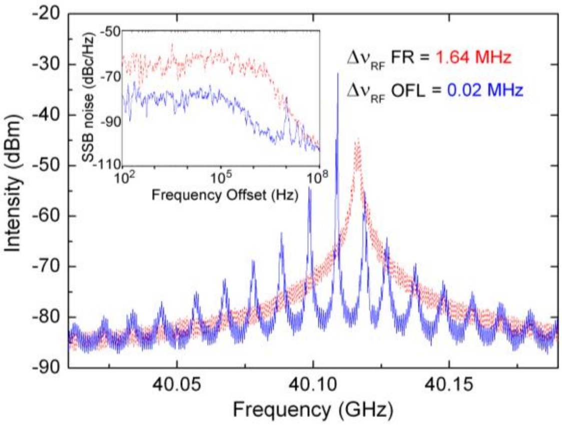

Figure 5.27 Main: RF spectrum after propagating through the OFL (blue trace) and free running (FR) (red dotted trace). Inset: Corresponding phase noise measurements.

Although the linewidth was significantly enhanced, some additional supermode noise spurs were observed, similar to those in [36], which are due to harmonic mode-locking effects [39]. These were formed by modal interactions of the fibre cavity resonance, which gave rise to large amplitude and phase fluctuations separated in frequency at ~10 MHz intervals, determined by the fibre cavity length. Increasing the EDFA gain resulted in a further increase in the supermodes, due to the larger signal propagating around the fibre loop. A substantial increase in the EDFA gain (> 5 dB) would eventually degrade the signal such that the autocorrelation trace of the emitted pulse train was distorted. This may be due to the coherence collapse regime [40], which is the dominating influence of spontaneous emission in the system by the increasing fluctuations stimulated by the loss of coherence. This severely degrades the mode-locking performance by disturbing the phase locking relations between the longitudinal modes.

There are a number of methods used to suppress the supermode noise, such as those used in harmonically mode-locked fibre lasers [41-50]. In this work, the composite cavity loop (CCL) technique was used (see Fig. 5.28(a)) [45-48]. A CCL is formed using a sub-cavity within the OFL, such that its associated modes coincide with the fundamental fibre cavity modes at large multiples of the free spectral range (FSR). This reduces the number of modes in the fibre cavity, thereby lessening the effect of supermode noise. A schematic representation of the modal alignment is shown in Fig. 5.28(b), which also depicts the noise reducing effects during feedback. For this configuration, a 20 GHz MLLD fabricated on a three-QW *AlGaInAs/InP* material structure (see chapter 2) was used to test the repeatability of the OFL delay line technique, while being observable on the RF spectrum analyser (which was limited to 40 GHz). Two 3 dB couplers were used to form a composite cavity (inner loop). Moreover, a dispersion shifted fibre (DSF) was added to the outer loop to maximise the fibre length without compromising the dispersion. The total length of the outer loop was ~66 m. A tunable delay line was added to the inner loop for accurate mode alignment. And finally an attenuator was positioned after the second coupler to control the feedback intensity.

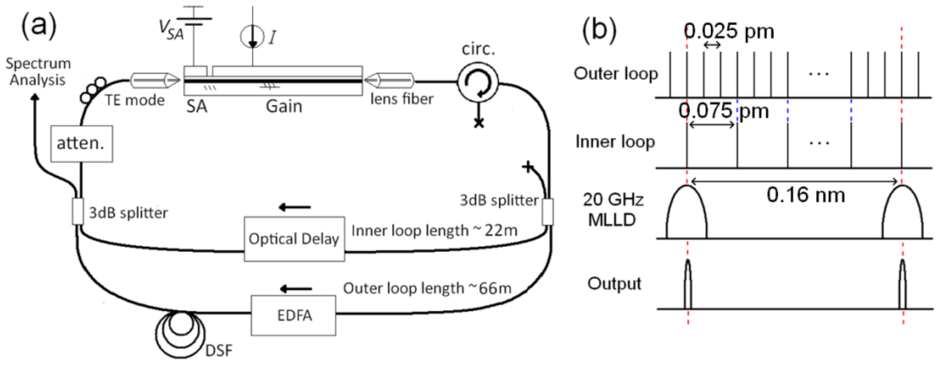

Figure 5.28 (a) Experimental configuration of the dual optical feedback loop. (circ.: optical circulator, atten.: optical attenuator), and (b) schematic diagram representing the alignment of modes in outer loop, inner loop, MLLD, and resulting output.

The laser was passively mode-locked when 80 mA was applied to the gain section, and -2.8 V was applied to the SA. The pulse width was measured as 900 fs, with an optical bandwidth of 6.2 nm (Fig. 5.30(c) and (d) – red traces). The total average output power was 1 mW. Figure 5.29 shows a comparison of the level of supermode noise extremities as the CCL length was tuned. When the CCL length was optimized to ~22 m (corresponding to an overlap of every third mode of the fundamental fibre cavity loop, as shown in Fig. 5.28(b)), the peak powers of the supermodes were reduced from ~ -80 dBm to less than -110 dBm. The 3 dB linewidth of the signal was measured at 192 Hz, with a phase noise of -113 dBc/Hz at a 1 MHz offset (blue solid trace in Fig. 30(b)), whereas that of the free running MLLD was 155 kHz (20 Hz RBW, 10 Hz VBW), with a phase noise of -77 dBc/Hz at a 1 MHz offset. The RMS jitter was reduced to as little as 340 fs (integrated from 10 kHz – 100 MHz); a significant improvement from that of the free running MLLD (4.7 ps). The difference in the phase noise characteristics of the 40 GHz and 20 GHz laser can be justified by the following factors: (i) The phase noise is directly proportional to the round trip frequency of the laser, as described in [2], and (ii) since the number of QWs in the 20 GHz laser was reduced from five to three, the spontaneous emission factor was reduced, leading to a reduction in phase noise when passively mode-locked [51]. The pulse width was 2.1 ps, which was again somewhat broader than that of the free running MLLD, with a 1.2 ps increase in pulse width as a result of dispersion in the fibre (Fig. 5.30(d)). The optical spectra, with and without the optical delay are shown in Fig. 5.30(c).

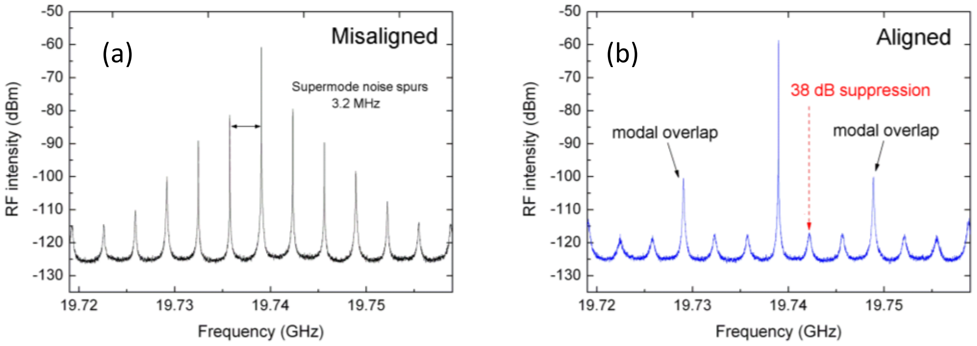

Figure 5.29 (a) Maximum and (b) minimum supermode noise.

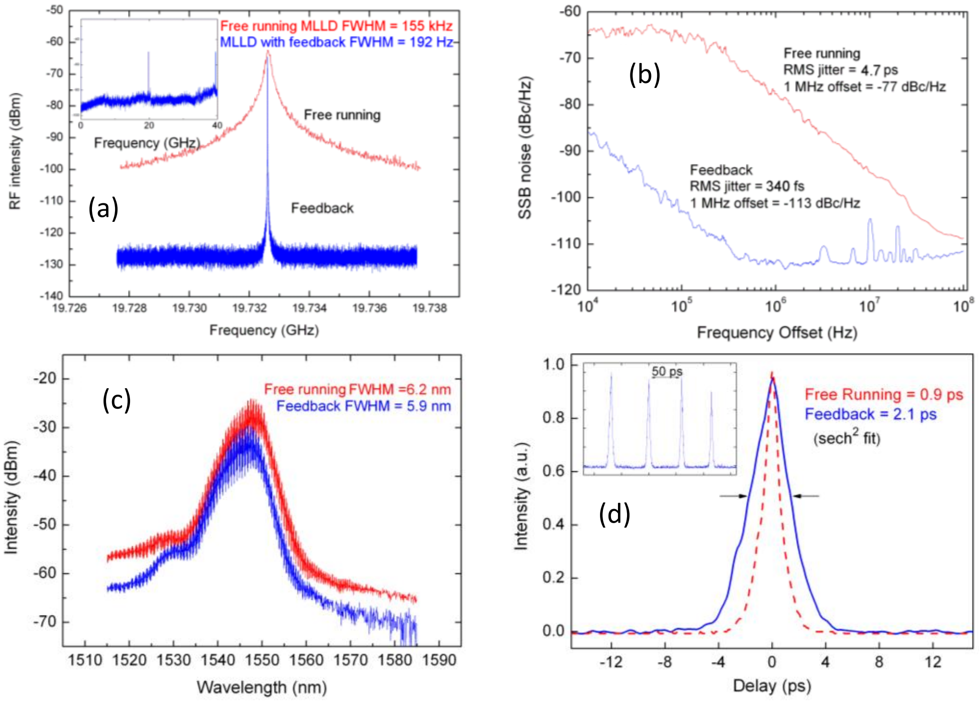

Figure 5.30 (a) The RF spectrum of the signal after supermode noise suppression, (b) SSB phase noise of the free running MLLD (red dashed trace), and while propagating through the OFL with supermode noise suppression (blue solid trace), (c) optical spectrum of the free running MLLD (red trace), and after OFL (blue trace), and (d) autocorrelation trace of the free running (red dashed trace), and at the output of the OFL (blue trace).

From general oscillator theory it is known that as the length of the delay is increased, so too is the *Q*-factor of the oscillator, which reduces the RF linewidth accordingly. This effect was studied by interchanging the DSF lengths in this experiment to provide a comparison of the RF linewidth using 28.5 m, 39.9 m, 51.1 m, and 66 m long fibre loop cavities. To ensure the intensity was uniform across all measurements, the inner composite cavity loop was removed and the signal intensities were matched at -26 dBm at the interface between the attenuator and lensed fibre. The results are plotted in Fig. 5.31. The narrowest linewidth (432 Hz) was acquired using a 66 m long fibre, whereas the widest linewidth (3.628 kHz) was measured using a 28.5 m long fibre. These results are consistent with the model in [52], which supports that the linewidth is proportional to 1/*L* (where *L* is the fibre length).

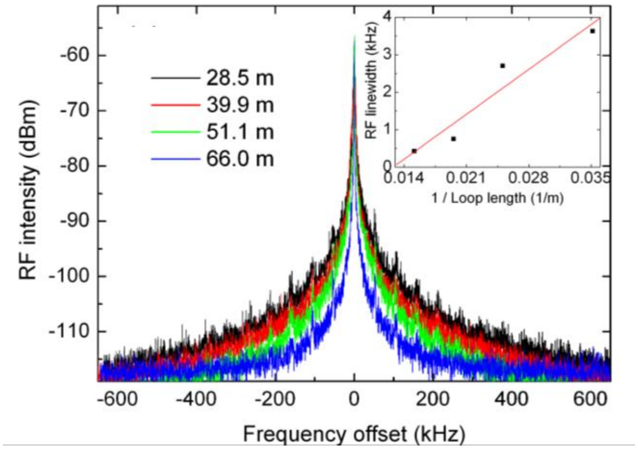

Figure 5.31 RF spectra of MLLD signal with feedback using different fibre lengths. Inset: RF linewidth vs. inverse feedback loop length (1/*L*) measured with a feedback signal intensity of -26 dBm (black squares); corresponding linear fit (red),

Furthermore, it is evident that the RF linewidth increased as the feedback power was reduced. Figure 5.32 shows the relationship between feedback power and linewidth. The lowest RF linewidths were obtained at the maximum feedback value, which was limited to -26 dBm in these experiments. As the feedback intensity was reduced, the linewidth was gradually increased to ~6 kHz until the feedback intensity fell below ~-40 dBm, at which point the linewidth increase was more sudden and tended towards that of the MLLD without feedback, indicating the lowest intensity required to sufficiently reduce the linewidth. This is consistent with the results obtained in [36] and [37]. At feedback levels below -34 dBm, some discrepancies were observed in the 1/*L* trend, which are due to the feedback intensities approaching their lower limit.

Finally, it is worth noting that the long term stability of the proposed system is inhibited due to mechanical and thermal instabilities in the fibre causing small changes in the optical path length over time. Since no cavity length stabilisation was in place, the supermode noise suppression via CCL was established only for a few minutes until retuning of the cavity length was required. This will become increasingly problematic when using longer lengths of fibre; however, the use of a dynamic differential feedback mechanism, as shown in [46] and [53], may be used to counteract the path length changes and greatly improve the stability of the system.

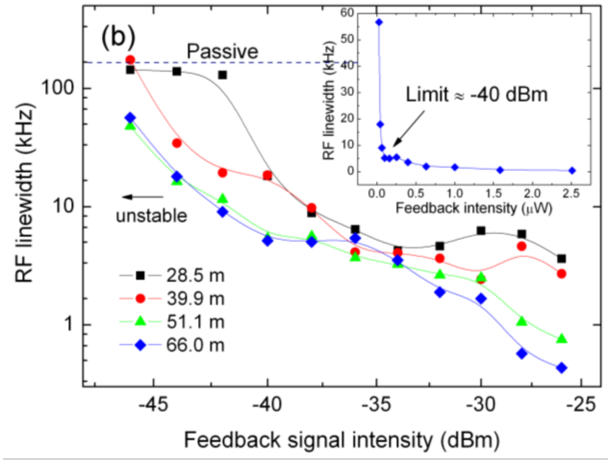

Figure 5.32 RF linewidth values of MLLD with feedback as a function of the feedback signal intensity plotted in a logarithmic scale using for different fibre lengths (listed in figure). Inset: RF linewidth vs. feedback intensity plotted in a linear scale for 66 m long fibre loop.

5.3.2 Discussions

To summarise, a novel method of reducing phase noise and linewidth of a passively operating MLLD using feedback via an optical delay line was described, resulting in an extremely low linewidth (192 Hz) and subpicosecond RMS jitter (340 fs, integrated from 10 kHz – 100 MHz) of a 20 GHz laser. A CCL structure was incorporated into the experimental setup to reduce the effects of supermode noise and further reduce the timing jitter. The technique was also shown to work on a 40 GHz MLLD and has the potential to operate at much higher pulse repetition frequencies. Further improvements of the linewidth and phase noise may be provided by employing longer fibre cavity lengths (although within the coherence limit), thereby extending the memory of the phase and providing further linewidth enhancements. Future work may include the monolithic integration of a waveguide loop design with a MLLD for on-chip linewidth refinements, which may be promising for the development of compact, low cost and low noise integrated system clock.

5.4 Chapter Summery

Three techniques for stabilising the jitter of a passively operating MLLD were described and investigated: Synchronous mode-locking (SML), hybrid mode-locking (HML), and self-stabilisation using an optical feedback loop (OFL). SML was shown to be the most versatile method of synchronising the pulse oscillations since the locking parameters were more tunable owing to the adjustability of the master laser source. A large LR was observed (~600 MHz) without amplitude modulation effects using the fourth subharmonic frequency at ~0 dBm. The pulse width was shown to reduce with increasing amplitude intensity of the injected signal; however, amplitude modulation effects were present at higher injection intensities. Nonetheless, there are a variety of uses for SML in optical systems, including on-chip clock distribution, all-optical switching, wavelength conversion, signal triggering, and frequency multiplexing.

HML was carried out using an electrical signal applied directly to the absorber of the MLLD via a customised microstrip transmission line to synchronise the phase of the pulses to that of an external clock. Unfortunately, synchronisation of the fundamental round trip frequency was not achieved due to weak harmonic generating effects of the optical signal. HML was shown to require high power and strict harmonic matching, and therefore is not suitable for providing stability at very high frequencies (> 100 GHz) due to electrical bandwidth limitations. Instead, SML via a laser stabilised by HML is an ideal option, where an optical pulse train generated at a lower order harmonic (via HML) is used to stabilise a MLLD at the *n*th multiple of the repetition frequency. On its own however, HML may be useful for pulse phase modulation, (see Chapter 7). HML using a microstrip for high frequency impedance matching is also useful as a low-cost and compact packaging option.

Self-stabilisation via an OFL was carried out at 20 and 40 GHz, and was shown to perform exceptionally well at reducing the phase noise and linewidth of a MLLD. Subpicosecond jitter values were obtained with sub kHz RF linewidths, due to the phase memory extension and greater energy storage using a fibre loop. While supermode noise spurs were apparent, raising the phase noise at large frequency offset values, a composite cavity loop was added to the system to counteract the additional resonances. An attempt at integrating a loop design with a MLLD may be promising for on-chip system clocking. Other uses of the OFL technique may include RF frequency combing, clocking and clock recovery and optoelectronic oscillation generation.

5.5 References

[1] R. Paschotta, A. Schlatter, S. C. Zeller, H. R. Telle, and U. Keller, “Optical phase noise and carrier-envelope offset noise of mode-locked lasers,” App. Phys. B, 82, pp 265-273, 2006.

[2] C. H. Henry, “Theory of the Linewidth of Semiconductor Laser,” IEEE J. Quant. Electron., vol. QE-18, No. 2, pp 259 – 264, 1982.

[3] A. Nirmalathas, H. F. Liu, Z. Ahmed, D. Novak, and Y. Ogawa, “Subharmonic Synchronous and Hybrid Mode-Locking of a Monolithic DBR Laser Operating at Millimeter-Wave Frequencies,” IEEE Photon. Technol. Lett., Vol. 9, No. 4, pp 434-436, 1997.

[4] V. B. Khalfin, J. M. Arnold, and J. H. Marsh, “A Theoretical Model of Synchronization of a Mode-Locked Semiconductor Laser with an External Pulse Stream,” IEEE J. Select. Top. Quant. Electron., Vol. 1, No. 2, pp 523-527, 1995.

[5] A. Nirmalathas, H. F. Liu, Z. Ahmed, D. Novak, and Y. Ogawa, “Subharmonic Synchronous Mode-Locking of a Monolithic Semiconductor Laser Operating at Millimeter-Wave Frequencies,” IEEE J. Select. Top. Quant. Electron., Vol. 3, No. 2, pp 261-269, 1997.

[6] Z. Ahmed, H. F. Liu, D. Novak, Y. Ogawa, M. D. Pelusi, and D. Y. Kim, “Locking Characteristics of a Passively Mode-Locked Monolithic DBR Laser Stabilized by Optical Injection,” IEEE Photon. Technol. Lett., Vol. 8, No. 1, pp 37-39, 1996.

[7] H. Kurita, T. Shimizu, and H. Yokoyama, “Experimental Investigations of Harmonic Synchronization Conditions and Mechanisms of Mode-Locked Laser Diodes Induced by Optical Pulse Injection,” IEEE J. Select. Top. Quant. Electron., Vol. 2, No. 3, pp 508-513, 1996.

[8] M. Attygalle, A. Nirmalathas, H. F. Liu, and D. Novak, “Injection Signal Wavelength Dependence of a Subharmonically Synchronous Mode-Locked Monolithic Semiconductor Laser,” Conf. Proc. on Optoelectron. and Microelectron Material Devices 1998, pp 206-208, 1999.

[9] S. Arahira, and Y. Ogawa, “Synchronous Mode-Locking in Passively Mode-Locked Semiconductor Laser Diodes Using Optical Short Pulses Repeated at Subharmonics of the Cavity Round-Trip Frequency,” IEEE Photon. Technol. Lett., Vol. 8, No. 2, pp 191-193, 1996.

[10] E. A. Avrutin, J. M. Arnold, J. H. Marsh, “Analysis of dynamics of monolithic passively mode-locked laser diodes under external periodic excitation,” IEE Proc. Optoelectron., Vol. 143, Issue 1, pp 81-88, 1996.

[11] H. L. Stover, and W. H. Steier, “Locking of Laser Oscillators by Light Injection”, App. Phys. Lett., Vol. 8, No. 4, pp 91-93, 1966.

[12] A. Nirmalathas, H. F. Liu, D. Novak, Z. Ahmed, and Y. Ogawa, “Comparison of Subharmonic Synchronous Mode-locking with Subharmonic Hybrid Mode-locking of a Monolithic DBR Laser Operating at Millimeter Wave Frequencies,” International Topical Meeting on Microwave Photon., TH1-4, 1996.

[13] M. Margalit, and M. Orenstein, “Multimode Effects on the Evolution and Long-Term Stability of a Passively Mode-Locked Laser Under Pulsed Injection Locking,” IEEE J. Quant. Electron., Vol. 33, No. 5, pp 710-718, 1997.

[14] S. Arahira, and Y. Ogawa, “High-repetition-rate optical pulse generation and control techniques,” Measurement Science and Technol., Vol. 13, No. 11, pp 1664-1670, 2002.

[15] M. Margalit, M. Orenstein, and H. A. Haus, “Injection Locking of a Passively Mode-Locked Laser,” IEEE J. Quant. Electron., Vol. 32, No. 1, pp 155-160, 1996.

[16] M. Attygalle, A. Nirmalathas, and H. F. Liu, “Novel Technique for Reduction of Amplitude Modulation of Pulse Trains Generated by Subharmonic Synchronous Mode-Locked Laser,” IEEE Photon. Technol. Lett., Vol. 14, No. 4, pp 543-545, 2002.

[17] E. A. Avrutin, V. B. Khalfin, J. M. Arnold, and J. H. Marsh, “Time- and frequency-domain theory of externally synchronised operation of a passively mode-locked laser diode,” Conf. on Lasers and Electro-Optics Europe (CLEO) 1994, CTuE6, 1994.

[18] S. Arahira, and Y. Ogawa, “480-GHz Subharmonic Synchronous Mode Locking in a Short-Cavity Colliding-Pulse Mode-Locked Laser Diode,” IEEE Photon. Technol. Lett., Vol 14, No. 4, pp 537-539, 2002.

[19] T. Hoshida, H. F. Liu, M. Tsuchiya, Y. Ogawa, and T. Kamiya, “Extremely Low-Amplitude Modulation in a Subharmonically Hybrid Mode-Locked Monolithic Semiconductor Laser,” IEEE Photon. Tech. Lett., Vol. 8, No. 9, pp 1160-1162, 1996.

[20] T. Hoshida, H. F. Liu, M. Tsuchiya, Y. Ogawa, and T. Kamiya, “Subharmonic Hybrid Mode-Locking of a Monolithic Semiconductor Laser,” IEEE Select. Top. Quant. Electron., Vol. 2, No. 3, pp 514-522, 1996.

[21] S. Arahira, N. Mineo, K. Tachibana and Y. Ogawa, “40 GHz hybrid mode-locked laser diode with impedence-matching circuit,” 28th Euro. Conf. Optical Comm (ECOC), pp 1-2, 2002.

[22] C. Ji, N. Chubun, R. G. Broeke, J. Coa, Y. Du, P. Bjeletich, and S. J. B. Yoo, “Electrical Subharmonic Hybrid Mode-Locked Laser at 28 GHz,” IEEE Photon. Tech. Lett., Vol. 17, No. 7, pp 1381-1383, 2005.

[23] Microwaves101, “Quarter-wave tricks,” (Online) Available from: http://www.microwaves101.com/encyclopedia/quarterwave.cfm [Accessed 29 July 2011]

[24] D. M. Pozar, “Microwave Engineering – Third Edition,” Wiley Publishing, NJ, 2005

[25] R. J. Helkey, D. J. Derickson, A. Mar, J. G. Wasserbauer, and J. E. Bowers, “Millimetre-wave signal generation using semiconductor diode lasers” (invited), Microwave and Opt. Technol. Lett., Vol. 6, No. 1, pp 1-5, 1993.

[26] B. A. Khawaja, and M. J. Cryan, “Millimeter-wave photonic active integrated antennas using hybrid mode-locked lasers,” Microwave and Opt. Technol. Lett., Vol. 54, No. 5, pp 1200-1203, 2012.

[27] S. Arahira, S. Kutsuzawa, Y. Matsui, D. Kunimatsu, and Y. Ogawa, “Generation of Synchronized Subterahertz Optical Pulse Train by Repetition-Frequency Multiplication of a Subharmonic Synchronous Mode-Locked Semiconductor Laser Diode Using Fiber Dispersion,” IEEE Photon. Technol. Lett., Vol. 10, No. 2, pp 209-211, 1998.

[28] S. Arahira, “Variable-in, Variable-out Optical Clock Recovery with an Optically Injection-locked and Regeneratively Actively Mode-Locked Laser Diode,” J. Quant. Electron., Vol. 47, No. 5, 2011.

[29] G. R. Hugget, “Mode-locking of cw lasers by regenerative rf feedback,” App. Phys. Lett., Vol. 13, No. 5, pp 186-187, 1968.

[30] D. E. Spence, J. M. Evans, W. E. Sleat, and W. Sibbett, “Regeneratively initiated self-mode-locked Ti:sapphire laser,” Opt. Lett., Vol. 16, No. 22, pp 1762-1764.

[31] M. Yoshida, A. Ono, and M. Nakazawa, “10 GHz regeneratively mode-locked semiconductor optical amplifier fiber ring laser and its linewidth characteristics,” Opt. Lett., Vol. 32, No. 24, pp 3513-3515, 2007.

[32] M. Nakazawa, and M. Yoshida, “Scheme for independently stabilizing the repetition rate and optical frequency of a laser using a regenerative mode-locked technique,” Opt. Lett., Vol. 33, No. 10, pp 1059-1061, 2008.

[33] M. Nakazawa, K. Kasai, and M. Yoshida, “C_2H_2 absolutely optical frequency stabilized and 40 GHz repetition rate stabilized, regeneratively mode-locked picosecond erbium fiber laser at 1.53 um,” Opt. Lett, Vol. 33, No. 22, pp 2641-2643, 2008.

[34] T. Ohno, K. Sato, T. Shimizu, T. Furuta, and H. Ito, “Recovery of 40 GHz optical clock from 160 Gbit/s data using regeneratively modelocked semiconductor laser,” Electron. Lett., Vol. 39, No. 5, pp 453-455, 2003.

[35] T. Ohno, T. Ito, K. Yoshino, K. Sato, and H. Ito, “Mode-locking Mechanism of the 40 GHz Regeneratively Mode-Locked Laser Diode with 160 GHz Optical Pulse Injection,” IEEE Sel. Top. Quant. Electron., Vol. 11, No. 5, pp 1121-1125, 2005.

[36] K. Mergham, R. Rosales, S. Azouigui, A. Akrout, A. Martinez, F. Lelarge, G. –H. Duan, G. Aubin, and A. Ramdane, “Low noise performance of passively mode locked quantum-dash-based lasers under external optical feedback,” App. Phys. Lett., Vol. 95, pp 131111, (2009).

[37] C. Lin, F. Grillot, N. A. Naderi, Y. Li, and L. F. Lester, “RF linewidth reduction in a quantum dot passively mode locked laser subject to external optical feedback,” App. Phys. Lett. 96, 051118 (2010).

[38] N. Yu, E. Salik, L. Maleki, “Ultralow noise mode locked laser with coupled optoelectronic oscillator configuration,” Opt. Lett. 30, 1231 (2005).

[39] S. Gee, F. Quinlan, S. Ozharar, and P. J. Delfyett, “Correlation of supermode noise of harmonically mode-locked lasers,” J. Opt. Soc. Am. B, Vol. 24, No. 7, pp 1490-1496, 2007.

[40] D. Lenstra, B. H. Verbeek, and A. J. D. Boef, “Coherence collapse in single mode semiconductor lasers due to optical feedback,” IEEE J. Quant. Electron., Vol. 21, pp 674, (1985).

[41] F. Rana, H. L. T. Lee, R. Ram, M. E. Grein, L. A. Jiang, E. P. Ippen, and H. A. Haus, “Characterization of the noise and correlations in harmonically mode-locked lasers,” J. Opy. Soc. Am. B, Vol. 19, No. 11, pp 2609-2621, 2002.

[42] S. Gee, F. Quinlan, Ozharar, P. J. Delfyett, “Correlation of supermode noise of harmonically modelocked lasers,” Conf. Lasers and Electro-opt., CTuP3, pp 1-2, 2006.

[43] J. Davila-Rodriguez, I. Ozdur, C. Williams, and P. J. Delfyett, “A semiconductor-based, frequency stabilized mode-locked laser using a phase modulator and an intracavity etalon”, Opt. Lett., Vol. 35, No. 24, pp 4130-4132, 2010.

[44] S. Gee, F. Quinlan, S. Ozharar, and P. J. Delfyett, “Simultaneous Optical Comb Frequency Stabilization and Super-Mode Noise Suppression of Harmonically Mode-Locked Semiconductor Ring Laser Using an Intracavity Etalon,” IEEE Photon. Tech. Lett., Vol. 17, No. 1, pp 199-201, 2005.

[45] N. Onodera, “Supermode beat suppression in harmonically mode-locked erbium-doped fiber ring lasers with composite cavity structure,” Electron. Lett., Vol. 33, No. 11, pp 962-963, 1997.

[46] O. Pottiez, et. al, “Experimental study of supermode noise of harmonically mode-locked erbium-doped fibre lasers with composite cavity,” Opt. Comm., 202, pp 161-167, 2002.

[47] O. Pottiez, O. Deparis, R. Kiyan, M. Haelterman, P. Emplit, P. Megret, and M. Blondel, “Supermode noise of harmonically mode locked erbium fiber lasers with composite cavity,” IEEE J. Quantum Electron. 38, 252 (2002).

[48] K. K. Gupta, and N. Onodera, “Regenerative mode-locking via superposition of higher-order cavity modes in composite cavity fiber lasers”, Opt. Lett., Vol. 30, No. 17, pp 2221-2223, 2005.

[49] F. Quinlan, S. Ozharar, S. Gee, P. J. Delfyett, “Harmonically mode locked semiconductor based lasers as high repetition rate ultralow noise pulse train and optical frequency comb sources,” J. Opt. A. 11, 103001 (2009).

[50] G. T. Harvey, L. F. Mollenauer, “Harmonically mode locked fiber ring laser with an internal Fabry Perot stabiliser for soliton transmission,” Opt. Lett. 18, 107 (1993).

[51] L. Hou, M. Haji, J. Akbar, B. Qui, A. C. Bryce, “Low divergence angle and low jitter 40 GHz AlGaInAs/InP 1.55 μm mode locked lasers,” Opt. Lett. 36, 966 (2011).

[52] S. Römisch, J. Kitching, E. Ferrè-Pikal, L. Hollberg, and F. L. Walls, “Performance evaluation of an optoelectronic oscillator,” IEEE Trans. Ultrasonics, Ferroelectrics, and Frequency Control, Vol. 47, pp 1159, (2000).

[53] R. Kiyan, O. Deparis, O. Pottiez, P. Megret, and M. Blondel, “Stabilisation of actively modelocked Er-doped fibre laser by minimizing interpulse noise power,” Electron. Lett., 34, 2410 (1998).

[54] E. A. Avrutin, and B. M. Russell, “Dynamics and Spectra of Monolithic Mode-Locked Laser Diodes Under External Optical Feedback,” IEEE J. Quant. Electron., Vol. 45, No. 11, pp 1456-1464, 2009.

[55] X. Wang, H. Yokoyama, and T. Shimizu, “Synchronized Harmonic Frequency Mode-Locking with Laser Diodes through Optical Pulse Train Injection,” IEEE Photon. Technol. Lett., Vol. 8, No. 5, pp 617-619, 1996.

[56] A. Nirmalathas, H. F. Liu, Z. Ahmed, M. Pesuli, and D. Novak, “Subharmonic Synchronous Mode-Locking of a Monolithic DBR Semiconductor Laser,” IEEE Int. Semiconduct. Laser Conf., Tu2.1, pp 53-54, 1996.

[57] M. Margalit, M. Orenstein, and G. Eisenstein, “Noise reduction by harmonic injection locking of passively mode-locked erbium-doped fiber lasers,” Optics Lett., Vol. 20, No. 18, pp 1877-1879, 1995.

[58] S. Arahira, Y. Kotah, and Y. Ogawa, “Generation and stabilization of ultrafast optical pulse trains with monolithic mode-locked laser diodes (invited),” Optical and Quant. Electron., Vol. 33, pp 691-707, 2001.

[59] M. Attygalle, A. Nirmalathas, and H. F. Liu, “All-optical coding of mode-locked semiconductor laser pulse trains for high bit rate optical communications,” Optics Communications, Vol. 217, pp 161-167, 2003.

Chapter 6

Coherent OCDMA using an asymmetric Mach Zehnder interferometer

In [1], the author categorised OCDMA into two broad categories; *coherent OCDMA*, and *incoherent OCDMA*. These differ by the means in which a particular user's code is applied to the optical signal. In a coherent OCDMA system, coding is generally applied via phase control of the optical signal, where the phase of some coherent wide band source is sequentially shifted according to a selected bipolar code sequence, and this manipulation is effectively reversed at the receiver. On the other hand, the amplitude of a signal is typically modulated in incoherent OCDMA systems. A further look at an incoherent system is provided in the next chapter. This chapter will describe a coherent OCDMA system based on temporal phase-coding systems using asymmetric Mach Zehnder interferometers (AMZI). First, a brief overview and description of an AMZI is given, followed by a description of the encoding and decoding processes. Next, the design of an AMZI based encoder system is discussed, with a particular focus on the waveguide structure. And finally, experimental results are shown using a semiconductor ring laser monolithically integrated with an AMZI on a single chip, demonstrating the ability to perform en/decoding operations using a high frequency optical pulse train.

6.1 OCDMA via temporal phase coding using an AMZI

The operational mechanism of a temporally phase coded (TPC) OCDMA system was fully described in section 3.3.1. It is understood that encoding is applied in the temporal domain rather than the spectral domain, such as in spectral amplitude coded (SAC) systems [1 - 4]. A mode-locked laser can be used as the optical source, and during encoding the short generated pulses are replicated into N pulse copies, each delayed such that they lie on an equally spaced time grid. Each pulse copy then undergoes a fine phase tuning, corresponding to a given user's assigned phase code. Phase coding can be applied using binary codes (such as 0 or π), or more advanced codes consisting of multilevel phase codes. Examples of these are shown in [1, 5, 21]. For this research, a 2×2 AMZI was used to apply an optical delay and a two-bit phase code onto a pulsed signal to form an encoded signal. Figure 6.1 illustrates the encoding operation carried out via the pulse (data bit) propagation through the AMZI. Data modulation, such as on-off keying or differential phase shift keying (DPSK), is ideally performed before the signal enters the encoder.

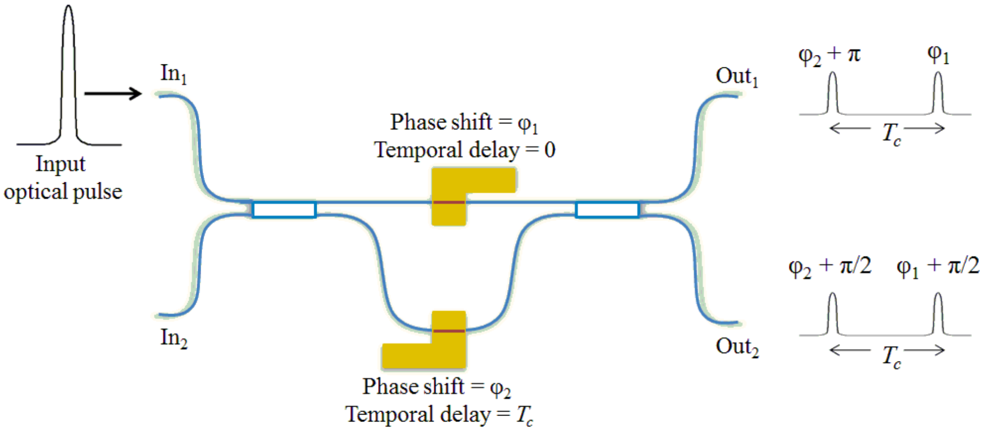

Figure 6.1 Schematic of a AMZI for two-bit encoding and the evolution of an optical pulse injected into port In$_1$, and the output states from ports Out$_1$ and Out $_2$.

Data encoding is carried out via the AMZI as follows: the data modulated pulse stream is coupled into the AMZI into either port In$_1$ or port In$_2$. The signal is then streamed through an MMI splitter, which produces two pulse copies of the signal image that is then sent through each of the waveguide arms at 3 dB of the total pulse amplitude. Each arm provides a relative binary phase shift by applying a forward bias to the phase sections. A temporal spreading of the pulse is achieved using a fixed path length difference between the two arms, such that a temporal chip interval is defined as:

$$T_c = \frac{n_g \Delta L}{c} \tag{1}$$

where n_g is the net group index of the waveguide, and ΔL is the relative path difference between the two arms. The frequency of the mode-locked laser pulses, f_{rep}, and thus the data rate of the system dictates the maximum length of the temporal chip interval due to the limit of the correlation functions at the receiver. This can be defined by the following relations [6, 7]:

$$T_c = \frac{1}{f_{rep}(2N_c - 1)}$$

where N_c is the number of pulses in a code word. For example, if a data rate of 10 Gb/s is used with a two-bit AMZI encoder, a maximum temporal delay line length corresponding to 50 ps is imposed. If the delay line is longer than this, a pulse segment requiring ‘0’ phase shift may coincide with a previous bit pulse segment that has experienced a π phase shift, which may cause unwanted interference between the correlation functions of adjacent data bits at the decoder, leading to large bit error rates.

Since the path delay is fixed, the phase shifts are the only variable parameters that are used to distinguish each user’s data stream within a network. A phase shifter on each of the two arms means a two-bit code can be generated, supporting up to four patterns of simultaneous data transmissions (i.e. ‘00’, ‘0π’, ‘π0’, and ‘$\pi\pi$’), such that code orthogonality is preserved [21]. Note that a $\pi/2$ phase shift occurs after each cross transition of the waveguides via the MMI due to the difference in coupling length [8, 9]. The modified pulse copies are then coupled into a second MMI, which combines the temporal and phase modifications of each pulse at the two output channels, forming a two bit code sequence, which can be sent towards a particular recipient through a synchronously controlled network.

Decoding is then a matter of reversing the processes carried out by the encoder. This is achieved here by using another AMZI, of which the two input arms are coupled with the output from the encoder. Figure 6.2 shows the decoding processes situated at the receiver circuit. To retrieve the optical pulses successfully, the code sequences applied to both the encoder and decoder must be matched such that the phases can realign constructively. If the code is unmatched, the cross-correlation of the resulting output signal will be zero, due to the misaligned phases and hence deconstructing interference occurs, resulting in a noise like signal at the receiver.

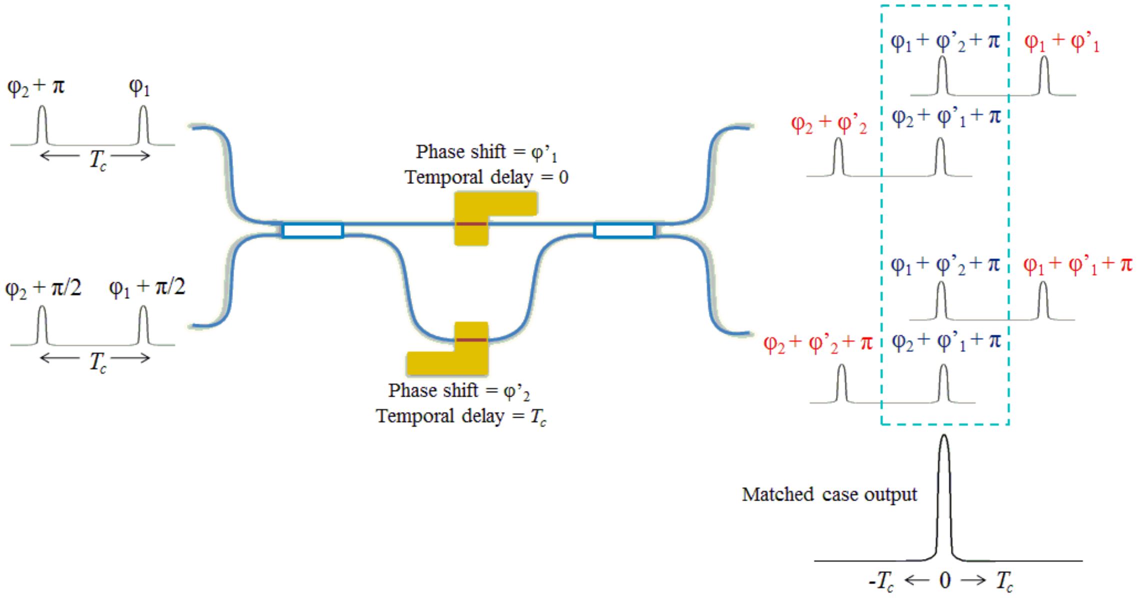

Figure 6.2 Schematic of a AMZI for decoding and the evolution of the optical pulses received from the encoder. The resulting output of a remerging single autocorrelation peak is shown on the right hand side.

6.2 Integrated asymmetric Mach Zehnder interferometer

Mach Zehnder interferometers (MZI) are highly practical components that are used in many applications, such as high speed optical switching [10], wavelength demultiplexing [11], and wavelength conversion [12]. MZIs have been recently designed and fabricated in the *Al*-quaternary substrate as part of a previous doctoral research [7]. In 2005, H. Y. Wong was one of the first to integrate MZIs in III-V based materials, using the bespoke quantum-well intermixing (QWI) technology [7, 13, 14]. More recently, S. McMaster has successfully integrated a semiconductor ring laser with 2×2 MZIs on a single chip [15], and devices integrated with AMZIs were thereby used in this research to characterise their encoding and decoding capabilities. A schematic of the monolithically integrated waveguide design is shown in Fig. 6.3.

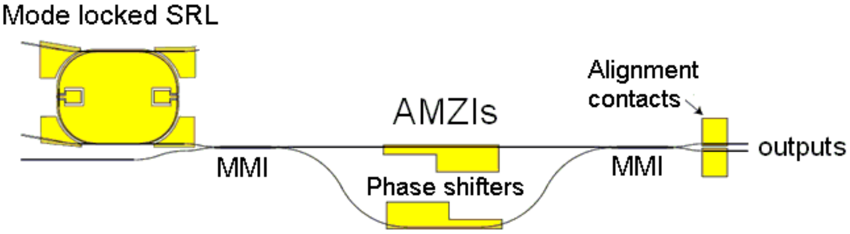

Figure 6.3 Schematic of TPC-OCDMA transmitter circuit

This system consisted of a mode-locked SRL, with its output directly coupled into port 1 of the AMZI. An MMI coupler was used to create duplicate images of the input signal along two waveguide arms, one of which was delayed before being recombined again via a second MMI coupler, leading to two output ports from which the encoded pulses would emit. Alignment contacts were added at the output waveguides to aid the positioning of a lensed fibre to the waveguide facet. The following sections shall describe each segment of the system in more detail.

6.2.1 Semiconductor ring laser

Mode-locked SRLs are highly valuable components in integrated optoelectronic systems due to their facetless operation, making them easily containable in integrated lightwave circuits [16]. here, it was used to deliver broad band pulses which were coupled directly to an input waveguide arm of the AMZI. The length of the ring cavity was 2297 μm, corresponding to a round trip frequency of ~36 GHz, with two saturable absorbers (SA) positioned halfway on each side of the ring. The lengths of each SA section were 23 μm (1% of the total cavity length), however, only one of these was reversed biased since its length had been optimised to provide the best mode-locking performance [15]. The remaining absorber was forward biased along with the remainder of the ring cavity to provide gain. Since the SRL was designed to operate bidirectionally, two AMZIs were integrated with a single SRL (above and below) to optimise space on the testing chip. Further details regarding the SRL can be found in [15].

6.2.2 Multimode interference coupler

MMI coupling is essential for many optical components which require coupling or splitting of waveguides, such as multi-laser arrays [17] and arrayed waveguide gratings (AWGs) [18]. Essentially, a MMI coupler is a waveguide segment with multiple ports used to generate a multimode interference pattern of an input beam. This pattern is optimised in space and focussed towards selected output waveguides, although with necessary intensity deductions due to power splitting. For example, a single beam of light propagating through a waveguide can split into two beams by an abrupt change in waveguide width at some focal distance. The dimensions of the

MMI coupler waveguide are therefore vital parameters and must be designed appropriately and according to the number of channels required. The multimode pattern varies with propagation distance L and the number of input/output channels N as described by:

$$L = \frac{3L_{\pi}}{N}$$

where L_{π} is the beat length and is represented as:

$$L_{\pi} \cong \frac{4n_{eff}W_{eff}^{2}}{3\lambda_{0}}$$

in which n_{eff} is the effective index of the waveguide, W_{eff} is the effective width, and λ_0 is the free space wavelength. The W_{eff} can be defined according to:

$$W_{eff} \cong W + \left(\frac{\lambda_0}{\pi}\right)\left(\frac{n_c}{n_{eff}}\right)^{2\sigma} \Big/ \sqrt{n_{eff}^{2} - n_{c}^{2}}$$

where n_c is the effective index of the cladding layer situated above the active region, and $\sigma = 0$ for TE polarization and $\sigma = 1$ for TM [15]. In this circuit, a 2×2 MMI was used to split the incoming signal from either two channels and form a duplicated image that was fed into two output waveguide channels at a length of 1/2($3L_{\pi}$), as shown in Fig. 6.4. A further length along the MMI would then effectively take the signal to the cross state, in which the image appears at the diagonally opposite port. Only after a length of 2($3L_{\pi}$) will the signal appear at the original y-offset.

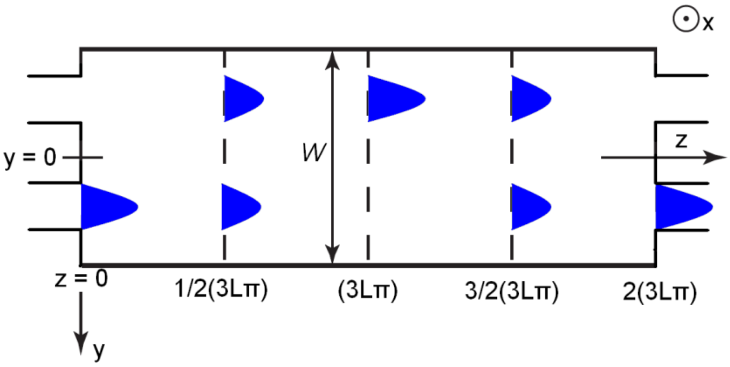

Figure 6.4 Evolution of the multimode pattern as a signal propagates in the z-direction through a 2×2 MMI coupler.

Taking this into account, and after optimisation of the MMI length using the 2.5D beam analysis software, Beamprop (Fig. 6.5), the MMIs were designed as 354 μm long and 15 μm wide (resulting from $W_{eff} = 16$ μm, using $n_{eff} = 3.201, n_c = 3.166$, and $\lambda = 1.55$ μm), with two 2 μm wide waveguide interconnections spaced apart by 3 μm. The MMIs were tapered up at 31° towards a 15 μm wide waveguide to ensure the suppression of any waveguide back reflections [19].

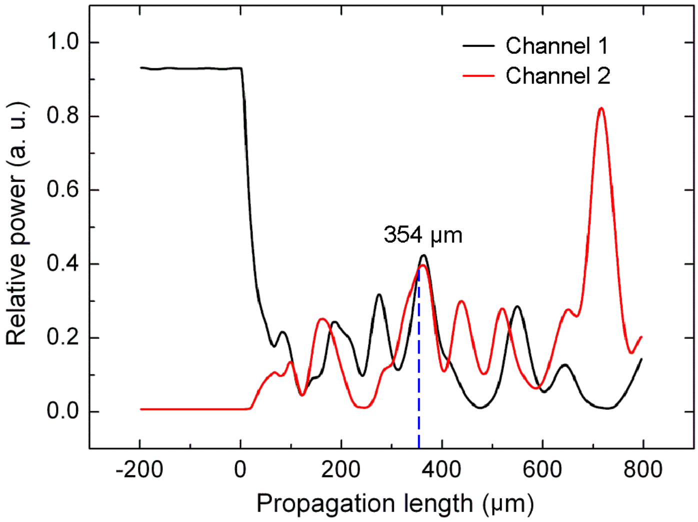

Figure 6.5 2.5D beam propagation simulation results of a MMI coupler using a physical waveguide width of 15 µm. The optimal 3 dB coupling length where the intensity of the two output modes is 354 µm.

6.2.3 Passive waveguides

The output of the MMI led to two waveguide arms, one of which was a straight path towards the second MMI coupler, and the other was curved to provide a delay before being coupled into the second MMI coupler. The difference in path length between the top and bottom arms of the AMZI was set at 423 µm long, corresponding to a relative optical path delay of 5 ps. The curved waveguide arm had a radius of 250 µm, in order to minimise cavity losses incurred via bending of the waveguide. A 1.9 µm deeply etched, 2 µm wide waveguide was passivated using the quantum-well intermixing (QWI) process to eliminate the need for bias and reduce waveguide losses due to interband absorption (*it was shown in chapter 2 that the waveguide losses were reduced from 15/cm*$^{-1}$ *to ~4.5/cm*$^{-1}$ *for the TE mode in the wavelength range of 1500 – 1580 nm as a result of QWI.*). The intermixing was performed around the sections requiring a bias, such as the SRL and phase shifting sections.

6.2.4 Phase shifters

A 500 µm long phase shifting section was added to each of the waveguide arms to enable precise phase modulation. These were essential for TPC-OCDMA to work using the AMZI, where code orthogonality is preserved with each user applying different combinations of biasing to the phase sections, and in turn providing a unique static phase encoding to the data stream (- phase modulation in semiconductor optoelectronic circuits is more fully discussed in section 3.3.2).

6.3 Encoding / decoding results

First, the TPC-OCDMA transmitter was characterised. The gain section of the ring laser was biased with 176 mA and the SA section was reverse biased with -3.3 V. The optical spectra taken at the output port 1 is shown in Fig. 6.6(a). Here, two mode spacing are apparent; (i) the shorter mode spacing at 0.29 nm corresponding to the mode-locking frequency, and (ii) the superimposed larger mode spacing at 1.74 nm, due to the transfer function of the AMZI, i.e. the path length difference of the two arms leads to an alternating wavelength selection at each output channel [7]. This meant that the pulses from the mode-locked SRL were being split and delayed as required.

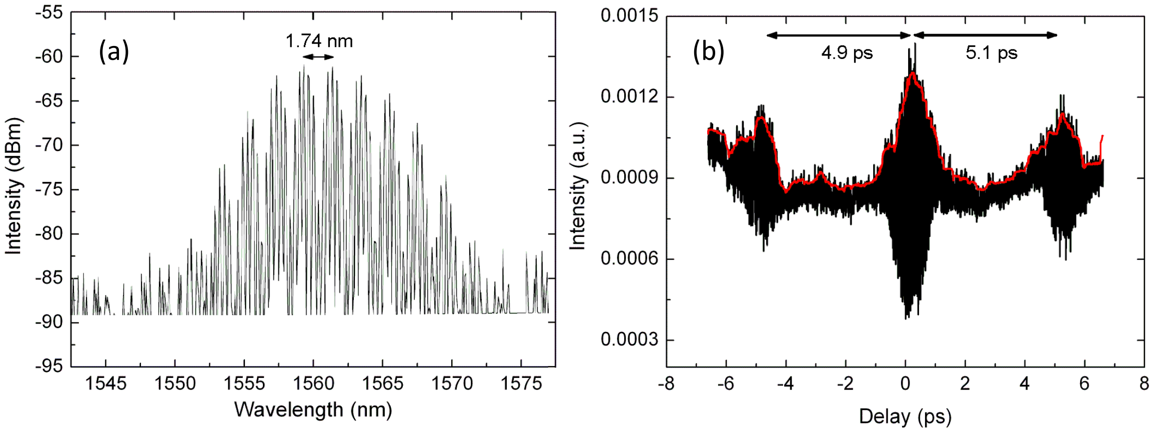

Figure 6.6 (a) Optical spectra measured at the output of the AMZI encoder, and (b) the measured time spread pulses in the temporal domain using a linear intensity autocorrelator (note: due to the nature of the autocorrelator, two adjacent pulses are represented as a single pulse with two weaker intensity side pulses).

However, due to the excessive losses in the passive waveguides, the output power was not sufficient enough to be viewed using a traditional second harmonic generation (SHG) autocorrelator. Instead, a linear intensity autocorrelator was used due to its high sensitivity. Figure 6.6(b) shows the output of the linear intensity autocorrelator, where a large intensity peak is apparent with two smaller intensity peaks at either side, separated by approximately 5 ps. This indicates that the pulses were indeed being split and delayed as required.

To assess the AMZIs decoding capability, a back-to-back design of the AMZI was used. The total waveguide loss of the entire chip was estimated to be ~70 dB. These losses, primarily resulting from intermixing process issues, made observations of the output signal difficult. Therefore, instead of generating pulses using the integrated SRL, a 10 GHz high power mode-locked fibre laser generating pulse widths of ~2 ps, was used and injected into the waveguide facet. The experimental set up as well as the device layout is shown in Fig. 6.7. The wavelength of the fibre laser was tuned to operate at 1.55 μm (where waveguide losses were minimum). A dispersion shifted erbium doped fibre amplifier (EDFA) was also used prior to the injection to increase the intensity of the signal, to minimise losses. After coupling the output signal using a lensed fibre, the signal was again passed through a second EDFA to compensate for the high insertion loss, before being filtered for amplified spontaneous emission (ASE) via a band-pass filter and fed into a high speed sampling oscilloscope (65 GHz nominal bandwidth) for observation.

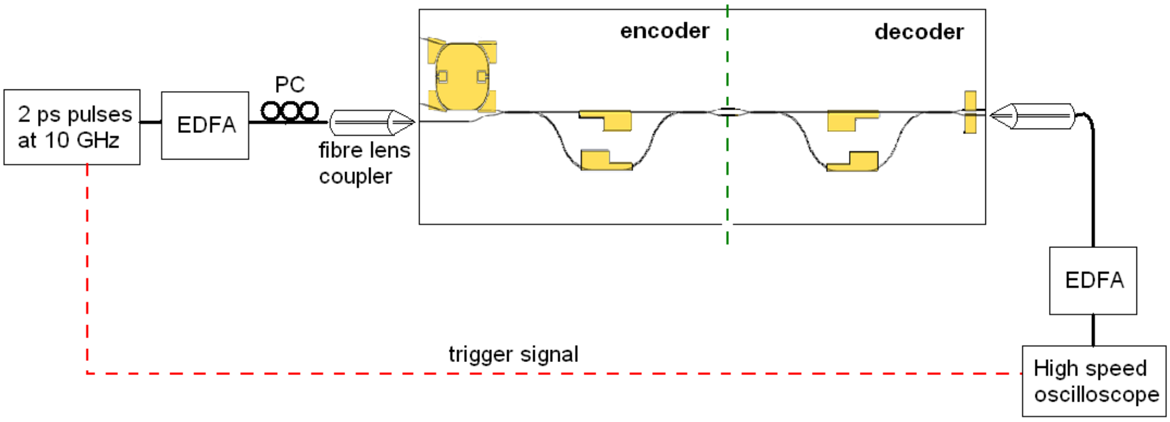

Figure 6.7 Schematic representation of the experimental setup used to test the encoding and decoding operation of two integrated back-to-back AMZIs.

Since the temporal delays of the AMZI arms were fixed, the phase shifts of the encoder and decoder were perfectly matched without any applied bias. The bias conditions of the phase sections of both the encoder and decoder were then varied to find the relative phase shifts of each segment. Table 6.1 shows the variations of codes that were tried in order to validate the matched and unmatched cases. Figure 6.8 subsequently shows the output traces as viewed on the high speed oscilloscope.

It is evident from Fig. 6.8 (a) and (b), that decoding was successful and the signal was well-reconstructed when the relative phase shifts at the encoder and decoder were equal. Alternatively, for the unmatched cases (Fig. 6.8 (c) and (d)), the pulses became suppressed due to the offset of the phases at the decoder AMZI, leading to destructive interference. It is apparent however that some of the pulse amplitude had remained, which is likely to be due to an uneven power splitting of the MMI combiners from the differential losses associated with the different waveguide path lengths. This may be improved by using tunable MMI splitters, as shown in [20].

Case	**Encoder**		**Decoder**	
	φ_1	φ_2	φ_1'	φ_2'
Matched 1	0	0	0	0
Matched 2	0	π	0	Π
Unmatched 1	π	0	Π	Π
Unmatched 2	π	0	0	0

Table 6.1 The relative phase conditions of the OCDMA encoder and receiver used during the experiment.

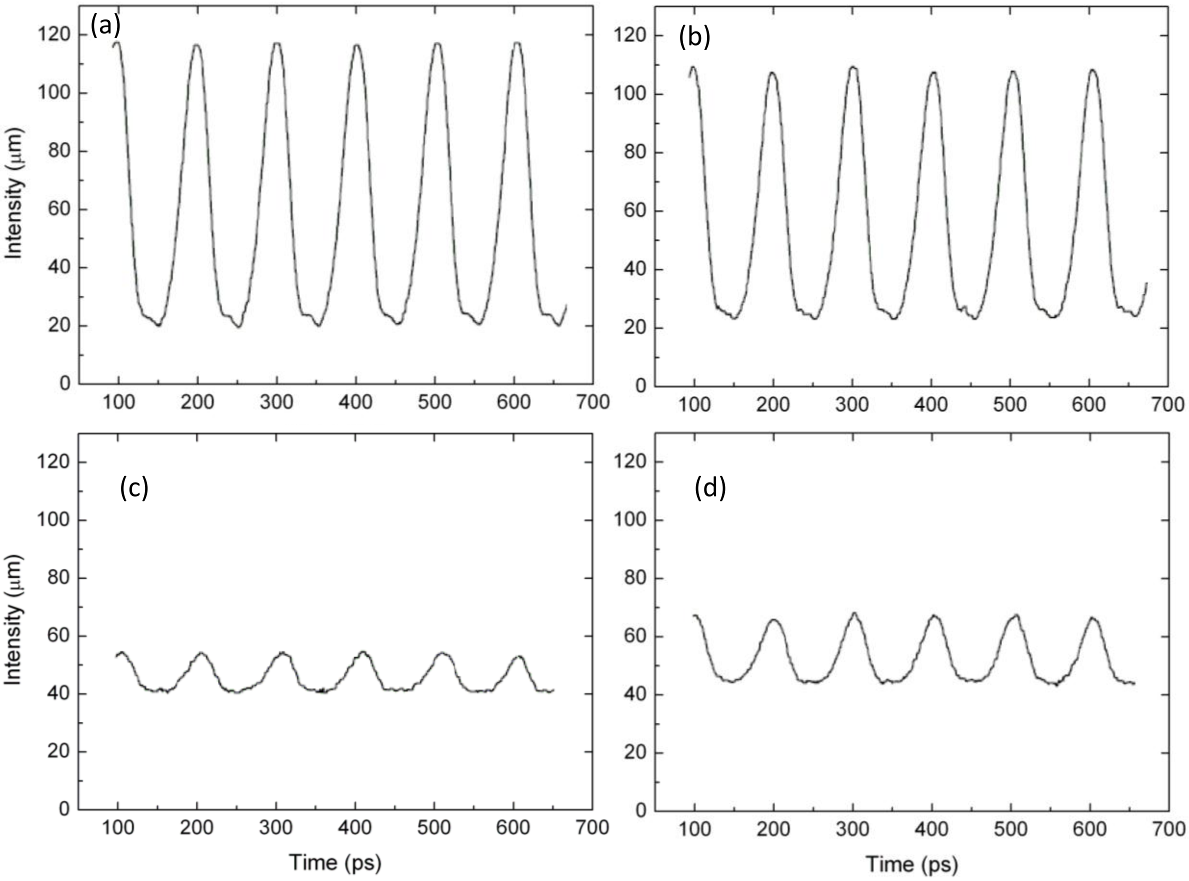

Figure 6.8 The output as viewed on the oscilloscope during the OCDMA experiment using (a) matched case 1, (b) matched case 2, (c) unmatched case 1, and (d) unmatched case 2.

6.5 Chapter summary

A 2-bit TPC-OCDMA encoder/decoder pair was formed using AMZIs, which were monolithically integrated with a mode-locked SRL operating at 36 GHz. The AMZI consisted of two optical waveguide arms, one of which was extended to provide a time delay of 5 ps (chip interval). Each arm contained a phase shifting section, which was used to statically provide 2-bit binary phase code to the incoming data stream, which could then be sent into a synchronous network while preserving the integrity of the data. This could then be decoded at a receiver circuit containing a similar AMZI, where both the delay and relative phase shifts were undone to restore the original data pulse sequence. It was shown experimentally that when the encoder and decoder phases were matched, the signal could be re-established at the receiver. And unmatched phases led to unbalanced splitting in the MMIs, resulting in the destructive interference of the signal. These results demonstrate the faculty of the AMZI structure for use in TPC-OCDMA applications. Further work could entail improving the high losses presented in the chip, and increasing in the number of AMZI arms to increase the number of phase codes available for more users in a TPC-OCDMA system.

6.6 References

[1] P. R. Prucnal, et al., “Optical code division multiple access – Fundamentals and applications,” CRC Taylor and Francis, 2006.

[2] A. M. Weiner, J. P. Heritage, and J. A. Salehi, “Encoding and decoding of femtosecond pulses,” Opt. Lett., Vol. 13, pp 300-302, 1988.

[3] J. A. Salehi, A. M. Weiner, and J. P. Heritage, “Coherent ultrashort light pulse code division multiple access communication systems,” J. Lightwave Technol., Vol. 8, pp 478-491, 1990.

[4] S. Etemad, et al., “Optical CDMA incorporating phase coding of coherent frequency bins: Concept, simulation, experiment,” Proc. Opt. Fiber Comms. Conf., FG5, 2004.

[5] G. C. Yang, and W. C. Kwong, “Prime codes with application to CDMA optical and wireless networks,” Norwood: Artech House, 2002.

[6] D. Sampson and D. Jackson, "Spread-spectrum optical fibre network basedon pulsed coherent correlation," Electron. Lett., Vol. 26, No. 19, pp 1550-1552, 1990.

[7] H. Y. Wong, "InGaAs/InAlGaAs Monolithically Integrated Mach-Zehnder Interferometer Devices," Ph.D. thesis , University of Glasgow, 2005.

[8] L. Soldano and E. Pennings, "Optical multi-mode interference devices based on self-imaging: principles and applications," J. Lightwave Technol., Vol. 13, No. 4, pp 615-627, 1995.

[9] M. Bachmann and P. A. Besse and H. Melchior, "General self-imaging properties in n x n multimode interference couplers including phase relations," Appl. Opt., Vol. 33, No. 18, pp 3905-3911, 1994.

[10] I. Glesk, P. J. Bock, P. Cheben, J. H. Schmid, J. Lapointe, and S. Janz, “All optical switching using nonlinear subwavelength Mach Zehnder on silicon,” Opt. Express, Vol. 19, pp 14031-14039, 2011.

[11] A. Yi-Yan, R. J. Deri, M. Seto, and R. J. Hawkins, “GaAs/GaAlAs Asymmetric Mach Zehnder demultiplexer with reduced polarisation dependence,” IEEE Photon. Technol. Lett., Vol. 1, No. 4, pp 83-85, 1989.

[12] M. Masonovic, V. Lala, J. S. Barton, E. J. Skogen, L. A. Coldren, and D. J. Blumenthal, “Monolithically integrated Mach-Zehnder interferometer wavelength converter and widely tunable laser in InP,” IEEE Photon. Technol. Lett., Vol. 15, No. 8, pp 1117-1119, 2003.

[13] H. Y. Wong, M. Sorel, A. C. Bryce, J. H. Marsh, and J. M. Arnold, “Monolithically integrated InGaAs/AlGaInAs Mach Zehnder interferometer optical switch using quantum well intermixing,” IEEE Photon. Technol. Lett., Vol. 17, No. 4, pp 783-785, 2005.

[14] H. Wong, W. Tan, A. C. Bryce, J. H. Marsh, J. M. Arnold, A. Krysa, and M. Sorel, "Current injection tunable monolithically integrated InGaAs-InAlGaAs asymmetric Mach-Zehnder interferometer using quantum-well intermixing," IEEE Photon. Technol. Lett., Vol. 17, No. 8, pp 1677-1679, 2005.

[15] S. McMaster, "Monolithically integrated mode-locked ring lasers and Mach-Zehnder interferometers in AlGaInAs," Ph.D. thesis , University of Glasgow, 2010.

[16] M. Sorel, G. Giuliani, A. Scire, R. Miglierina, S. Donati, and P. J. R. Laybourn, “Operating regimes of GaAs-AlGaAs semiconductor ring lasers: experiment and model,” IEEE J. Quant. Electron., Vol. 39, No. 10, pp 1187-1195, 2003.

[17] L. Hou, M. Haji, B. Qui, and A. C. Bryce, “Mode-locked laser array monolithically integrated with MMI combiner, SOA, and EA modulator,” IEEE Photon. Technol. Lett., Vol. 23, No. 15, pp 1064-1066, 2011.

[18] P. Munoz, D. Pastor, and J. Capmany, “Analysis and design of arrayed waveguide gratings with MMI couplers,” Opt. Express, Vol. 9, pp 328-228 (2001).

[19] R. Hanfoug, L. Augustin, Y. Barbarin, J. van der Tol, E. Bente, F. Karouta, D. Rogers, S. Cole, Y. Oei, X. Leijtens, and M. Smit, "Reduced reflections from multimode interference couplers," Electron. Lett., Vol. 42, No. 8,pp 465-466, 2006.

[20] J. Leuthold and C. Joyner, "Multimode interference couplers with tunable power splitting ratios," J. Lightwave Technol., Vol. 19, No. 5, pp 700-707, 2001.

[21] Y. L. Chang, and M. E. Marhic, “Fiber optic ladder networks for inverse decoding coherent CDMA,” IEEE J. Lightwave Technol., Vol. 10, No. 12, pp 1952-1962, 1992.

Chapter 7

Incoherent OCDMA system using WHTS en/decoder

In general, incoherent OCDMA systems predominantly use amplitude modulation based encoding. Unlike coherent systems, this allows the use of two-dimensional coding schemes, providing better code performance with a better code flexibility and a larger system capacity over conventional one-dimensional codes [1]. Wavelength-hopping time-spreading (WHTS) OCDMA systems use 2D encoding where the codes are spread in both the wavelength and time domains simultaneously, providing zero correlation side lobes as well as low cross-correlations, with reduced code lengths [2]. For this research, a WHTS OCDMA transceiver circuit was designed and developed on a single chip using an array of mode-locked lasers incorporating distributed Bragg reflectors (DBRs). This chapter will present the experiments and characterisations performed using the integrated WHTS OCDMA system. First, encoding and decoding using the proposed system is discussed, with particular details regarding the design and circuit functions. Next, the integrated WHTS OCDMA circuit is presented, along with characterisation results. Experiments on system clock synchronisation are then presented, using the optical injection method. And finally, the potential for wavelength-time hopping is discussed, and a microstrip delay line is proposed for implementing the time-hop code.

7.1 WHTS OCDMA using a mode-locked laser array

The operational mechanism of a WHTS OCDMA system is fully described in section 3.3.1. Based on the requirement to produce a multiwavelength optical source, a WHTS system was designed using a MLLD array with integrated distributed Bragg gratings (DBR), each tuned to filter different regions of the gain spectra of its respective laser using quantum-well intermixing (QWI). To reduce chip complexity, no temporal delay paths were designed. The temporal offset could instead be applied in the electrical domain using electrical delay lines. Further details regarding the MLLD with integrated DBRs can be found in chapter 4.

Another purpose of the integrated DBRs is to provide partial reflectivity of the MLLD promoting the build up of gain while allowing the generated light pulses to couple into subsequent passivated waveguides. A multimode interference coupler is then used to combine the light from the multiple lasers in the multiwavelength MLLD array and guide them into a single channel for amplification and data modulation via a semiconductor optical amplifier (SOA), and electro-absorption modulator (EAM), respectively. A WHTS chip sequence is formed via the wavelength separation provided by the multiple laser array, and temporal spreading derived via the electrical delay lines feeding in a clock signal to each laser at multiples of π/2 phase shifts (Fig. 7.1). Data modulation can then be performed by switching each chip sequence on and off to represent binary data.

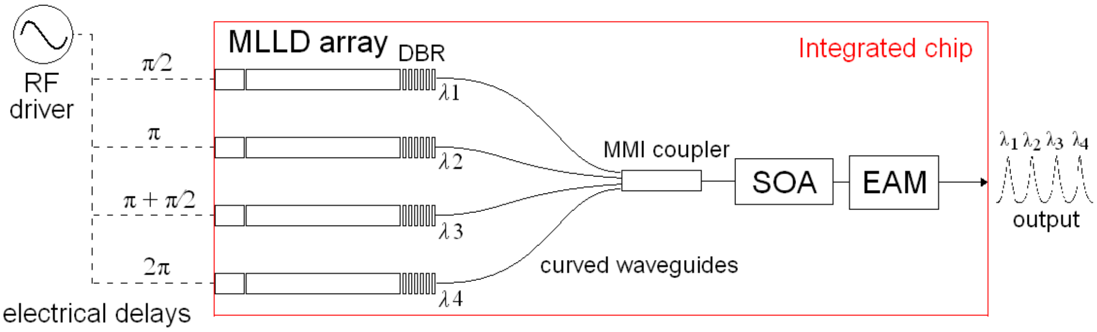

Figure 7.1 Schematic of the WHTS transmitter circuit design

The receiver circuit, shown schematically in Fig. 7.2, uses the same integrated components as the transmitter, although the components work in reverse. The encoded signal is injected into the waveguide, which is the amplified using the SOA, before being evenly split towards each of the MLLDs, which are instead are used as photodetectors. The DBRs are used to selectively filter out wavelengths outside the window of the commissioned discrete bandwidth, so that the pulses are isolated in separate waveguides according to their wavelength. The photocurrent of the light is then extracted from the SA section of what was the MLLD, and electrical delay lines are used to realign the pulses to form an electrical binary signal derived from the encoded signal at the transmitter.

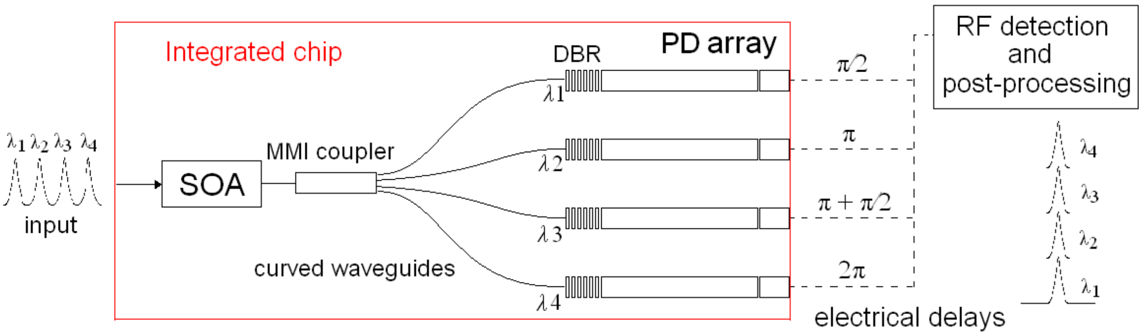

Figure 7.2 Schematic of the WHTS receiver circuit design

7.2 Mode-locked laser array characterisation

Laser arrays are very useful components in a number of systems ranging from digital printer heads [3], optical spectroscopy [4] and WDM networks [5]. Previously, mode-locked laser arrays have been fabricated for use in rapid beam scanning systems [6] and WDM systems [7]. Mode-locked laser arrays in *AlGaInAs/InP* (five-QWs) were recently fabricated for this research. A schematic of the integrated chip is shown in Fig. 7.3. The chip consists of four mode-locked lasers with S-bend waveguides leading to 4:1 MMI combiner, a SOA section and an EAM section.

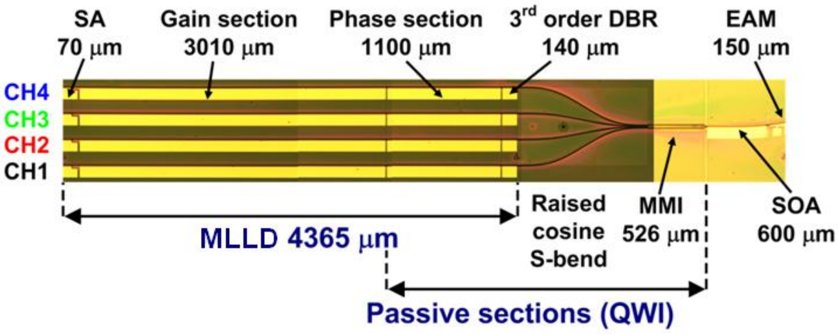

Figure 7.3 Microscope picture of the laser array integrated with an MMI combiner, SOA and EAM sections.

The design of the integrated chip is based on that explained in section 7.1. The raised cosine S-bends were 1200 μm long and curved patterns were used to avoid discontinuities in the radius of curvature, thus minimising the losses associated with mode mismatching [8]. The single output of the MMI led to a curved waveguide with an SOA and EAM section along its path. The SOA consisted of a 300 μm long straight part, followed by a 300 μm long curved waveguide, extending to a 150 μm EAM section. The curvature was such that the waveguide and the cleavage plane formed an angle of 80°. A 10° angled facet was then formed when the device was cleaved to reduce the optical reflectivity [9]. A 30 μm long electrical isolation slot was used between the EAM and SOA sections.

7.2.1 Wavelength optimisation of MLLDs using DBRs

The mode-locked lasers consisted of 70 μm saturable absorber (SA) and 2010 μm gain sections, and passivated 1100 μm phase and 140 μm DBR sections which were each shifted in wavelength by 100 nm using the QWI method (Fig. 7.4). The subsequent S-bend waveguides as well as the MMI combiner were also passivated in the same way. The DBRs were similarly tuned using QWI so that a discrete bandwidth gain window was formed for each laser. The period of the DBR was varied from 734 nm to 740 nm from channel 1 (CH1) to channel 4 (CH4), respectively to accommodate the wavelength shift. A DBR slot width of 180 nm was selected due to a trade-off between reduced scattering losses and fabrication feasibility, while still providing adequate reflectivity [10]. As a result of the high coupling efficiency κ, the effective length of the DBR was ~55 μm, providing and effective cavity length of ~4280 um, corresponding to a round-trip frequency of approximately 10 GHz. The separation between two adjacent lasers was 250 μm.

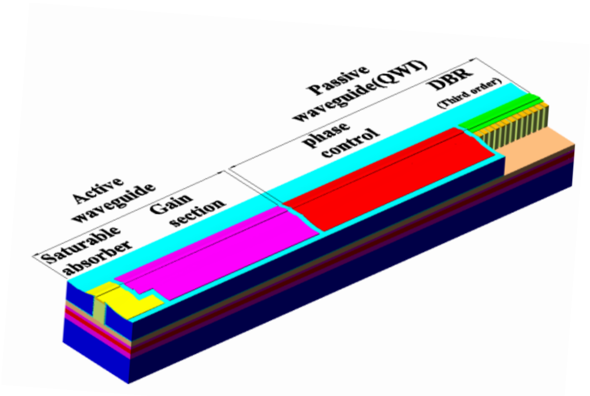

Figure 7.4 Schematic drawing of a single MLLD within the laser array

In chapter 4, characterisation results for CH3 were shown, and this can be considered as an example of the characteristics of all lasers in this array. However, since the DBR grating pitches were varied for each laser, the optical power, frequency and spectrum was slightly different for each channel. This will be shown later in this chapter.

7.2.2 MMI coupler design

The theory of MMI couplers was described in chapter 6. For this device, using the Beamprop™ simulation tool, the 4:1 MMI coupler was optimised at 526 μm long with a width of 30 μm (Fig. 7.5). In order to reduce the reflectivity from the MMI coupler, the stemming input waveguides were tilted at 45° in order to suppress the back reflections [11] which could otherwise deteriorate the quality of the MLLDs. The simulated modal pattern of the 4×1 MMI coupler is shown in Fig. 7.5(a), and is shown to create four equidistant modes after a length of 526 μm. Figure 7.5(b) shows the relative intensity of the modes which overlap at 526 μm which agrees well with the simulated modal pattern. This confirms the optimal waveguide length of the MMI to split a signal four ways, and vice versa.

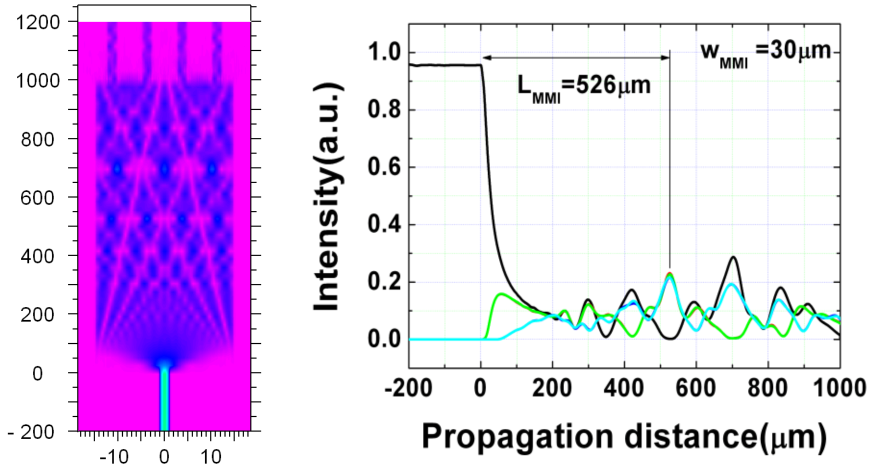

Figure 7.5 Simulated results showing (a) the modal propagation and interactions through a 30 μm wide waveguide, and (b) the correlation of the mode intensities as a function of propagation distance.

7.2.3 Semiconductor optical amplifier

SOAs are often used in semiconductor circuits to amplify an optical signal. They are useful for providing sufficient output power levels for transmitting a signal over a network without compromising the signal integrity at the detection circuit, which requires an acceptable level of bit error rate (typically in the order of 10^{-9}). SOAs are essentially similar to lasers, but with very low optical feedback so that they are prevented from reaching threshold [12]. This is achieved here by using a curved waveguide, so that back reflections from the end facet are subdued, while the amplified spontaneous emission (ASE) gain is increased.

Here, it is shown that the SOA can further boost the output power of the MLLDs with negligible effects on the pulse quality. Figure 7.6(a) shows the typical output power measured from the EAM side of the device as a function of the SOA current, with the gain section of CH3 biased at 300 mA. When the operating current for the on-chip SOA was set at 200 mA, the output power from CH3 reached almost 8 mW. The net optical gain was estimated to be 20 dB. A further increase of the driving current of SOA would reduce the output power, due to the heating of the SOA active region. Figure 7.6(b) shows the ASE spectrum of the SOA with different bias conditions. The gain peak at 200 mA is located at the wavelength of 1560 nm with a gain ripple below 0.5 dB, measured on an optical spectrum analyser (OSA) with a 1 nm resolution bandwidth (RBW). This is consistent with the expected theoretical optical reflectivity of less than $1 \cdot 10^{-5}$ using a 10° tilt angle [9].

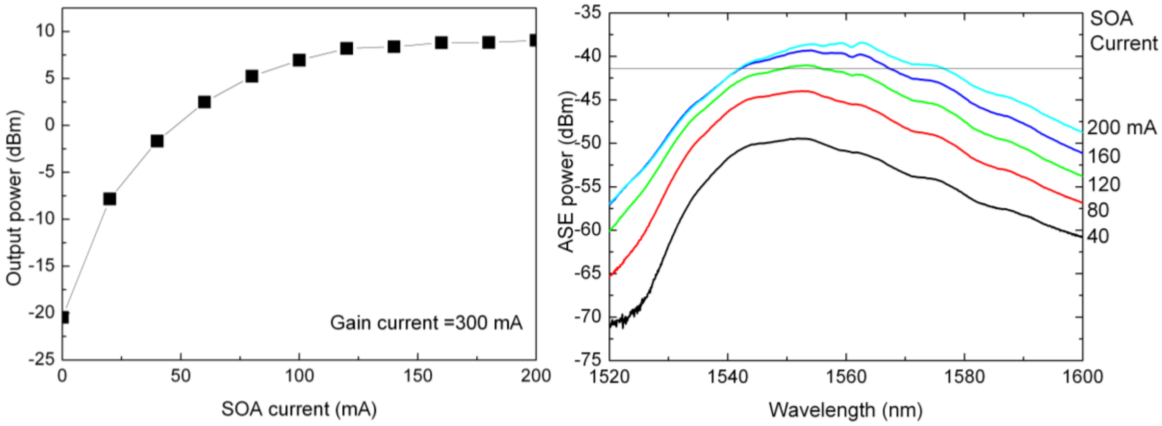

Figure 7.6 SOA characteristics: (a) Output power as a function of the bias on the SOA, and (b) ASE spectra as the bias was varied.

7.2.4 Channel characterisation for wavelength hopping

To characterise the chip, the *LI* characteristics of each laser were measured and the results are shown in Fig. 7.7(a). A kink-free lasing was observed for each channel and the threshold current with an unbiased SA was 74 mA, with a current deviation of ~10 mA between the channels. The output power was slightly lower for CH1 and CH4 due to the increased curvature of the cosine S-bends, leading to increased bending losses. Moreover, the peak wavelengths of CH1 and CH4 were offset from the gain peak of the SOA, resulting in a greater amplification of CH2 and CH3. These effects are better illustrated in the spectral measurements: simultaneous CW lasing spectra (RBW 0.06 nm) of the four MLLD channels from the same array are shown in Fig. 7.7(b). The spacing of the spectra was about 5 nm. The 3 dB bandwidth was within 0.8 and 1.3 nm. Figure 7.7(c) shows the corresponding simultaneous RF signals, which confirmed that the four channels can be operated either simultaneously, with four corresponding pulse repetition frequencies (f_r), or individually, enabling the selection of a single f_r. The corresponding autocorrelation trace is shown in Fig. 7.7(d), and has a small pedestal and some amplitude modulation due to the slightly different f_r of each channel, three of which were untriggered. Varying the bias on the DBR, phase, gain, and the voltage sections could enable tuning of f_r at the cost of shifting the designated wavelength registration [13]; however, due to the 5 nm channel spacing, obtaining the same f_r is extremely difficult to achieve when passively mode-locking as there is no feedback reference for each laser to align itself to the same carrier frequency.

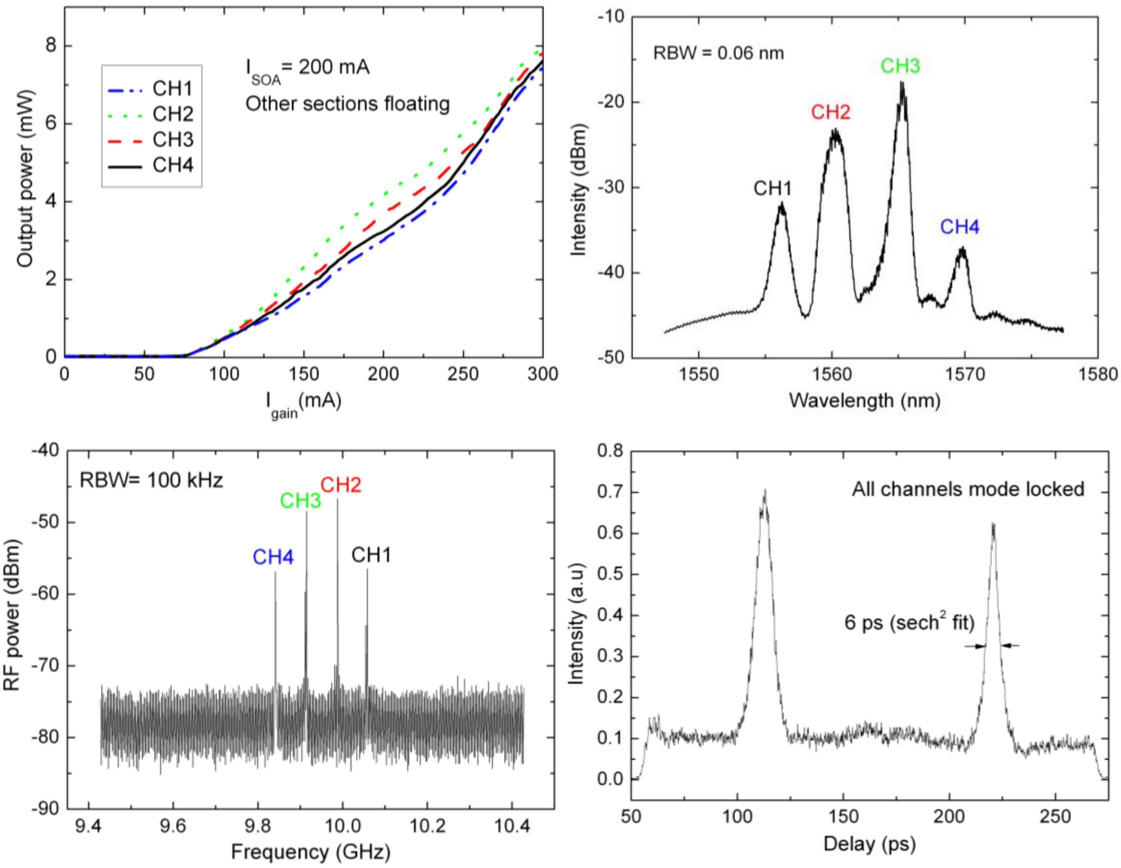

Figure 7.7 (a) *LI* characteristics of each laser in the array, (b) simultaneous lasing spectra of all channels, (c) corresponding RF spectrum, and (d) free running autocorrelation trace of all channels running simultaneously.

7.2.5 Electroabsorption modulator

EAMs were described in chapter 3 of this thesis. To measure the characteristics of the integrated EAM, the gain section of each laser and the SOA were biased with 118 mA and 200 mA respectively, while a varied reverse bias was applied to the EAM. The resulting output was measured using both a power meter and an OSA. One of the main parameters of an EAM is the extinction ratio (ER), which is a measure of the amount of light absorbed for a given bias [19]. Using the measured data, the ER was calculated and the results are shown in Fig. 7.8. It is evident that a direct current ER of ~ 20 dB at V < 4 was achieved for each channel. It was also clear that for a given reverse bias < 3 V, the ER was greater for the lasers operating at shorter wavelengths i.e. CH1 and CH2, whereas CH3 and CH4 required relatively larger biasing to achieve the same ER. This is due to the absorption band edge shifting to lower energies as the bias is increased (caused by the quantum confined stark effect (QCSE)) [14].

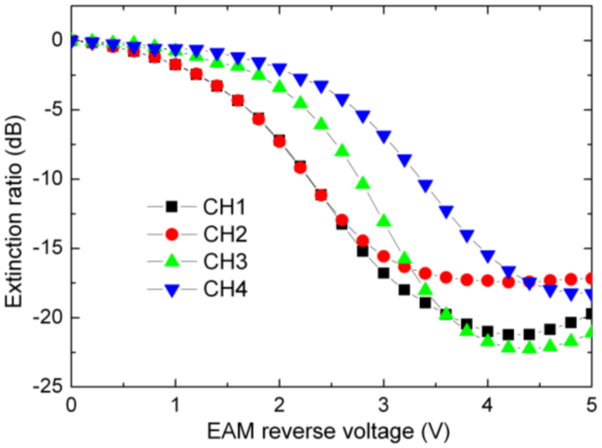

Figure 7.8 EAM DC absorption behaviour of each laser in the array.

7.3 Laser array clock synchronisation

The importance of synchronising the carrier frequency of the lasers in the WHTS circuit is paramount for the allocation of discrete and invariable time-spaces to take form. When operating passively, the lasers operate independently and at different wavelengths, and different repetition frequencies as a result. While tuning the phase sections provides some control of the pulse repetition frequencies, it is important that the pulses are aligned equally in the temporal domain. In chapter 5, several methods of pulse stabilisation were discussed, and above all, optical synchronous mode-locking (SML) proved to be the most versatile and efficient method as it was simpler and provided the largest locking range (600 MHz range at a pulse repetition rate of 40 GHz). Thus, it was considered suitable to synchronise multiple lasers in the array. The SML technique was particularly useful for this application since there were multiple laser frequencies required to be pulled into a single stable clock frequency, and so a large locking range was important.

For this experiment, a 10 GHz active mode-locked fibre laser was employed, and its pulses passed through a pulse compressor to increase the locking range [15], followed by an optical power attenuator. The 730 fs pulses were then fired into the angled EAM side facet of the integrated chip towards the MLLDs. A circulator was used to isolate the response of the integrated circuit, which was visualised on an optical spectrum analyser, RF spectrum analyser and high speed oscilloscope that was triggered using the same clock as the injection laser. A schematic of the experimental setup is shown in Fig. 7.8.

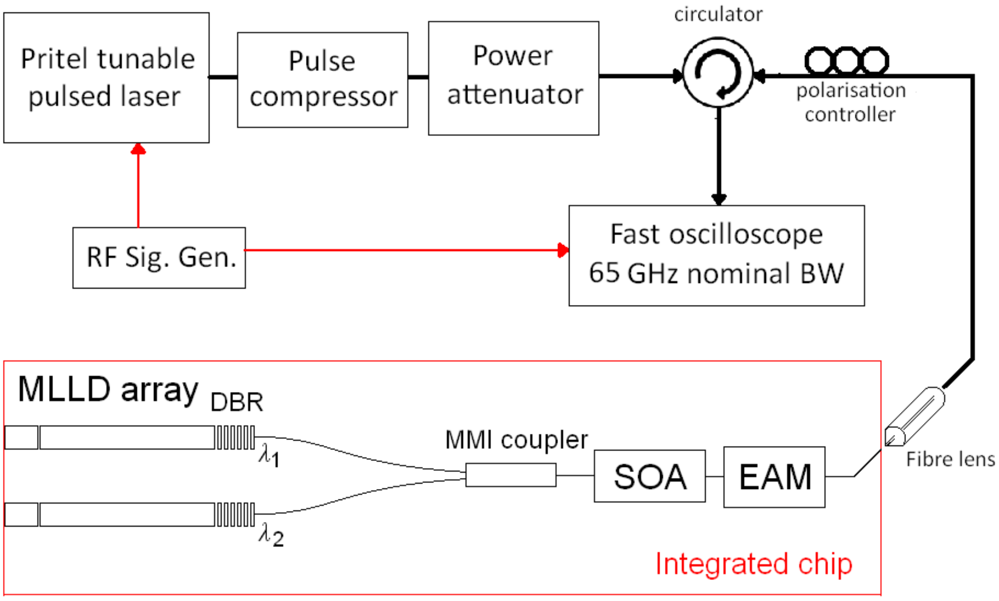

Figure 7.8 Schematic of the experimental setup for clock synchronisation of 2 channels.

The lasers were first biased to achieve mode-locking, and the SOA was biased with 200 mA in order to compensate for the waveguide losses. The total output power of the master laser was ~10 dBm. The injection wavelength was optimised using the same methods described in chapter 5, and the wavelength was set to operate at 1550 nm. The optical spectra of the master laser and the resulting output of the synchronised lasers are shown in Fig. 7.9. It is evident that the bandwidth of the compressed injection pulses was far greater than the MLLDs, and the modes were suitably overlapped. Due to the insertion losses of the integrated chip (i.e. unbiased EAM section, MMI back reflection suppression and waveguide splitting), a vast amount of injection power was required in order to sufficiently influence the timing of the MLLDs. The total losses (i.e. insertion loss and coupling loss) were estimated to be ~21 dB along the waveguide (~5 dB coupling loss, 6 dB waveguide splitting loss, ~10 dB MMI loss).

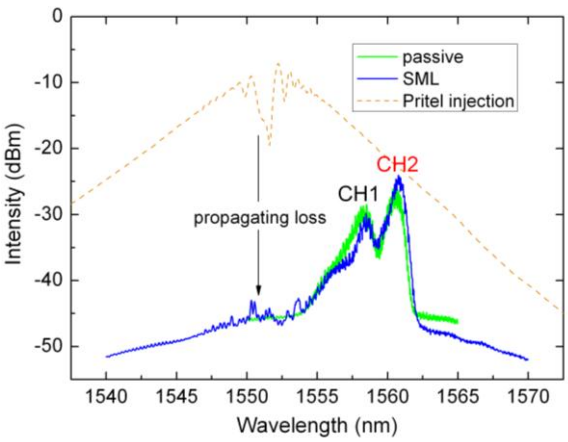

Figure 7.9 OSA spectra of the injection signal (orange dotted line), 2 lasers simultaneously free running (green line) and the resulting spectra of the two synchronised channels (blue line).

When the injection power was more than 10 dBm, both channels were synchronised at 10 GHz (Fig. 7.10(a)). This was maintained until the power fell below 0 dBm, where the peaks of the two MLLDs began to emerge. At -15 dBm, the master laser power was not sufficient enough to modulate the MLLDs, and the RF spectrum and phase noise were similar to that when the lasers were free running. The linewidth in this case was 2.5 MHz for CH1 and 881.5 kHz for CH2. The linewidth of the synchronised output was < 1 kHz, similar to that of the Pritel actively mode-locked fibre laser.

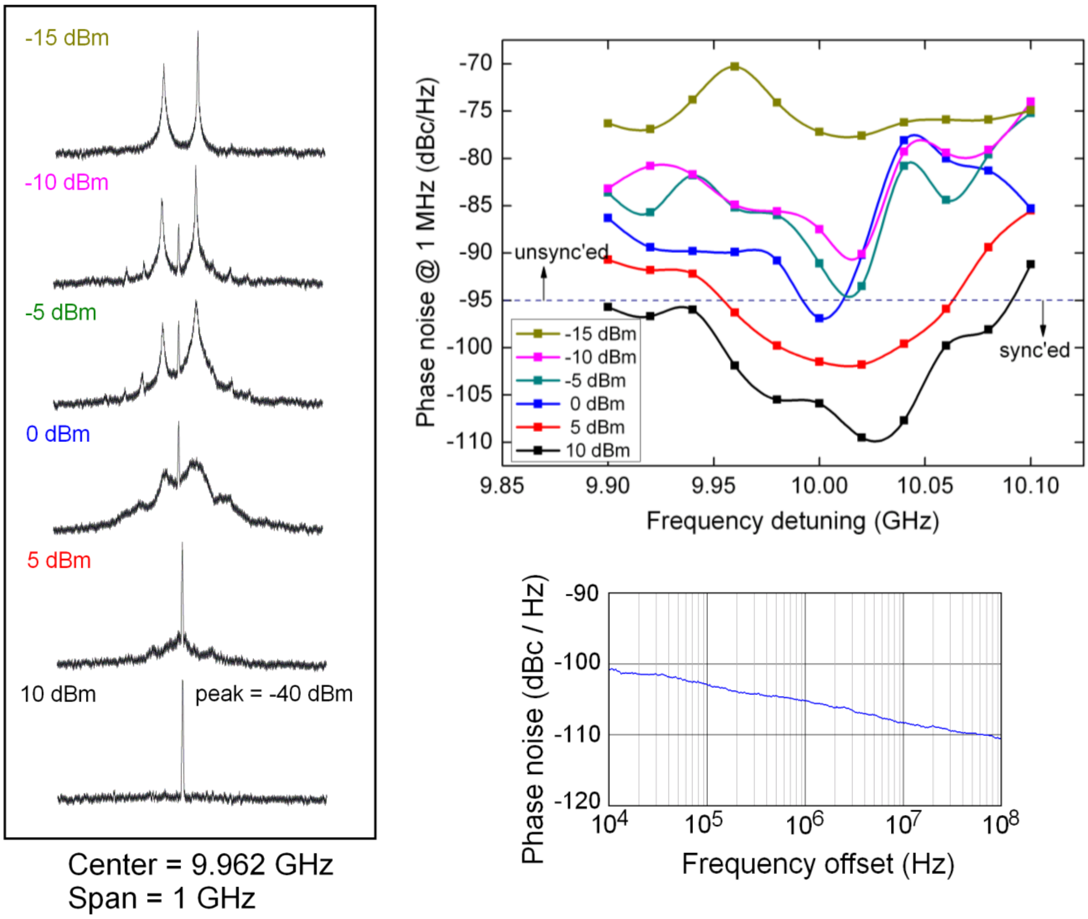

Figure 7.10 (a) RF spectrum of the synchronised output as the injection power was varied from -15 dBm (top trace) to 10 dBm (bottom trace), in steps of 5 dBm, (b) the corresponding locking range as the power was varied, and (c) phase noise of the synchronised lasers at 10 dBm injection power.

According to [20], a laser is considered to be suitably locked when the phase noise level falls below -95 dBc/Hz at an offset of 1 MHz from the peak of the signal. Therefore to calculate the locking range, the phase noise was measured rather than the linewidth. At 10 GHz, using an injection power of 10 dBm, the phase noise was -105.6 dBc/Hz at an offset of 1 MHz (Fig. 7.10(c)). Subsequent measurements were taken across the frequency detuning of 1 GHz at 100 MHz intervals as the injection power was varied. The resulting phase noise plots are shown in Fig. 7.10(b). Using this method, a locking range of ~700 MHz was measured with 10 dBm injection power, which was reduced to ~500 MHz when the power fell to 5 dBm. At 0 dBm injection power, the laser was only locked when positioned precisely between the mode-locking frequencies of the MLLDs, and was otherwise unable to pull the independent oscillations together. An autocorrelation trace is shown in Fig. 7.11, for the unsynchronised (top green trace) and synchronised (bottom blue trace) output signal. It is evident that the autocorrelation trigger was only locked to a single, more dominant laser. Two peaks are distinctly shown when the lasers were free running simultaneously, although an elevated noise floor (pedestal) was present, which may be due to the untriggered signal of the second MLLD. When the optical injection was applied, the noise floor was removed, which indicates that the lasers were suitably locked in phase. The pulse width of the combined synchronised signals was 3.14 ps (figure 7.11), assuming a sech^2 pulse shape, which is less than the free running value of 5.39 ps.

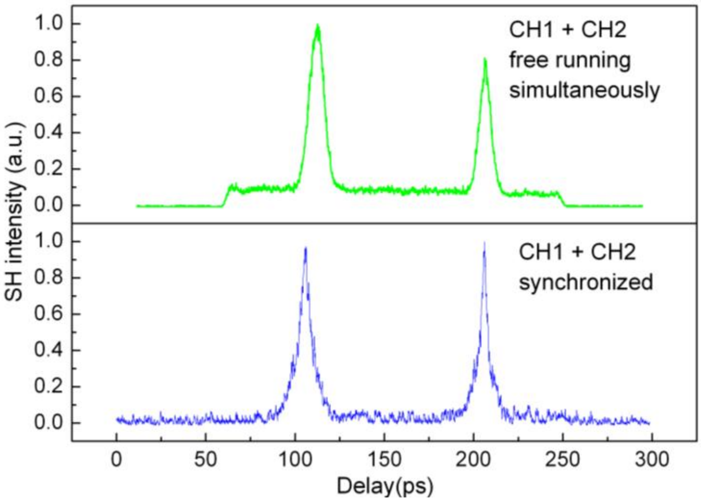

Figure 7.11 SHG autocorrelation traces of 2 lasers free running simultaneously (top green trace) and after synchronisation (bottom blue trace).

7.4 Time spreading techniques

So far, the wavelength hopping functionality has been experimentally established, however, due to the predetermined nature of the integrated circuit design, (the fixed length waveguides), the facilitation of temporal spreading required an externally controlled delay to implement a fully functional WHTS system. In order to achieve this, various techniques can be used. One method which is viable is to implement electronic delays, as described in section 7.2. This method is synonymous to the hybrid mode-locking experiments performed in chapter 5, where an impedance matching microstrip was used to carry a high frequency electrical signal to the SA section of a MLLD. For the WHTS application however, multiple microstrips are required, with a line spacing identical to that of the MLLD spacing on chip. Furthermore, the electrical path lengths for each microstrip line is required to be shifted by π, such that the trigger time for each pulsed produced by the MLLDs is shifted adequately without overlapping. Thus, the collective frequency of the pulses at the output of the integrated circuit is $f_c = N_a \times f_{MLLD}$, where N_a is the number of lasers in the array, and f_{MLLD} is the pulse repetition frequency of the lasers.

A microstrip delay line was thereby designed with two delay paths. This was based on both the branchline coupling method [16] and the two-port Wilkinson power splitter [17] techniques. The designed circuit was optimised using the microstrip design tool Advanced Design Systems™ 2008 accompanied by the *S*-parameter simulation tool Momentum™. The design is shown in Fig. 7.12, and Fig. 7.13 subsequently shows the microstrip layout.

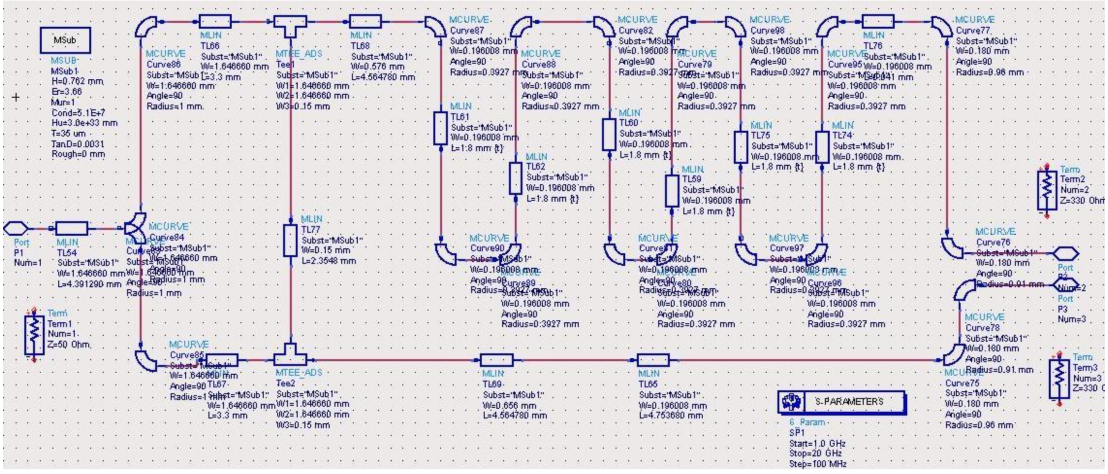

Figure 7.12 Design of the 1:2 port microstip circuit designed using ADS 2008.

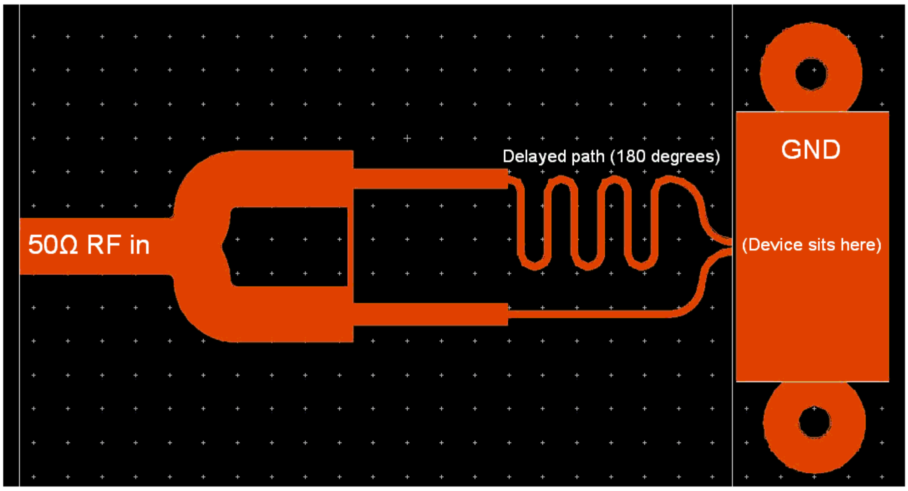

Figure 7.13 Corresponding microstrip design as viewed in Momentum.

The path lengths were varied to accommodate a difference of 180° (i.e. π) between two adjacent MLLDs. The power was almost equally divided between both output channels, which was important so that both lasers were given the same amount of RF power. Figure 7.14(a) shows the simulated S_{21} intensity of -3.2 dB, and the S_{31} intensity was -3.5 dB at 10 GHz. Importantly, the reflected S_{11} power was suppressed by over 25 dB at 10 GHz. The strip-lines were simulated at 50 (port 1) to 330 Ω (port 2) to match the resistance of the SA sections, to which the electrical signal would be applied. Due to the change in the impedance, and the small size of the microstip ends, actual *S*-parameter and phase results were not obtained. This would require high frequency matched probes with a small footprint for contact with the strip-line ends for network analysis to be performed. Nonetheless, in chapter 5, it was confirmed experimentally that the Momentum simulation tool was somewhat reliable at predicting *S*-parameters on the Rogers8000™ microstrip substrate. The advantage of this technique is that it is relatively compact and easy to package, since there are no extra parts.

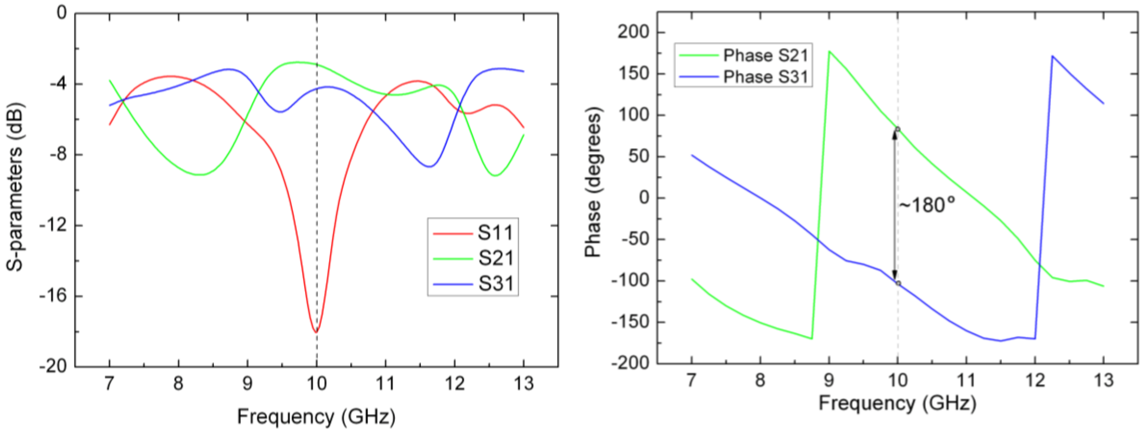

Figure 7.14 (a) Simulated *S*-parameters in Momentum, and (b) corresponding phase offset simulation results.

Another option for time spreading is to implement all-optical delays. Similar to the SML methods shown in section 7.4, an optical pump laser could be driven to trigger each laser at different times using optical fibre based delay lines, a schematic of which is shown in Fig. 7.15. This relatively simple method requires an optical circulator to feed back the output of a synchronised laser towards the next laser, arriving aptly at a time delay of π. This effect can be cascaded to work on multiple lasers in the array, by simply feeding multiple and appropriate length delay lines to each laser. This technique also requires efficient power splitting of the circulated signal, as well extremely stringent alignment of a lensed fibre array, which must be matched to the spacing of the optical modes of each laser. The advantage of this method is that all optical synchronisation is much easier to perform than hybrid mode-locking due to the low power requirements, large locking range, and no impedance matching issues, and can therefore be considered a much simpler method of achieving time spreading for this particular integrated OCDMA circuit.

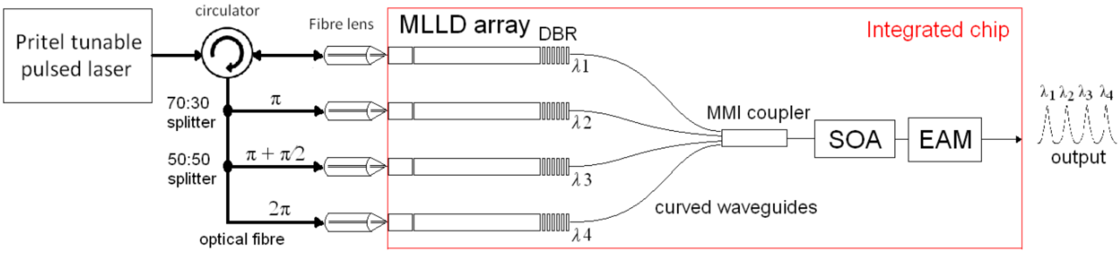

Figure 7.15 Schematic of the experimental setup required for all-optical clock synchronisation for WHTS based OCDMA.

7.5 Chapter summary

A multiwavelength laser array was designed and fabricated to operate primarily as an optical transceiver circuit for a WHTS OCDMA system. The laser consisted of four mode-locked DBR lasers which were coupled into a single channel using a MMI combiner, which led to a SOA and EAM section for subsequent data encoding. The integrated chip was shown to function with all the lasers running simultaneously at discrete wavelengths – an important criterion for WHTS OCDMA. However since each laser was effectively operating independently with no phase coherence, synchronisation to a single clock frequency was required. Synchronisation of two lasers was established by optical injecting 700 fs actively mode-locked pulses into the EAM side of the device. This served as a system clock signal which was distributed to each laser via the on chip MMI splitter. The pulses generated by the two lasers were locked in phase at the same fundamental frequency, which is essential for WHTS OCDMA systems where pulse timing is critical for the accurate provisioning of time-hopping sequences. A locking range of ~700 MHz was achieved using an injection power of 10 dBm. The noiseless autocorrelation trace indicated that the pulses were temporally overlapping and thus suitably locked to a single frequency. For code sequence generation using this system, a microstrip delay line was designed to incorporate the time-spreading functionality. The delay lines consisted of two channels, spaced apart by 250 μm (similar to the spacing between adjacent laser SA sections). The channels were phase shifted apart by 180°, potentially enabling each laser to be clocked at a π phase difference of an electrically injected signal. Using this method, the output pulses from the lasers, operating at different wavelengths, can be temporally spread according to a predefined coding sequence. These results indicate the potential of the laser array based WHTS systems, although more optimisation is required to minimise channel cross-talk and heating, which was a severely limiting factor during these experiments.

7.6 References

[1] G. C. Yang, and W. C. Kwong, "Prime codes with application to CDMA optical and wireless networks," Norwood: Artech House, 2002.

[2] L. Tancevski, and I. Andonovic, "Wavelength hopping/time spreading code division multiple access systems," Electron. Lett., Vol. 30, No. 9, pp 721-723, 1994.

[3] S. P. Najda, and J. H. Marsh, "Laser printing: laser arrays transforming printing," Nature Photon., Vol. 1, pp 387-389, 2007.

[4] B. G. Lee, M. A. Belkin, R. Audet, J. MacArthur, L. Diehl, C. Pflugl, and F. Capasso, "Widely tunable single-mode quantum cascade laser source for mid-infrared spectroscopy," App. Phys. Lett., Vol. 91, pp 231101, 2007.

[5] M. G. Young, T. I. Koch, U. Koren, D. M. Tennant, B. I. Miller, M. Chein, and K. Feder, "Wavelength uniformity in λ/4 shifted DFB laser array WDM transmitters," Electron. Lett., Vol. 31, No. 20, pp 1750-1752, 1995.

[6] C. L. Tang, C. F. Lin, T. Fujita, and A. Schremer, "Rapid beam scanning using a mode-locked laser-driven laser array," IEEE J. Quant. Electron., Vol. 24, No. 10, pp 1955-1957, 1988.

[7] L. Davis, M. G. Young, D. Dougherty, S. Keo, R. Muller, and P. Maker, "Multi-wavelength arrays of mode-locked lasers for WDM applications," Electron. Lett., Vol. 34, No. 19., pp 1858-1860, 1998.

[8] W. J. Minford, S. K. Korotky, and R. D. Alfferness, "Low-loss Ti:LiNbO3 waveguide bends at 1.3 μm," IEEE J. Quant. Electron., Vol. 18, No. 10, pp 1802-1806, 1982.

[9] A. J. Collar, G. D. Henshall, J. Farre, B. Mikkelsen, Z. Wang, L. Eskildsen, D. S. Olesen, and K. E. Stubkjaer, "Low residual reflectivity of angled-facet semiconductor laser amplifiers," IEEE Photon. Technol. Lett., Vol. 2, No. 8, pp 553-555, 1990.

[10] L. Hou, R. Dylewicz, M. Haji, P. Stolarz, B. Qui, and A. C. Bryce, "Monolithic 40 GHz passively mode-locked AlGaInAs/InP 1.55μm MQW laser with surface etched distributed Bragg reflector," IEEE Photon. Technol. Lett., Vol. 22, No. 20, pp 1503-1505, 2010.

[11] R. Hanfoug, L. Augustin, Y. Barbarin, J. van der Tol, E. Bente, F. Karouta, D. Rogers, S. Cole, Y. Oei, X. Leijtens, and M. Smit, "Reduced reflections from multimode interference couplers," Electron. Lett., Vol. 42, No. 8, pp 465-466, 2006.

[12] A. E. Kelly, "Optimisation of semiconductor optical amplifiers for optical networks," Ph.D. thesis, University of Strathclyde, 1999.

[13] L. Hou, M. Haji, R. Dylewicz, B. Qui, and A. C. Bryce, “10 GHz mode locked extended cavity laser integrated with surface-etched DBR fabricated by quantum-well intermixing,” IEEE Photon. Technol. Lett., Vol. 23, No. 2, pp 82-84, 2011.

[14] N. Dagli, “Wide bandwidth lasers and modulators for RF photonics,” IEEE Trans. Microwave Theory and Techniques, Vol. 47, No. 7, pp 1151-1171, 1999.

[15] Z. Ahmed, H. F. Liu, D. Novak, Y. Ogawa, M. D. Pelusi, and D. Y. Kim, “Locking characteristics of a passively mode-locked monolithic DBR laser stabilized by optical injection,” IEEE Photon. Technol. Lett., Vol. 8, No. 1, pp 37-39, 1996.

[16] Microwaves101, “Wilkinson power splitters,” (Online) Available from: http://www.microwaves101.com/encyclopedia/Wilkinson_splitters.cfm [Accessed 19 September 2011].

[17] Microwaves101, “Branchline couplers,” (Online) Available from: http://www.microwaves101.com/encyclopedia/Branchline_couplers.cfm [Accessed 19 September 2011].

[18] K. Wang, J. Li, S. Popov, and G. Jacobson, “4x40 GHz multi-colored optical pulse generation using single two-arm modulated Mach-Zehnder modulator,” Asia communications and exhibitions technical digest, paper TuE4, 2009.

[19] J. Liu, et al, “Waveguide integrated, ultralow energy GeSi electro absorption modulators,” Nature Photon. Lett., Vol. 2, pp 433-437, 2008.

[20] A. Nirmalathas, H. F. Liu, Z. Ahmed, D. Novak, and Y. Ogawa, “Subharmonic Synchronous and Hybrid Mode-Locking of a Monolithic DBR Laser Operating at Millimeter-Wave Frequencies,” IEEE Photon. Technol. Lett., Vol. 9, No. 4, pp 434-436, 1997.

Chapter 8

Conclusions

This research was primarily focused on the development of integrated optical code division multiple access (OCDMA) systems using the *AlGaInAs/InP* semiconductor material system. This material was considered due to its excellent intrinsic properties for fabricating optoelectronic devices, compared with the conventional *InGaAsP/InP* material system. The well-known passivation technique known as quantum-well intermixing (QWI) was used for increasing the bandgap of the material, postgrowth, allowing multiple sections on a chip to be used as passive components such as waveguides, couplers and distributed Bragg reflectors (DBRs). Two OCDMA systems were fabricated on the *Al*-quaternary substrate, both with integrated optical sources and embedded en/decoding functions.

The first system considered in this research was based on the coherent temporal-phase coded (TPC) OCDMA method. A semiconductor ring laser (SRL) was monolithically integrated with an asymmetric 2×2 Mach-Zehnder interferometer (AMZI) with phase shifters situated on each arm. A 2-bit binary phase code could then be applied, supporting up to four simultaneous users. Since coding is performed statically in this system, faster pulse repetition rates could be used to enable extremely high speed operation (albeit limited by the chip period defined by the delays). The second system was based on the incoherent wavelength-hopping time-spreading (WHTS) OCDMA technique, which is distinguishable from all other schemes of OCDMA due to its two-dimensionality, allowing it to accommodate more users with shorter codes and more efficient bandwidth provisioning. A mode-locked laser array was combined with a multimode interference coupler, leading to a semiconductor optical amplifier (SOA) and electroabsorption modulator (EAM). Both of these systems were designed and characterised to demonstrate their potential for use in high speed transmission systems.

This chapter will provide a general summary of the thesis and include a discussion about the main achievements of this research, as well as suggestions for further work to be performed.

8.1 Research summary

8.1.1 Absorption in *AlGaInAs/InP*

Since the *Al*-quaternary material system is relatively immature, some characterisation was required in order to better understand the absorption properties while undergoing a reverse bias. This involved using the well-known pump-probe technique for cross-absorption modulation (XAM). A short (50 μm) waveguide sample was used and injected with a continuous wave (CW) signal (probe) along with high power pulses (pump) operating at another wavelength. A variable bias was then applied to the sample while the reflected signal was observed in the time domain after filtering out the pump and leaving the probe. An exponentially decaying pulse was detected on a high speed oscilloscope, and the time of this decay was reduced (also exponentially) as the applied reverse bias was increased. An absorption recovery time of less than 3 ps was observed at voltages less than -4 V, which is relatively fast compared with the reported recovery times of the *P*-containing QWs, although the applied electric field was greater in this experiment.

These results provide an insight into the short pulse generation in *Al*-quaternary based MLLDs, as well as high speed EAMs for use in integrated optical systems. A 3 ps absorption time can lead to data modulation speeds of up to ~300 GHz. Moreover, using the pump-pulse setup described, all-optical gating techniques can be developed, which is important for MAI filtering at the receiver circuit of OCDMA systems.

8.1.2 Mode-locked laser characterisation

During this research, a number of mode-locked lasers were fabricated as part of a project run simultaneously by fellow researchers. The remit of this project was to develop high power semiconductor mode-locked lasers [1]. As a result, several types of mode-locked lasers were available for measurement and experimentation, which lead to the characterisation of high speed, narrow pulsed lasers that were suitable for use in OCDMA systems. The most relevant ones were discussed in chapter 4. In particular, the 1.5 μm range 10 GHz lasers integrated with DBR and phase sections was useful for its ability to finely tune the wavelength and pulse repetition frequency. This was integrated into the WHTS OCDMA system as a result. Using this laser, pulse widths of less than 4 ps at were achieved with a ~2 nm wavelength tunability and ~30 MHz pulse repetition rate tunability.

Another important laser feature was to generate high frequency pulse repetition rates (>100 GHz). This was demonstrated using harmonic mode-locked lasers, and two methods of which were explored and described in chapter 4: compound cavity (CCM), and colliding pulse mode-locked lasers (CPM). Pulse repetition rates of 160 GHz were achieved with high quality 980 fs pulses without any evidence of *Q*-switching or pedestal modulation (a frequent occurrence in high frequency lasers due to the overlap of neighbouring pulses). Of the two types of lasers, the CPM was shown to have better mode selection of the compound cavity, leading to a wider operating range. On the other hand, higher repetition rates have been reported using the CCM approach due to the higher order harmonic selection using intercavity mirrors.

8.1.3 Pulse stabilisation methods

Due to the large noise presence in passively mode-locked lasers, predominantly caused by spontaneous emission, it was important to stabilise the temporal behaviour of the pulse oscillations by synchronisation to an external clock. This was achieved using both optical and electrical injection methods, which are better known as synchronous (SML) and hybrid mode-locking (HML), respectively. Of the two techniques, SML was shown to be more able to influence the fundamental frequency of the passive mode-locking oscillation for stability. This technique was particularly useful when synchronising to higher order harmonics, due to the strong harmonic generation of the injected optical pulses. During these experiments, the fourth order harmonic was used (~9 GHz), and a locking range of ~600 MHz was measured at 36 GHz with a RF linewidth less than 1 kHz using an average injection power of 0 dBm. This was significant to this research as it meant that a number of oscillations within the locking range could effectively be pulled towards a single frequency. Therefore a configuration involving many oscillations such as the mode-locked laser array in the WHTS OCDMA system (chapter 7) could be synchronised in phase, even when using a subharmonic injection frequency. The effortlessness of synchronisation using high order subharmonic injection makes this technique particularly suitable to operate at frequencies well above 40 GHz.

On the other hand, HML was shown to withstand synchronisation attempts when using higher subharmonic orders (the fourth harmonic at 9 GHz was tried). This was due to the weak harmonic generation of the electrical signal being injected. Frequency pulling at the fundamental frequency was achieved using the *Q*-switching oscillation of the laser, and a tuning range of 800 MHz was achieved with a high injection intensity at 10 dBm. Since very high frequency electrical clocks are scarce, HML is more suited for synchronising frequencies less than 20 GHz.

Also during this research, a passive alternative method for stabilisation and jitter reduction was explored (the term passive is used here to imply an ‘RF injection free’ operation). This technique was borrowed from the *Q*-factor enhancement methods used in optoelectronic oscillators which use long lengths of optical fibre for storing the oscillation energy. By feeding the output of the laser back into itself using a fibre loop, the memory of the phase could be extended, and in turn, the noisy fluctuations would improve. This noise reduction was enhanced further with the addition of a composite cavity. The primary function of this cavity was to reduce the supermode noise artefacts presented due to harmonic mode-locking effects in the fibre loop. Using this technique, with a 66 m long dispersion shifted fibre loop, a record low linewidth of 192 Hz was achieved, making it a promising tool for use as an all-optical system clock.

8.1.4 Integrated coherent TPC-OCDMA system

The integrated TPC-OCDMA system consisted of a SRL embedded with a 2×2 AMZI with two MMI couplers and phase shifting arms for encoding the pulses during propagation. QWI was used to passivate the waveguide arms of the AMZI and the MMI couplers. The integrated system was characterised by biasing the SRL to stimulate mode-locking, while observing the output of the AMZI. Due to the high material losses presented as a result of QWI exposed passive regions and material diffusion from heating, the output power was substantially reduced at the AMZI facet. However, after using a more sensitive linear intensity autocorrelation setup, the pulses were shown to split into two peaks, separated by a distance corresponding to the predefined delay. This confirmed the temporal spreading capability of the AMZI.

To characterise the laser’s phase coding abilities, a back-to-back design of the AMZI was used to serve as both an encoder and decoder on the same chip. An external high power mode-locked fibre laser was used as the optical source, which was injected into the SRL facet. After propagation through both the AMZIs, the signal was fully reconstructed at the output. Unmatched coding was demonstrated by applying a phase shift to only one of the AMZI arms, such that the coupling at the subsequent MMI coupler was unbalanced, causing the signal to destructively interfere with itself and thus, no signal was observed at the output. On the other hand, by applying a complementary phase shift to the second AMZI (decoder), the balance was restored in the MMI coupler, promoting a reconstruction of the original pulse sequence. Thus, the encoding and decoding of the signal using 2-bit binary phase codes were successfully demonstrated. This system could potentially be extended to employ several more AMZI arms to increase the number of users in the system. But first, there are a few fabrication issues that must be addressed.

8.1.5 Integrated incoherent WHTS-OCDMA system

The integrated WHTS-OCDMA consisted of four mode-locked laser diodes, each operating at a different wavelength separated by ~5 nm, with integrated DBRs and phase sections for fine tuning the wavelength and pulse repetition frequency, respectively. The outputs of all channels were then combined using an integrated 4×1 MMI coupler, which led to a single waveguide which included a SOA and EAM. The system was characterised by passively operating each laser individually, and then simultaneously while observing the output at the EAM side of the chip. While there was some cross-talk evident between the lasers due to their close proximity and associated thermal effects, four discrete wavelengths were observed by carefully tuning each section of the lasers. Thus, the discrete wavelength formation of the system was demonstrated, showing four independent oscillations, each operating at a different wavelength as required. The output power of the chip was 8 dBm. The EAM was also shown to have excellent extinction ratios for enabling the modulation of all channels with data. Since each laser was functioning independently, the RF spectrum showed four discrete peaks, corresponding to each different laser wavelength. These could be detuned using the phase sections of the laser, although too much detuning would disturb the wavelength stability.

The lasers were then synchronised to a single frequency, using the effective SML technique. In order to access each laser with the synchronising signal, the master laser was injected through the EAM side of the device, and a circulator was used to isolate the synchronised output. While operating two lasers in the laser array, and injecting the pump signal at a pulse repetition frequency directly between them, synchronisation was established after increasing the pump signal intensity to > 0 dBm. A single peak was observed in the RF spectrum with a linewidth of < 1 kHz. The locking range was 700 MHz at an injection power of 10 dBm, all in which the phase noise was less than -95 dBc/Hz at a 1 MHz offset. The two wavelength peaks remained unchanged in the optical spectrum, and the noiseless autocorrelation trace indicated the simultaneous operation of the lasers synchronised in time to an external clock signal. Thus, the wavelength spreading and time synchronous capabilities of the integrated chip were demonstrated, and the potential for this type of system to be used in WHTS was shown. Temporal spreading using electrical and optical delay lines were also discussed.

8.2 Future work

Future works recommended as a follow up to this PhD study are outlined below:

All optical gating using XAM

- Due to its simplicity and potential integratability, using the XAM method (used in chapter 3 for determining absorption recovery times in *AlGaInAs/InP*) for all optical time gating is something which should be explored as an alternative to the fibre based gating methods. One method of executing this would be to use a MLLD as a pump pulse stream (control), integrated with an EAM which includes an addition port (through an MMI combiner) in which incoming data stream can be injected. This device can be positioned within the receiver circuit to minimise multi-access interference (MAI).

Optical fibre loop feedback

- Although a record low RF linewidth has already been achieved using the mode-locked laser feedback via fibre loop architecture (described in chapter 5), there are still a number of ways to improve this. It is particularly worth attempting to reduce the fibre losses by using a suitable intermediate dispersion fibre between the standard single mode and dispersion shifted fibre (or perhaps replacing all fibre with dispersion flattened fibre, although this may be more costly). This would allow for a reduction in the EDFA pump power, which is a source of ASE, and should improve the linewidth and phase noise.

- Bidirectional feedback may also be an interesting experiment worth exploring. A CPM laser can be used as the pulse generating source with the SA section positioned in the middle of the laser cavity, and a fibre loop to provide the bidirectional feedback. Such configuration may provide exceptional phase noise reductions with shorter fibre lengths.

- The feedback design can also be integrated, although with a limited feedback length. To accommodate longer lengths, QWI can be used to fabricate a racetrack or snail type waveguide loop, which can be fed back towards the SA section of the laser. This may be useful for on-chip passive phase noise improvements.

TPC-OCDMA system

- The detrimental effects caused by erroneous QWI procedures made the AMZI en/decoders extremely lossy due to the high interband absorption. It would be beneficial if this could be investigated further, and the QWI method optimised for accurately defining passive regions on a chip. Another solution is to add SOAs around the waveguide arms to boost the signal intensity while propagating through the AMZI, although this may complicate the fabrication and testing processes further by adding more components.

- An EAM section may also be added to the TPC-OCDMA system after the MLLD to allow data modulation before encoding.

- The experimental criterion for validating the use of a TPC-OCDMA system is a field trial testing of two separate integrated en/decoder chips to establish high speed coded data communications with low bit error rates.

WHTS OCDMA system

- Using the microstrip designs for providing four strip lines out of phase by 90°, it would be interesting to see whether a time-hop code could be added to the WHTS-OCDMA system.

- Adding EAMs to each channel for direct code modulation, eliminating the need for microstrip embedding. Although the system would still require some form of clock synchronisation, in which case an investigation into channel syncing would be advantageous. One probable solution is to use an intracavity reflector along the path splitter after the MMI combiner, providing a reflection of the channels back into themselves. This way, only one channel requires synchronisation for all channels to be temporally aligned.

- Testing the circuit as a receiver requires the SA section of the lasers to be used as photodetectors. A study into electrically extracting pulses from this material would be highly useful for understanding how to optimise the same transmission circuit for receiving signals also.

- The experimental criterion for validating the use of a WHTS-OCDMA system is a field trial testing of two separate integrated en/decoder chips to establish high speed coded data communications with low bit error rates.

8.3 Other technologies

Fully functional integrated OCDMA systems still require a lot of work before any real implementations arise. At present, current access technologies are more than capable of performing network tasks, given the current demand for bandwidth. Recently, orthogonal frequency division multiplexing (OFDM) based optical networks have been touted for use in ultra-high bit rate networks in the near future [2]. Data rates of 26 Tbit/s have recently been demonstrated using a highly nonlinear fibre with wavelength selective switched sent through a 16-QAM subcarrier system before being multiplexed via polarisation at the transmitter circuit. The receiver circuit consisted of a cascaded AMZI system for demodulating the 16-QAM aspect through Fourier transformation before entering an EAM gate for subsequent demultiplexing. It is evident that this system is fairly complex and a full-integration will be an immense challenge. Furthermore, OFDM systems do not incorporate the physical layer security that comes naturally with OCDM systems.

In contrast, optical steganography is a relatively new method that is being heavily researched due to its data ‘hiding’ attributes [3]. This is achieved by stealthily burying the transmitted signal under the noise presented in a network. Optical fibres with high group velocity dispersion is used for temporally stretching the data pulses before transmitting the signal through a network; and at the receiver, a fibre with the opposite slope of dispersion is used to revive the data stream [4]. In [3], this technique was used in tandem with spectral amplitude coded (SAC) OCDMA techniques, for adding another dimension to the security measures. Although several km of dispersive fibre was used in this technique, a miniaturised version could possibly include a pair of Bragg gratings for pulse stretching and compression. This will require a large amount of chirp, which could possibly be performed in semiconductor by varying the refractive index profile of a DBR using multiple grating segments. This may be something to consider in future when developing OCDMA systems.

8.4 References

[1] A. C. Bryce, et al. ESPRC grant. URL : http://gow.epsrc.ac.uk/ViewGrant.aspx?GrantRef=EP/E065112/1.

[2] D. Hillerkuss, R. Schmogrow, T. Schellinger, M. Jordan, M. Winter, G. Huber, T. Vallaitis, R. Bonk, P. Klienow, F. Fray, M. Roeger, S. Koenig, A. Ludwig, A. Marculescu, J. Li, M. Hoh, M. Dreschmann, J. Meyer, S. Ben Ezra, N. Narkiss, B. Nebendhal, F. Parmigiani, P. Petropoulos, B. Resan, A. Oehler, K. Weingarten, T. Ellermeyer, J. Lutz, M. Moeller, M. Huebner, J. Becker, C. Koos, W. Freude, and J. Leuthold, "26 Tbit s^{-1} line-rate super-channel transmission utilizing all-optical fast Fourier transform processing," Nature Photon., Vol. 5, pp 364-371, 2011.

[3] P. R. Prucnal, M. P. Fok, K. Kravtsov, and Z. Wang, "Optical steganography for data hiding in optical networks," 16th Int. Conf. Digital Sig. Processing, pp 1-6, 2009.

[4] Z. Wang, and P. R. Prucnal, "Optical steganography over a public DPSK channel with asynchronous detection," IEEE Photon. Technol. Lett., Vol. 23, No. 1, pp 48-50, 2011.